N° d'ordre : 919

UNIVERSITÉ CLERMONT AUVERGNE
U.F.R. Sciences et Technologies

KARLSRUHER INSTITUT FÜR TECHNOLOGIE
Fakultät für Physik

ÉCOLE DOCTORALE DES SCIENCES FONDAMENTALES

THÈSE

présentée pour obtenir le grade de

DOCTEUR D'UNIVERSITÉ
Spécialité : Physique de l'Atmosphère

par **Thibault HIRON**
Diplômé du Master Sciences des Matériaux, spécialité Physique et Chimie pour l'Environnement

---

Experimental and modeling study of heterogeneous ice nucleation on mineral aerosol particles and its impact on a convective cloud

---

Soutenue publiquement le 29 septembre 2017 devant le jury composé de:

Président	M.	Wolfram WOBROCK	Professeur, UCA, Clermont–Ferrand Laboratoire de Météorologie Physique
Rapporteur.e.s	Mme.	Corinna HOOSE	Professeure, KIT, Karlsruhe Institut für Meteorologie und Klimaforschung — TRO
	Mme.	Évelyne RICHARD	Directrice de recherche, CNRS, Toulouse Laboratoire d'Aérologie
	M.	Miklós SZAKÁLL	Docteur HDR, JGU, Mayence Institut für Physik der Atmosphäre
Directrice de thèse	Mme.	Andrea FLOSSMANN	Professeure, UCA, Clermont–Ferrand Laboratoire de Météorologie Physique
Directeur de thèse	M.	Thomas LEISNER	Professeur, KIT, Karlsruhe Institut für Meteorologie und Klimaforschung — AAF

Acknoledgments

It is now time to put an end to what have been overall seven intense enriching years, from the first time I touched the cold stage at the IMK–AAF to the day I wrote the final words of this manuscript.

A PhD is first and foremost the first professional experience in academic research, and I would like to thank my supervisors, Andrea Flossmann and Thomas Leisner for all I have learned in these last years. My work has been structured in the beginning around the cold stage experiment and it has not always been easy to balance the two parts of the thesis. Andrea's level of requirement, patience and kindness were essential in the advancement of the modeling work. Particularly, her trust in the evolution I gave to the thesis subject and the developments of DESCAM were crucial, significantly when I would spent weeks debugging the source.
This entire adventure started with a very prompt response from Thomas Leisner to my internship request. The cold stage was my first contact with atmospheric research and his advice, attention and trust were decisive in my further academic training. I immediately felt welcome at the institute and coming back for my PhD to further develop the cold stage was a natural outcome of the internship. In spite of his very demanding head of the institute position, he found time to help me to see through the experimental process and the analysis of my data.
Finally, I would like to thank warmly Alexei Kiselev. I am amazed by his capacity to find a solution to every problem in the lab and the richness of his ideas for developments of the experimental setup. It was always a pleasure to work with him and his perpetually uplifting mood.

I would like to thank my three referees, Corinna Hoose, Évelyne Richard and Mikló Szakáll for taking the time to review my manuscript in such a short time during the vacations season. Their remarks on the manuscript and my work were priceless, particularly the thorough reviewing by Corinna which lead to substantial improvements in my presentation of the modeling study.
I would also like to thank Wolfram Wobrock for presiding the defense committee and for the discussions we had during my time at the LaMP.

If I returned to Karlsruhe, the cohesion and atmosphere in the institute played a non–negligible role. There is always something going on and this makes every single day interesting!
I particularly want to thank Susanne, as without her help and care, things would have not been the same. Her door was always open and it was a pleasure to sometimes meet

by chance at the Staatstheater. The German administration is still a mystery to me, but she helped me get things right.
Thank you to Andreas and Nadine for their precious help in the lab and of course thank you to Annika, Denis, Fritz, Jens, Mario, Martin, Paul, Shirley, Thea, Tobias and Wei for the discussions and various plans.
Finally I would like to thank all the researchers of the institute who helped me on different occasions as well as the technical team whose precious help has been many times needed with all the ongoing developments on the experiment.

Thank you Marie for helping me get a foot on the DESCAM ladder. A particular thanks to Céline, for the late boosting chats when I was a struggling first year PhD student and for her precious advice while I was finalizing my defense presentation.
I would finally like to thank all the researchers I got to interact with during those years in Clermont and to the administrative staff and particularly Florence whose help was valuable in dealing with all the surprises of a joint PhD program.

Quatre ans dans un bureau, six collègues différents au gré des années. Une pensée particulière pour Aurélien, Jimmy et Alexandre qui ont été plus que des co–bureau. En plus de l'ambiance toujours positive qui régnait dans le bureau, ils ont eu la gentillesse de m'héberger lorsque je revenais à Clermont pour une semaine par–ci, par là alors que je résidais en Allemagne.
Merci à Christina pour sa gentillesse, pour les innombrables discussions que nous avons pu avoir et pour son soutien indéfectible dans les moments difficiles. Merci aussi à Hélène pour nos échanges qui rompaient agréablement la monotonie des journées de rédaction.
Merci enfin à l'ensemble des collègues, Alexis, Anaïs, Brice, Dani, Gwennolé, Ibrahim, Kevin, Pierre et Tony.

Je garderai toujours en mémoire la générosité et la gentillesse de Paméla et Pierre qui m'ont accueilli pendant la préparation de la soutenance alors que j'avais rendu tout logement à Clermont. Ma porte vous sera toujours ouverte!

Nombre de mes nuits d'itinérance rédactionnelle à Clermont on été rendues possibles par Pierre, généralement associées de virées chez Hicham ou Barrique, toujours des plus agréables.
S'il y a eu de l'itinérance à Clermont, il y eut aussi de nombreuses nuits en transit, dans cette même ville, mais aussi à Karlsruhe, Paris, Lausanne et Lyon. Je tiens donc à remercier pour leur précieux accueil Alexis et Andreea, Alice, Benoît et Cécile, Bérénice, Carmen, Charlotte, Élise, Gelincik, Guillaume et Tania, Jean, Sénior, Jean–Marie, Kwami, Laurent, Manon, Mickaël, Nolwenn, Sabine et Christophe, Stachou, Thalia, Bichon et Yann-Ké. Merci aussi à Faustine de m'avoir mené de ville en ville.

Je ne serais peut–être jamais arrivé à Karlsruhe sans Anne–Sixtine, son aide dans la recherche du stage a été précieuse. Elle m'a ouvert bien des portes et appris bien des choses.

Pour se ressourcer pendant une thèse qui peut souvent être éprouvante, rien de tel qu'un festival de Marciac et l'ambiance délirante qui règne au sein des bénés et les amitiés qui peuvent s'y sceller. Merci à Adrien, Antonin, Arnaud, Carmen, Charlotte, Gauthier, Hanna, Julie, Julien, Louise, Luke, Mathilde, Mickaël, Pierre, Thalia, Thomas et la famille Menu.
Et qui dit jazz dit HLM Trio, Jean et Cédric, merci pour tout! Nul ne sait où sera la prochaine session, mais la distance n'a jamais été un problème.

Enfin, un très grand merci aux Pottier, aux Hiron et aux Bédiée pour toutes ces semaines passées ensemble même lorsque j'avais la tête dans les nuages.
Merci à Christiane pour son accueil toujours chaleureux, à Nanou pour son accompagnement dans la préparation de la soutenance, à Stachou pour son stachouisme et à mes parents, Jean, Lucie et Élise pour leur amour inconditonnel, leur générosité et leur soutien indefectible.

Abstract

One of the main challenges in understanding the evolution of Earth's climate resides in the understanding the ice formation processes and their role in the formation of tropospheric clouds as well as their evolution.

A newly built humidity–controlled cold stage allows the simultaneous observation of up to 200 monodispersed droplets of suspensions containing K–feldspar particles, known to be very active ice nucleating particles. The ice nucleation efficiencies of the individual residual particles were compared for the different freezing modes and the relationship between immersion ice nuclei and deposition ice nuclei were investigated. The results showed that the same ice active sites are responsible for nucleation of ice in immersion and deposition modes.

The atmospheric implications of the experimental results are discussed, using DESCAM (Flossmann et al., 1985), a 1.5–D bin–resolved microphysics model in a case study aiming to assess the role of the different ice nucleation pathways in the dynamical evolution of the CCOPE convective cloud (Dye et al., 1986). Four mineral aerosol types (K–feldspar, kaolinite, illite and quartz) were considered for immersion and contact freezing and deposition nucleation, with explicit Ice Nucleation Active Site density parameterizations.

In sensitivity studies, the different aerosol types and nucleation modes were treated seperately and in competition to assess their relative importance. Immersion freezing on K–feldspar was found to have the most pronounced impact on the dynamical evolution and precipitation for a convective cloud.

Keywords: detailed numerical atmospheric modeling, cloud microphysics, aerosol–cloud–precipitation interaction, laboratory heterogeneous nucleation experiments, ice nucleation, INAS densities, mineral aerosol particles.

Résumé

L'un des enjeux principaux dans l'appréhension de l'évolution du climat planétaire réside dans la compréhension du role des processus de formation de la glace ainsi que leur rôle dans la formation et l'évolution des nuages troposphériques.
Un cold stage nouvellement construit permet l'observation simultanée de jusqu'à 200 gouttes monodispersées de suspensions contenant des particles de K–feldspath, connues comme étant des particules glaçogènes très actives. Les propriétés glaçogènes des particules résiduelles de chaque goutte sont ensuite comparées pour les différents modes de glaciation et le lien entre noyau glaçogène en immersion et en déposition est étudié. Les premiers résultats ont montré que les mêmes sites actifs étaient impliqué dans la glaciation par immersion et par déposition.
Les implications atmosphériques des résultats expérimentaux sont discutés à l'aide de Descam (Flossmann et al., 1985), un modèle 1.5–d à microphysique détaillée dans une étude de cas visant à rendre compte du rôle des différents mécanismes de glaciation dans l'évolution dynamique du nuage convective CCOPE (Dye et al., 1986). Quatre types d'aérosol minéraux (K–feldspath, kaolinite, illite et quartz) sont utilisés pour la glaciation en immersion, par contact et par déposition, à l'aide de paramétrisations sur la densité de sites glaçogènes actifs.
Des études de sensibilité, où les différents types d'aérosols et modes de glaciation sont considérés séparément et en compétition, permettent de rendre compte de leurs importances relatives. La glaciation en immersion sur les particules de K–feldspath s'est révélée comme ayant le plus d'impact sur l'évolution dynamique et sur les précipications pour un nuage convectif.

Mots-clés : modélisation atmosphérique numérique détaillée, microphysique des nuages, interaction aérosol–nuage–précipitation, expériences de laboratoire de nucléation hétérogène, glaciation, densités INAS, particules d'aérosol minérales.

Zusammenfassung

Eine der größten Herausforderungen zur Vorhersage des Klimawandels liegt im Verständnis der Rolle von Eisnukleation auf die Entwicklung troposphärischer Wolken.
Mit einer neuentwickelten feuchtigkeitskontrollierten „Cold Stage“wurden bis zu 200 monodispe Tröpfchen, bestehend aus einer K-feldspar Suspension, beobachtet. Die Eisnukleationsfähigkeiten von individuellen Residualpartikeln für Immersionsgefrieren und Depositionnukleation und ihre Wechselwirkung wurden untersucht. Die ersten Ergebnissen zeigten, dass die gleichen eisaktiven Stellen am Immersiongefrieren und an der Depositionnukleation beteiligt sind.
Die atmospährischen Auswirkungen unserer experimentellen Ergebnisse wurden mit DESCAM (Flossmann et al., 1985), einem 1.5D detaillierte Mikrophysikmodell, untersucht in einer Fallstudie zur Rolle verschiedener Eisnukleationsmechanismen auf die dynamische Entwicklung der CCOPE konvektive Wolke (Dye et al., 1986). Vier Mineralaerosoltypen (K-Feldspath, Kaolinit, Illit und Quartz) trugen zum Immersion- und Kontaktgefrieren und zur Depositionnukleation bei durch explizite Ice Nukleation Aktive Stellen Dichte Parametrisierungen.
Die verschiedenen Aerosoltypen und Eisnukleationsmechanismen wurden in Empfindlichkeitsstudien getrennt und zusammen behandelt, um ihre relative Bedeutung zu beurteilen. Immersiongefrieren auf K-Feldspath Partikeln zeigte die größte Wirkung auf eine konvektiven Wolke.

Schtichwörter: detaillierte atmosphärische numerische Modellierung, Wolken Mikrophysik, Aerosol–Wolken–Niederschlag Interaktion, heterogene Nukleation Laborexperimente, Eisnukleation, INAS Dichte, mineral Aerosolpartikeln.

Contents

Appendices

List of Figures

List of Tables

Acronyms

ABO	aerosols of biological origin.
AOD	aerosol optical depth.
ATD	Arizona Test Dust.
CCN	cloud condensation nuclei.
CCOPE	Cooperative COnvective Precipitation Experiment.
CINAS	contact ice nucleating active sites.
CS	Cold Stage.
Descam	Detailed Scavenging Model.
DPM	dew point mirror.
EDB	electrodynamical balance.
ESEM	environmental electron microscopy.
FS02	K–feldspar particles (Bureau of Analyzed Samples, UK, standard BCS 376 — provided by the University of Leeds, UK)..
IMK–AAF	Institute for Meteorology — Atmospheric Aerosol Research division.
IN	ice nuclei.
INAS	ice nucleating active sites.
INNE	integrated number of ice nucleation events.
INP	ice nucleating particle.
IWC	ice water content.
KIT	Karlsruhe Institute of Technology.
LaMP	Laboratoire de Méréorologie Physique.
LWC	liquid water content.
MFC	mass flow controller.
NWP	numerical weather prediction.
RH	relative humidity.
RWC	precipitating liquid water content.
SBM	Soccer Ball Model.
SWC	precipitating ice water content.
UCA	Université Clermont Auvergne.

Notation

a_w	water activity.
C	concentration of K–feldspar particles in the suspension.
ε_a	solubility of the aerosol particle.
f_i	frozen fraction (number of ice crystals with respect to the original total number of droplets — or aerosol particles).
Γ_{cont}	portion of aerosol particles that can act as ice nuclei in the contact freezing mode.
J_{hom}	homogeneous ice nucleation rate.
κ	hygroscopicity parameter.
M_a	molecular mass of the aerosol particle.
$\mathcal{M}_a$	dry aerosol particles mass size distribution.
$\mathcal{M}_d$	aerosol particles in the droplets mass size distribution.
$\mathcal{M}_i$	aerosol particles in the ice crystals mass size distribution.
M_w	molecular mass of water.
$\mathcal{N}_a$	dry aerosol particles number size distribution.
$\mathcal{N}_d$	aerosol particles in the droplets number size distribution.
$\mathcal{N}_i$	aerosol particles in the ice crystals number size distribution.
n_{IN}	number concentration of ice nucleating particles.
N_d	droplets number size distribution.
N_i	ice crystals number size distribution.
ν	number of ions released per molecule.
ϕ_a	osmotic coefficient of the aerosol particle.
$p_{\text{sat},w}$	saturation water vapor pressure over water.
R	universal gas constant.
r_{dry}	radius of the dry aerosol particle.
RH_i	relative humidity over ice (%).
ρ_a	density of the aerosol particle.
ρ''_s	density of the aqueous solution dropt.
ρ_w	density of water.
RH_w	relative humidity over water (%).
r_a	unactivated aerosol particle radius.
r_d	radius of the droplet.
r_i	ice crystal radius.

$\mathcal{S}_a$	dry aerosol particles surface size distribution.
$\mathcal{S}_d$	aerosol particles in the droplets surface size distribution.
$\mathcal{S}_i$	aerosol particles in the ice crystals surface size distribution.
S_{BET}	surface of aerosol particle per unit of mass.
$\sigma_{w,a}$	surface tension between air and water.
S_p	surface of aerosol particle per droplet.
$s_{v,i}$	supersaturation over ice.
$s_{v,w}$	supersaturation over water.
T	temperature.
$T_{50\%}$	temperature at which 50% of the droplets are frozen.
V_d	droplet volume.

Résumé substantiel

Introduction

De façon constante, les dernières années ont été enregistrées comme étant les plus chaudes depuis 1880 (NOAA National Centers for Environmental Information, 2017) et la température moyenne annuelle devrait continuer à augmenter au cours de ce siècle (IPCC, 2013, Summary for Policy Makers). Ce réchauffement climatique s'accompagne de sécheresses sévères sur l'ensemble de la planète (Ault et al., 2014) mais aussi d'inondations de plus en plus fréquentes (Hirabayashi et al., 2013), *etc.* Ces catastrophes naturelles sont un problème de société dans la mesure où elles impactent fortement les ressources alimentaires et les infrastructures. Les inondations et les sécheresses correspondent soit à un excès ou à un manque de précipitations. Par conséquent, la compréhension des mécanismes sous-tendant la formation de la pluie est essentielle pour la prévision météorologique et pour prédire l'évolution des précipitations à l'échelle globale dans des climats changeants.

L'évolution des nuages et l'initialisation des précipitations sont fortement influencées par les particules d'aérosol Flossmann and Wobrock (2012), qui sont définies comme *un ensemble de particules solides ou liquides en suspension dans l'air, dont la taille varie généralement de* 0.01 *à* 10 µm *et qui séjournent dans l'atmosphère plusieurs heures au moins.* [Elles] *peuvent être d'origine naturelle ou anthropique* (IPCC, 2013, Glossary). On remarque ces particules, par exemple, lors de pics de pollution car elles absorbent et diffusent le rayonnement solaire incident de même que le rayonnement tellurique infrarouge. L'interaction des particules d'aérosol avec les rayonnements solaire et tellurique ont un impact sur l'équilibre radiatif de la Terre, appelé effet direct (IPCC, 2013, FIGURE 7.3) ; la différence avec l'équilibre radiatif en 1750 est appelé forçages radiatifs. Selon leur nature, les particules d'aérosol ont des comportements radiatifs différents : les particules qui diffusent le rayonnement solaire incident (notamment les particules de sulfate et de carbone organique) ont tendance à diminuer le forçage radiatif tandis que les particules absorbant le rayonnement (notamment les suies) ont tendance à augmenter les forçage radiatif. Les propriétés optiques de particules d'aérosol et leur impact direct sur l'équilibre radiatif sont largement étudiés (*par exemple* Chauvigné et al., 2016 ; *voir* Yu et al., 2006 pour une revue) et le forçage radiatif net résultant est estimé avec un haut niveau de confiance, mais il reste des incertitudes quant à sa contribution quantitative.

De plus, les particules d'aérosol interagissent avec la vapeur d'eau et fournissent un support sur lequel les nuages se développent et elles ont par conséquent une grande influence sur leur évolution et les précipitations en résultant. La prédiction de ces précipitations est

très importante pour la prévision météorologique : que ce soit pour la prévention d'événements extrêmes comme les orages ou les inondations, ou pour des besoins agricoles, la précision des prévisions est un problème de société. Toutefois, même si les modèles de prévision météorologique numérique (NWP) améliorent en permanence leurs résultats, leur principale faiblesse reste dans l'exactitude temporelle et spatiale des précipitations prévues. Une des raisons est le manque de connaissances dans les interactions aérosol-nuage : si le rôle des particules d'aérosol sur le développement des gouttelettes de nuage (en tant que noyau de condensation — CCN) est bien connu (théorie développée par Köhler, 1936), la formation des cristaux de glace (nucléation hétérogène, où les particules d'aérosol interviennent comme noyau de congélation — IN) est toujours assez mal comprise et sujette à d'intenses recherches et débats. La bonne compréhension de la formation de la glace est d'une importance cruciale dans la mesure où une très grande part des nuages contient de la glace (soit dans des nuages en phase mixte ou contenant uniquement de la glace, *voir* FIGURE 2–33 dans Pruppacher and Klett, 1997 et les références citées) et qu'à mi-latitudes, la plupart des précipitations sont initiées dans la phase glace.
En outre, les nuages interagissent avec les rayonnements solaire et tellurique. Selon leur phase et la taille des hydrométéores[1] qu'ils contiennent, les nuages se comportent différemment et peuvent soit augmenter ou diminuer le forçage radiatif, même si à l'échelle mondiale, la couverture nuageuse tend à le diminuer (IPCC, 2013, Chapitre 7). Ainsi, les interactions aérosol-nuage ont des implications radiatives dans la mesure où elles influencent fortement la taille et le nombre d'hydrométéores (Flossmann and Wobrock, 2012) ainsi que leur phase ; on parle d'effet indirect (IPCC, 2013, Chapitre 7). Les incertitudes concernant celui-ci sont supérieures à celles pour l'effet direct, étant donné que les processus de changement de phase sont encore assez mal compris. Par conséquent, le niveau de confiance dans le forçage radiatif net indirect des particules d'aérosol reste bas.

La formation de la phase glace est appelée nucléation de la glace.
Pour des températures inférieures à 0°C, des embryons de glace (groupes de molécules d'eau cristallisées) commencent à se former dans la phase liquide des gouttelettes d'eau en surfusion, qui gèlent lorsqu'un embryon de glace atteint une taille critique. La formation d'un embryon de glace de taille critique ainsi que la croissance de l'embryon au sein de la gouttelette résultent en une barrière d'énergie ; ainsi, l'eau est dans un état métastable sous 0°C. Si l'embryon se forme uniquement à partir de la phase liquide, sans l'intervention d'une particule d'aérosol, on parle de nucléation homogène et cela nécessite généralement des températures inférieures à −35°C.
Cependant, dans l'atmosphère, on observe de la nucléation de la glace à des températures pouvant aller jusqu'à −5°C et qui ne peut être expliquée par la nucléation homogène.

La formation de cristaux de glace à haute température implique un abaissement de la barrière d'énergie évoquée précédemment. Elle est abaissée par la présence de particules d'aérosol permettant une diminution de l'énergie de formation du germe de glace de rayon critique. On parle alors de nucléation hétérogène.
Les particules d'aérosol ayant cette capacité à diminuer l'énergie de formation du germe de glace de rayon critique sont appelées des noyaux glaçogènes et permettent la glaciation suivant plusieurs processus (FIGURE 1) :

---

[1] les hydrométéores sont l'ensemble des gouttelettes de nuages et des cristaux de glace

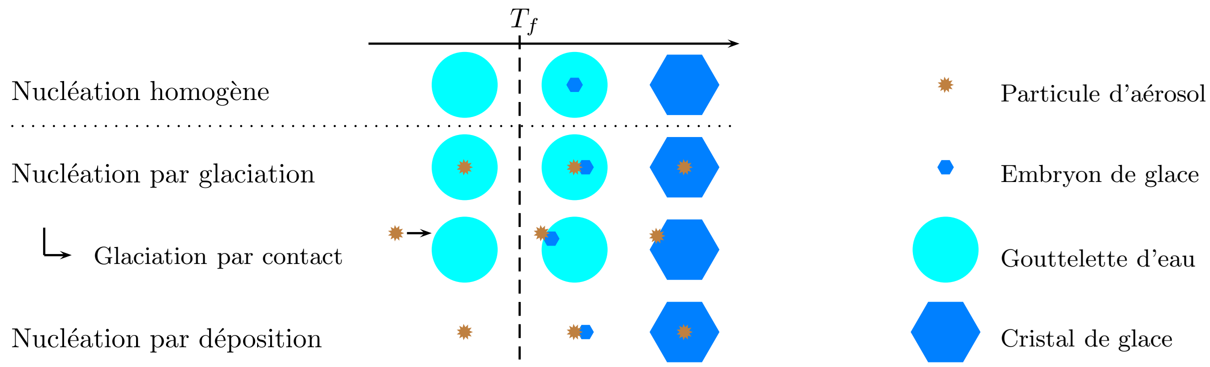

Figure R.1 – Diagramme schématique de la formation de la glace comme décrite par (Vali et al., 2015). La nucléation par glaciation contient la glaciation par immersion, par condensation et par contact, seul ce dernier est détaillé ici.

(I) la nucléation par glaciation qui nécessite l'existence d'une gouttelette d'eau et qui comporte trois mécanismes distincts :

  (a) la « *glaciation par immersion* [qui fait référence] *à la nucléation de la glace initiée par une particule contenant un noyau de congélation* (ice nucleating particle — INP) […] *située dans un corps liquide* »(Vali et al., 2015)[2] ;

  (b) la « *glaciation par contact* [qui est] *initiée par une INP* […] *à l'interface air–eau lorsque l'INP entre en contact avec le liquide ou se forme à une triple interface air–liquide–particule* » ;

  (c) et la « *glaciation par condensation qui est définie comme ayant lieu lorsque la glaciation est initialisée parallèlement à la formation initiale de liquide sur un noyau de condensation à des températures inférieures au point de fusion de la glace.* […] *Il n'est pas entièrement déterminé si la glaciation par condensation à une échelle microscopique, si elle à lieu, est vraiment différente de la nucléation par déposition ou séparée de la glaciation par immersion. Par conséquent, l'utilisation de ce terme nécessite des précautions.* »

(II) la nucléation par déposition, définie comme la « *nucléation de la glace à partir de vapeur sursaturée sur une INP* […] *sans la formation préalable de liquide.* »

Les INP présentent à leur surface des sites préférentiels pour la nucléation de la glace, on parle de sites actifs. Ainsi, pour décrire de façon précise la nucléation hétérogène, on utilise la notion de densité de sites actifs de nucléation (ice nucleating active sites densities — densité INAS) qui « *décrit le nombre de sites actifs de nucléation à une certaine température et sursaturation, normalisé par la superficie de particules d'aérosol. Cette approche se base sur la supposition que l'échantillon de particules d'aérosol étudiée est de composition uniforme. La dépendance temporelle n'est pas prise en compte.* » (Hoose and Möhler, 2012)

---

[2] toutes les citations à venir dans ce paragraphe, écrites en italiques, sont directement extraites et traduites de (Vali et al., 2015), utilisé comme point de référence pour les définitions sur la nucléation de la glace.

Le but de cette thèse est d'améliorer la compréhension de la nucléation hétérogène et son impact sur le développement des nuages à l'aide de moyens expérimentaux et de travaux de modélisation. En particulier, les buts de la thèse sont : (I) d'explorer expérimentalement la relation entre glaciation par immersion et nucléation par déposition induites par les particules minérales, (II) d'appliquer dans une étude de modélisation les résultats obtenus sous la forme d'une paramétrisation de la nucléation de la glace, et (III) d'explorer numériquement la réponse d'un système nuageux à la modification du schéma de paramétrisation de différents mécanismes de glaciation.

Le travail expérimental (présenté dans la partie I) se concentre sur une expérience de cold stage, dévelopée depuis Hiron (2011) pour étudier la glaciation par immersion et la nucléation homogène. La configuration originale a été associée à une cellule de flux[3] de façon à pouvoir étudier également la nucléation par déposition.
Une telle étude combinée des deux mécanismes de glaciation n'a, à la connaissance de l'auteur, jamais été réalisée.

Ce développement répond à plusieurs objectifs scientifiques :
(I) Étudier la glaciation par immersion et la nucléation par déposition sur un échantillon comportant des particules d'aérosols identiques pour les différents mécanismes. Les particules d'aérosols choisies pour cette études sont des particules de feldspath, le principal minéral constitutif de la croûte terrestre et très présent dans l'atmosphère : des mesures *in situ* ont montré que, dans l'Atlas, la fraction massique de feldspath se situait entre 10% lors d'une tempête de poussières et 25% dans des conditions de faible concentration de poussières (Kandler et al., 2009). De plus, le feldspath riche en potassium (K–feldspath) a été identifié comme étant un noyau de congélation très actif (Atkinson et al., 2013) et est très étudié depuis (Yakobi-Hancock et al., 2013; Peckhaus et al., 2016; Kiselev et al., 2017).
(II) Étudier les liens entre glaciation par immersion et nucléation par déposition. En effet, Marcolli (2014) a proposé que la nucléation par déposition pouvait être considérée comme de la glaciation par immersion ayant lieu dans les pores et cavités des particules d'aérosols, suggérant que le processus physique impliqué dans les deux mécanismes est identique. L'extension du cold stage dans cette thèse vise ainsi à répondre à la question suivante : « *est-ce qu'être un bon noyau de congélation pour la glaciation par immersion implique être un bon noyau de congélation pour la nucléation par déposition ?* »
(III) Développer de nouvelles paramétrisations pour la glaciation par immersion et la nucléation par déposition impliquant des particules de K–feldspath.

Ce résumé se concentre sur le (II), à savoir liens entre glaciation par immersion et nucléation par déposition.

Les paramétrisations obtenues dans le (III) sont intégrées au travail de modélisation de cette thèse (présenté dans la partie II), qui de façon plus générale se concentre sur l'impact des paramétrisations de la nucléation de la glace sur le développement du nuage convectif CCOPE (Dye et al., 1986) et les précipitations qui en résultent, modélisé à l'aide du

---

[3] « flow cell », élément permettant de faire parcourir un flux d'air au sein de la chambre du cold stage

modèle à microphysique détaillée DESCAM (Detailed Scavenging Model, Flossmann et al., 1985).

Dans leurs conclusions, Leroy et al. (2006) indiquent que, pour DESCAM, « *des améliorations dans le traitement des processus de microphysique de la phase glace (fonte, forme des cristaux et nucléation) sont nécessaires.* » L'impact de la fonte a été étudié par Planche et al. (2014). Cette thèse se concentre sur l'amélioration du traitement de la nucléation de la glace.

À partir de Monier et al. (2006), la paramétrisation de Meyers et al. (1992) a été implémentée dans DESCAM pour représenter la nucléation hétérogène. Cette paramétrisation présente l'avantage d'être particulièrement simple à intégrer dans la mesure où la paramétrisation fournit directement une concentration de noyaux glaçogènes uniquement en fonction de la sursaturation. Ceci est très avantageux lorsque l'on considère des modèles particulièrement coûteux en calcul, comme la version 3–D de DESCAM et fournit des concentrations en cristaux de glace réalistes. Cette paramétrisation est également utilisée dans de nombreux modèles de prévision météorologique. Toutefois, quatre problèmes apparaissent par l'utilisation de cette paramétrisation.
Premièrement, les données expérimentales ont montré que, pour tous les mécanismes de nucléation hétérogène, la température joue un rôle majeur (Hoose and Möhler, 2012). Deuxièmement, la nature des particules d'aérosols joue un rôle majeur dans son efficacité à former la glace (Hoose and Möhler, 2012). Troisièmement, les données expérimentales ont montré que la nucléation hétérogène est fortement dépendante de la taille des particules (dépendance en superficie, Welti et al., 2009; Hoose and Möhler, 2012). Enfin, la paramétrisation de Meyers et al. (1992) ne représente pas de façon précise l'ensemble des mécanismes de nucléation hétérogène étant données les limites de la configuration expérimentale qui a fourni les données à partir desquelles la paramétrisation a été déterminée. En particulier, le cas des grosses gouttes formées par collision–coalescence qui contiennent plus d'une particule d'aérosol ne peuvent pas être prises en compte.

De façon à améliorer la simulation de la formation de la glace dans le modèle, la paramétrisation de Meyers et al. (1992) a dans un premier temps été combinée à d'autres paramétrisations pour représenter l'ensemble des mécanismes de nucléation hétérogène. Cependant, les paramétrisations ajoutées ne permettent pas de traiter les trois premiers problèmes identifiés avec la paramétrisation de Meyers et al. (1992).
Ainsi, la taille des particules d'aérosol et la température ont été prises en compte dans la glaciation en adaptant DESCAM à la représentation en densité INAS. De plus, la dépendance en la nature des particules d'aérosols a été étudiée en considérant différents types de particules minérales comme potentielles particules contenant un noyau de congélation.

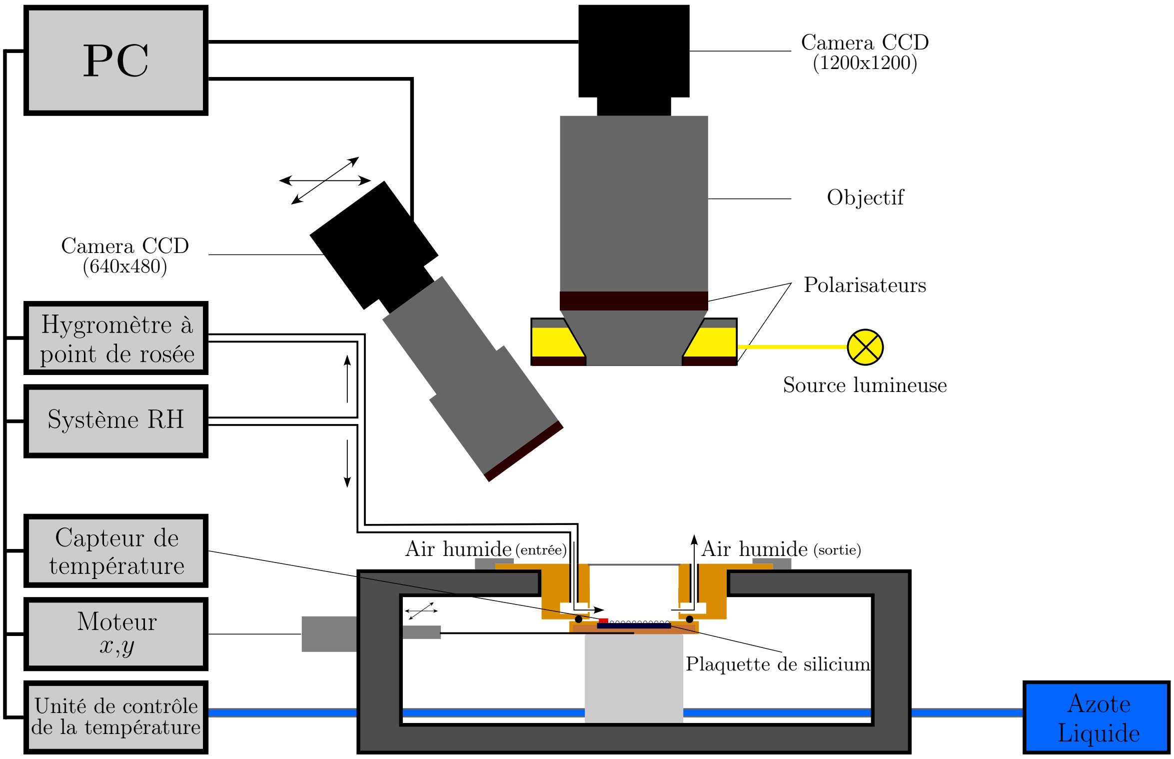

FIGURE R.2 – Schéma expérimental de l'expérience du cold stage développé pour observer la glaciation par immersion et les nucléations homogènes et par déposition.

I Étude expérimentale de particules de K–Feldspath : L'expérience du « *Cold Stage* »

I.1 Système expérimental

L'ensemble du système est représenté dans le schéma FIGURE R.2.

L'expérience est basée sur un cold stage motorisé, développé par Linkam Scientific Instruments (modèle MDBCS–196). L'élément central du cold stage est un cylindre d'argent (rectangle gris clair FIGURE R.2) dont la température peut être contrôlée entre −196°C et +125°C et refroidi à l'aide d'azote liquide avec des vitesses de refroidissement allant de 0.01 à 150 $\mathrm{K.min^{-1}}$.
Au début de l'expérience, une seringue piézoélectrique (non représentée) permet de déposer des gouttes de suspensions sur une plaquette de silicium (l'ensemble est appelé échantillon ci–après) placée dans un support (présentant un creuset de 10x10 mm pour accueillir l'échantillon) posé sur le cylindre d'argent (FIGURE R.2). La seringue génère des gouttes monodispersées, d'un volume allant de 100 pl à quelques nl.

Durant l'expérience, l'échantillon est observé à l'aide d'une caméra CCD (1200x1200 pour une définition de 8.7 µm/pixel) et éclairé par une source lumineuse polarisée. La caméra est associée à un objectif à champ large couplé à un analyseur.
L'enregistrement vidéo de l'expérience est contrôlé par une routine LabView et la glaciation des gouttes est détectée en post-traitement par dépolarisation de la lumière.

Suspension	**A**	**B**	**C**
Concentration (C, g.L^{-1})	$(2.5 \pm 0.1) \cdot 10^{-1}$	$(2.5 \pm 0.2) \cdot 10^{-2}$	$(2.5 \pm 0.2) \cdot 10^{-3}$
S_p (cm^2)	$(3.76 \pm 2.40) \cdot 10^{-6}$	$(3.76 \pm 2.42) \cdot 10^{-7}$	$(3.76 \pm 2.42) \cdot 10^{-8}$

TABLE R.1 – Résumé des suspensions utilisées dans cette étude

De façon à pouvoir également observer la nucléation par déposition, une cellule d'écoulement a été développée. Cette cellule est composée de deux éléments principaux : le nouveau support en cuivre évoqué précédemment ainsi qu'un nouveau couvercle pour le cold stage. Ce nouveau couvercle minimise le volume de la chambre autour de l'échantillon et permet l'utilisation d'un flux continu d'air humide.

La température de point de gel du flux d'air humide est contrôlée par le système RH en mélangeant plusieurs flux d'air partiaux. Le point de rosée en sortie du système RH varie entre -50°C et 7°C. Le flux d'air traversant la cellule d'écoulement durant les expériences de nucléation par déposition est fixé à 150 mL.min^{-1}.

I.2 Expériences avec le K–feldspath

Le travail de cette thèse se concentre sur l'étude de la glaciation hétérogène faisant intervenir des particules de feldspath riche en potassium (K–feldspath).
De la poudre de K–feldspath fournie par l'université de Leeds (présentée sous la référence FS02 dans Peckhaus et al., 2016) a été utilisée pour conduire les expériences.

I.2.1 Suspensions

Une suspension mère (**A**) a été obtenue en mélangeant 13.2 ± 0.5 mg de poudre de FS02 avec 52.6 ± 1.0mL d'eau hautement purifiée (34877–M END Millipore, HPLC Plus — σ–Aldrich). Deux suspensions filles (**B** et **C**) ont ensuite été obtenues par dilution au dixième et au centième respectivement.

Les gouttelettes déposées sur la plaquette de silicium dans l'ensemble des expériences présentées ici ont un volume moyen $V_d = 569 \pm 363$ pL. De plus, d'après Peckhaus et al. (2016), la surface totale de K-Feldspath par unité de masse pour la poudre de FS02 est déterminée par la méthode BET (Brunauer et al., 1938) et donne $S_{\mathrm{BET}} = 2.64\,\mathrm{m}^2.\mathrm{g}^{-1}$. Ainsi, la surface totale de particules d'aérosol par gouttelette (résumée dans la TABLE R.1) est donnée par :

$$S_p = V_d \cdot C \cdot S_{\mathrm{BET}}$$

I.2.2 Déroulement de l'expérience

Chacune des trois suspensions est traitée de la façon suivante :

i. À la température de point de rosée de la pièce, 169 gouttelettes sont déposées en un tableau de 9 600 µm de côté avec une distance inter–gouttelettes de 800 µm.

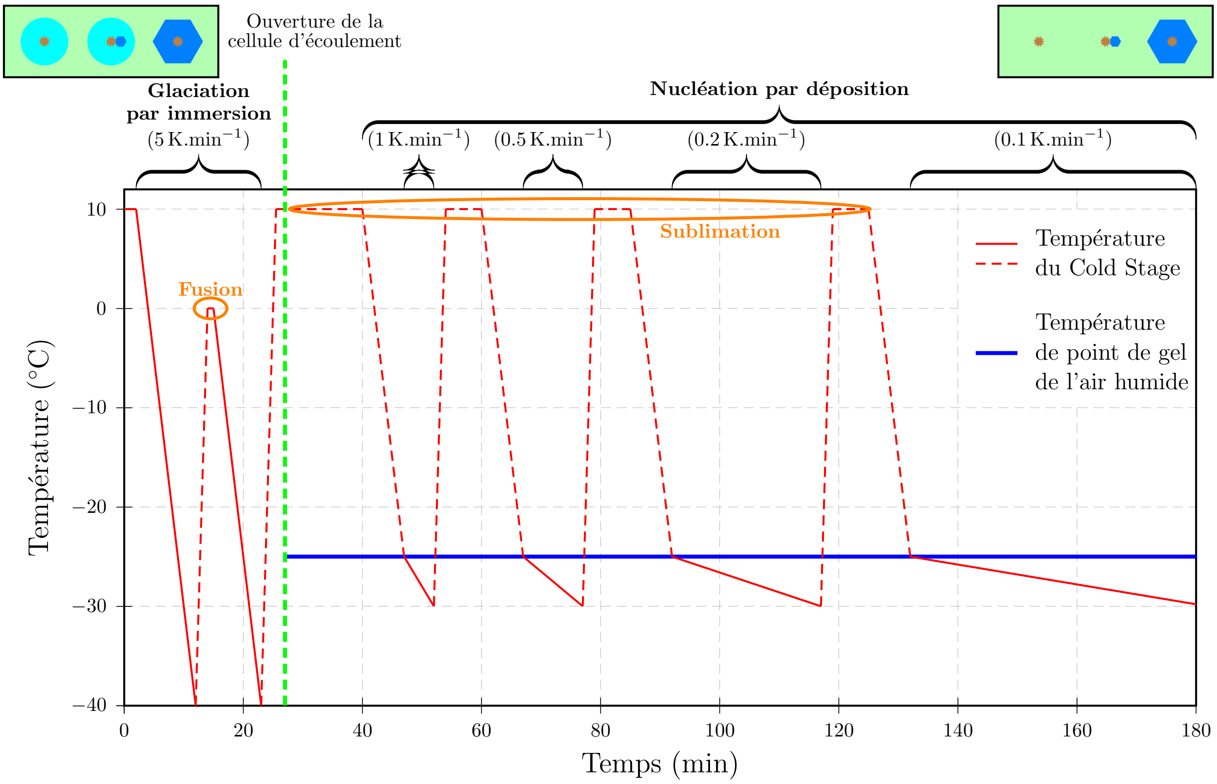

Figure R.3 – Procédure expérimentale idéale : les gouttelettes sont déposées sur la plaquette de silicium à 10°C, s'en suivent deux cycles de congélation/fusion à 5 K.min^{-1}. Après le second cycle, un flux d'air humide ayant pour température de point de gel −26°C est mis en place et quatre cycles de déposition/évaporation sont réalisés pour quatre différentes vitesses de refroidissement.

ii. Glaciation par immersion :
le cold stage est refroidi à 5 K.min^{-1} jusqu'à −40°C (température à laquelle l'ensemble des gouttes à gelé par glaciation homogène ou hétérogène) ;
le cold stage est alors réchauffé à 0°C pour laisser fondre l'ensemble des cristaux de glace obtenus.
Cette étape est répétée plusieurs fois puis le cold stage est réchauffé jusqu'à 10°C.

iii. Ouverture de la cellule d'écoulement.

iv. Nucléation par déposition :
le cold stage est refroidi à 5 K.min^{-1} jusqu'à la température de point de gel de l'air humide parcourant la cellule d'écoulement ;
le cold stage est alors refroidi jusqu'à 5°C en dessous de la température de point de gel.
Cette étape est répétée plusieurs fois pour des vitesses de refroidissement décroissantes : 1, 0.5, 0.2, 0.1 K.min^{-1}.

Les cycles de nucléation par déposition sont réalisés pour plusieurs températures points de gel fixés (et mesurées par l'hygromètre à point de rosée) : −20, −23, −26, −29.5 et −34°C.

Dans la suite de cette section, les résultats pour la glaciation par immersion seront présentés ensemble dans un premier temps, suivis des résultats pour la nucléation par déposition.

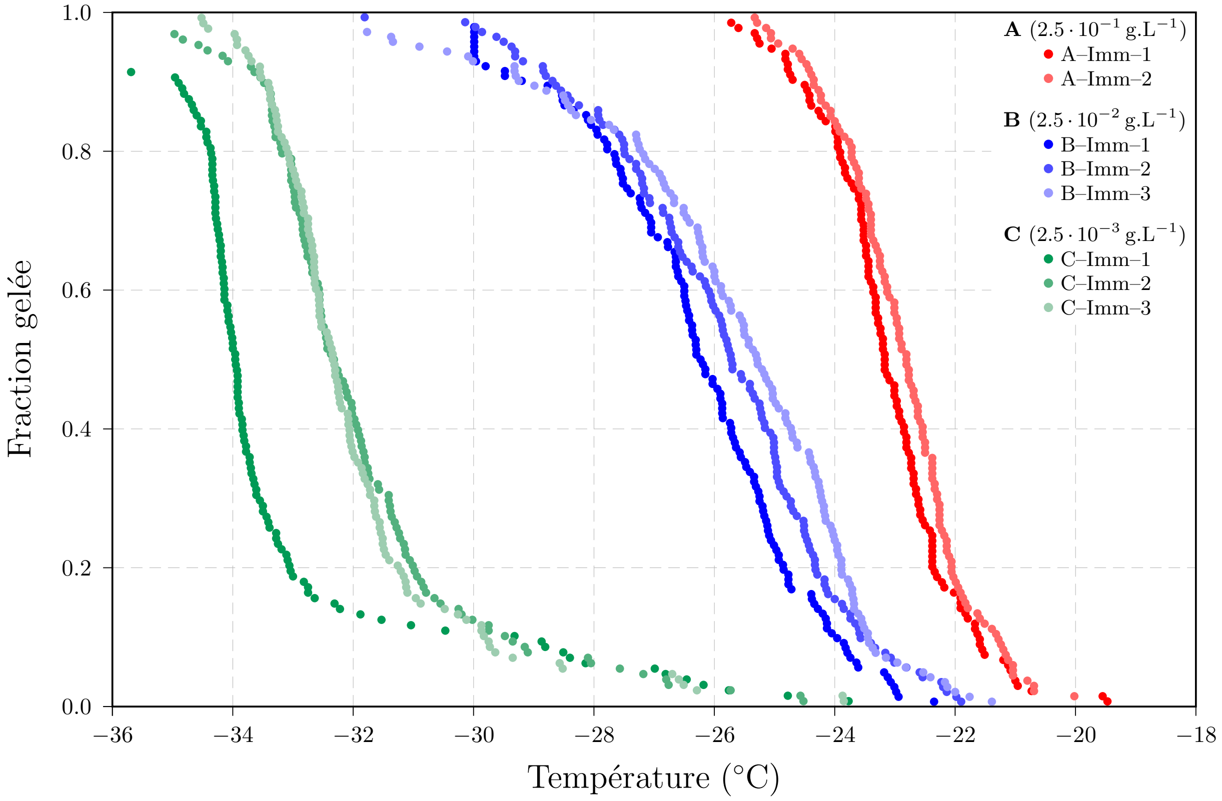

FIGURE R.4 – Fraction gelée des gouttes en fonction de la température pour les suspensions **A** (points rouges), **B** (points bleus) et **C** (points verts).

I.2.3 Glaciation par immersion

Pour chacune des suspensions, les cycles de glaciation/fonte sont répétés plusieurs fois avec une vitesse de refroidissement de 5 K.min^{-1} : deux cycles sont réalisés pour la suspension mère **A** et trois cycles pour les suspensions filles **B** et **C**.
La fraction gelée des gouttes (nombre de gouttes gelées rapporté au nombre total de gouttes) est calculée pour chacun des cycles (FIGURE R.4).

On observe que lorsque la concentration des suspensions diminue, la température de point de gel des gouttes observée diminue ($T_{50\%,\mathbf{A}} \simeq -23$°C, $T_{50\%,\mathbf{B}} \simeq -25.7$°C et $T_{50\%,\mathbf{C}} \simeq -33$°C). De plus, pour les suspensions **A** et **B**, les courbes obtenues pour la fraction gelée des gouttes son similaires et on note que la température de point de gel des gouttes augmente avec les cycles successifs. Cependant, le nombre de cycles effectués (respectivement 2 et 3) ne permet pas de tirer des conclusions (*voir par exemple* Kaufmann et al., 2017).

Pour la suspension **C**, on remarque deux régimes de glaciation : pour des températures supérieures à −30°C, la pente de la fraction gelée est faible (cela correspond environ aux 15 premières gouttes gelées) en revanche, pour les températures inférieures, la pente de la fraction gelée est aussi forte que pour la suspension **A** et l'ensemble des gouttes gèle en 2°C.
On observe une augmentation de la température de point de gel pour la partie pentue

de la fraction gelée, mais que les 15 premières gouttes gelées ont le même comportement dans chacun des cycles.

I.2.4 Nucléation par déposition

Lors de l'évaporation des gouttes présentes sur le substrat, les particules de feldspaths forment un cercle à l'endroit où se trouvaient les gouttes, on parle de particules résiduelles (ci–après, « particules résiduelles »désignera l'ensemble des particules résiduelles pour une goutte).

Chacune des particules résiduelles contient plusieurs particules de feldspath. Or l'objectif de cette expérience est de comparer le rôle de noyau de congélation du feldspath dans les deux modes de glaciation. Lors des expériences de glaciation par immersion, seul le noyau de congélation le plus actif initie la glaciation de la goutte mais il n'est pas possible d'identifier sa localisation au sein de la goutte et à plus forte raison au sein des particules résiduelles après évaporation. Lors des expériences de nucléation par déposition, là aussi dans la très grande majorité des cas, seul le noyau de congélation le plus actif sert au développement d'un cristal de glace. Cependant, il est cette fois possible d'identifier la position du noyau de congélation au sein des particules résiduelles : les positions des cristaux de glaces formés par nucléation par déposition pour une goutte de la suspension **A** et deux gouttes de la suspension **C** sont ainsi représentées Figure 4.6.

Pour pouvoir comparer l'activité d'un noyau de congélation pour la glaciation par immersion et la nucléation par déposition, il faut s'assurer que c'est bien le même noyau qui est mis en jeu dans les deux cas. Aussi, le bas de la Figure 4.6 montre que pour la nucléation par déposition utilisant les suspensions **A** et **B**, il y a plusieurs sites de glaciation : entre 5 et 9 pour la suspension **A** et entre 3 et 5 pour la suspension **B**. Pour la suspension **C**, il n'y a en général qu'un seul site actif à l'exception de deux cas présentés Figure 4.6 où deux positions différentes ont été détectées.

Par conséquent, les informations quant au lien entre activé glaçogène par immersion et par déposition peuvent être obtenues à l'aide de la suspension **C**.

I.3 Relation entre glaciation par immersion et nucléation par déposition

Afin de déterminer s'il existe une telle relation, on regarde quelles sont les gouttelettes concernées par la glaciation dans chacun des deux modes pour la suspension **C**. En particulier, on s'intéresse aux 15 premières gouttes gelées par le mécanisme de glaciation par immersion que l'on compare aux 15 premiers résidus sur lesquels se sont formés des cristaux de glace par le mécanisme de nucléation par déposition ($1\,\mathrm{K.min}^{-1}$) :

C-Imm-1 :[46, 15, 13, 37, 77,103,138,136,124, 58, 52, 82, 96, 33, 89]
C-Imm-2 :[15, 46, 13,138, 77, 76, 37,103, 58, 96, 16,132, 33, 26,136]
C-Imm-3 :[46, 15, 13, 77,136, 37, 58,138, 96, 74, 82, 39, 99, 88,103]
C-Dep-2 :[15, 13, 46, 37, 42, 58, 96,103,136,133, 77, 33, 82,104,132]
C-Dep-3 :[116, 42, 46, 60, 77, 15, 53, 13,104,103, 87, 96, 78, 37,138]...58
C-Dep-4 :[77, 13, 49, 46,116, 96,103, 15, 18, 95, 32, 60, 58, 90, 87]...37

On note que les mêmes sites de nucléation sont impliqués pour les différentes expériences mais dans des ordres différents. Cela n'indique cependant pas nécessairement un lien entre glaciation par immersion et nucléation par déposition : en effet, le fait que les sites actifs pour la nucléation par déposition soient les mêmes que ceux pour la glaciation par immersion peut être du à une préactivation des sites lors des cycles de glaciation par immersion.
Toutefois, si l'on se reporte à la FIGURE R.4, on note que le comportement glaçogène des 15 premières gouttes n'est pas influencé par les cycles successifs, contrairement aux autres gouttes (fraction glacée entre 0.15 et 1).

Ainsi, la comparaison des sites de nucléation pour la glaciation par immersion et la nucléation par déposition dans le cas de la suspension **C** indique l'existence d'un lien pour les sites glaçogènes entre être efficace pour la glaciation par immersion et pour la nucléation par déposition.

En résumé

L'observation des séquences de glaciations successives pour la glaciation par immersion et la nucléation par déposition a permis de montrer que la nucléation hétérogène avait lieu sur des sites spécifiques dans chacun de mécanismes.

À partir des résultats des expériences, deux paramétrisations — basées sur la représentation en densité INAS (Hoose et al., 2010) — ont été développées pour la formation de la glace par les particules de K–feldspath :

- $n_{s,\mathrm{dep}}(T, RH_i) = \exp(11.2 - 0.18 \cdot T) \cdot [1 - \exp(0.02 \cdot (127 - RH_i))]$
- $n_{s,\mathrm{imm}}(T) = \exp(10.3 \cdot \exp[-\exp(0.345 \cdot (T + 21.2))] + 6.05)$

Les expériences consécutives de glaciation par immersion et de nucléation par déposition sur de mêmes particules identifiées montrent que les bons noyaux glaçogènes pour la glaciation par immersion semblent être bon noyaux glaçogènes pour la nucléation par déposition. D'autre part, les densités INAS sont relativement similaires dans les deux modes de nucléation.

II Étude de la nucléation de la glace sur les particules d'aérosol minérales à l'aide de DESCAM

Après l'étude expérimentale des mécanismes de glaciations présentée dans la première partie, on s'intéresse à l'impact de chaque mécanisme dans l'atmosphère. Pour se faire, on étudie le rôle des différents mécanismes de glaciation et de différents types de particules minérales sur le développement d'un nuage convectif.
Cette étude nécessite une « *amélioration du traitement des processus de microphysique de la glace* »(Leroy et al., 2006).

Le travail de modélisation se découpe en deux parties : dans une étude préliminaire, la méthodologie est déterminée en utilisant des paramétrisations standardes pour les mécanismes de glaciation. Ensuite, une étude de cas est réalisée en utilisant les particules minérales comme support de paramétrisations de la glaciation plus développées.

Dans cette étude, les paramétrisations déterminées dans les expériences de cold stage sont intégrées au modèle.

Description du modèle

Le travail de modélisation fait appel au modèle DESCAM, développé par Andrea Flossmann et ses collègues (Flossmann et al., 1985; Flossmann, 1987; Flossmann and Wobrock, 2010; Hiron and Flossmann, 2015). Une description détaillée du modèle est faite en anglais §5.1 et en annexe A.

La version du modèle utilisée dans cette étude utilise une représentation dynamique simplifiée, dite à 1D5 : l'atmosphère est représentée intégralement dans sa composante verticale mais la composante horizontale est limitée à deux cylindres concentriques (Asai and Kasahara, 1967). Le cylindre intérieur correspond au développement d'un nuage convectif où toute la microphysique est calculée, le cylindre extérieur correspond à la zone de subsidence où les variables microphysiques sont considérées comme constantes.
La dynamique du modèle est initialisée à l'aide de CCOPE (Cooperative COnvective Precipitation Experiment, Dye et al., 1986; Leroy et al., 2006), un cas d'étude bien documenté d'un épisode orageux ayant eu lieu le 19 juillet 1981 dans le Montana.

DESCAM est un modèle à microphysique détaillée : on suit de façon explicite — c'est à dire sur plusieurs classes de tailles — les spectres en nombre des particules d'aérosols, des gouttelettes et des cristaux de glace. On suit également la masse de particules d'aérosols contenue dans chacun des trois réservoirs.
Ainsi, dans l'étude préliminaire, le modèle comporte 6 distributions en taille.

II.1 Étude préliminaire

L'étude préliminaire, résumée dans ses grandes lignes ici et présentée de façon détaillée dans le chapitre 5, utilise une représentation simplifiée des processus de glaciation : chaque paramétrisation ne dépend que des variables thermodynamiques et, le cas échéant, du volume d'eau contenu dans la particule d'aérosol ou dans la goutte considérée. Cette étude préliminaire correspond dans les grandes lignes au travail publié dans (Hiron and Flossmann, 2015).

II.1.1 Processus de glaciation

Les paramétrisations présentées ci-après sont détaillées en anglais §5.2.

Nucléation homogène : la paramétrisation utilisée est celle de (Koop et al., 2000) adaptée à Descam d'après le travail de (Monier et al., 2006). Le taux de nucléation homogène (J_{hom} en $\mathrm{cm}^{-3}.s^{-1}$) est déterminé comme une fonction de l'activité de l'eau et de l'humidité relative.

Glaciation par immersion : la formule de (Bigg, 1953) donne la variation du nombre de gouttes et de cristaux en fonction du volume d'eau contenu dans les gouttes considérées et de la température des gouttes (assimilé à la température de l'atmosphère). Cette paramétrisation n'est appliquée qu'aux gouttes ayant un rayon supérieur à 16 µm.

Glaciation par contact : le nombre de particules d'aérosol jouant un rôle de noyau de congélation est déterminé par la paramétrisation de (Meyers et al., 1992) qui fournit une concentration d'IN par unité de volume en fonction de la température de la goutte capturant les particules.

Glaciation par condensation et nucléation par déposition : les deux mécanismes sont ici traités à l'aide de la même paramétrisation issue (Meyers et al., 1992). Celle-ci permet de déterminer le nombre de noyaux glaçogènes par unité de volume en fonction de la sursaturation uniquement.
Ce nombre est ensuite réparti sur les particules d'aérosol d'un rayon supérieur à 0.1 µm et sur les gouttes fraichement activées, c'est à dire d'un rayon inférieur à 16 µm.

II.1.2 Méthode

Pour pouvoir différencier l'impact des différents mécanismes, une série d'études de sensibilité a été réalisée dans laquelle chaque mécanisme de glaciation a d'abord été considéré comme seul source de glace pristine avant de considérer l'ensemble des mécanismes en compétition (cas 2). Chacun de ces cas a également été comparé à un cas « *référence* » dans lequel aucun mécanisme de glaciation n'est actif (cas 1).

II.1.3 Cas *référence*

Le nuage commence à se former aux alentours de 3 km d'altitude après 8 min de simulation et se développe rapidement sur 27 min pour atteindre 9.5 km, altitude à laquelle le courant ascendant a faibli. Les précipitations sont initiées entre 8 et 8.7 km d'altitude après 23 min de vie du nuage.
Le système précipitant peut être divisé en deux parties distinctes (Figure r.5b) : un premier fort pic appelé par la suite pic de *pluie chaude*, situé entre 41.5 et 45 min de

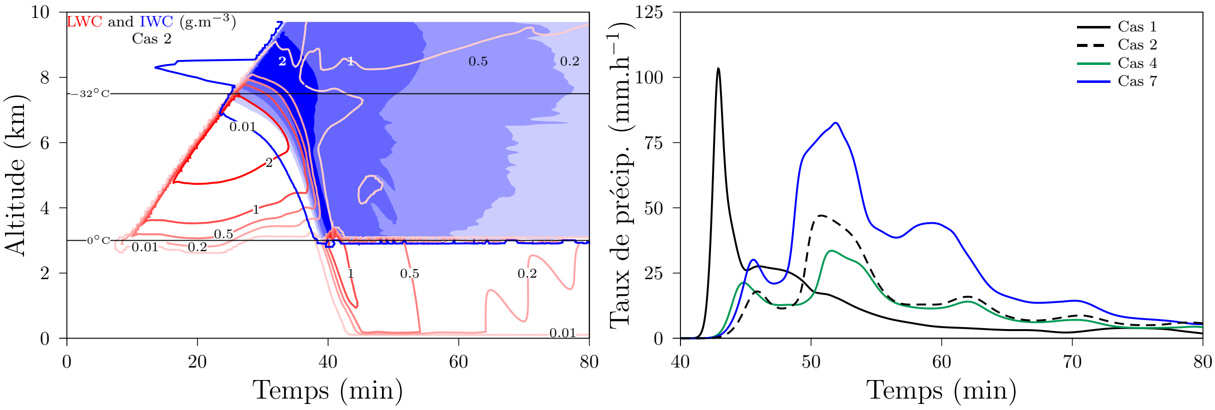

Figure R.5 – (**a**, gauche) Contenu en eau liguide (g.m^{-3}, rouge) et contenu en glace (g.m^{-3}, bleu) simulé par Descam en fonction de l'altitude et du temps pour le cas où tous les mécanismes de glaciation sont actifs (cas 2). (**b**, droite) Évolution temporelle du taux de précipitation (mm.h^{-1}) pour le cas *référence* (cas 1, noir continu), pour le cas où tous les mécanismes sont considérés comme actifs (cas 2, noir discontinu), pour le cas de la glaciation par immersion comme seul mécanisme (cas 4, vert) et pour la glaciation par condensation considérée comme seul mécanisme (cas 7, bleu).

simulation avec une valeur haute de 103 mm.h^{-1} et associé à de forts contenus en eau liquide précipitante (jusqu'à 9.0 g.m^{-3}) ; et un régime plus stable avec des taux de précipitation entre 7.6 et 27.6 mm.h^{-1}, situé entre 45 et 56 min, associé à de relativement faibles contenus en eau liquide précipitante (entre 0.2 et 1.0 g.m^{-3}) combinés à un faible courant descendant.

Les 25 minutes de simulation restantes contribuent à 22% du total des précipitations et correspondent à une dynamique assez stable (vents très faibles) et de faibles contenus en eau liquide précipitante (moins de 0.2 g.m^{-3}).

II.1.4 Cas incluant tous les processus

L'évolution en fonction du temps (min) et de l'altitude (km) du contenu en eau liquide et du contenu en glace (IWC) dans le cas où tous les processus de glaciation sont pris en compte est présentée dans la Figure R.5a. Le développement précoce du nuage est similaire à celui observé dans le cas 1, cependant, on note l'apparition d'une formation de glace similaire à un cirrus à haute altitude et à l'extérieur du nuage. La glace commence à se former au sommet du nuage lorsque celui-ci atteint une altitude de de 4.2 km (taux de glaciation supérieur à 1 m^{-3}.min^{-1}), cependant, la glace ne devient remarquable au sommet du nuage lorsque celui-ci atteint une altitude de 7.1 km. Les précipitations sont initiées à 6.0 km pour l'eau liquide et 7.1 km pour la glace après respectivement 35 et 33 min de simulation.

Figure R.5b, on note que le pic de *pluie chaude* est plus faible et retardé dans le cas 2 par rapport au cas 1. Ce qui est identifié comme le régime plus stable est fortement modifié par la prise en compte de la glace : le taux de précipitation est fortement augmenté principalement à cause d'un courant descendant plus marqué (supérieur à 10 m.s^{-1}).

II.1.5 Conclusions et limites

L'étude préliminaire a permis de mettre en évidence que la formation nuageuse précoce à haute altitude semble être dominée par la nucléation par déposition, en accord avec les

mesures *in situ* de (Cziczo et al., 2013).
Une forte influence du régime de température et du mode de glaciation sur le développement du nuage a également pu être mise en évidence.
La méthode employée permet l'identification des paramètres déterminants quant à l'impact de la formation de la glace sur le développement du nuage.

Cependant, cette étude fait appel à une représentation simplifiée de la formation de la glace : il n'y a aucune dépendance sur la nature des particules d'aérosol et aucune dépendance sur la taille des particules d'aérosols, or ce sont deux facteurs prépondérants dans l'efficacité des processus de nucléation hétérogène Hoose and Möhler (2012). De plus, les paramétrisations utilisées dans cette étude préliminaire sont assez datées (1956 et 1992), or depuis une dizaine d'années, des paramétrisations plus précises sont développées, faisant appel à la notion de densité INAS.

II.2 Étude explicite des particules minérales : Représentation en densités INAS de la nucléation hétérogène

II.2.1 Extension du modèle

Le but de la thèse étant d'étudier de façon précise l'impact de la nucléation hétérogène par les minéraux sur la dynamique d'un nuage, le modèle utilisé dans la première étude a besoin d'être étendu.

À la population de particules d'aérosol de fond déjà présente dans le modèle, on ajoute quatre populations de particules minérales : le feldspath (assimilé pour la suite au K–feldspath), l'illite, la kaolinite et le quartz. Les distributions en taille pour la concentration de chacun des minéraux sont tirées de mesures *in situ* réalisées par (Kandler et al., 2009, détails sur les distributions en taille §6.1). Pour assurer une bonne comparaison avec les résultats précédents, les concentrations mesurées *in situ* sont réduites d'un facteur 10 ; l'impact de la concentration en minéraux sur le nuage étant discutée dans une étude de sensibilité (§6.4.2.2).

Les densités INAS (n_s, cm^{-2}) sont déterminées expérimentalement comme suit :

$$f_i = 1 - \exp(-n_s \cdot S)$$

où f_i est la fraction gelée et S la surface moyenne par particule d'aérosol contenue dans les hydrométéores.
Ainsi, pour pouvoir utiliser la représentation en densités INAS pour la nucléation hétérogène, il est nécessaire de disposer dans le modèle du nombre total et de la surface totale de particules d'aérosol dans chacun des trois réservoirs.
Le nombre de distributions en taille dans le modèle passe ainsi de 6 à 47 :

- nombre de particules d'aérosol [x5] : $\mathcal{N}_a$, $\mathcal{N}_d$ et $\mathcal{N}_i$;
- surface de particules d'aérosol [x5] : $\mathcal{S}_a$, $\mathcal{S}_d$ et $\mathcal{S}_i$;
- masse de particules d'aérosol [x5] : $\mathcal{M}_a$,$\mathcal{M}_d$ et $\mathcal{M}_i$;
- nombre d'hydrométéores : N_d et N_i

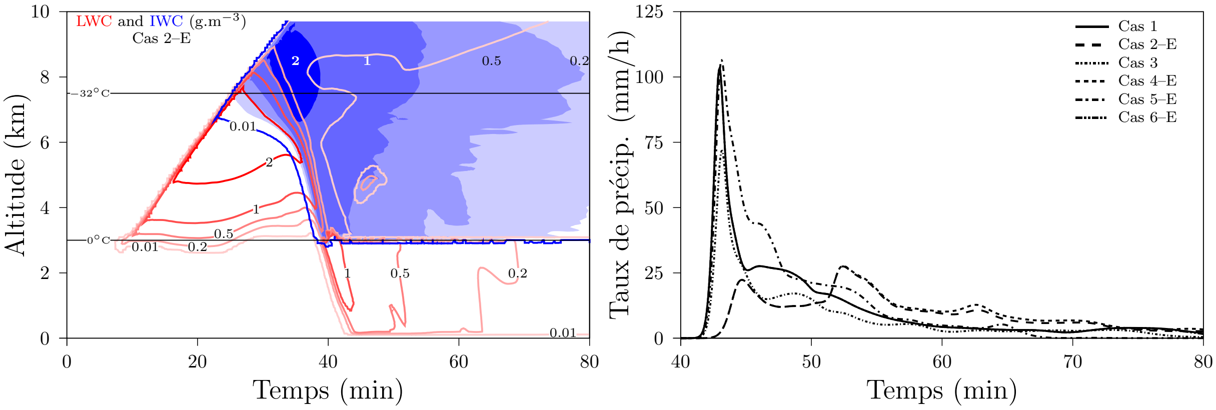

FIGURE R.6 – (**a**, gauche) Contenu en eau liguide (g.m^{-3}, rouge) et contenu en glace (g.m^{-3}, bleu) simulé par DESCAM en fonction de l'altitude et du temps pour le cas où tous les INP et mécanismes de glaciation sont actifs (cas 2–E). (**b**, droite) Évolution temporelle du taux de précipitation (mm.h^{-1}) pour le cas *référence* (cas 1, nior continu), et pour les cas où tous les INP et où tous les mécanismes sont considérés comme actifs (cas 2–E, violet discontinu), où la nucléation homogène est considérée seule (cas 3, noir pointillé–discontinu court), où la glaciation par immersion est considérée seule (cas 4–E, violet discontinu court), où la glaciation par contact est considérée seule (cas 5–E, violet pointillé–discontinu) et où la nucléation par déposition est considérée seule (cas 6–E, violet double pointillé–discontinu).

II.2.2 Résultats

Glaciation par immersion sur le K–feldpsath

La glaciation par immersion induite par le K–feldspath est calculée à l'aide de la paramétrisation de (Atkinson et al., 2013, équation et représentation graphiques présentée §6.2.3).

Le développement précoce du nuage est identique à ce qui a été observé dans l'étude préliminaire avec une formation après 8 min de temps simulé et une évolution dynamique très proche celle du où seulement la glaciation par immersion est considérée dans l'étude préliminaire (§5.4.1.2).

On retrouve donc le même fort impact de la glaciation par immersion que ce qui avait été observé dans l'étude préliminaire.

Glaciation par immersion sur tous les minéraux

Si l'on considère les autres minéraux, à l'aide de paramétrisations issues de la littérature (Table 6.3), l'évolution dynamique du nuage n'est pas modifiée. On obtient un taux de précipitation égal à celui du cas où seulement le K–feldspath était pris en considération.

Comme cela a été noté dans l'étude préliminaire, le minéral offrant la paramétrisation la plus active à haute température (et donc tôt dans le développement du nuage) est celui qui a le plus d'impact sur la dynamique globale du nuage : le K–feldspath domine la glaciation.

Autres mécanismes de nucléation hétérogène

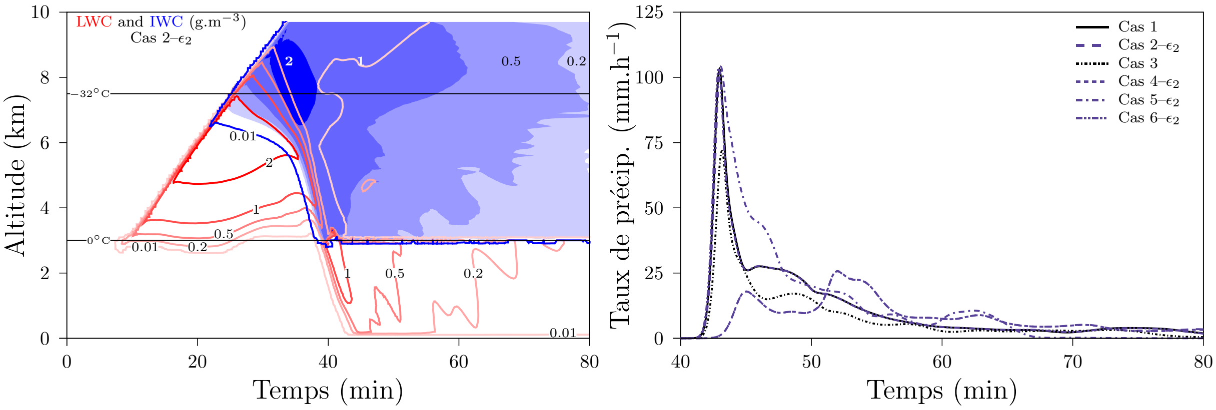

FIGURE R.7 – (**a**, gauche) Contenu en eau liguide (g.m^{-3}, rouge) et contenu en glace (g.m^{-3}, bleu) simulé par DESCAM en fonction de l'altitude et du temps pour le cas où tous les INP et mécanismes de glaciation sont actifs avec une représentation simlpifiée de $\mathcal{S}$ et un seul type de particules d'aérosol (cas 2–ϵ_2). (**b**, droite) Évolution temporelle du taux de précipitation (mm.h^{-1}) pour le cas *référence* (cas 1, continu), et pour les cas avec une représentation simlpifiée de $\mathcal{S}$ et un seul type de particules d'aérosol où tous les INP et où tous les mécanismes sont considérés comme actifs (cas 2–ϵ_2, discontinu violet), où l a nucléation homogène est considérée seule (cas 3, pointillé–discontinu court), où la glaciation par immersion est considérée seule (cas 4–ϵ_2, discontinu court violet), où la glaciation par contact est considérée seule (cas 5–ϵ_2, pointillé–discontinu violet) et où la nucléation par déposition est considérée seule (cas 6–ϵ_2, double pointillé–discontinu violet).

La glaciation par contact est déterminée à l'aide des résultats dans (Hoffmann, 2015, §6.2.4) et la nucléation par déposition à l'aide de résultats de la littérature pour l'illite et la kaolinite et des résultats de l'expérience du cold stage pour le K–feldspath (§6.2.5).
La nucléation par déposition n'a pratiquement aucun impact sur la dynamique du nuage, dans la mesure où la plupart des particules d'aérosol pouvant être noyau de congélation sont activées. De plus, les paramétrisations utilisées par défaut fournissent un faible taux de noyaux de congélation, ce qui supprime l'apparition de la formation de glace similaire à un cirrus notée dans l'étude préliminaire (§6.3.2.4). Toute fois, dans une étude de sensibilité, une paramétrisation (Steinke et al., 2015) plus efficace a été utilisée, assimilant l'ensemble des particules minérales à de l'Arizona Test Dust (ATD) et a conduit à la formation de glace en plus grande quantité à haute altitude. Enfin, en raison de l'algorithme de calcul, la nucléation par déposition à l'intérieur du nuage a été interdite. Si celle–ci est autorisée, la nucléation par déposition a un impact sur la dynamique du nuage lorsque considérée comme seul mécanisme de glaciation, mais ne joue toujours pas de rôle lorsque considérée en compétition avec les autres mécanisms (§6.4.2.4).
La glaciation par contact n'a pas d'impact sur le développement du nuage, dans la mesure où la capture des particules d'aérosol est assez faible, mais impacte fortement le contenu en glace précipitante ce qui mène à une augmentation des précipitations au sol (§6.3.2.3).
Lorsque tous les mécanismes sont pris en considération (FIGURE R.6), c'est la glaciation par immersion qui domine largement avec une contribution mineure de la nucléation homogène. La glaciation par contact et la nucléation par déposition ne contribuent pas à l'évolution dynamique du nuage et la quantité de glace pristine issue de ces mécanismes est marginale.

II.2.3 Discussion

Évolution vers d'autres cadres dynamiques

L'ajout de 41 nouvelles distributions en taille dans DESCAM en font un modèle couteux en temps de calcul. De plus, ces modifications ne sont pas applicables à d'autres cadres dynamiques, notamment la version 3–D de DESCAM.
Il est donc nécessaire de faire des simplifications.

L'algorithme pour la glaciation par immersion comporte deux schémas numériques différents (§6.2.3). En effet, pour les gouttes d'un rayon inférieur à 16 µm, le nombre de gouttes contenant une particule d'aérosol correspond au nombre de particules d'aérosols dans les gouttes car il est possible de supposer que chaque goutte ne contient qu'une seule particule d'aérosol (Figure 6.2). En revanche, pour les gouttes d'un rayon strictement supérieur à 16 µm, le nombre de particules d'aérosol augmente rapidement avec le volume de la goutte et on considère alors que chaque goutte contient un même mélange homogène de particules aérosol.
Une étude de sensibilité a permis de déterminer l'impact de cette séparation algorithmique sur l'évolution du nuage (§6.4.2.3).

Réduction de la complexité (§6.4.3)

La première simplification consiste à éliminer les nouvelles distributions en taille. La distribution en taille pour la surface de particules d'aérosol est :

- paramétrée dans les hydrométéores (eq. 6.22) :
$$\begin{cases} \mathcal{S}_d \propto f(r_d) \cdot \mathcal{M}_d^{\frac{2}{3}} & \text{si} \quad r_d < 16\,\mu\text{m} \\ \mathcal{S}_d \propto \mathcal{M}_d & \text{sinon} \end{cases}$$
- calculée dans les particules d'aérosols (eq. 6.23) :
$$\mathcal{S}_a \propto \mathcal{N}_a \cdot \left(\frac{\mathcal{M}_a}{\mathcal{N}_a}\right)^{\frac{2}{3}}$$

La distribution en taille sur le nombre de particules d'aérosols dans les hydrométéores était surtout importante pour le calcul de la glaciation par immersion, mais l'étude de sensibilité sur l'algorithme (§6.4.2.3) a permis de montrer que la généralisation à un algorithme considérant un mélange homogène des particules d'aérosol au sein des gouttes ne modifiait que marginalement l'évolution du nuage. Cette distribution peut donc être simplement omise pour la glaciation par immersion.
Pour la nucléation par déposition, on considère que chaque cristal ne contient qu'une seule particule d'aérosol et la proportion de chaque type d'aérosol dans les cristaux est déterminée à l'aide de sa proportion en masse.

La deuxième étape consiste à éliminer les types de particules d'aérosol minérales. La masse de particules d'aérosol minérales est donc déterminée :

- par paramétrisation dans les hydrométéores (eq. 6.24) :
$$\begin{cases} \mathcal{M}_d \propto g(r_d) \cdot \sum \mathcal{M}_d & \text{si} \quad r_d < 16\,\mu\text{m} \\ \mathcal{M}_d \propto \sum \mathcal{M}_d & \text{sinon} \end{cases}$$

- par proportionalité dans les particules d'aérosol (eq. 6.25) :
  $\mathcal{M}_{a,\text{mrl}} = \dfrac{\mathcal{M}_{a,\text{bkg}}}{\mathcal{F}_{\text{bkg}}} \cdot \sum \mathcal{F}_{\text{mrl}}$

Suite à ces simplifications, l'impact relatif des différents mécanismes de glaciation reste le même. Il y a quelques changements dans la dynamique suite à la modification du traitement de la surface des particules d'aérosol (réduction de 15% du cumul de précipitations dans le cas où tous les mécanismes sont considérés comme actifs) mais la simplification sur les types d'aérosols a un impact minimal (2% d'augmentation du cumul de précipitations par rapport au cas où seul le traitement du nombre et de la surface des particules d'aérosol est pris en compte).
Les résultats sont proches de ceux obtenus dans le cas de référence (FIGURES R.6 et R.7).

En résumé

L'étude présentée ici a permis l'extension du modèle pour un traitement plus détaillé de la nucléation hétérogène de la glace par l'implémentation des densités INAS et la nature et la taille des particules d'aérosol peuvent désormais être prises en compte.
Le K–feldspath est le minéral le plus actif dans la formation de la glace et est celui qui a le plus d'impact sur la dynamique du nuage, particulièrement dans le cas de la glaciation par immersion qui est le mécanisme dominant dans ce cadre dynamique, même à des altitudes élevées où la nucléation homogène est active.
Enfin, des simplifications des algorithmes de calcul de la nucléation hétérogène permettent l'adaptation future à des dynamiques plus complexes.

Conclusion et perspectives

La compréhension de la formation des cristaux de glace dans l'atmosphère, appelée nucléation, est d'une importance cruciale pour la modélisation du climat et la prévision météorologique. La nucléation de la glace comporte deux types de mécanismes : la nucléation homogène, où la glace se développe au sein de la phase liquide de l'eau ; et la nucléation hétérogène, où la glace se développe sur la surface d'une particule d'aérosol solide. Cette thèse avait pour but de fournir une meilleure compréhension de la nucléation hétérogène et son impact sur le développement des nuages par un travail expérimental et de modélisation.

Le travail expérimental s'appuyait sur le développement d'une cellule de flux pour une expérience de cold stage, développée précédemment à l'institut de météorologie et de recherche sur le climat — département de recherche sur les aérosols atmosphériques IMK–AAF à Karlsruhe, de façon à élargir le champ des mécanismes de nucléation de la glace pouvant être étudiés.
Avec cette nouvelle configuration, une série d'expérience de refroidissement ont été conduites pour étudier la glaciation par immersion et la nucléation par déposition sur le K–feldspath, un type de particules d'aérosol minérales pertinent atmosphériquement identifié comme l'un des plus actives quant à la formation de la glace. Ces expériences ont été menées dans deux buts : (I) explorer la relation entre glaciation par immersion et nucléation par déposition induites par des particules d'aérosol minérales, (II) et de fournir des paramétrisations de densités INAS pour les deux mécanismes de nucléation de la glace.

L'étude expérimentale élargit les travaux de Peckhaus et al. (2016) qui utilisait la même configuration de cold stage sans la cellule de flux.
Trois suspensions contenant des particules de K–feldspath on été préparées avec des concentrations entre $2.5 \cdot 10^{-1}$ et $2.5 \cdot 10^{-3}\,\mathrm{g.L^{-1}}$. Les résultats obtenus pour la glaciation par immersion s'avèrent être en accord avec ceux de Peckhaus et al. (2016) pour la plage de températures basses utilisée dans la mesure où les faibles concentrations de particules d'aérosol utilisées limitaient l'étude à des températures inférieures à −20°C. Comme il a été déjà suggéré dans d'autres études (Peckhaus et al., 2016; Steinke, 2013), une forte corrélation dans l'ordre de glaciation pour des expériences successives de glaciation par immersion a été observée.
Les gouttelettes contenant du K–feldspath étaient ensuite évaporées, laissant les particules résiduelles sur la plaquette de silicium. Celles–ci étaient alors exposées à un flux d'air humide maintenu à une température de point de gel constante. Les températures de point de rosée étudiées variaient entre −20 et −33°C. Pour des températures de point de rosée supérieures à −24°C, des gouttes formées par condensation sur les particules résiduelles ont été observées, permettant l'étude de la glaciation par condensation. Pour des températures de point de rosée plus faibles, la nucléation par déposition a été observée.
Les expériences de glaciation par condensation ont montré un très bon accord avec les expériences de glaciation par immersion dans l'évolution en fonction de la température de la fraction gelée.

Aucune tendance claire dans l'ordre d'apparition des cristaux de glace n'a pu être observée pour les expériences successives de nucléation par déposition. Cependant, l'analyse de la corrélation dans l'ordre d'apparition des cristaux pour les deux suspensions les plus concentrées était difficile dans la mesure où plus d'un site actif de nucléation par déposition était identifiable par gouttelette. La suspension la moins concentrée ne comprenait qu'un seul site actif de nucléation par déposition par gouttelette évaporée, permettant la comparaison de la glaciation par immersion et de la nucléation par déposition pour des particules résiduelles uniques.
Ces expériences ont montré que les gouttelettes ayant gelé de façon hétérogène aux températures les plus élevées contenaient des particules de K–feldspath responsables de la nucléation par déposition aux plus faibles sursaturations.

Ceci indique que *les bons sites actifs de nucléation pour la glaciation par immersion sont également de bons sites actifs pour la nucléation par déposition.*
Ce lien entre les mécanismes pourrait impliquer que les deux mécanismes de nucléation de la glace sont en compétition pour dominer la formation de la glace. Par exemple, les particules ayant servi de noyau de congélation pour la glaciation par immersion dans un nuage précipitant ne seraient pas disponibles pour la nucléation par déposition plus tard en raison du lessivage des particules par les précipitations.

Le travail de modélisation visait à généraliser le travail expérimental et à obtenir un aperçu plus large des mécanismes de formation de la glace. Ce travail utilise DESCAM, un modèle à microphysique détaillée développé au Laboratoire de Météorologie Physique par Andrea Flossmann et ses collègues depuis 1985. Pour cette thèse, le modèle était couplé à un système dynamique à 1.5–D simulant le nuage convectif bien documenté CCOPE. Dans ce système dynamique, la réponse d'un fort système nuageux convectif aux différents mécanismes de nucléation de la glace était étudiée.
Dans un premier temps, des paramétrisations indépendantes des caractéristiques des aérosols ont été intégrées à DESCAM et leurs impacts respectifs sur la dynamique du nuage ont été évalués en considérant tout d'abord chaque mécanisme comme le seul moyen de formation de la glace puis en considérant leurs rôles respectifs dans la formation de la glace quand tous les mécanismes contribuent à la formation de glace primitive. La nucléation hétérogène sur les gouttelettes fraîchement formées (glaciation par condensation) a le plus d'impact sur le nuage en raison de son efficacité à des températures élevées : la nucléation de la glace commence tôt dans le développement du nuage, ce qui change légèrement la dynamique du nuage par le dégagement de chaleur latente mais surtout parce que le processus de Bergeron réduit la taille maximale des gouttelettes dans le nuage. Ceci retarde la formation des précipitations au sol et impacte beaucoup le cumul de pluie. Mais ces paramétrisations indépendantes des caractéristiques des aérosols ont quelques limites dans leur utilité dans la mesure où les processus de nucléation hétérogène dépendent de la concentration, de la taille et des propriétés physico-chimiques des particules d'aérosol qui contiennent un noyau de congélation.

Par conséquent, l'approche des densités INAS a été intégrée à DESCAM.
Les mêmes mécanismes de nucléation de la glace ont été considérés et les particules minérales ont été prises comme particules d'aérosol contenant un noyau de congélation en

raison de leur pertinence atmosphérique et de leur propriétés pour la formation de la glace, mesurée en laboratoire et sur le terrain. Quatre types de particules minérales ont été ajouté à DESCAM avec des concentrations issues de mesures *in situ* : le K–feldspath (environ 20% de la concentration minérale totale dans Kandler et al., 2009, représentant environ 35% de la concentration minérale totale intégrée à DESCAM), l'illite (environ 40% de minéraux intégrés), la kaolinite (environ 8%) et le quartz (environ 17%). Les paramétrisations des densités INAS ont été prises dans la littérature à l'exception de la nucléation par déposition sur le K–feldspath et le quartz, pour lesquelles aucune paramétrisation n'a été trouvée.

Les données obtenues dans l'expérience de cold stage ont permis de d'obtenir une autre paramétrisation pour la glaciation par immersion et une paramétrisation pour la nucléation par déposition sur les particules de K–feldspath. La paramétrisation pour la nucléation par déposition est déterminée sur la base d'un petit nombre d'expériences contenant un assez petit nombre de cristaux de glace et nécessite d'être confirmée par de plus amples expériences à l'avenir. Néanmoins, étant donné que cette paramétrisation est la seule existante, elle a été intégrée par défaut à DESCAM. Pour s'assurer de la fiabilité des conclusions, une étude de sensibilité a été menée en utilisant une paramétrisation basée sur l'Arizona Test Dust.

L'intégration des paramétrisations utilisant les densités INAS dans le modèle assurent une meilleure représentation de la nucléation hétérogène : les mécanismes dépendent maintenant de la taille des particules d'aérosol, ce qui n'était pas le cas par exemple avec la paramétrisation de Meyers et al. (1992). Des études expérimentales (*voir par exemple* Hoffmann, 2015) ont montré une dépendance en taille de l'efficacité de la nucléation de la glace : plus les particules d'aérosol sont grandes, plus la fraction gelée est élevée ; par conséquent, le fait de remplacer des paramétrisations indépendantes des caractéristiques des aérosols par des paramétrisations utilisant les densité INAS améliore la fiabilité des conclusions des études de modélisation.

Dans cette thèse, les résultats de l'étude utilisant la représentation en densités INAS pour la nucléation hétérogène ont confirmé ceux obtenus avec les paramétrisations indépendantes des caractéristiques des aérosols : la glaciation par immersion a le plus d'impact sur le développement à cause de son activité tôt dans le développement du nuage. Cependant, la glaciation par immersion sur les gouttelettes fraîchement formées (glaciation par condensation) n'a pas autant d'impact sur la dynamique du nuage convectif que dans la première étude en raison de son activité plus faible à haute température, ce qui réduit l'influence du processus de Bergeron.

Les deux mécanismes dépendant des particules des particules d'aérosol non–activées (glaciation par contact et nucléation par déposition) jouent un rôle négligeable sur l'évolution dynamique du nuage, comme cela avait déjà été observé dans la première étude. Toutefois, cette conclusion pourrait être biaisée par le type de nuage étudié : le nuage convectif étudié dans cette thèse a un rayon d'activation légèrement supérieur à 100 nm, ce qui est considéré comme le rayon minimal pour qu'une particule possède éventuellement un noyau de congélation (Pruppacher and Klett, 1997). Par conséquent, il ne reste dans le nuage que très peu de candidats potentiels pour la formation de glace par glaciation par contact ou par nucléation par déposition, dans la mesure où toutes les grosses particules d'aérosol ont déjà servi de noyau de condensation.

De nombreuses études de sensibilité ont été menées pour tester l'influence des différents paramètres (par exemple la distribution en taille des particules d'aérosol, les algorithmes de calcul) et ont confirmé les conclusions présentées.

Parmi les minéraux considérés, le K–fedspath est celui qui a le plus d'impact sur le développement du nuage, à la fois en raison de sa forte activité de nucléation de la glace (la glaciation par immersion a été observée en laboratoire pour des températures montant jusqu'à −5°C) mais aussi en raison de sa concentration relativement élevée par rapport aux autres minéraux.

Perspectives

La nouvelle configuration du cold stage s'est révélée efficace pour obtenir des informations théoriques sur la glaciation par immersion et la nucléation par déposition. Cependant, l'échantillon sur lequel l'étude a été menée est assez petit. Plus d'expériences sont nécessaires pour étudier plus en profondeur la question sous–jacente de cette thèse : *est–ce qu'être un bon noyau de congélation pour la glaciation par immersion implique être un bon noyau de congélation pour la nucléation par déposition ?*
La méthode expérimentale doit être améliorée pour augmenter la gamme de températures de point de rosée atteignable dans la cellule de flux.

De plus, une méthodologie améliorée avec un nombre adapté de particules résiduelles est nécessaire pour obtenir une paramétrisation plus fiable pour la nucléation par déposition : un plus grand nombre de gouttelettes ne contenant qu'un seul site actif de nucléation permettrait une meilleure analyse statistique de la nucléation par déposition et un meilleur calcul des densités INAS.
La combinaison d'expériences de cold stage à de la microscopie électronique à balayage environnemental (Environmental Scanning Elecron Microscopy — ESEM) fournirait de plus amples informations quant à la structure des particules glaçogènes les plus actives.

De telles améliorations permettraient d'augmenter le niveau de confiance en une paramétrisation de la nucléation par déposition basée sur les données expérimentales. De plus, même si les résultats de modélisation présentés dans cette thèse sont robustes, ils ne s'appliquent qu'à un certain type de dynamique. Il est nécessaire de regarder l'impact des différents mécanismes de nucléation de la glace sur le développement des nuages dans d'autres dynamiques (par exemple pour des nuages stratiformes).

Aussi, une dynamique plus complexe, par exemple dans un modèle 3–D devrait être privilégiée. La paramétrisation des concentrations en nombre et en masse des particules d'aérosol minérales en fonction de celles des particules d'aérosol de fond ainsi qu'une simplification des schéma de calcul de la nucléation hétérogène sont déjà proposées en fin de thèse.

Il est indiqué dans cette thèse que la glaciation par immersion et la déposition par nucléation ont probablement lieu sur les mêmes sites actifs. Les possibles améliorations dans la procédure expérimentale devraient idéalement conduire à une paramétrisation liant glaciation par immersion et nucléation par déposition, dans une relation du type suivant :

$$n_{s,\mathrm{dep}}(T, RH_i) = n_{s,\mathrm{imm}}(T) \cdot f(T, RH_i)$$

Une telle paramétrisation peut ensuite être testée dans une étude de modélisation.

Parlez-moi de la pluie et non pas du beau temps
Le beau temps me dégoûte et m'fait grincer les dents
Le bel azur me met en rage
Car le plus grand amour qui m'fut donné sur Terr'
Je l'dois au mauvais temps, je l'dois à Jupiter
Il me tomba d'un ciel d'orage

Georges Brassens, *L'orage*

à Jean et Guillaume Bédiée

Introduction

In a continuing trend, the last years have been recorded as the warmest since 1880 (NOAA, 2017) and the annually averaged global temperature is expected to continue to rise over the new century (IPCC, 2013, Summary for Policy Makers). This global warming is accompanied by severe droughts all over the world (Ault et al., 2014) as well as an increased frequency of floods (Hirabayashi et al., 2013), *etc.* Those natural hazards are a societal problem as they impact notably food supply and infrastructures. Floods and droughts correspond to either an excess of precipitation or a lack thereof. Therefore, understanding the mechanisms behind precipitation formation is of crucial importance to weather forecast and to predict the evolution of precipitations on a global scale with changing climates.

The evolution of clouds and the initiation of precipitations are strongly influenced by aerosol particles (Flossmann and Wobrock, 2012), which are defined as a *suspension of airborne solid or liquid particles, with a typical size between* 0.01 *and* $10\,\mu\text{m}$ *and residing in the atmosphere for at least several hours.* [They] *may be of either natural or anthropogenic origin* (IPCC, 2013, Glossary). These aerosol particles are noticed, for example, during pollution spikes (*e.g.* smogs) as they absorb and diffuse incoming solar radiation; as well as outgoing infrared radiation from the earth.
The interaction of aerosol particles with solar and telluric radiation has an impact on the earth's radiative balance (for which the variations with respect to the radiative fluxed since 1750 are called radiative forcing) and is called the aerosol direct effect (IPCC, 2013, Figure 7.3; top bar in Figure I.1). Depending on their nature, aerosol particles have different behaviors regarding the radiative forcing: particles that diffuse the incoming solar radiation tend to lead to a decrease (*e.g.* sulfate and organic carbon particles) whereas particles absorbing the radiations tend to lead to an increase of the radiative forcing (*e.g.*

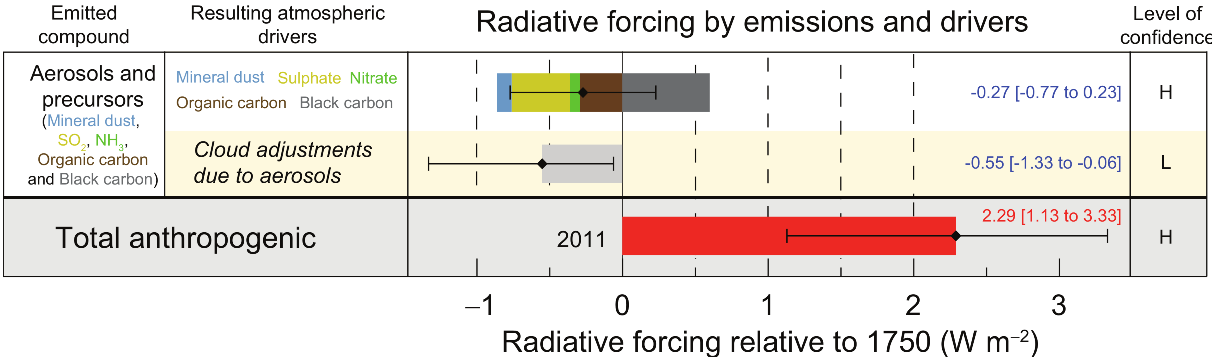

Figure I.1 – Radiative forcing with respect to 1750 due to the direct and indirect effect of aerosol particles (Excerpt from IPCC, 2013, Summary for Policy Maker, Figure SPM.5).

black carbon). The optical properties of aerosol particles and their resulting direct impact on the radiative balance is widely studied (*e.g.* Chauvigné et al., 2016; *see* Yu et al., 2006 for a review) and the resulting net forcing is estimated with a high level of confidence, but some uncertainties remain as to its quantitative contribution.

Furthermore, aerosol particles interact with water vapor and provide the support on which clouds develop and therefore have a major influence on their evolution and the resulting precipitations. The prediction of these precipitations is very important in weather forecasting: be it for extreme events predictions like storms or floods, or for agricultural purposes, accurate predictions are a societal issue. However, even though numerical weather prediction (NWP) models constantly improve their performance, their major weakness remains in the timing and location of the forecasted precipitation. One reason is the lack of knowledge of aerosol–cloud interactions: while the role of aerosol particles on the development of cloud droplets (as cloud condensation nuclei — CCN) is relatively well known (theory developed by Köhler, 1936), the formation of the ice crystals (heterogeneous ice nucleation, where aerosol particles act as ice nuclei — IN) is still poorly understood and under intense investigation and debate. The correct understanding of ice formation is of crucial importance as a very large portion of clouds contain ice (either mixed–phase or ice clouds, *see* Figure 2–33 in Pruppacher and Klett, 1997 and references therein), and at mid-latitudes most of the precipitations originate through the ice phase.
Clouds incidentally interact with solar and telluric radiation. Depending on on the size and phase of the contained hydrometeors[4], clouds behave quite differently and can either increase or decrease the radiative forcing, though, on a global scale, the cloud cover leads to a decrease (IPCC, 2013, Chapter 7). Therefore, cloud–aerosol interactions have radiative implications as they strongly influence the size and number of hydrometeors (Flossmann and Wobrock, 2012) as well as their phase. These implications are called the indirect effect (IPCC, 2013, Chapter 7; middle bar in Figure I.1). The uncertainties regarding the latter are even larger than for the direct effect, as the processes leading to phase changes in clouds are still poorly understood. Therefore, the level of confidence in the aerosol indirect radiative net forcing remains low.

The phase transition from unactivated aerosol particles and liquid droplets to ice crystals is referred to as *ice nucleation* and comprises two types of mechanisms: homogeneous nucleation where the ice phase develops solely from the liquid phase, and heterogeneous nucleation where the ice phase develops with the help of an aerosol particle.
Heterogeneous ice nucleation and its impact on cloud life are investigated through several means: *in situ* measurements, laboratory experiments, and modeling, combined through the development of parameterizations to be used as input for the models. However, laboratory–based ice nucleation parameterizations are generally very specific (*e.g.* ice nucleating active sites — INAS — density, *see* Chapter 2) and cannot be used as input for NWP models with low levels of detail in the representation of aerosol particles. In such models, broader ice crystal parameterizations, typically based solely on the atmospheric conditions are used, as for example the Meyers et al. (1992) parameterization for heterogeneous nucleation, in use in most NWP models (*e.g.* RAMS, Cotton et al., 2003; WRF, Halder et al., 2015) which is only dependent on the relative humidity over ice.

---

[4] The hydrometeors correspond to the larger particles forming a cloud: the droplets and the ice crystals.

The transition from ice nucleation parameterization to ice crystals prediction parameterization has to be made using more precise models (i.e. moment or bin resolved).

This thesis aims to achieve a better understanding of heterogeneous ice nucleation and its impact on cloud development by experimental and modeling means. Specifically, the goals of the thesis are: (1) to explore experimentally the relationship between immersion freezing and deposition nucleation induced by mineral dust particles;, (2) to apply the obtained results in form of an ice nucleation parameterization to a modeling study, (3) and to numerically explore the response of a cloud system to the modification of the parameterization scheme of different ice nucleation mechanisms.

The experimental work presented in Part I focuses on improving our knowledge with respect to immersion freezing and deposition nucleation, two heterogeneous nucleation mechanisms, on K–Feldspar particles. They have recently been identified as one of the most ice active particles of mineral origin (Atkinson et al., 2013). Furthermore, as recent experiments have shown (Kiselev et al., 2017), the study of the poorly understood deposition nucleation will permit potentially important advances in our theoretical understanding of heterogeneous ice nucleation.
A cold stage setup (Peckhaus et al., 2016) in use at the Institute for Meteorology — Atmospheric Aerosol Research division (IMK–AAF) at the Karlsruhe Institute of Technology (KIT) has therefore been expanded in this thesis to further investigate heterogeneous ice nucleation: a flow cell was developed to extend the experimental abilities of the cold stage setup to the investigation of deposition nucleation (Chapter 2).

The combined study of immersion freezing and deposition nucleation on K–Feldspar particles in a cold stage setup presented in this thesis has, to the best of the author's knowledge, never been done. Furthermore, the particular setting of this cold stage, with well defined positions for small droplets of suspension containing K–Feldspar particles, allows to compare ice nucleation by immersion freezing (Chapter 3 and by deposition nucleation (Chapter 4). Thus, the modified setup allows us to address the following question: "*Does being a good immersion freezing ice nucleus imply being a good deposition nucleation ice nucleus?*".

Finally, the experimental investigation of ice nucleation serves a further purpose: providing ice nucleation parameterizations as input for models. The experimental study from this thesis proposes two new INAS density–based parameterizations for ice nucleation by K–Feldspar particles: one for immersion freezing and one for deposition nucleation.

These two parameterizations are used as input in the modeling work of this thesis presented in Part II, which more generally focuses on the impact of ice nucleation parameterizations on the development of the Cooperative COnvective Precipitation Experiment (CCOPE) convective cloud (Dye et al., 1986) and the resulting precipitations, modeled by the Detailed Scavenging Model (DESCAM), a bin–detailed model.

Leroy et al. (2006) noted that, for DESCAM, "*improvements in the treatment of the microphysical ice processes (melting, crystals shape and nucleation) are necessary*". The impact of melting was investigated by Planche et al. (2014). This thesis focuses on the improvement of the treatment of heterogeneous ice nucleation.

The Meyers et al. (1992) parameterization for deposition nucleation and condensation freezing was implemented into DESCAM as, in addition to its efficiency at warm temperatures (Walko et al., 1995), its extrapolation to low temperatures proved to yield good results for cirrus clouds during the Interhemispheric Differences in Cirrus Properties due to Anthropogenic Emissions (INCA) campaign (Monier et al., 2006). Furthermore, its implementation was particularly simple, as the parameterization directly gives a concentration of ice nuclei, solely as a function of supersaturation. This comes as a great advantage when considering particularly computationally expensive models, such as the 3–D version of DESCAM, and allows for realistic ice crystal concentrations. It is also used in a large range of NWP and other mesoscale models. However, the following four issues appear when using this parameterization.
First, experimental data have shown that, for all heterogeneous nucleation mechanisms, temperature is playing a major role (Hoose and Möhler, 2012). Second, the nature of the aerosol particle plays a major role in its ice nucleation efficiency (Hoose and Möhler, 2012). Third, experimental data have shown that heterogeneous ice nucleation is strongly size-dependent (surface area-dependence, Welti et al., 2009; Hoose and Möhler, 2012). Finally, the Meyers et al. (1992) parameterization hardly depicts all heterogeneous ice nucleation mechanisms accurately, given the limitations of the experimental setup that provided the data on which the parameterization was determined. Particularly, the case of large droplets formed through collision–coalescence which contain more than one aerosol particles cannot be taken into account.

In an attempt to improve the simulation of ice formation in the model, the Meyers et al. (1992) parameterization originally implemented in DESCAM was first combined with the Meyers et al. (1992) parameterization for contact freezing and the Bigg (1953) for immersion freezing to represent all heterogeneous ice nucleation mechanisms. The competition of the different mechanisms and their respective role in the development of a convective cloud is studied in Chapter 5.

However, the implementation of these parameterizations do not resolve the first three issues identified with the Meyers et al. (1992) parameterization.
In Chapter 6, the size and temperature parameters are taken into account by adapting DESCAM to the INAS density representation. Furthermore, the aerosol type dependance is investigated by considering different types of minerals as potential ice nucleating particle (INP). The impact of the new parameterizations for immersion freezing and deposition nucleation obtained during the cold stage experimental study is tested.

Finally, the conclusion summarizes the major findings of the thesis and identifies remaining gaps in our understanding of heterogeneous ice nucleation for future research.

Chapter 1

State of the Art of Aerosol–Cloud Interactions

1.1 Aerosol–cloud interactions — Theory

Aerosol particles are at the core of both drop and ice crystal formation. In the former case, they act as cloud condensation nuclei (CCN) and serve as a base for water vapor condensation to form cloud droplets. In the latter case, they act as ice nuclei (IN) and initiate the formation of ice crystals.

1.1.1 Cloud Condensation Nuclei

The CCN role of aerosol particles is well known and described by the Köhler (1936) theory (Figure 1.1), which describes the equilibrium between a droplet of solution and the surrounding humid air. This equilibrium is determined by two separate contributions: the Kelvin law (Pruppacher and Klett, 1997, eq. 6–16b), corresponding to the equilibrium between a pure water droplet and the humid air, and the Raoult law (Pruppacher and Klett, 1997, eq. 4–60) corresponding to the equilibrium between a flat surface of solution and the humid air.

The Köhler equation is expressed as (Pruppacher and Klett, 1997, eq. 6–33):

$$RH_w = \exp\left(\frac{A}{r} - B \cdot \frac{r_{\text{dry}}^3}{r^3 - r_{\text{dry}}^3}\right) \qquad \text{with} \qquad \begin{cases} A = \dfrac{2M_w\sigma_{w/a}}{RT\rho_w} \\ B = \nu\Phi_a\varepsilon_a\dfrac{\rho_a}{\rho_w}\dfrac{M_w}{M_a} \end{cases} \tag{1.1}$$

with A corresponding to the Kelvin law, depending on the temperature (T) and surface tension ($\sigma_{w,a}$); B to the Raoul law, depending on the nature of the aerosol particle (ν is the number of ions released per molecule, ϕ_a the osmotic coefficient, ε_a the solubility, ρ_a the density and M_a the molecular mass of the aerosol particle); ρ_w and M_w the density and molecular mass of water respectively; R the universal gas constant; and r_d and r_{dry} the droplet and dry aerosol particle radii respectively. RH_w is the equilibrium relative humidity (RH) with respect to water, and corresponds to the ratio between the equilibrium water vapor pressure and water vapor saturation pressure.
The equilibrium supersaturations ($s_{v,w} = RH_w - 1$) predicted by the Köhler equation for

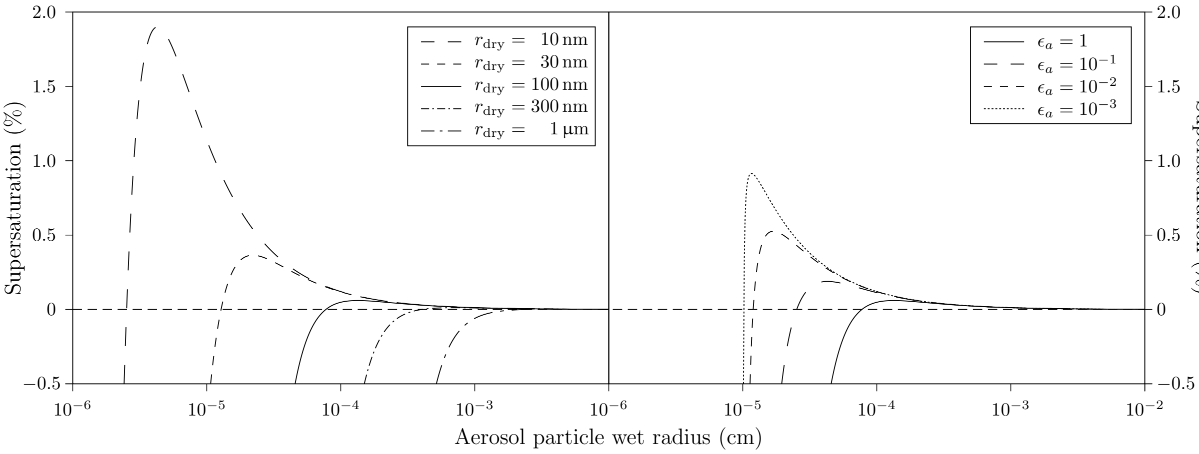

Figure 1.1 – Supersaturation over water ($s_{v,w} = RH_w - 1$) at which the aerosol particle is in equilibrium with the humid air as a function of its wet radius for (**left**) soluble particles of ammonium sulfate of different dry radii and (**right**) particles of ammonium sulfate of a dry radius of 100 nm with different solubilities.

ammonium sulfate particles of different dry radii and solubilities are represented in Figure 1.1.

An aerosol particle grows with increasing supersaturation and stays in equilibrium with humid air. When the supersaturation reaches a critical value corresponding to the maximum of the curve (*e.g.* in the left graph in Figure 1.1, for a dry radius of 30 nm, the critical supersaturation is reached for $s_{v,w} = 0.37\%$ corresponding to an activation radius of 220 nm); no further increase of humidity is needed to increase the size of the aerosol particle: it grows into a droplet. This process is called activation.
An aerosol particle with a wet radius smaller than the activation radius is called an unactivated particle, whereas once it has grown into a droplet, it is called an activated particle.

1.1.2 Ice Nucleation

The formation of cloud droplets allows us to understand the formation of warm clouds (*i.e.* containing only liquid water). However, a large part of the tropospheric clouds contain ice crystals. The origin of ice crystals in the atmosphere therefore needs to be addressed.
There are two distinct types of mechanisms leading to the formation of ice crystals, called ice nucleation: either only the liquid phase is involved (homogeneous nucleation) or a solid aerosol particle intervenes in the process (heterogeneous nucleation). Those two types of mechanisms are presented hereafter.

1.1.2.1 Homogeneous ice nucleation

Homogeneous ice nucleation is defined by Vali et al. (2015) as: "*ice nucleation without any foreign substance aiding the process*".

At below 0°C temperatures, ice embryos (clusters of crystallized water molecules) start forming in the liquid phase of supercooled water droplets, which freeze when an ice embryo

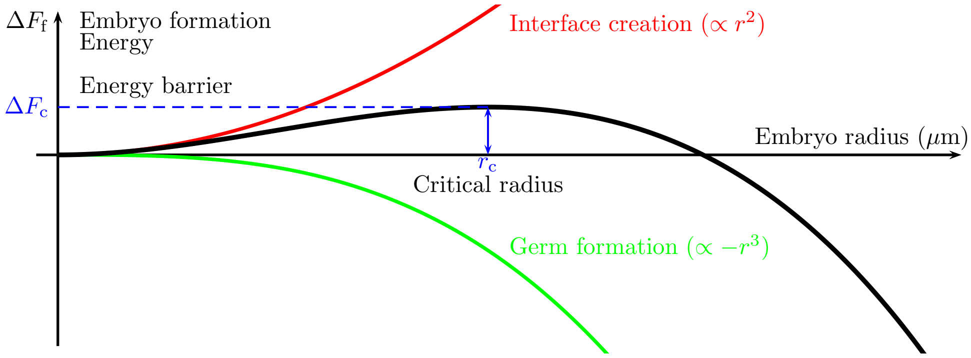

Figure 1.2 – Free energy of the ice embryo formation depending on the embryo radius.

reaches a critical size (Pruppacher and Klett, 1997, Chapter 7). In the case of homogeneous freezing, this critical size can be reached for temperatures below -35°C). The evolution of the embryos follows the *Classical Description* of homogeneous nucleation with two major assumptions: (1) the nucleus is considered as a sphere characterized by the macroscopic density and surface tension, and (2) the distribution of the nuclei follows the Boltzmann law.

Below their critical size, the embryos remain in an equilibrium with their environment in which the bonding and breaking rates are assumed equal ($A_{i-1} + A_1 \rightleftharpoons A_i$ with A_i a cluster of i molecules — *i.e.* i–mer). As the phase change is assumed to occur at constant temperature T and total volume (embryo and liquid phase), the system can be described using the Helmholtz free energy $F = U - TS$, with U the inner energy and S the entropy. Therefore the size distribution of the embryos is expressed as (Pruppacher and Klett, 1997, eq. 7–25):

$$N_i = N_\mathrm{sat} \exp\left(-\frac{\Delta F_i}{kT}\right) \tag{1.2}$$

with N_i the number of i–mers, N_sat the number of water molecules in the droplet for conditions at saturation with respect to a flat water surface and ΔF_i the energy to form an i–mer. This energy can be separated into two parts:

$$\Delta F_i = \Delta F_\mathrm{f} + \Delta F_\mathrm{diff} \tag{1.3}$$

where ΔF_f is the energy needed to form the embryo and ΔF_diff the energy needed for diffusion of water molecules across the water–ice boundary.

The energy of formation of the embryo corresponds to the difference of energy between as system of i molecules of water and a system of i molecules of water with an ice embryo of j molecules:

$$\begin{aligned}\Delta F_\mathrm{f} &= i \cdot \mu_w - [(i-j)\cdot \mu_w + j \cdot \mu_i + 4\pi r_e^2 \cdot \sigma_{w/i}] \\ &= -\frac{4}{3}\pi r_e^3 \cdot n_w \cdot (\mu_w - \mu_i) + 4\pi r_e^2 \cdot \sigma_{i/w}\end{aligned} \tag{1.4}$$

with μ_w and μ_i the chemical potentials of water and ice respectively, n_w the number concentration of water molecules in the droplet, $\sigma_{i/w} = -\sigma_{w/i}$ the surface tension between the embryo and the liquid phase and r_e the radius of the embryo.

As $\mu_w - \mu_i$ and $\sigma_{i/w}$ are two positive quantities, ΔF_f increases until a critical radius r_c (term

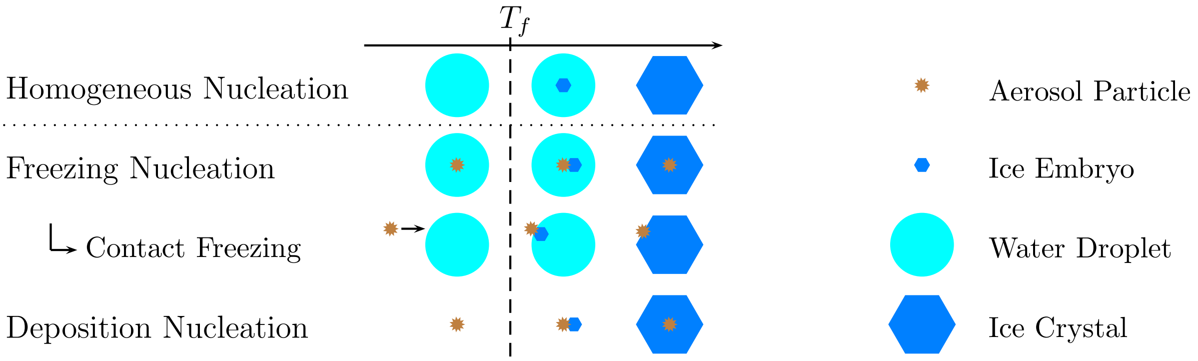

Figure 1.3 – Schematic diagram of ice nucleation mechanisms as depicted by Vali et al. (2015). Freezing nucleation contains immersion, condensation and contact freezing with only the latter depicted here.

in r_e^2 dominates) before decreasing rapidly (term in r_e^3 dominates, Figure 1.2). The energy $\Delta F_\mathrm{c} = \Delta F_\mathrm{f}(r_c)$, necessary to form an embryo of critical radius therefore corresponds to an energy barrier that can be expressed as:

$$\Delta F_\mathrm{c} = \frac{4}{3}\pi \cdot \sigma_{i/w} \cdot r_c^2 \tag{1.5}$$

The energy of diffusion of the water molecules across the water–ice boundary can be expressed as (Zobrist et al., 2007):

$$\Delta F_\mathrm{diff} = \frac{\partial}{\partial T}[\ln(D_v)] \cdot kT^2 \tag{1.6}$$

with D_v the diffusion coefficient of water.

Based on this activation energy, one can calculate the homogeneous ice nucleation rate (classical nucleation theory, *see e.g.* Pruppacher and Klett, 1997, Chapter 7). In models, homogeneous ice nucleation rates are rather computed using parameterizations for practical reasons (*e.g.* DeMott et al., 1997, Tabezadeh et al., 2000, Koop et al., 2000, ...).

1.1.2.2 Heterogeneous ice nucleation: Impact of ice nucleating particles

Heterogeneous ice nucleation is defined by Vali et al. (2015)[1] as follows: "*Ice nucleation aided by the presence of a foreign substance* (ice nucleating particle, INP) *so that nucleation takes place at lesser supersaturation or supercooling than is required for homogeneous ice nucleation*".

The physical principle of heterogeneous ice nucleation is similar to that of homogeneous ice nucleation: it depends on the formation and growth of an ice embryo. The difference resides in the fact that the ice embryo now forms onto an aerosol particle called ice nuclei or ice nucleating particle. This aerosol particle lowers the energy barrier ΔF_c (Mason, 1971) and therefore allows the ice embryo to reach the critical size for conditions where homogeneous ice nucleation wouldn't take place.

---

[1] all following citations, written in italics, in this section are directly taken from Vali et al. (2015), used as reference point on ice nucleation definitions (the reference will not be explicitly written).

Pruppacher and Klett (1997) identify four main requirements for aerosol particles to act as IN: (1) the aerosol particle needs to contain a large insoluble core; (2) to have the ability to form hydrogen bonds at their surface; (3) a crystallographic structure as close as possible to that of ice (although this has recently proven not to be an exclusive requirement, *see* Pedevilla et al., 2016); (4) and the presence of local active sites capable of adsorbing water. These requirements can help identify which aerosol particles might act as INP, however, they cannot account for their actual ice nucleating efficiency.

Heterogeneous ice nucleation mechanisms

Ice nucleating particles can lead to heterogeneous nucleation through two different types of nucleation: either freezing nucleation, defined as "*Ice nucleation within a body of supercooled liquid ascribed to the presence of an INP, or equivalent*" or through deposition nucleation, defined as "*Ice nucleation from supersaturated vapor on an INP or equivalent without prior formation of liquid.*" (Figure 1.3)

Freezing nucleation contains three main types of freezing: immersion, condensation and contact freezing. "*Immersion freezing refers to ice nucleation initiated by an INP, or equivalent, located within the body of liquid.*" In this mechanism, the INP is immersed inside a droplet before initiating the freezing.
"*Contact freezing is initiated by an INP, or equivalent, at the air–water interface as the INP comes into contact with the liquid, or forms at an air–liquid–particle triple interface.*" In this mechanism, a free (unactivated) aerosol particle comes into contact with a liquid droplet through impaction scavenging. Compared to other ice nucleation mechanisms, there are only few experiments investigating contact freezing but the data show a higher freezing efficiency than for immersion freezing. Therefore contact freezing might play a non negligible role in clouds, particularly in the mixing areas of convective clouds where unactivated aerosol particles are mixed with cloud droplets (Ladino Moreno et al., 2013).
"*Condensation freezing is defined as taking place when freezing is initiated concurrently with the initial formation of liquid on a cloud condensation nuclei at temperatures below the melting point of ice. This was envisaged as a possible sequence in clouds but evidence for its existence is minimal. Whether condensation freezing on a microscopic scale, if it occurs, is truly different from deposition nucleation, or distinct from immersion freezing, is not fully established. Hence, the use of this term requires added circumspection.*" In some parameterizations (*e.g.* Meyers et al., 1992), it has been considered that condensation freezing was the mechanism responsible for the ice nucleation. However, the experimental distinction between condensation freezing and immersion freezing or deposition nucleation is hard to determine.

Deposition nucleation is defined as "*Ice nucleation from supersaturated vapor on an INP or equivalent without prior formation of liquid.*" This mechanism has been under thorough investigation over the last decade (*e.g.* Zimmermann et al., 2007; Eastwood et al., 2008; Schill et al., 2015) and tremendous progress in our understanding of deposition nucleation were recently done by combined use of crystallography and electron microscopy on deposition nucleation experiments (Pedevilla et al., 2016; Kiselev et al., 2017). However, a recent study by Marcolli (2014) has suggested that deposition nucleation at relative humidities with respect to water below 100% corresponds to either homogeneous nucleation (for T<235 K) or immersion freezing (for T>235 K) in water–filled pores at the surface of the INP. Even though it might not be of large importance for in–cloud ice nucleation, this mechanism could be highly significant climatically, because of its role in cirrus formation (Hiron and Flossmann, 2015; Cziczo et al., 2013).

INAS density

To represent accurately heterogeneous nucleation, the concept of ice nucleating active sites (INAS) density, defined originally by DeMott (1995), is extensively used to obtain size–dependent parameterizations for ice nucleation.
"*The INAS density describes the number of ice nucleation active sites at a certain temperature and supersaturation, normalized by the aerosol surface area. The approach is based on the assumption that the investigated aerosol sample is of uniform composition. Time dependence is not taken into account.*" (Hoose and Möhler, 2012)

The INAS density n_s (generally in cm^{-2}) is defined as follows:

$$f_i = 1 - \exp(-n_s \cdot S) \tag{1.7}$$

with f_i the frozen fraction[2] and S the mean surface per aerosol particle or hydrometeor. The frozen fraction corresponds to the ratio between the number of ice crystals and the total number of droplets and/or aerosol particles at the beginning of the experiment, the mean surface is calculated over all considered aerosol particles, whether frozen or not.

1.1.3 Aerosols in the atmosphere

The aerosol particles found in the atmosphere have different origins: the co–condensation of gases (*e.g.* Rose, 2014); emission from the ground (anthropogenic activities, mechanical erosion, sea spray, biomass burning, volcanoes, ...; Pruppacher and Klett, 1997, Chapter 8) and extraterrestrial (*e.g.* fragments of meteorites). The chemical nature of the aerosol particles varies and the most abundant are composed of sulfate, sea salt, minerals, soot (biomass burning) and organic material.
The seasonal repartition of aerosol particles in the atmosphere is represented, by the mean of the aerosol optical depth (AOD), in Figure 1.4. The high concentrations of aerosol particles (areas in red) result from two different source types: biomass burning (west coast of Africa in frames **a** and **b**; southern Africa and Amazonia in frames **c** and **d** and eastern China in frame **c**) and desert dust (Sahara and middle east in frames **b** and **c**).

The aerosol particles emitted by biomass burning are essentially soot, which are rather poor ice nuclei (Hoose and Möhler, 2012; Ullrich et al., 2017). They are the main contributors to the direct effect of aerosol particles on the radiative forcing (Ramanathan and Carmichael, 2008; IPCC, 2013, Chapter 7), but their impact on clouds is rather small.

---

[2] the frozen fraction corresponds to the ratio between the total amount of hydrometeors and the number of ice particles

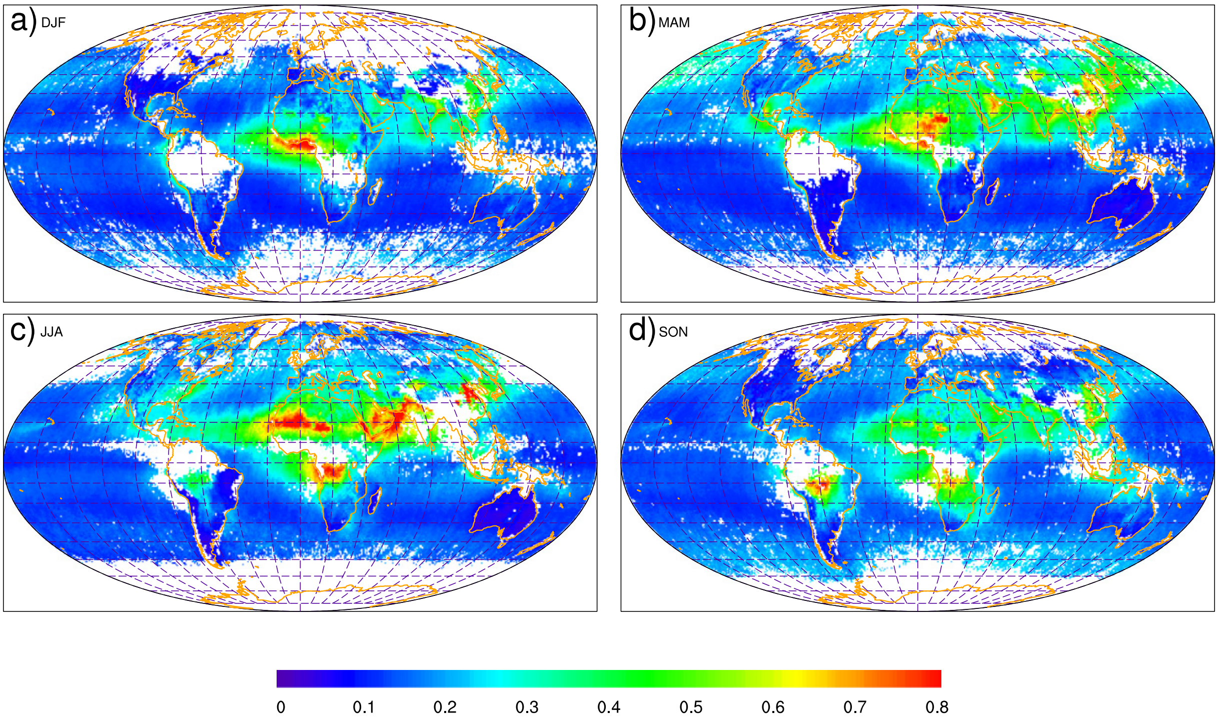

Figure 1.4 – Seasonally averaged AOD at 0.55 µm from 2001 to 2011 retrieved from the Multiangle Imaging Spectroradiometer (MISR) in (a) DJF, (b) MAM, (c) JJA and (d) SON. (Excerpt from Choobari et al., 2014, Figure 1)

Dust particles on the other hand represent more than half of the total global aerosol burden (Zender et al., 2004) and have proven to be rather good ice nuclei (Hoose and Möhler, 2012). They have recently been identified as one of the main drivers of ice nucleation even in regions where homogeneous nucleation was thought to be dominant (Cziczo et al., 2013).
Finally, the last group of aerosol particles that might play an important role in aerosol–cloud interactions are the aerosols of biological origin (ABO, *e.g.* bacteria — and fragments of bacteria, pollen, . . .). Some have proven to be highly efficient IN, forming ice at temperatures as high as −2°C (Hoose and Möhler, 2012) but their abundance in the atmosphere is rather low (Burrows et al., 2009) and the representativeness of highly IN active biological aerosols for the entirety of ABO is quite uncertain. Previous work (Hiron, 2013; Hiron and Flossmann, 2015) indicated that an unrealistic concentration of highly ice active ABO is needed to have a significant impact on the dynamics and precipitations of a convective cloud. This comes in agreement with Hoose et al. (2010), who found a contribution from ABO to ice nucleation rates ranging from 10^{-5} to 0.6% and a minor importance of '*bioprecipitations*' on a global scale.

Given their ubiquity and good IN efficiency, mineral aerosols have been largely studied (Hoose and Möhler, 2012). At the time of the review, the experimental data essentially focused on clay minerals (kaolinite, illite, montmorillonite) and Arizona Test Dust, a commercially available surrogate for desert dusts. But more recent studies (*e.g.* Atkinson et al., 2013) have shown that the most present mineral in the earth crust, Feldspar, is actually a better ice nucleus.

1.2 The role of ice nucleation in Aerosol–Cloud Interactions

To improve our knowledge of aerosol–cloud interactions, different methods have to be combined: remote–sensing, *in situ* measurements, laboratory experiments and modeling studies. Remote–sensing is necessary in order to validate the different models (Zwiebel, 2015; Planche et al., 2010) while *in situ* measurements and laboratory experiments provide key elements for theory development and microphysics understanding (*e.g.* Kiselev et al., 2017) as well as parameterizations as input for the models.
The CCN properties of different types of aerosol particles are continuously being investigated, with a recent development to facilitate the model representation of the theory (κ–Köhler Theory, Petters and Kreidenweis, 2007; *see* Chapter 6 for more details), particularly mineral aerosol particles (*e.g.* Koehler et al., 2009; Karydis et al., 2011).
The knowledge about the heterogeneous ice nucleation is, on the other hand, rather poor. Its experimental investigation has therefore recently gained in intensity (DeMott et al., 2011) and is the focus of the next section.

1.2.1 Freezing experiments

Laboratory freezing experiments cover a large range of sampling volumes: they range from single–droplet experiments (*e.g.* Duft and Leisner, 2004) to cloud expansion over several cubic meters (*e.g.* the AIDA facility, Möhler et al., 2003; *see also* DeMott et al., 2011 and Hoose and Möhler, 2012 for a summary of existing experimental setups).
Ice nucleation chambers work with large numbers of particles and hydrometeors, leading to bulk results on large populations. They allow for precise measurements of ice nucleation efficiency in atmospherically relevant conditions for different materials (Welti et al., 2009; Hiranuma et al., 2015), but do not permit the detailed observation of microphysical processes.
Experiments like the electrodynamical balance (EDB) setup (Duft and Leisner, 2004) allow for observation of single–droplet freezing. This setup is particularly relevant for the investigation of contact freezing (Hoffmann, 2015). Furthermore in recent developments, the EDB setup, coupled to a fast camera has proven very helpful in observing and understanding secondary ice processes (Pander, 2015; Lauber, 2016). However, after a freezing event, the object of study is renewed which does not permit comparative observations for different conditions.

Cold stage setups correspond to an intermediate scale: several droplets are observed simultaneously (yielding direct statistical information) with each droplet being precisely located and identified (*e.g.* Murray et al., 2011). Furthermore, as the droplets are deposited on a substrate, it is possible to make cycled experiments for a wide range of temperatures, cooling rates. This setup alone only permits investigation of immersion freezing and homogeneous nucleation. It can however be coupled with a flow cell in order to achieve humidity control in the chamber and to inject aerosol particles to observe the other ice nucleation mechanisms (*e.g.* Shaw et al., 2005; Schill et al., 2015).

Such a cold stage setup has been developed at the Institute for Meteorology — Atmospheric Aerosol Research division (IMK–AAF), Karlsruhe since 2011 (Hiron, 2011) to complement the AIDA facility (Steinke, 2013) and the EDB experiments (Peckhaus, 2016). The setup proved able to observe homogeneous ice nucleation in spite of the droplets being in contact with a silicon wafer substrate (Hiron, 2011; Steinke, 2013) and was further used to study the ice nucleation abilities of K–rich feldspar in the immersion freezing mode (Peckhaus et al., 2016).

1.2.2 Atmosphere and cloud modeling

In order to understand the impact of the experimental results on aerosol–cloud interactions and to be able to generalize their importance for the development and life cycles of clouds, we have to resort to modeling. The following section presents a brief review of existing models and their particularities and an overview of the state of the art of the cloud–resolving models at the Laboratoire de Méréorologie Physique (LaMP), Université Clermont Auvergne (UCA) in Clermont–Ferrand, that were used during this thesis.

1.2.2.1 Types of models

As was the case for the freezing experiment setups, the atmospheric models cover a large range of space and time scales, with a similar compromise between the level of detail and the modeling scale. Therefore, it is necessary to adapt the model specificity to the atmospheric processes that are to be studied.

Climate and operational numerical weather prediction (NRP) models need simplified representations of cloud physics, due to their complexity and large scale for the former and the necessary speed of execution for the latter. They therefore rely on parameterizations for the cloud cover, extent and water phase (*e.g.* Kessler, 1969 and Kärcher and Lohmann, 2003).
For a finer representation of clouds in the atmosphere, smaller scale models (from 0–D air parcel to 3–D meso–scale models) resort to two different types of microphysical models: moment or bin resolved models.

In moment models, the dimensional distribution of aerosol particles and hydrometeors (droplets and ice crystals) are represented by the mean of a predetermined function (log-normal, gaussian, gamma, ...) for which the parameters (center, width, integral, ...) evolve following the different microphysical processes. The cloud properties are then derived from the different moments of the distributions. Using a number concentration distribution $N(r)$, the i–th moment M_i is given by:

$$M^i = \int_{\text{spectrum}} N(r) r^i \mathrm{d}r \tag{1.8}$$

The zeroth moment gives the total number of particles, the second moment is proportional to the total area of the particles and the sixth moment is proportional to the radar reflectivity.

In spectral or bin resolved models, the dimensional distribution of aerosol particles and hydrometeors is discretized onto a size (or mass) grid, with each separate bins then evolving separately. The degree of complexity and the computing cost of such models strongly depend on the number of bins (in this thesis, the number of bins was set to 39). This type of model allows for a refined representation of water vapor exchange, collection processes, terminal velocities, *etc.*

Bin detailed models are the most precise when it comes to studying aerosol–cloud interactions but come with a strong computing cost when compared to parameterized models.

1.2.2.2 Ice nucleation in bin resolved models developed at the LaMP

The Detailed Scavenging Model (DESCAM) is a cloud–resolving bin resolved model developed since 1985 by Andrea Flossmann and her coworkers (Flossmann et al., 1985; Flossmann, 1987). Originally developed to study the wet removal of atmospheric pollutants with a particular emphasis on the phenomenon of acid rains through the dissolution of sulfuric acid in rain drops, it has been extended to include ice nucleation processes, using various ice nucleation parameterizations over time (Flossmann and Wobrock, 2010 and references therein).

In a cirrus–formation modelling study, Monier et al. (2006) compared different heterogeneous and homogeneous nucleation parameterizations in a microphysics module that in addition resolves the aerosol particle distribution inside a drop class (EXMIX, Wobrock, 1986). The size–independent heterogeneous nucleation parameterization of Meyers et al. (1992) proved to be the most accurate in depicting crystal residual aerosol spectra and was implemented into DESCAM conjointly with the homogeneous nucleation parameterization of Koop et al. (2000).

These were the ice nucleation parameterizations used in Hiron (2013), starting point of this thesis as well as in Quérel et al. (2014).

Part I

Experimental Study of K–feldspar Particles: The Cold Stage Experiment

Chapter 2

The Cold Stage Experiment: Experimental Setup and Method

The first part of the thesis focuses on the experimental results obtained with the Cold Stage (CS) present at the Institute for Meteorology — Atmospheric Aerosol Research division (IMK–AAF).

A greater understanding of heterogeneous ice nucleation mechanisms is needed, particularly how the different mechanisms can be related to each other. It has been suggested that deposition nucleation could be viewed as immersion freezing occurring in aerosol particles pores and cavities (Marcolli, 2014); suggesting that the physical process behind both ice nucleation mechanism was identical. Our cold stage setup was extended to answer to the following question: "*Does being a good immersion freezing ice nucleus imply being a good deposition nucleation ice nucleus?*".

The experimental methodology proposed to answer this problematic consists in the consecutive measurement of immersion freezing and deposition nucleation on the same identified aerosol particles in atmospherically relevant conditions (temperatures in $[-40°\mathrm{C}; 0°\mathrm{C}]$).

This experimental study focuses on K–rich feldspar (later referred to as K–feldspar) particles.

Feldspar is the main mineral constitutive of the Earth's crust and is ubiquitous in the atmosphere: *in situ* measurements have shown a mass fraction of feldspar in the Atlas mountains between 10% in a dust storm and 25% in low dust conditions (Kandler et al., 2009), however, the mass fraction further away from the dust sources is rather uncertain (Nickovic et al., 2012). Feldspar might play an essential role in the cloud ice nucleation as it was identified as one of the most ice active minerals.

Various experiments have been recently conducted on feldspar in different setups. Deposition nucleation has been investigated using environmental electron microscopy (ESEM), showing that K–feldspar was ice active at a low relative humidity over ice and high temperatures (onset $RH_i = 105\%$ at $-12°\mathrm{C}$; Zimmermann et al., 2007). In a diffusion chamber, Yakobi-Hancock et al. (2013) found that 200 nm washed K–feldspar particles presented an activated fraction of 0.1% at $-40°\mathrm{C}$ for a relative humidity over ice of 127%.

Immersion freezing on K–feldpsar particles has been particularly investigated in droplet freezing assay experiments (*e.g.* Atkinson et al., 2013; Peckhaus et al., 2016; Harrison et al., 2016) showing that K–feldspar particles initiate ice nucleation at the warmest temperature among the main mineral dust components. In a recent study, Boose et al. (2016)

have shown in a field campaign in Spain on Saharan air masses, that the submicron ice nucleating particle (INP) concentration was fairly well correlated with feldspar tracers.

In this chapter, the features of the cold stage and the flow cell developed for this thesis are presented, followed by the data acquisition chain and analysis method. Subsequently, the preparation of the investigated material is described. Finally, the experiments are explained as well as the processing of the raw data.

2.1 The Cold Stage

2.1.1 Original Setup

The cold stage has been in service at the IMK–AAF since Hiron (2011) with little development (Pt–100 temperature sensor). This setup was already presented in Peckhaus et al. (2016) and the following section summarizes the main features. All features presented are sketched in Figure 2.1, except for the syringe.

Cold stage

The experiment resolves around a commercially available motorized cold stage from Linkam Scientific Instruments (model MDBCS–196). The center part of the cold stage is a silver block, which can be set to temperatures between −196°C and +125°C and is cooled by liquid nitrogen with cooling rates from 0.01 to 150 $\mathrm{K.min^{-1}}$ with a temperature stability of 0.1°C.
The investigated sample is placed on a copper plate (sample holder) in contact with the silver block. This plate can be moved over 15 mm by means of two motors in order to investigate different areas of the sample. In our setup, the motors are used to deposit the droplets on defined positions on the sample.
The temperature at the surface of the sample is measured by a Pt–100 sensor, calibrated in the range of [−40°C; +30°C], with an accuracy of ±0.1°C.

Syringe

The droplets are deposited on the sample, at room dew point temperature, by a piezo–driven drop–on–demand generator (GeSIM, Model A010–006 SPIP, cylindrical case, *see e.g.* Hoffmann, 2015). This syringe generates mono–disperse sized droplets (from 100 pL to a few nL) with an accuracy of 1% reported by the manufacturer (GESIM, 2014).

Camera

Over the course of experiment, the sample is observed through a lid port hole and recorded by a CCD Camera (EO progressive, 1600x1200 — cropped to 1200x1200) mounted with a wide field objective (DiCon fiberoptics Inc.). The sample is lit by an annular polarized light source. A second polarizator (analizator) is mounted on the objective to detect depolarization.

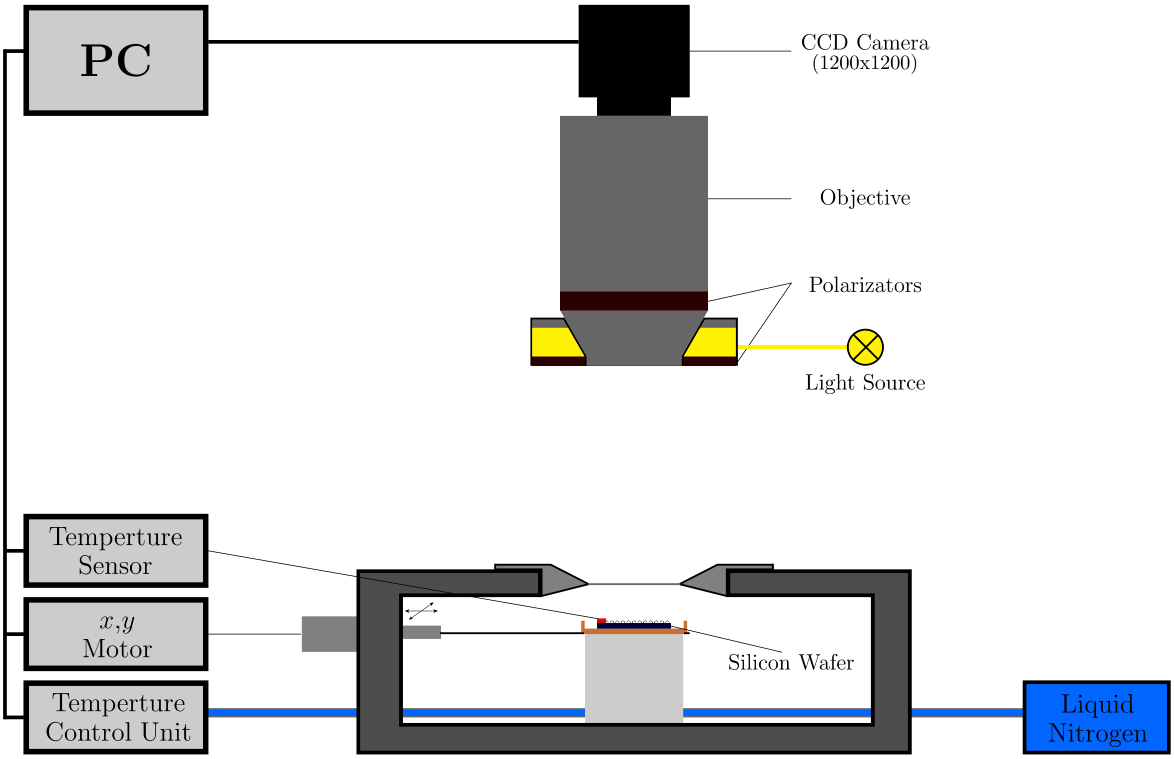

Figure 2.1 – Original setup for the cold stage as described in Peckhaus et al. (2016)

The video recording of the experiment is controlled by a LabView routine for post–treatment and analysis. The frame rates range from 0.1 to 5 per second and the definition of the image is 8.7 µm/pixel.

2.1.2 Adaptations to the setup and new developments

The main experimental focus of this thesis is on deposition nucleation. To investigate this heterogeneous ice nucleation mechanism, material developments were needed as even though the original Linkam cold stage setup allows for controlled air to flow through the chamber, two main problems arose:

- it had occurred over previous campaigns that the droplets' stability was an issue as they frequently evaporate before freezing. This was corrected by covering the sample with silicone oil (Peckhaus et al., 2016) which incidentally prevented interaction between the droplets.

- the chamber around the cold stage is quite large (several cL) and homogeneity is hard to obtain. Particularly, as the coldest element in the chamber is the silver block, the developing frost complicated the control over the dew point temperature. The metallic link between the sample holder and the motors showed similar behavior.

Therefore, a new lid was designed for the setup to reduce the chamber volume in order to ensure better control and homogeneity (Figure 2.2).

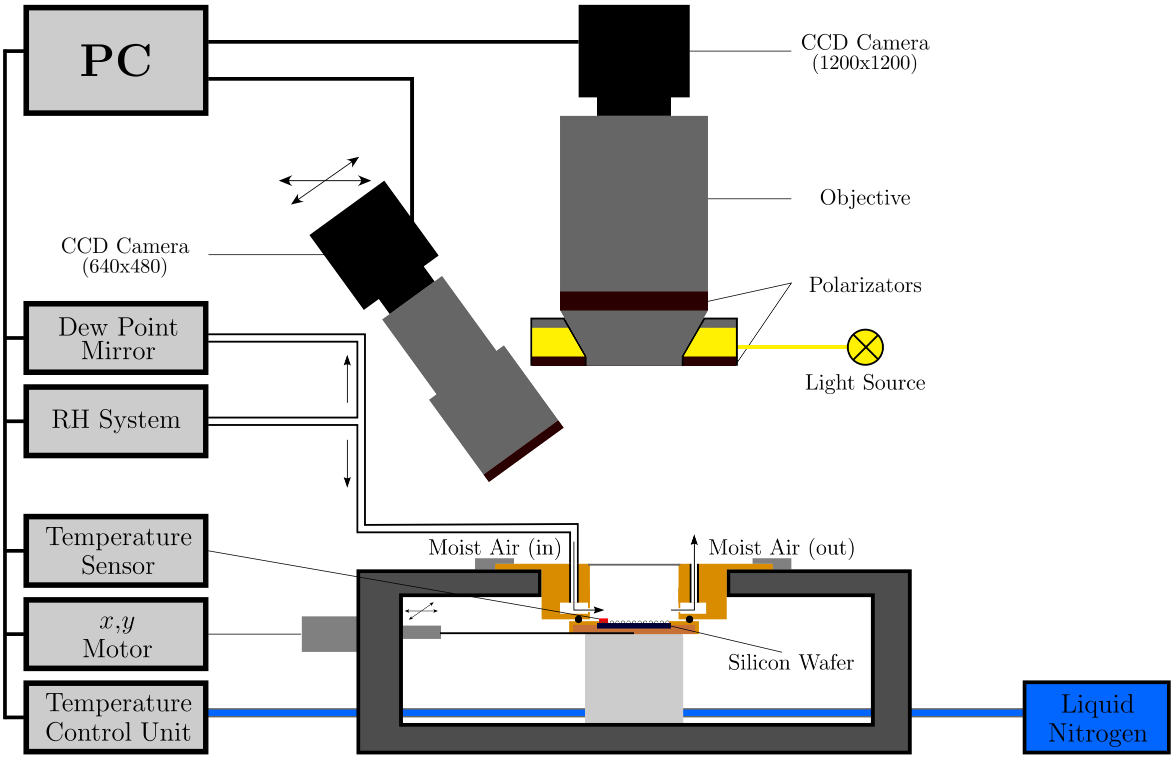

Figure 2.2 – New setup for the cold stage

2.1.2.1 Flow Cell

The new cell comprises two main features: a new copper sample holder with a 10x10 mm enclosure for the silicon wafer and a new PEEK lid. To prevent frost on the sample holder, a PEEK cover was also designed.
The isolation from the flow cell is ensured by pressure from the clampings on the lid and a toric joint between the lid ans the PEEK cover. The wafer is pressed in contact with the sample holder by the PEEK cover.
The lid port hole is sealed by a 1 mm–thick flat lens held by silicone glue.

The lid contains an annular chamber separated for incoming and outgoing moist air. Each side of the annular chamber is drilled regularly with eleven 200 µm diameters holes, sized to ensure isotropic air flux.

2.1.2.2 Relative Humidity control system

The flow cell is supplied by a relative humidity (RH) system represented in Figure 2.3 in which the incoming compressed air (with a specified dew point temperature of −45°C) is separated into three controlled partial flows.
The first flow (upper box in Figure 2.3) is used as input to a humidifier developed by ANSYCO. In the humidifier, the flow is once again split: the constant rate top flow remains unchanged while a computer controlled mass flow controller (MFC) sets the rate of flow bubbling in the water bath. Both flows are recombined as an output to the humidifier.
The second flow remains unchanged and its rate stays constant over the course of the experiment.

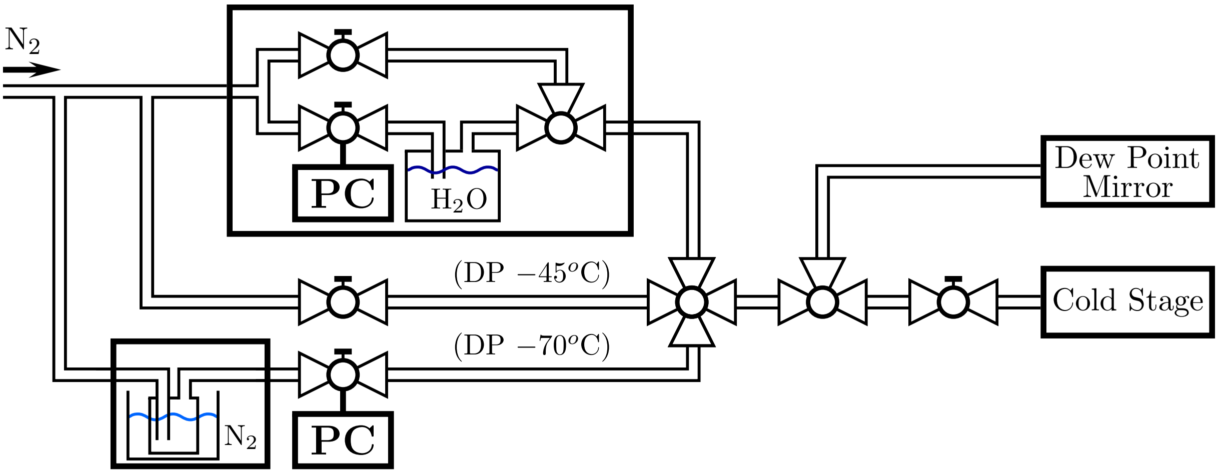

Figure 2.3 – Relative Humidity control system

The third flow is lead through a cold trap plunged in liquid nitrogen. The rate of flow of this very dry air (dew point of *ca* −70°C) is set by a computer controlled mass flow controller.

The three partial flow are then recombined and used as input for the flow cell. The incoming rate of flow is set by a manually set MFC and remains constant throughout the experiment. The remaining flow is directed towards the dew point mirror (DPM, MBW calibration) for measure, read by the LabView controlling program.

The RH control system has a dew point range of $[-50°\text{C}; 7°\text{C}]$ with a low response time in the flow cell (over a minute) partly because of the distance from the RH system to the cold stage. Furthermore, the dew point mirror also has a slow response time (for abrupt changes of dew point temperatures, the dew point mirror needs over 5 min to give a stabilized measure).
Finally, the dew point mirror needs a rather large incoming flow of about $1\,\text{L.min}^{-1}$ to function properly, so that measuring the humidity of the flow cell outgoing flow is not possible.

Because of the slow response time of the RH control system, a flow cell bypass is set for immersion freezing experiments: in such experiments, because of the wide range of temperature investigated (over 40°C), the continuous flow of dry or humid air would dramatically unstabilize the deposited droplets as they would rapidly grow or evaporate, depending on the relative humidity in the chamber. With the bypass, the humid air in the chamber remains steady, therefore, the droplets and ice crystals can only grow by diffusion of water vapor, which limits the growth speeds, even though the chamber is generally in supersaturated conditions with respect to water (the droplets are deposited at room dew point temperature, which is therefore also the dew point temperature inside the flow cell).

2.1.2.3 Zoom Camera

A second CCD–camera (IC, 640x480) is added to look closer at portions of the sample with an angle of around 30°. This camera is set on a micrometric rotative translation tray

and mounted with an objective and a polarizer.
This camera has a definition of 2 μm/pixel.

2.2 Analysis method

The results obtained by the cold stage experiment are based on the video recorded by the main CCD–camera combined with a file containing the thermodynamic informations.

2.2.1 Video treatment

At the beginning of the experiment, the two polarizators are set in parallel. As the droplets do not affect the polarization upon reflection, all reflected light is detected by the camera. A built–in LabView routine searches for bright objects on the sample and their positions and bounding boxes to the detected object are stored. The detection of freezing is done by measuring the evolution of the mean grey level over each bounding box.
During an immersion freezing experiment, the two polarizators are set orthogonally, therefore, the droplets and wafer are not detected by the camera anymore as they do not affect the polarization upon reflection. The ice crystals however, do change said polarization, which allows for automatic detection on the video by "*enlightenment*" which translates into a jump of the mean grey level.
During a deposition nucleation experiment, the apparition of an ice crystal is more subtle. Indeed, the ice crystal grows from residual particles that are hardly detected by the CCD camera. Therefore the polarizators are set at an angle of approximately 45° to get a better glimpse at early ice formation. In ideal cases, the detection can be automated, but generally necessitates manual intervention to detect most precisely the ice nucleation point.
The data analysis output is the number of frozen droplets as a function of time (and therefore as a function of the thermodynamic parameters).

2.2.2 Correlation

As the positions and bounding boxes have been previously stored, two consecutive experiments can be processed using the same position mask.
In the data analysis output file, the number of each droplet is written upon freezing. It is therefore possible to give to each of the frozen droplet a freezing rank in each separate experiment. The correlation between the freezing ranks of the droplets is calculated using the Pearson's correlation coefficient and used to assess the stochasticity of the freezing process. A correlation coefficient close to 0 corresponds to a stochastic freezing process, for example in the case of homogeneous nucleation whereas a correlation close to 1 corresponds generally to heterogeneous nucleation (Peckhaus, 2016).

2.3 Sample preparation

The samples investigated in this thesis consist in two parts: (1) a 100 cm^2 square silicon wafer (Plano GmbH) used as substrate for (2) suspensions containing K–feldspar particles

(Bureau of Analyzed Samples, UK, standard BCS 376 — provided by the University of Leeds, UK — thereafter identified as FS02).

2.3.1 Wafer

The silicon wafer was prepared in a seven step cleaning procedure to ensure the purity of the surface and minimize interference in the freezing process. First, the silicon wafer is plunged into four consecutive ultrasonic baths for 5 minutes, containing respectively dichloromethane, ethanol, 35% nitric acid and double distilled water (NanoPure, Barnstead Thermolyne Corporation, Infinity Base Unit, $18.2\,\mathrm{M\Omega.cm^{-1}}$). Then, the silicon wafer is blown out dry by pressurized gaseous nitrogen and rinsed in dicloromethane. Finally, the silicon wafer is blown out dry and stored in a clean Petri dish.

2.3.2 Suspension

The suspensions were prepared using double distilled water and milled K–feldspar. Three suspensions were prepared for this study on a base of 0.025 weight percent (wt%) and dilutions to the tenth and to the hundredth.

The base suspension (suspension **A**) was obtained by mixing $13.2 \pm 0.5\,\mathrm{mg}$ of FS02 in $52.6 \pm 1.0\,\mathrm{mL}$ of highly pure water (34877–M EMD Millipore, HPLC Plus — σ–Aldrich) yielding a concentration of $C_A = 0.25 \pm 0.01\mathrm{g.L^{-1}}$ ($2.5 \cdot 10^{-2}\mathrm{wt\%}$). The suspension was stored in a closed Erlenmeyer and magnetically agitated to prevent particle sedimentation.

Suspension **B** was obtained by diluting $5.0 \pm 0.2\,\mathrm{mm}$ of suspension **A** in $45 \pm 1\,\mathrm{mm}$ of highly pure water. The same procedure was repeated using suspension **B** in order to obtain suspension **C**. Both suspensions were stored in the same fashion as suspension **A**.

2.3.3 Total particle surface per droplet

As the results are analyzed by the mean of ice nucleating active sites (INAS) density representation (*see* Chapter 1), it is necessary to have an estimate of the total FS02 surface per droplet in each sample.

The calculation is based on Peckhaus (2016) where the Feldspar samples were thoroughly characterized by BET methodology (Brunauer et al., 1938) and by electron microscopy. FS02 particles radii were found to range in [0.3; 4 µm] with a maximum for approximately 700 nm for a total surface per unit of mass of: $S_{\mathrm{BET}} = 2.64\,\mathrm{m^2.g^{-1}}$.

Once the total FS02 surface per unit of mass is calculated, the total surface per droplets can be calculated based on the droplet volume.

Before starting the cooling, a few frames are recorded with a parallel polarizator, offering a view of the droplets shortly after their deposition on the silicon wafer. We use these frames for each immersion freezing experiment (*see* Chapter 3), to calculate the apparent diameter of the droplets. We fit the obtained diameter using a Gaussian function (Figure 2.4), yielding a mean apparent diameter of $17.0 \pm 2.9\,\mathrm{pixel}$.

Even though the droplets were deposited onto the wafer at room dew point temperature, some evaporation might be responsible for the quite large dispersion, particularly

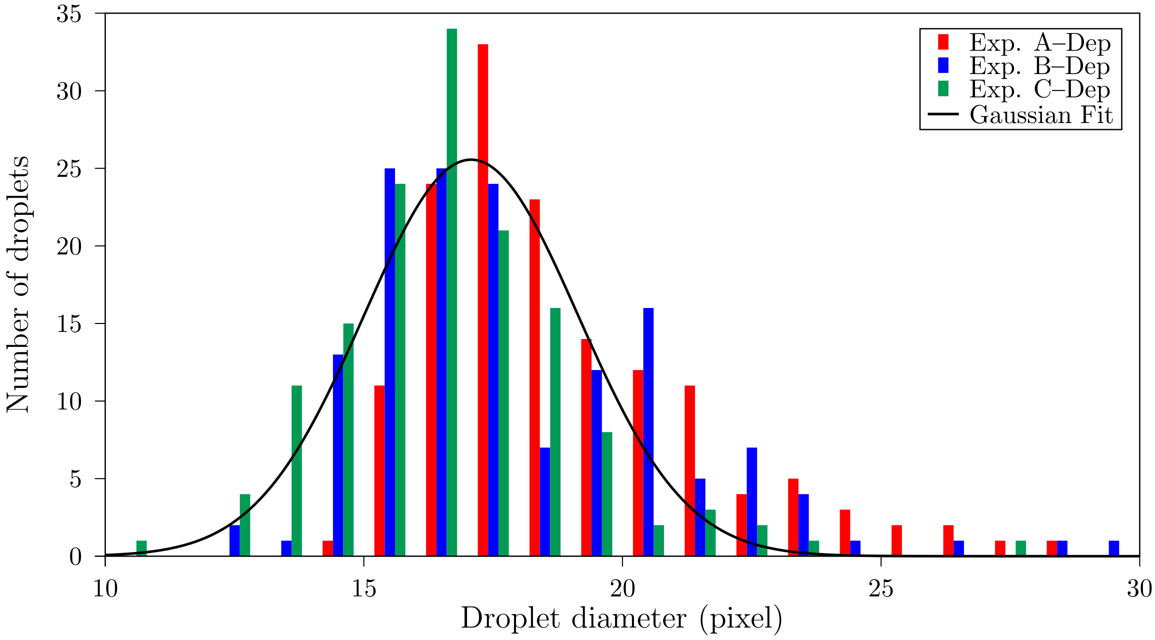

Figure 2.4 – Number of droplets for the three immersion freezing experiments as a function of their apparent diameters (bins of one pixel).

Suspension	**A**	**B**	**C**
Concentration (g.L^{-1})	$(2.5 \pm 0.1) \cdot 10^{-1}$	$(2.5 \pm 0.2) \cdot 10^{-2}$	$(2.5 \pm 0.2) \cdot 10^{-3}$
S_p (cm^2)	$(3.76 \pm 2.40) \cdot 10^{-6}$	$(3.76 \pm 2.42) \cdot 10^{-7}$	$(3.76 \pm 2.42) \cdot 10^{-8}$

Table 2.1 – Summary of the suspensions used in this study

in experiment 121 (blue bars). The measured apparent diameter is minimized by this method. Furthermore, the diameter is determined based on the reflection of the droplet and therefore further minimized.

The deposited droplets have a geometry of a spherical cap with the volume defined as (Bourges-Monnier and Shanahan, 1995):

$$V_d = \frac{\pi D^3 \cdot (1 - \cos\alpha)^2 \cdot (2 + \cos\alpha)}{24 \sin^3\alpha} \tag{2.1}$$

with D the droplet diameter and $\alpha = 74° \pm 10°$ (Peckhaus, 2016) the contact angle between the substrate and the droplet.
From this, we obtain the volume of the droplets: $V_d = 569 \pm 363\,\mathrm{pL}$.

The total surface of aerosol particle per droplet (summarized in Table 2.1) are given by:

$$S_p = V_d \cdot C \cdot S_{\mathrm{BET}} \tag{2.2}$$

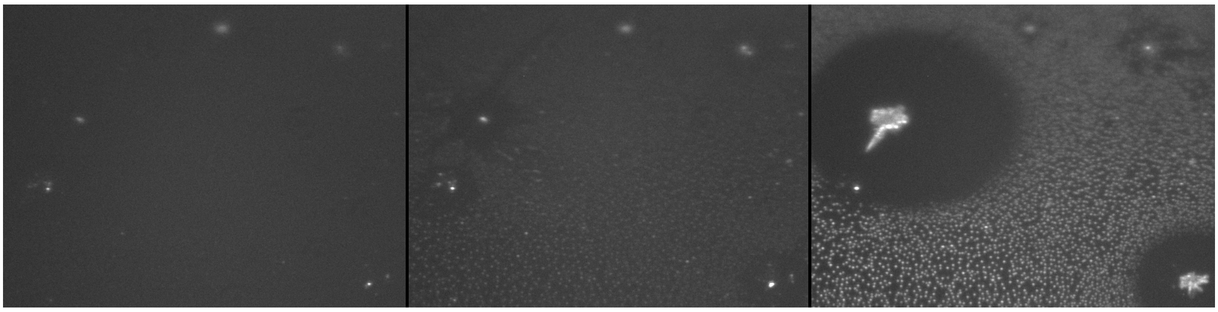

Figure 2.5 – Image recorded by the zoom camera for experiment **A**–Imm–1 at a cooling rate of 0.5 K.min^{-1} (*see* Chapter 3 for experiment description) respectively 20s before (left), 20s after (center) and 5min 40s (right) after condensation started on the wafer.

2.4 Corrections

2.4.1 Temperature

During the deposition nucleation experiments, the use of the Pt–100 temperature sensor was not possible as preliminary experiments showed an influence of the Pt–100 sensor on the course of the experiment. Therefore, the temperature at the surface of the wafer was determined *via* a temperature calibration:

$$\begin{cases} T = 0.77 + 0.958 \cdot T_{\text{CS}} & \text{if the flow cell is bypassed} \\ T = 0.93 + 0.951 \cdot T_{\text{CS}} & \text{otherwise} \end{cases} \tag{2.3}$$

This temperature calibration was obtained by a specific calibration experiment: the Pt–sensor was placed on the silicon wafer, maintained in good thermal contact by thermal paste. The wafer was cooled from +15 to −40°C for different cooling rates (ranging between 10K.min^{-1} and 1K.min^{-1}) with and without a flow of air through the flow cell. The measured temperature at the surface of the wafer ($T_{\text{Wafer}} \equiv T$) was the represented as a function of the cold stage temperature (T_{CS}) and the temperature calibration formulas were obtained through a linear fit.

2.4.2 Humidity

The dew point mirror was use to measure the humidity at the outflow of the RH system. But the humidity observed in the chamber showed discrepancies with respect to the measured humidity. Indeed, ice nucleation was observed for a relative humidity over ice well below 100%.

However, the cold stage itself can act as a dew point mirror: when the relative humidity over water reaches 100%, droplets start forming on the surface at spots without residual particles. In Figure 2.5 are presented three images recorded by the zoom camera shortly before and after condensation starts and 5 minutes after condensation started.
From the temperature at which condensation starts on the wafer, we can estimate the dew point temperature in the flow cell. The condensation on the wafer can be detected typically with a precision of 0.1K (30 frames at 1 K.min^{-1}). The measured dew point temperatures in the experiments presented in this thesis ranged from −22 to −33°C which yield a

relative uncertainty regarding the saturation water vapor pressure $p_{\mathrm{sat},w}$ ranging between 1.4 and 1.6%.
For the ice crystals formed by deposition nucleation, the frame of freezing is typically determined with a precision of at least 10 frames, and therefore the freezing temperature is determined with a precision smaller than 0.1 K. Therefore, the calculated supersaturation of ice nucleation presented in Chapter 4 is determined with a precision of 2%.
The temperature range on which each deposition nucleation was conducted ensured a temperature low enough to observe some condensation on the wafer. However, as for these experiments, ice crystals were formed long before the condensation was observed, the estimated dew point temperature might be lowered because of the locally decreased relative humidity surrounding the ice crystals. Therefore, the uncertainty regarding the supersaturation over ice for these cases might be larger than 2%.

A large variability (over 1 K) in the flow cell dew point temperature was observed when considering consecutive experiments with the same setting of the RH control system and stable frost point temperatures measured by the dew point mirror. Therefore, a calibration of the dew point in the flow cell chamber as a function of the RH control system setting and of the frost point temperature measured by the dew point mirror is not possible.
This variability is due to unadapted experimental procedures that need to be corrected in the future: the waiting period between two consecutive cooling cycles was too short and and some water remained accumulated in the flow cell chamber. Indeed, for almost all experiments, the flow cell dew point temperature rose with consecutive experiments.

2.5 Thermodynamic course of the experiment

In the campaign presented in the following chapters (immersion freezing in Chapter 3 and deposition nucleation in Chapter 4), all three suspensions are treated as follows: the droplets are deposited on the silicon wafer in an array of 9, 600 µm width and an interdroplet distance of 800 µm, for a total number of 169 droplets deposited. This rather large interdroplet distance, yielding a low number of droplets when compared to previous experiments using this setup (Peckhaus et al., 2016), is chosen in order to ensure a minimal interference between the residual particles during deposition nucleation experiments. A theoretical run is presented in Figure 2.7.

The cold stage is then cooled down at a rate of 5 K.min^{-1}. When all droplets are frozen, the cold stage is heated up at 20 K.min^{-1} to the melting point of water and once the crystals melted, the cycle repeats.

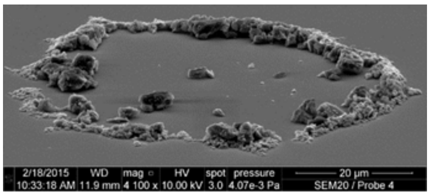

Figure 2.6 – Residual particles for a concentrated suspension (courtesy of A. Kiselev)

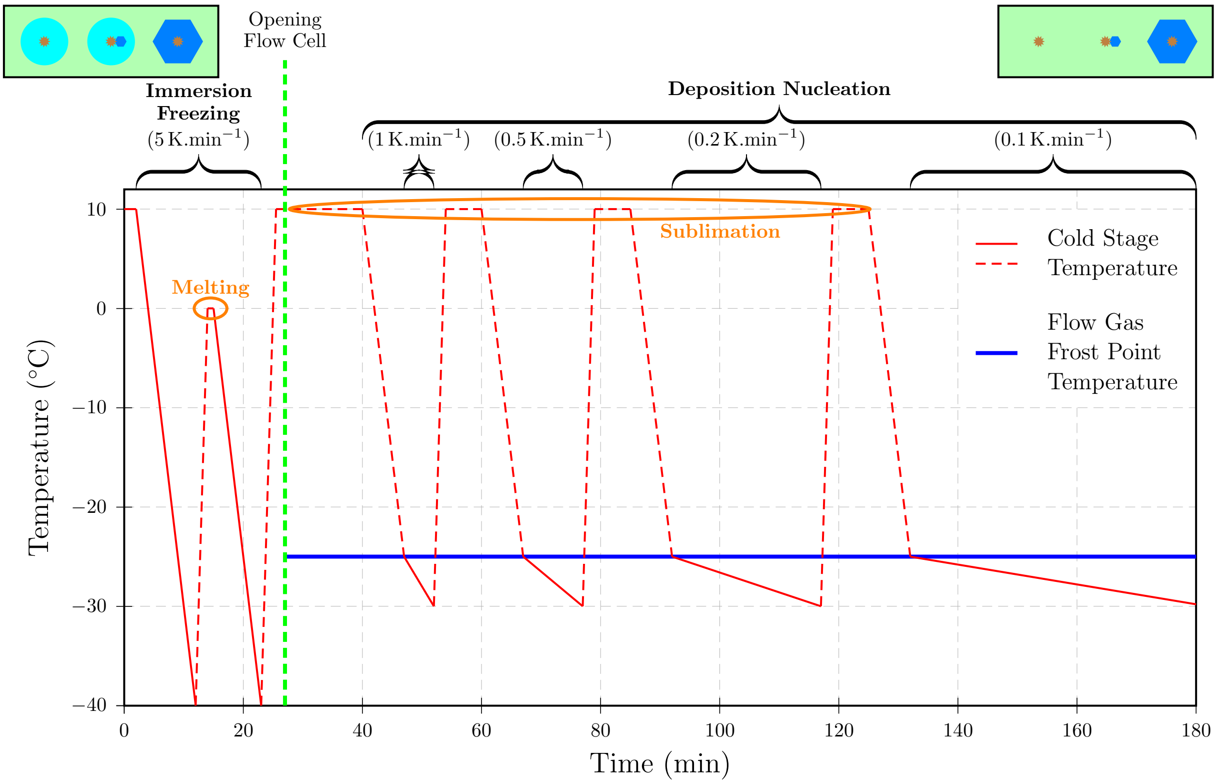

Figure 2.7 – Ideal experimental procedure: the droplets are deposited at 10°C, follow two freeze–thaw cycles at 5 K.min^{-1}. After the second cycle, a flow of humid air with a frost point temperature of −26°C is set in the flow cell and four cycles of deposition–evaporation are followed for different cooling rates.

These freeze–thaw cycles are repeated two or three times (depending on the volume of the droplets after each cycle).

After the last cycle, the cold stage is heated up to 10°C to let the droplets totally evaporate with only residual particles (Figure 2.6) remaining on the silicon wafer. At this point, the humid air is allowed in the flow cell to set the frost point in the chamber.
Then deposition–sublimation cycles take place: the cold stage is cooled down to the frost point temperature at a cooling rate of 5 K.min^{-1} before the experiment starts with cooling down to 5°C below the frost point at different cooling rates (1, 0.5, 0.2 and 0.1 K.min^{-1}). These cycles are repeated for different set frost points (measured by the dew point mirror): −20, −23, −26, −29.5 and −34°C.

Chapter 3

The Cold Stage Experiment: Immersion Freezing

The first step in the experiment series presented in this thesis consists of immersion freezing experiments.
As was explained in the previous chapter, for each suspension (**A**, with a concentration of FS02 particles of $2.5 \cdot 10^{-1}\,\mathrm{g.L^{-1}}$; **B**, with a concentration of $2.5 \cdot 10^{-2}\,\mathrm{g.L^{-1}}$; and **C**, with a concentration of $2.5 \cdot 10^{-3}\,\mathrm{g.L^{-1}}$), 169 droplets were deposited in an array on a silicon wafer. The PEEK cover to the sample holder (*see* Chapter 2) covered some of the initially present droplets, yielding a slightly lower total number of droplets detected by the camera (Figure 3.1).

In a first section, the results of the freeze–thaw cycle experiments for the different suspensions are presented.
The analysis of those results and particularly the characteristics of immersion freezing and differences in comparison with homogeneous nucleation are then discussed, along with a comparison of the results in this experiment with previous experiments using the same materials at the IMK–AAF.
Finally, the INAS densities for the investigated K–feldspar (FS02) are presented and a parameterization for immersion freezing is proposed.

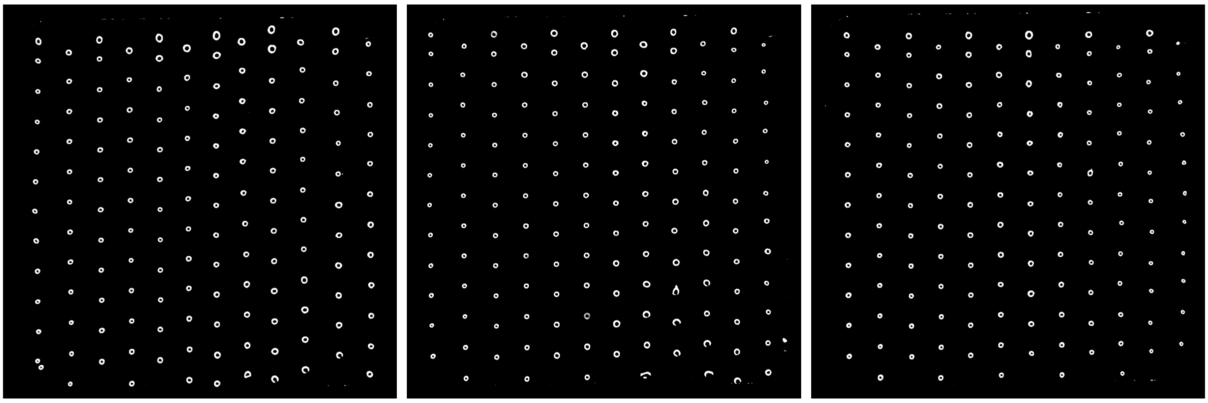

Figure 3.1 – Droplets of suspensions **A**, **B** and **C** on their respective wafer shortly after deposition (first frame of the videos).

Suspension	Droplets	Exp No.	Cooling rate	Crystals	$T_{50\%}$
A $[2.5 \cdot 10^{-1}\,\mathrm{g.L^{-1}}]$	147	**A**–Imm–1	$5\,\mathrm{K.min^{-1}}$	132	−23.2°C
$S_p = 3.76 \cdot 10^{-6}\,\mathrm{cm^2.drop^{-1}}$		**A**–Imm–2	$5\,\mathrm{K.min^{-1}}$	134	−22.8°C
B $[2.5 \cdot 10^{-2}\,\mathrm{g.L^{-1}}]$	146	**B**–Imm–1	$5\,\mathrm{K.min^{-1}}$	139	−26.2°C
$S_p = 3.76 \cdot 10^{-7}\,\mathrm{cm^2.drop^{-1}}$		**B**–Imm–2	$5\,\mathrm{K.min^{-1}}$	142	−25.7°C
		B–Imm–3	$5\,\mathrm{K.min^{-1}}$	138	−25.3°C
C $[2.5 \cdot 10^{-3}\,\mathrm{g.L^{-1}}]$	143	**C**–Imm–1	$5\,\mathrm{K.min^{-1}}$	117	−34.0°C
$S_p = 3.76 \cdot 10^{-8}\,\mathrm{cm^2.drop^{-1}}$		**C**–Imm–2	$5\,\mathrm{K.min^{-1}}$	124	−32.3°C
		C–Imm–3	$5\,\mathrm{K.min^{-1}}$	128	−32.4°C

Table 3.1 – List of the immersion freezing experiments with the number of detected droplets at the beginning of each experiment as well as the number of detected frozen droplets at the end of each cycle. $T_{50\%}$ corresponds to the temperature at which half of the droplets are frozen.

3.1 Results

For each suspension, a series of consecutive cooling cycles was done at a cooling rate of $5\,\mathrm{K.min^{-1}}$ as presented in Table 3.1. The corresponding frozen fractions as a function of temperature are represented in Figure 3.2.

For the more concentrated suspensions **A** (Figure 3.2, red dots) and **B** (Figure 3.2, blue dots), the freezing occurred well above the homogeneous nucleation temperature — which was found to be of −37°C in previous experiments using this setup (Steinke, 2013) — with 90% of the droplets frozen at -24.5 ± 0.2°C and -28.0 ± 0.4°C respectively. In both experiments, heterogeneous nucleation by the immersed K–feldspar particles was observed.
It is noticeable that for each consecutive experiment, the freezing temperature of the droplets (reprensented by $T_{50\%}$, the temperature at which the frozen fraction reaches 50%) rose slightly (+0.4°C for suspension **A**, +0.4°C for suspension **B**), but the number of cycles (respectively 2 and 3) is too low to draw any conclusion (*e.g.* Kaufmann et al., 2017 investigated for different materials over 40 consecutive freeze–thaw cycles and no clear trend in the evolution of the freezing temperature was noticed).

When considering suspension **C** (Figure 3.2, green dots), the freezing of the droplets occurred at temperatures close to the homogeneous nucleation temperature, particularly in the first freezing experiment with most droplets freezing for a wafer temperature below −34°C.
As was observed for the suspensions **A** and **B**, the second and third freezing cycles (experiments 1553 and 1554) showed warmer freezing temperatures. There is a gap of 1.6 ± 0.1°C between the measured freezing temperatures for the first and the two other cycles.

The freezing behavior observed for the experiments using the more concentrated suspensions **A** and **B** is very different from the one observed for experiments using suspension **C**.

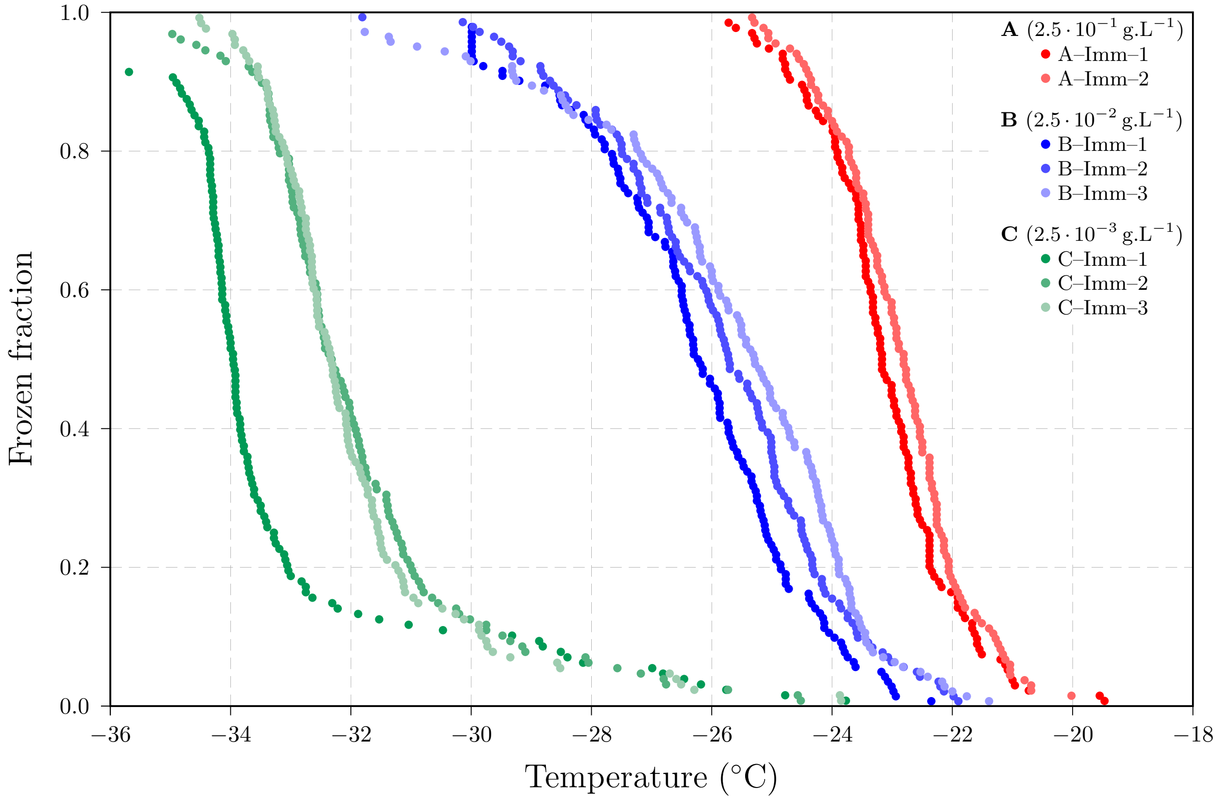

Figure 3.2 – Frozen fraction as a function of temperatures for suspensions **A** (red dots), **B** (blue dots) and **C** (green dots). The frozen fractions are calculated with respect to the maximal number of frozen droplets detected for one suspension.

Experiments **A**–Imm–1 and 2 show a rather rapid freezing of all the droplets over a narrow temperature range: $[-20, -26°\mathrm{C}]$; yielding a steep freezing curve. Suspension **B** being diluted to the tenth, the freezing occurs at colder temperatures but also over a larger temperature range: $[-22, -32°\mathrm{C}]$. The freezing curve obtained is less steep, as was already obtained in previous experiments on FS02 using this setup (Peckhaus et al., 2016). All immersion freezing experiments using these two suspensions can be appropriately fitted using sigmoid functions[1].

Such a function cannot be used to fit the freezing curves for experiments **C**–Imm–1, 2 and 3: there are two distinct regimes. First, a small number of droplets freeze over a large temperature range ($[-24, -33°\mathrm{C}]$ in experiment **C**–Imm–1 and $[-24, -31°\mathrm{C}]$ in experiments **C**–Imm–2 and 3) yielding flattened freezing curves. Then, the remaining droplets all freeze over 2°C, yielding a freezing curve of a steepness close to that of experiments **A**–Imm–1 and 2.

---

[1] A sigmoid function is defined as: $f_i(T) = f_{i,max} \cdot \left[1 + \exp\left(\frac{T_{50\%} - T}{c}\right)\right]^{-1}$ with T the temperature, $f_{i,max}$ the maximum of the frozen fraction, $T_{50\%}$ the temperature at which 50% of the droplets are frozen and c the steepness of the freezing curve.

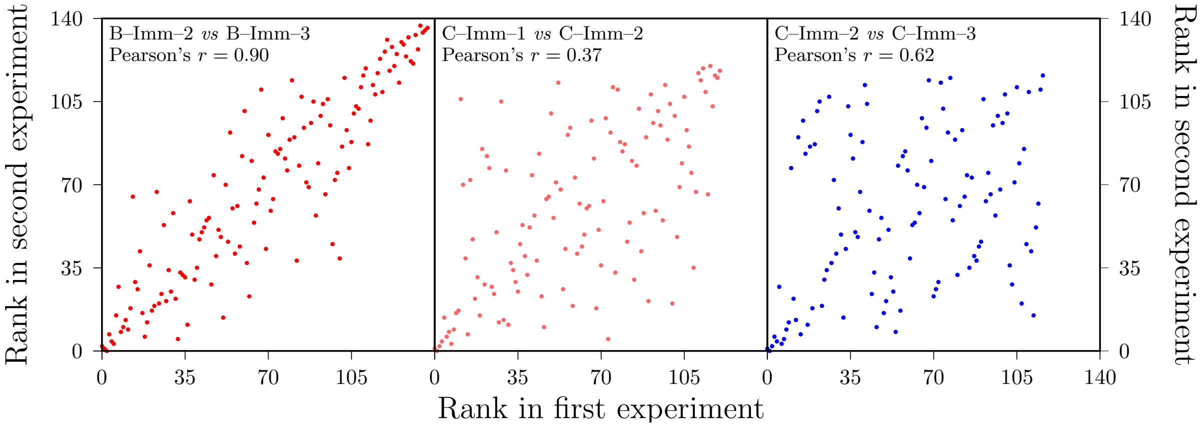

Figure 3.3 – Freezing rank correlation between: (**a**, left) experiments **B**–Imm–2 and **B**–Imm–3 ($r = 0.90$); (**b**, center) experiments **C**–Imm–1 and **C**–Imm–2 ($r = 0.37$); and (**c**, right) experiments **C**–Imm–2 and **C**–Imm–3 ($r = 0.62$). The correlation plots between experiments **A**–Imm–1 and **A**–Imm–2 ($r = 0.79$); **B**–Imm–1 and **B**–Imm–2 ($r = 0.86$); **B**–Imm–1 and **B**–Imm–3 ($r = 0.84$); and **C**–Imm–1 and **B**–Imm–3 ($r = 0.45$) are not shown.

3.2 Analysis

In order to further analyze the freezing behavior presented in the previous section, we first look into the correlation between consecutive freezing cycles.
In Figure 3.3 are presented the correlation in freezing ranks (*see* Chapter 2 for details) for experiments **B**–Imm–2 and **B**–Imm–3 (left); **C**–Imm–1 and **C**–Imm–2 (center); and **C**–Imm–2 and **C**–Imm–3 (right).

3.2.1 Correlation between consecutive freezing cycles

Suspension A and B

For these suspensions (*e.g.* Figure 3.3a), the correlation in freezing rank is very high, ranging between $r = 0.79$ and $r = 0.90$, a correlation in good agreement with Peckhaus et al. (2016) for concentrated K–feldspar suspensions (r larger than 0.8). These high correlations suggest that ice nucleation occurs on the same preferred sites for the different experiments. This means that through these experiments with the highest concentrations in this study, we probe the best ice nucleating active site available inside each droplet.

Suspension C

In contrast to the higher concentrated suspensions **A** and **B**, the correlations in freezing rank observed for experiments using suspension **C** are rather low. In Figure 3.3b and c, we can notice a locally higher correlation for the first 15 frozen droplets, which correspond to the flatter part of the frozen fraction curves in Figure 3.2 (droplets frozen between −24 and −33°C for experiment **C**–Imm–1 and between −24 and −31°C for experiments **C**–Imm–2 and **C**–Imm–3. The rest of the droplets seem to freeze rather randomly, as would be the case for homogeneous nucleation. Furthermore, as has been noticed in the previous section, the freezing rate for these three experiments is rather high (comparable to that of suspension **A**) when a low freezing rate would be expected, as for low concentrated suspensions, a lower freezing rate is expected (*e.g.* Peckhaus et al., 2016).

These results suggest that most of the droplets frozen in experiments using suspension **C**, homogeneous nucleation was involved. However, the temperature at which the freezing occurs indicates rather a heterogeneous nucleation process. This might indicate either the presence of aerosol particles with a rather low ice nucleating ability that serve as surrogate for ice nucleation on non-specific surfaces or an influence of the ions that migrated from the FS02 particles to come in solution in the water (*see* Peckhaus et al., 2016; supplement, Figure S6).

As it is out of scope for this experimental campaign, the rise of freezing temperature between experiments **C**–Imm–1 and experiments **C**–Imm–2 and **C**–Imm–3, as well as the steepness of the freezing curve and the increased correlation for consecutive freeze-thaw cycles were not further investigated.

3.2.2 Comparison with previous results

The K-feldspar (FS02) investigated in this study was already used in Peckhaus (2016) for freezing experiments using the cold stage setup at IMK–AAF.
The experimental protocol then used was slightly different: smaller droplet (215 pL ± 70) were deposited on the wafer in a larger amount (up to 1 000) and the droplets were covered by a mineral oil to prevent evaporation during the experiment. In Figure 3.4 are represented the freezing curves for the suspension **A** and **B** as well as for two series of experiments from Peckhaus (2016) for two different K–feldspar concentrations: 0.1 wt% (similar concentration to that of suspension **A**) and 0.01 wt% (similar concentration to that of suspension **B**), with the total surface per drop calculated from Figure 22 in Peckhaus (2016).

In Figure 3.4, the frozen fractions as a function of temperature are presented for the two more concentrated suspensions used, along with the results from the Peckhaus et al. (2016) study: in the left panel, the total surface per droplet are estimated respectively at $3.76 \cdot 10^{-6}\,\mathrm{cm}^2.\mathrm{drop}^{-1}$ (red dots) and $5 \cdot 10^{-6}\mathrm{cm}^2.\mathrm{drop}^{-1}$ (black dots); in the right panel, the total surface per droplet are estimated respectively at $3.76 \cdot 10^{-7}\,\mathrm{cm}^2.\mathrm{drop}^{-1}$ (red dots) and $4.5 \cdot 10^{-7}\mathrm{cm}^2.\mathrm{drop}^{-1}$ (black dots).
In both cases, the freezing curves obtained in the current study are steeper than the results obtained by Peckhaus et al. (2016) and freezing occurs over a shorter range of temperature (*e.g.* $[-20, -26°\mathrm{C}]$ for experiment **A**–Imm–1 *vs* $[-18, -28°\mathrm{C}]$ for the experiment in black dots from Peckhaus et al., 2016). The first frozen droplets are observed for colder temperatures but the $T_{50\%}$ are higher in the current study: a shift of 1.7°C between both concentrated (**A** and 0.1 wt%) suspensions; and of 1.5°C between both diluted suspensions.

The results obtained in this present study and the one from Peckhaus et al. (2016) seem to show discrepancies, as for lower total surface of aerosol particle per droplet in this experiment with regards to Peckhaus et al.'s experiment (factor of 0.75 for the concentrated

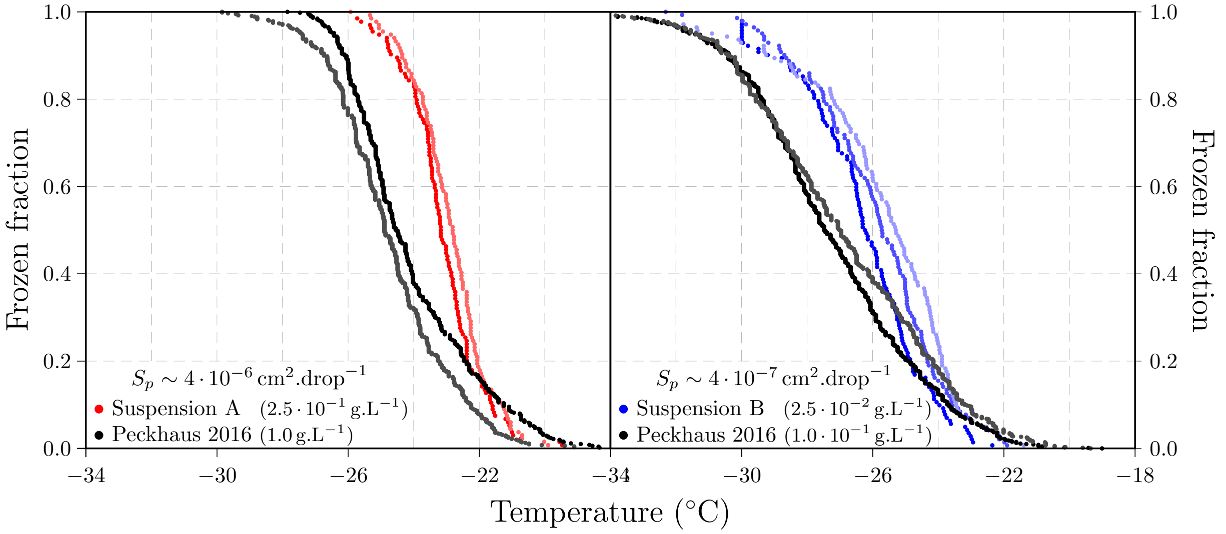

Figure 3.4 – Comparison of the frozen fraction as a function of temperature for experiments with *ca* $4 \cdot 10^{-6}$ (**left**) and $4 \cdot 10^{-7}$cm^2.drop^{-1} (**right**) at a cooling rate of 5K.min^{-1}. The curves in red and blue correspond to the study presented in this thesis, the curves in grey shades correspond to experiments from Peckhaus (2016).

and of 0.84 for the diluted suspensions), a higher frozen fraction is observed for every temperature. However, in Figure 22 in Peckhaus (2016), it is shown that for diluted suspensions and therefore particularly for suspension **B**, the BET calculation underestimates the total surface of aerosol particles.

Furthermore, in contrast to the study of Peckhaus et al. (2016), the droplets in the current study are not covered by mineral oil immediately after deposition on the silicon wafer, and though they are deposited at a temperature close to the room dew point temperature, some evaporation might take place before the first frame is recorded. Therefore, the diameter and subsequently the volume of the droplets might be underestimated. In this study, the same droplet volume has been applied for all three suspensions in the calculation of S_p as the droplets were all deposited using the same injector parameters. But as shown previously in Figure 2.4, the droplets of suspension **A** (central radius of Gaussian fit of 17.8 pixel) are larger than those of suspension **B** (17.1 pixel). With this latter value, the total surface of aerosol particle per droplet for suspension **A** reaches $S_p = 4.27 \cdot 10^{-6}$ cm^2.drop^{-1}.

3.2.3 Parameterization: ice nucleating active sites density representation

Tu further analyze the freezing behavior of the different suspensions from this study, we use INAS densities (*see* Chapter 1).

3.2.3.1 INAS densities calculation

INAS densities are calculated using the following equation (from eq. 1.6):

$$n_s(T) = -\frac{1}{S_p} \ln\left[1 - f_i(T)\right] \tag{3.1}$$

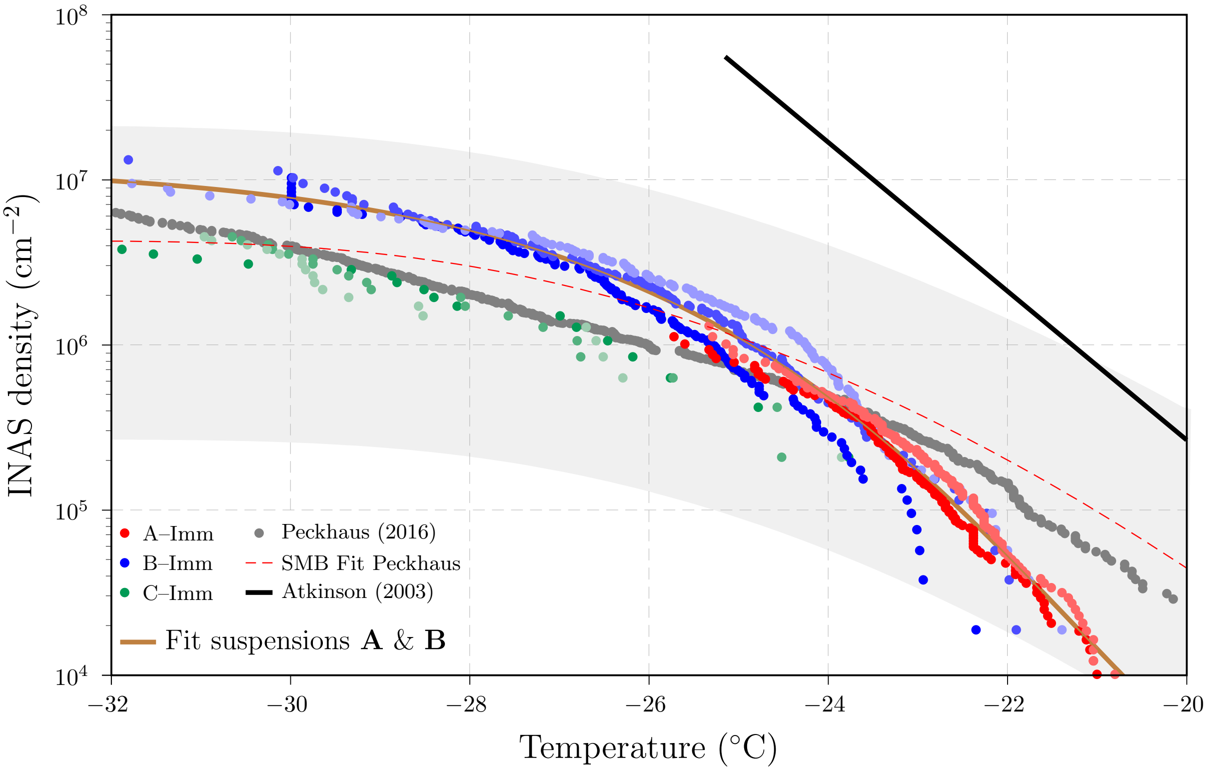

Figure 3.5 – Ice nucleating active site INAS density as a function of temperature for immersion freezing experiments using suspensions **A** (red dots), **B** (blue dots) and **C** (green dots). The brown curve represents the proposed fit for INAS densities obtained in this study for suspensions **A** and **B**: $n_{s,imm}(T) = \exp(10.3 \cdot \exp[-\exp(0.345 \cdot (T + 21.2))] + 6.05)$
In grey dots are presented results from Peckhaus et al. (2016) for a suspension with a concentration of FS02 particles of 0.05 wt% using a cooling rate of 1 K.min^{-1} (Figure 9 in the article), along with the SBM based fit of INAS densities for FS02 (red dashed curve and surrounding grey shade).
The thick black line corresponds to the Atkinson et al. (2013) parameterization for FS02.

with f_i the frozen fraction, n_s the INAS density and S_p the total surface of aerosol particle per droplet. Based on the results of suspensions **A** and **B**, we can retrieve INAS densities for temperatures between −20°C and −32°C. The results linked to suspension **C** are also presented, but are limited to the first 15 frozen droplets in each experiment.

Figure 3.5 shows a very good agreement between the INAS densities obtained for suspension **A** and suspension **B**. The densities retrieved from suspension **C** are lower by a factor 3, but as the suspension is particularly diluted ($2.5 \cdot 10^{-4}$ wt%), the BET surface might be underestimated.

As was to be expected from Figure 3.4, there is a stronger variation of the INAS density with temperature in the current study as was measured by Peckhaus et al. (2016) corresponding to the steeper curves observed, but the results remain in the same order of magnitude (particularly, the present results are within the grey shade from the classical nucleation theory based fits using the Soccer Ball Model (SBM, Niedermeier et al., 2014) for the wide range of concentrations used — from 0.01 to 0.8 wt%).
As the current study only coonsiders a small number of droplets (*ca* 140) in comparison to the Peckhaus et al. (2016) study (*ca* 1000), the access to higher temperature ranges

for a same order of magnitude of S_p is harder to obtain as there is a lower probability of having a highly active ice nucleating active site among the studied droplets. This small number of droplets also plays a role in the rapid decrease of the INAS density for the higher investigated temperatures: as Δf_i is quite large, each of the first frozen droplets strongly increase the INAS density, particularly for the low value of n_s (bottom right part of Figure 3.5).

Due to the smaller number of droplets and low weight concentration of the feldspar suspensions used in this study, only the low temperature population of active sites was accessible in this study. In this range, the measurements of Peckhaus et al. (2016) also deviate from the parameterization of Atkinson et al. (2013) by more than one order of magnitude.

3.2.3.2 Proposed parameterization for immersion freezing

We can derive a parameterization for immersion freezing by K–feldspar particles based on the experiments for suspensions **A** and **B**. We use a double exponential, the same fit function that was used by Hiranuma et al. (2015) for illite NX (brown curve in Figure 3.5), and obtain:

$$n_{s,\mathrm{imm}}(T) = \exp(10.3 \cdot \exp[-\exp(0.345 \cdot (T + 21.2))] + 6.05) \quad [\mathrm{cm}^{-2}] \tag{3.2}$$

for Celsius temperatures in $[-32; -20°\mathrm{C}]$ with the following uncertainties: 10.3 ± 0.2, $0.345 \pm 0.03°\mathrm{C}^{-1}$, $21.2 \pm 0.2°\mathrm{C}$ and 6.05 ± 0.2.

3.3 Summary for immersion freezing experiments

The first part of the experiments conducted in this thesis on K–feldspar particles consisted in freeze–thaw cycles at a cooling rate of $5\,\mathrm{K.min}^{-1}$, using an array of *ca* 140 nanoliter droplets of FS02 suspensions deposited on a silicon wafer. The three suspensions investigated were based on a mother suspension **A** with a concentration of K–feldspar particles of $2.5 \cdot 10^{-1}\,\mathrm{g.L}^{-1}$ then diluted to the tenth (**B**) and to the hundredth (**C**).

The temperature evolution of the frozen fractions for suspensions **A** and **B** showed a decrease of the mean freezing temperature as well as of the steepness of the freezing process when the concentration decreased, as had already been observed using the same material in Peckhaus et al. (2016). The heterogeneous nucleation process took place on specific ice nucleating active sites as was confirmed by the high correlation between consecutive freezing cycles for those two suspensions.

This was not the case for suspension **C** where two different modes were to be observed: for the higher temperatures (above −30°C), heterogeneous nucleation takes place with a low freezing rate, in agreement with the decreased concentration of the suspension; for colder temperatures, the freezing rate rapidly increases with a steepness of the frozen fraction temperature evolution close to that of suspension **A**. This indicates a homogeneous nucleation process in an ion–concentrated solution or a heterogeneous nucleation on non–specific sites, which is confirmed by the lack of correlation between the freezing ranks between consecutive experiments for this suspension.

From these experiments, we can derive ice nucleating active site densities which showed good agreement for the results from suspensions **A** and **B**. The results obtained in the current study were coherent with those of Peckhaus et al. (2016), however, because of the differences in the experimental method (*e.g.* lower number of droplets investigated, highly diluted suspensions, droplets in contact with air in the cell, different wafer cleaning procedure) lead to differences in the evolution of the INAS densities as a function of temperature. As those differences in the sample preparation were out of scope for this study concentrated on the link between immersion freezing and deposition nucleation, their relevance regarding the apparent discrepancies between both experimental campaigns is not assessed in this thesis.

From the INAS densities calculated, we propose a new K–feldspar parameterization for temperatures below $-20°\mathrm{C}$, which will be implemented in the Detailed Scavenging Model (DESCAM) in Chapter 6 for sensitivity studies.

Chapter 4

The Cold Stage Experiment: Deposition Nucleation

The second part of the experiments presented in this study correspond to deposition nucleation experiments conducted using the flow cell for the cold stage setup developed during this thesis (*see* Chapter 2).
The silicon wafers on which the droplets were deposited for immersion freezing (*see* Chapter 3) were warmed to 30°C to let the droplets evaporate, leaving dry residual particles on which deposition nucleation experiments were conducted. The former droplet each contain several K–feldspar particles (Figure 2.6).

In this chapter, '*residual particles*' correspond to the total K–feldspar particles present at a given position in place of an evaporated droplet, and therefore contain several FS02 particles.

4.1 Results

For all three suspensions, the same set conditions were applied: for four different measured frost point temperature (-21.1 ± 0.4°C; -23.5 ± 0.5°C, -26.2 ± 0.2°C, -29.7 ± 0.2°C and -33.7 ± 0.3°C), four consecutive cooling rate experiments were performed (1, 0.5, 0.2 and 0.1K.min^{-1}). However, because of the low concentrations of the suspensions and the low number of ice nucleating active sites at higher temperatures already noticed in Chapter 3, not all combinations are presented in this section: for suspension **A**, for a set frost point temperature of -21.1°C, the cooling rates of 0.2 and 0.1 K.min^{-1} were not investigated; for suspension **B**, the set frost point temperature of -21.1°C didn't provide results; for suspension **C**, the set frost point temperatures of -21.1°C and -23.5°C as well as the cooling rate of 0.1 K.min^{-1} were not investigated.

The frozen fraction are calculated with respect to the total number of identified droplets in the previous chapter. The number of crystals is calculated as a function of the positions: only the first crystal nucleated on the residual particles is taken into account and eventual further nucleated ice crystals on the residual particles from the same droplets are dismissed.

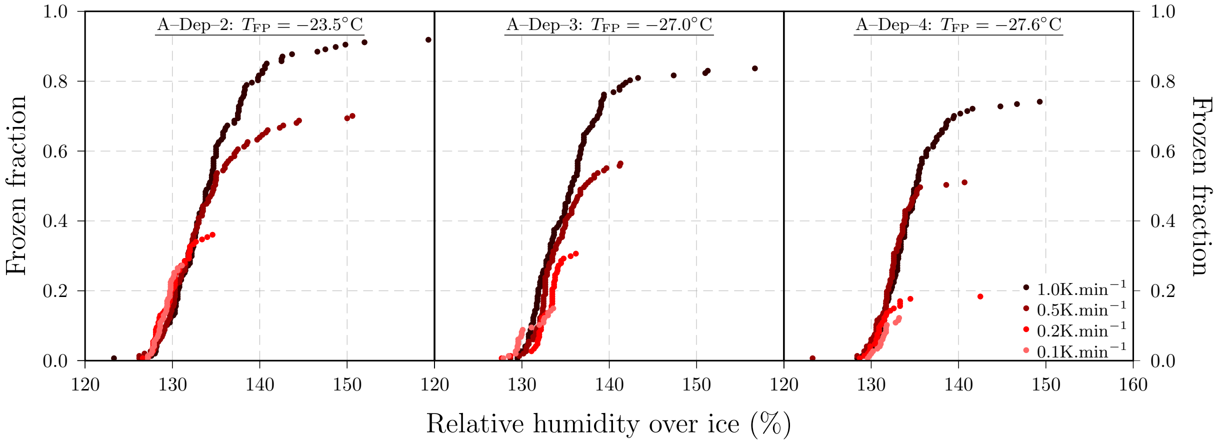

Figure 4.1 – Frozen fraction as a function of relative humidity for different cooling rates (1 K.min^{-1} in brown, 0.5 K.min^{-1} in dark red, 0.2 K.min^{-1} in red and 0.1 K.min^{-1} in pink) for experiments **A**–Dep–2 (**a**, left), **A**–Dep–3 (**b**, center) and **A**–Dep–4 (**c**, right), presented in Table 4.1.

4.1.1 Suspension A

The summary of the deposition nucleation experiments for suspension **A** are found in Table 4.1; frozen fractions are represented in Figure 4.1.

Two different types of freezing behaviors were observed. For a high frost point temperature ($T_{FP} > -21°C$), the number of ice crystals grows rather linearly (experiments **A**–Dep–0 and 1, shown in Figure 4.4 and detailed in §4.1.4). For lower frost point temperatures ($T_{FP} < -23°C$), the frozen fraction as a function of the relative humidity follows a sigmoid like evolution (experiments **A**–Dep–2, 3 and 4, Figure 4.1).

For each of the three colder frost point temperatures, the steepness of the frozen fraction as a function of relative humidity is not depending on the cooling rate. Opposite to what was observed for immersion freezing by Steinke (2013), the cooling rate does not impact the freezing temperatures, the mechanism of deposition nucleation seems rather time independent.

However, we notice a decrease in the number of ice crystals formed on the residual particles when the cooling rate increases: for lower cooling rates, the end temperature was higher,

Exp No.	DPM Frost Point T°	CS Frost Point T°	Nucleated Crystals
A–Dep–0	-20.7 ± 0.1°C	-17.8 ± 0.2°C	[129, 87]
A–Dep–1	-23.1 ± 0.1°C	-20.5 ± 0.2°C	[138, 117, 89, 55]
A–Dep–2	-26.1 ± 0.1°C	-23.5 ± 0.4°C	[136, 103, 53, 40]
A–Dep–3	-29.5 ± 0.1°C	-27.0 ± 0.4°C	[123, 83, 45, 22]
A–Dep–4	-33.6 ± 0.2°C	-27.6 ± 0.6°C	[109, 75, 27, 18]

Table 4.1 – List of deposition nucleation experiments for suspension **A** and the number of ice crystals created for the different cooling rates (ordered by decreasing cooling rates). The dew point mirror (DPM) Frost Point temperature corresponds to the temperature measured at the output of the relative humidity system and the cold stage (CS) Frost Point temperature is derived from the dew point observed on the experiment video recording. Both frost point temperatures correspond to the mean values over the different cooling rates.

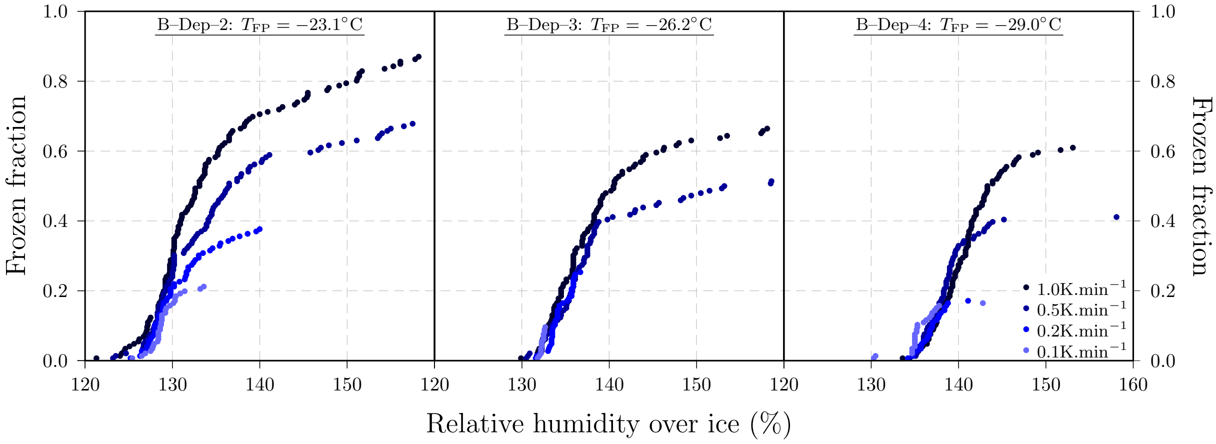

Figure 4.2 – Frozen fraction as a function of relative humidity for different cooling rates (1 K.min^{-1} in brown, 0.5 K.min^{-1} in dark blue, 0.2 K.min^{-1} in blue and 0.1 K.min^{-1} in light blue) for experiments **B**–Dep–2 (**a**, left), **B**–Dep–3 (**b**, center) and **B**–Dep–4 (**c**, right), presented in Table 4.2.

therefore a smaller relative humidity with respect to ice was reached; also, we notice in each of the experiments presented in Figure 4.1 that the freezing curve flattens at lower relative humidity for lower cooling rates. As the nucleated crystals are formed at a similar relative humidity for each of the cooling rate, the lower the cooling rate, the more the ice crystals grow and therefore create a locally diminished relative humidity, preventing the less ice active residual particles from nucleating an ice crystal.

For decreasing frost point temperatures, the relative humidity at which the first ice crystals are observed are increasing (125% for $T_{\mathrm{FP}} \simeq -23.5°\mathrm{C}$ and 128% for $T_{\mathrm{FP}} \simeq -27.5°\mathrm{C}$).

4.1.2 Suspension B

The summary of the deposition nucleation experiments for suspension **B** are found in Table 4.2.
As was already observed for suspension **A**, there are two types of freezing behaviors. The results for the higher frost point temperature (experiment **B**–Dep–1) are presented in §4.1.4. The frozen fractions for the lower frost point temperature (experiments **B**–Dep–2, 3 and 4) are represented in Figure 4.2.

As was observed for suspension **A**, the cooling rate does not impact the steepness of the freezing curve and the remarks on the decrease of nucleated ice crystals remain valid.
There are however differences in the obtained freezing curves: as was the case when we

Exp No.	DPM Frost Point T°	CS Frost Point T°	Nucleated Crystals
B–Dep–1	-23.7 ± 0.1°C	-21.2 ± 0.3°C	[123, 111, 80, 39]
B–Dep–2	-26.2 ± 0.1°C	-23.1 ± 0.1°C	[134, 105, 55, 31]
B–Dep–3	-29.8 ± 0.1°C	-26.2 ± 0.6°C	[98, 75, 37, 14]
B–Dep–4	-33.9 ± 0.1°C	-29.0 ± 0.5°C	[101, 61, 25, 24]

Table 4.2 – List of deposition nucleation experiments for suspension **B**.

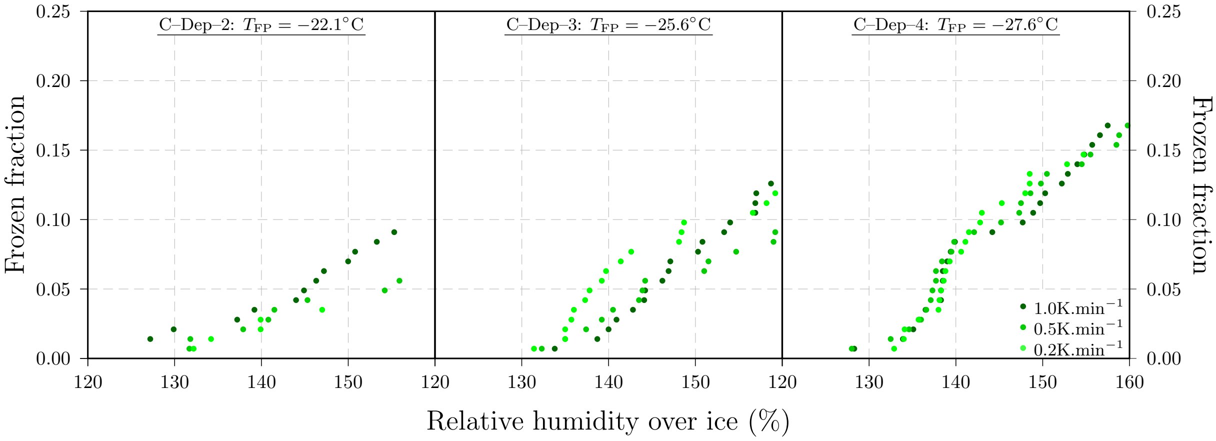

Figure 4.3 – Frozen fraction as a function of relative humidity for different cooling rates (1 K.min^{-1} in dark green, 0.5 K.min^{-1} in green and 0.2 K.min^{-1} in light green) for experiments **C**–Dep–2 (**a**, left), **C**–Dep–3 (**b**, center) and **C**–Dep–4 (**c**, right), presented in Table 4.3.

considered immersion freezing (*see* Chapter 3), the decrease of the total surface of aerosol particle per droplets, and therefore per residual particle, lead to a decrease in the steepness of the freezing curve. In experiment **A**–Dep–3 (Figure 4.1b), for a cooling rate of 0.5 K.min^{-1} (CS frost point temperature of −26.8°C), the frozen fraction goes from 0 to 0.55 when the relative humidity goes from 130 to 140%, whereas in experiment **B**–Dep–3 (Figure 4.2b), for a cooling rate of 0.5 K.min^{-1} (CS frost point temperature of −26.8°C), the frozen fraction goes from 0 to 0.4.

For suspension **B**, the relative humidity at which the first ice crystals are observed increase with decreasing frost point temperatures (125% for $T_{FP} \simeq -23.1$°C, 130% for $T_{FP} \simeq -26.5$°C and 135% for $T_{FP} \simeq -28.8$°C).

4.1.3 Suspension C

The summary of the deposition nucleation experiments for suspension **C** are found in Table 4.3; the corresponding frozen fraction are represented in Figure 4.3.
As was already noticed for immersion freezing (Chapter 3), the number of ice nucleating particles on the sample used for suspension **C** is rather low. This is confirmed by the low crystal count obtained in all three deposition nucleation experiments, with a maximum of 37 ice crystals (Table 4.3). Because of this low ice crystal count, a global behavior of the sample cannot be identified as was the case for the two previous suspensions.

Exp No.	DPM Frost Point T°	CS Frost Point T°	Nucleated Crystals
C–Dep–2	−26.4 ± 0.1°C	−22.1 ± 0.2°C	[15, 10, 5]
C–Dep–3	−29.7 ± 0.1°C	−25.6 ± 0.3°C	[35, 27, 17]
C–Dep–4	−33.9 ± 0.1°C	−27.6 ± 0.3°C	[37, 32, 21]

Table 4.3 – List of deposition nucleation experiments for suspension **C**.

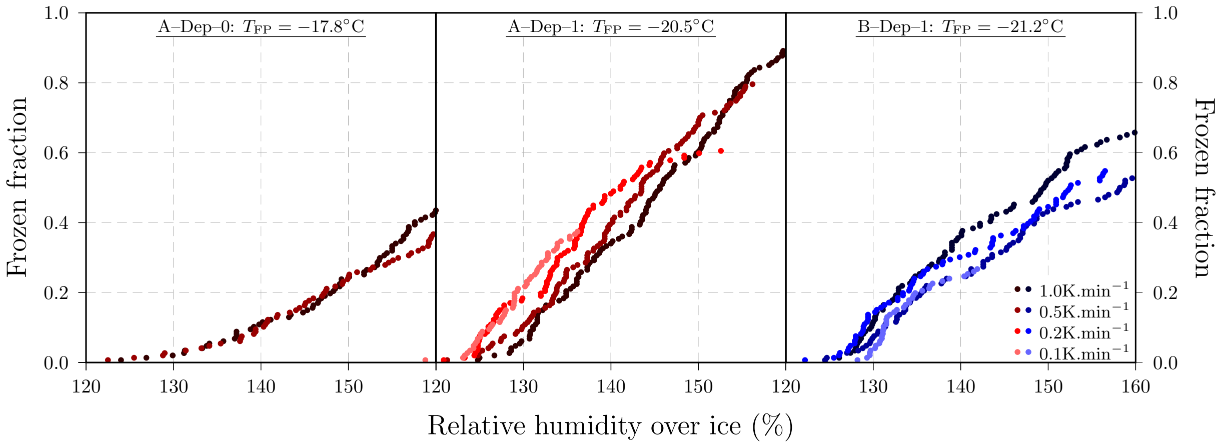

Figure 4.4 – Frozen fraction as a function of relative humidity at different cooling rates (1 K.min^{-1} in brown, 0.5 K.min^{-1} in dark red and blue, 0.2 K.min^{-1} in red and blue and 0.1 K.min^{-1} in pink and light blue) for experiments **A**–Dep–0 (**a**, left), **A**–Dep–1 (**b**, center) and **B**–Dep–1 (**c**, right).

Despite the low maximal ice crystal count, we notice that for each of the cooling rates, the similarities in freezing curves' shapes are once again observed. Also, as was already noticed when comparing experiments based on the residual particles of suspensions **A** and **B**, the decrease in total surface of aerosol particle leads to a decrease in the steepness of the freezing curves.

For suspension **C**, the first ice crystals are observed at 127% for $T_{\mathrm{FP}} \simeq -22.1°\mathrm{C}$, 131% for $T_{\mathrm{FP}} \simeq -25.6°\mathrm{C}$ and 128% for $T_{\mathrm{FP}} \simeq -27.6°\mathrm{C}$.

4.1.4 Condensation Freezing

As was previously mentioned, experiments with high frost point temperatures ($T_{\mathrm{FP}} < -21.5°\mathrm{C}$) showed a different behavior than the experiments with lower frost point temperatures. The frozen fractions from those experiments are presented in Figure 4.4.

For these three experiments (**A**–Dep–0, **A**–Dep–1 and **B**–Dep–1), the measured frost point temperature was warmer as the temperature of the first frozen droplets for the corresponding immersion freezing experiments. Particularly, in experiments **A**–Dep–0 and **B**–Dep–1, the measured dew point was particularly close to the temperature of the first frozen droplets in the immersion freezing mode: respectively $T_{\mathrm{DP}}(\mathbf{A}\text{–Dep–0}) = -19.8 \pm 0.3°\mathrm{C}$ and $T_{\mathrm{DP}}(\mathbf{B}\text{–Dep–1}) = -23.4 \pm 0.4°\mathrm{C}$.

Therefore, the freezing curves obtained for these three experiments correspond to condensation freezing rather than deposition nucleation where the ice crystals develop from a droplet formed on the residual particles. In our setup, the two mechanisms (deposition nucleation and condensation freezing) yield very different evolutions of the frozen fraction on identical samples using the same cooling rates.

For condensation freezing, as was the case for immersion freezing and deposition nucleation, the decrease of the total surface of aerosol particles between experiments **A**–Dep–1 and **B**–Dep–1 — conducted with close frost point temperatures — leads to a decrease of the steepness of the freezing curve (Figure 4.4b and c).

4.2 Analysis

4.2.1 Comparison of immersion and condensation freezing

Condensation freezing corresponds to the freezing of freshly formed growing droplets and was observed in experiments **A**–Dep–0, **A**–Dep–1 and **B**–Dep–1.
It was pointed out in the previous section that condensation freezing yielded freezing curves showing a very different evolution from those for deposition nucleation.

In the condensation freezing mechanism, the ice crystal germ develops in the liquid phase on an ice nucleating active site. Therefore, this ice nucleation mechanism is very similar to immersion freezing, as was pointed out by Vali et al. (2015): "*Whether condensation freezing* [...] *is truly different from deposition nucleation, or distinct from immersion freezing, is not fully established.*"
Figure 4.5 presents the frozen fraction as a function of temperature for the three condensation freezing experiments as well as the corresponding immersion freezing experiments.

The frozen fractions from experiment **A**–Dep–0 closely replicate that of the corresponding immersion freezing experiments. This is also the case for experiment **B**–Dep–1 for frozen fractions larger than 0.1. However, as the measured dew point for this experiment is of −23.6°C, no ice crystal is formed before this temperature is reached.
Experiment **A**–Dep–1 was conducted with a measured dew point of −22.8°C, three degrees below the temperature of the first frozen droplet in experiment **A**–Imm, therefore the freezing curve cannot replicate results from immersion freezing, but shows an evolution similar to those of the other condensation and immersion freezing experiments for suspension **A**.

The replication of the evolution of the immersion freezing frozen fraction as a function of temperature for experiments **A**–Dep–0 and **B**–Dep–1 indicate that the same sites and particles acted as ice nucleating particle in both immersion and condensation freezing experiments. To confirm or infirm this assumption, we look into the correlation in freezing rank between the two types of experiments.
Quite counterintuitively, there is no correlation in the freezing ranks between the two types of experiments: for suspension **A**, the mean Pearson's correlation coefficient is $r = 0.20$ and for suspension **B**, $r = 0.39$.

Furthermore, as was the case for immersion freezing experiments, there is some correlation in the freezing ranks between consecutive condensation freezing experiments: $r(\mathbf{A}\text{–Dep–0}) = 0.51$, $r(\mathbf{A}\text{–Dep–1}) = 0.70$ and $r(\mathbf{B}\text{–Dep–1}) = 0.54$.
A first explanation for the lack of correlation between the two type of experiments could reside in the difference in droplet activation on the different residual particles. However, the relative humidity over water in these experiments rapidly increases and reaches values where all aerosol particles should be activated ($RH_w > 110\%$). An other explanation could

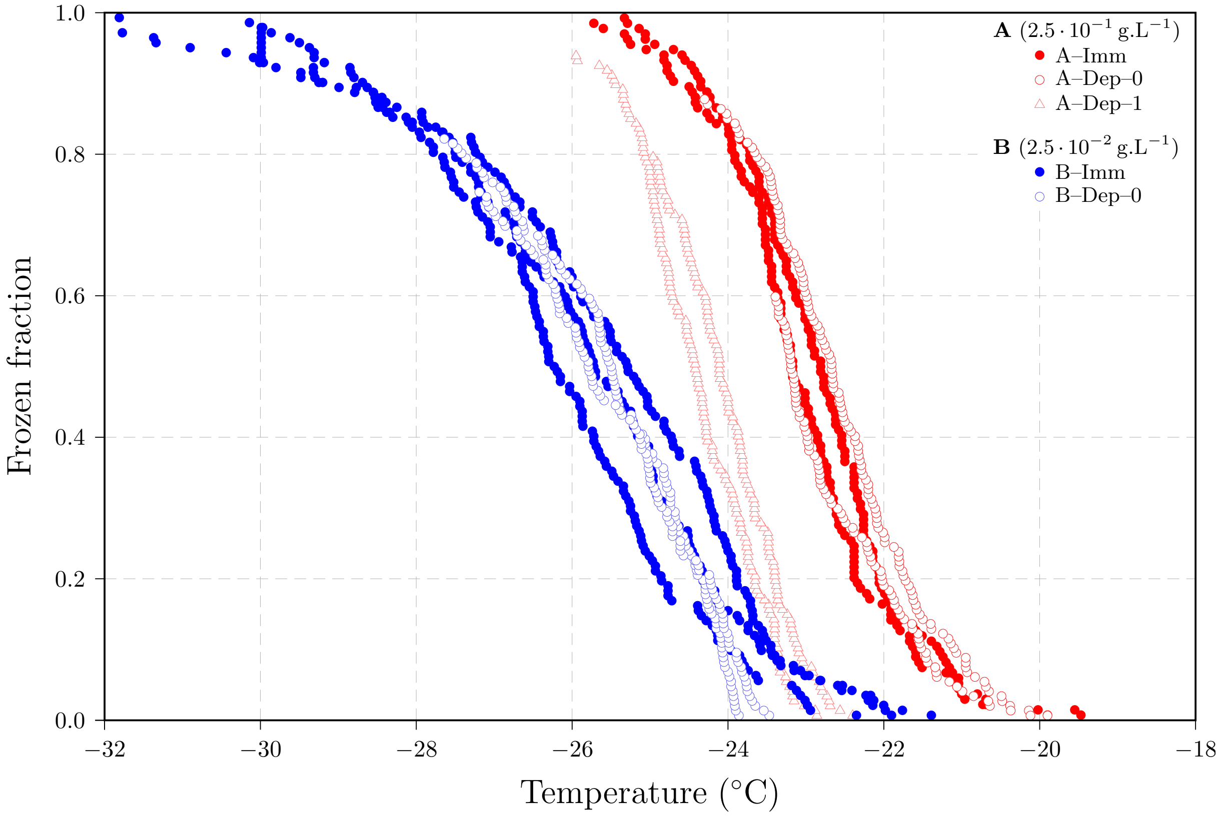

Figure 4.5 – Frozen fraction as a function of temperature for immersion (dots) and condensation freezing experiments (circles and triangles) for suspensions **A** (red and pink) and **B** (blue).

be the repartition of the residual particles: they form a ring during the evaporation and therefore, the droplets developing during the condensation of water vapor do not necessarily contain the same aerosol particles at the same moment. Furthermore, the residual particles consist of several FS02 particle aggregates which should not form a suspension in the new droplet: they rather remain *sedimented* and in contact with the silicon wafer. This means that the ice nucleating active sites responsible for the freezing of the droplets in the immersion freezing experiments, which were the most active among all particles present in the droplets might not be available during the condensation freezing experiments. However, there should be a large number of ice nucleating active sites among each of the residual particles, particularly for suspension **A** as the 100th dilution still contains some active sites in at least 10% of the droplets.

4.2.2 Number of active sites per droplet in the deposition nucleation mode

In order to evaluate the number of different ice nucleating active sites present in the residual particles for each sample, we look into the precise position at which ice nucleation first occurred in the consecutive deposition nucleation experiments. For suspension **A**, 4 residual particles nucleated ice in each of the 12 experiments and 2 in every experiment except one. For suspension **B**, 3 residual particles nucleated ice in each of the 12 experiments, 3 in every experiment except one. For suspension **C**, 4 residual particles nucleated ice in each of the 9 experiments and 4 in every experiment except one.

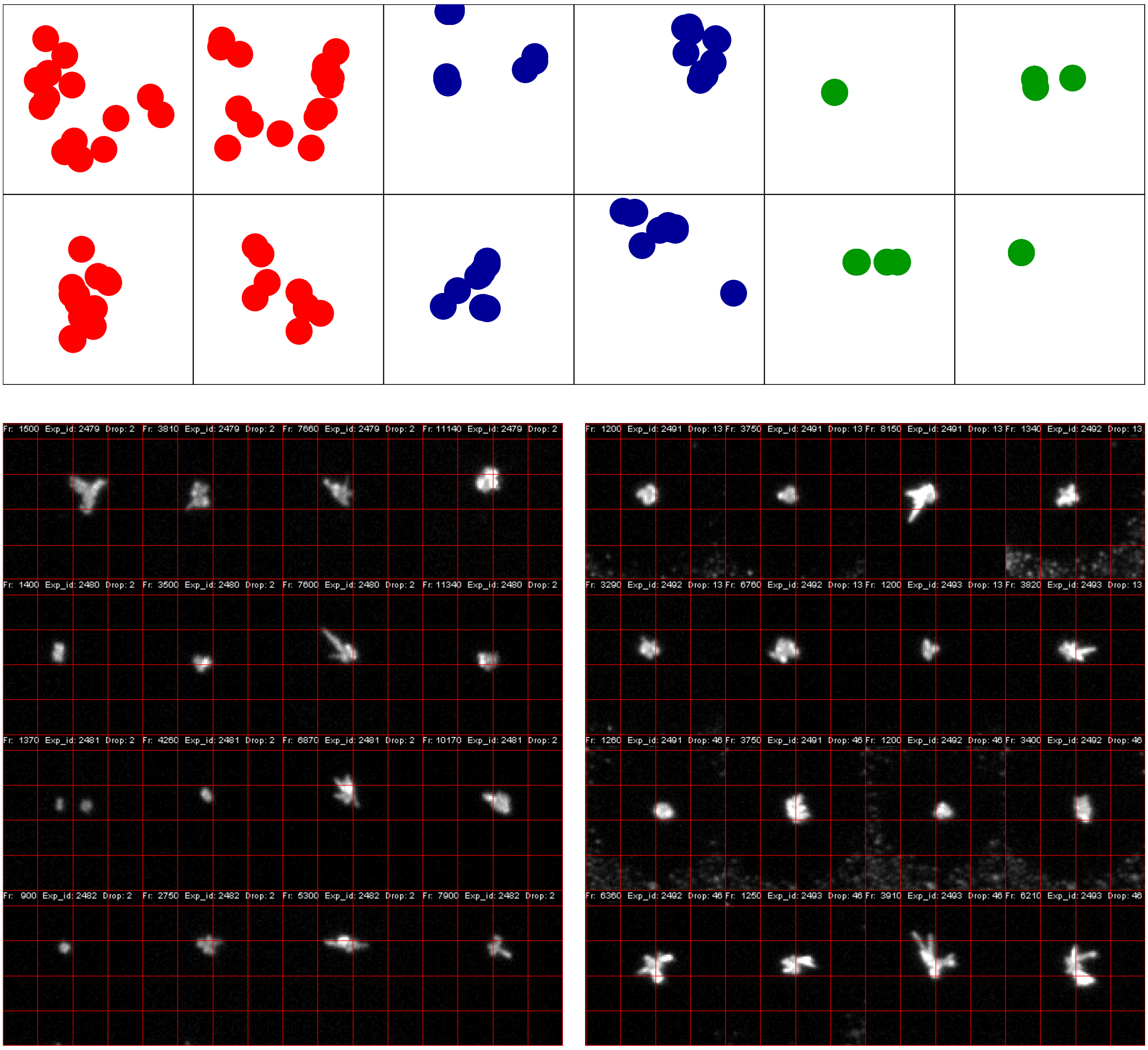

Figure 4.6 – (**Top**) Positions on which the ice crystals were nucleated for four different droplets for the three suspensions (**A** in red, **B** in blue and **C** in green). Each square has a side length of *ca* 180 µm (20 pixel). Because of the resolution of the original video, very close dots might correspond to a single position (particularly for suspension **C**). (**Bottom**) Snapshots of nucleated crystals 4 min after the ice nucleation event for droplet #2 from suspension **A** (left; corresponding to the top left square in top figure), for which at least 7 different ice nucleation positions are identifiable; and droplets #13 and #46 from suspension **C** (right; corresponding to the top and bottom square from the fifth column in top figure), for which 1 and 2 different ice nucleation positions are identifiable respectively. In the snapshots, the distance between two red lines corresponds to 25 pixel.

These droplets were isolated into separate video files focused on the frames shortly before and after the ice nucleation occurred; and for each observed ice crystal, the position at which it was first noticed was marked as the position of the ice nuclei. Examples of these positions are shown in Figure 4.6.

We notice that the number of ice nucleating position decreases with the concentration of the original suspension: for suspension **A**, the number of positions ranges between 5 and 9; for suspension **B**, the number of positions ranges between 3 and 5; and for suspension **C**, there is generally only one position, except for two cases shown where two different positions are noticed.

Implications regarding the analysis of the experiments

This large number of different ice nucleating active sites on the residual particles for the more concentrated suspensions induces that the comparison between consecutive experiments might be biased as the sites on which the ice nucleation occurred might not be the same. For example, this explains part of the lack of correlation between immersion and condensation freezing experiments even though the temperature evolution of the frozen fractions are very similar: different ice nucleating active sites might be involved on a single droplet position. The water condenses on the residual particles gradually and all ice nucleation sites from the immersion freezing experiments might not be available for freezing. However, because of the multiplicity of active sites on the residual particles, condensation freezing follows the same freezing curve as immersion freezing.

This also means that evaluating the INAS density for K–feldspar from this experiment cannot be done from the results obtained using suspensions **A** and **B**. A corrective factor could be applied, but determining the order of magnitude of said factor is difficult: for example, for suspension **A**, up to 9 different sites were identified, but only 12 experiments were conducted, whereas for suspension **C**, up to 2 different sites were identified over 9 experiments. Furthermore, with a few exceptions, for each of the different cooling cycles, only one single ice crystal was formed, as as soon as a crystal grows, it lowers locally the relative humidity and prevents ice nucleation on the other active sites.
Therefore, a much larger number of experiments would be needed to correctly determine such a corrective factor.

4.2.3 Correlation between successive deposition nucleation experiments

The same methodology as for immersion freezing was used to compute the correlation between consecutive deposition nucleation experiments. For each considered set frost point temperature temperature (−26, −29.5 and −33.5°C), six different correlation coefficients were calculated for suspensions **A** and **B** and three for suspension **C**. The correlation coefficients are summarized in Table 4.4.

When we considered immersion freezing experiments previously, the correlation coefficients were not subject to precaution: between two successive experiment, about the same number of droplets were detected as frozen and always amounted to a number close to the total number of identified droplets. This is not the case for deposition nucleation: *e.g.* for experiment **B**–Dep–2, the number of detected ice crystals decreases strongly, from 134 to 31. Therefore, the correlation coefficients need to be associated to the proportion of crystals involved in the calculation $\mathcal{R}$ (number of crystals taken into account for the correlation calculation with respect to the smaller number of detected crystals, Table 4.4) to have a better physical meaning.
For example, in experiment **B**–Dep–2, the correlation between the cooling rate of 0.2 and 0.1 K.min^{-1} is of 82%. However, for these two cooling cycles, the number of detected ice

		Pearson's r			Crystals involved $\mathcal{R}$		
Experiment	Frost Point T°	Min	Mean	Max	Min	Mean	Max
A–Dep–2	-23.5 ± 0.4°C	0.52	**0.64**	0.71	65	**91**	100
A–Dep–3	-27.0 ± 0.4°C	0.36	**0.50**	0.61	77	**89**	100
A–Dep–4	-27.6 ± 0.6°C	0.36	**0.56**	0.71	72	**80**	93
B–Dep–2	-23.1 ± 0.1°C	0.48	**0.61**	0.82	87	**96**	100
B–Dep–3	-26.2 ± 0.6°C	-0.19	**0.11**	0.50	86	**96**	100
B–Dep–4	-29.0 ± 0.5°C	0.22	**0.42**	0.51	54	**86**	100
C–Dep–2	-22.1 ± 0.2°C	-0.10	**0.23**	0.50	100	**100**	100
C–Dep–3	-25.6 ± 0.3°C	0.26	**0.39**	0.59	89	**96**	100
C–Dep–4	-27.6 ± 0.3°C	0.56	**0.61**	0.64	75	**82**	86

Table 4.4 – Summary of the Pearson's correlation coefficient r for the different deposition nucleation experiments and proportion of ice crystals ($\mathcal{R}$) involved in the calculation of r with respect to the smaller number of crystals available (*ie* for experiment 128, for a cooling rate of 1 and 0.5 K.min^{-1}, there are respectively 123 and 111 observed ice crystals and the correlation is calculated on 108 crystals, therefore, $\mathcal{R} = 108/111 = 97\%$)

crystals is only of 55 and 31 respectively, out of 146 original droplets. Therefore, if deposition nucleation occurred on entirely random K–feldspar particles, only a few of the detected ice crystals would correspond to common residual particles and the high correlation could result from a calculation over a handful of ice crystals. We therefore associate r and $\mathcal{R}$ to obtain this supplementary information: for the two considered experiments, the correlation coefficient is calculated over 27 ice crystals yielding a $\mathcal{R}$ of 87%:

$$\mathcal{R} = \frac{N_{\text{pts}}(\text{corr}_{1,2})}{\min(N_i^1, N_i^2)} \tag{4.1}$$

with $N_{\text{pts}}(\text{corr}_{1,2})$ the number of residual particles on which the correlation was computed and N_i^j the number of ice crystals nucleated during experiment j.

On a global level, the correlation between consecutive deposition nucleation experiments in the same conditions is much lower than for immersion freezing (the mean correlation over all experiments is slightly over 0.50 when it was close to 0.85 for immersion freezing). For experiment **B**–Dep–3, there is even no correlation at all ($r = 0.11$). No clear trend can be determined regarding the evolution of the correlation coefficient as a function of the frost point temperature. There is however a noticeable trend in the evolution of the proportion of crystals involved in the calculation of the correlation coefficient: as the frost point temperature decreases, $\mathcal{R}$ decreases also.

This trend can be interpreted as an increase of the number of ice nucleating active sites with decreasing temperature. At lower cooling rates, as the growth of the first ice crystals nucleated locally creates a diminished relative humidity, it undermines the neighboring ice nucleating active sites' capacity to form an ice crystal. Therefore, with the increase of the number of active sites with decreasing temperatures, the same residual particles might not be involved in consecutive experiments.

A further look into suspension C

Because of their high number of ice nucleation sites per residual particles, suspensions **A** and **B** are difficult to analyze in terms of representativeness for deposition nucleation: only a fraction of the ice nucleating active sites can act as substrate for deposition nucleation. Therefore, the suspension **C**, with only one ice nucleation site per residual provides more unbiased information.

In experiment **C**–Dep–2, for a mean frost point temperature of -22.1 ± 0.2°C, the proportion of ice crystals involved in the calculation of the correlation coefficient is constant and equal to 100%: the ice nucleating active sites available at this temperature are only on the 15 positions on which ice crystals were created at a cooling rate of $1\,\mathrm{K.min^{-1}}$. Furthermore, out of the 10 crystals created at a cooling rate of $0.5\,\mathrm{K.min^{-1}}$, 8 were among the 10 first crystals at a cooling rate of $1\,\mathrm{K.min^{-1}}$. Therefore, even though the results seem like they do not show any correlation, if we consider the broader sample of the original 143 droplets, there is a rather high correlation between the different experiments regarding which ice nucleating active sites serve as substrate for deposition nucleation at a frost point temperature of -22.1 ± 0.2°C
The results for lower frost point temperatures show better correlation but $\mathcal{R}$ is slightly lower. For both experiments **C**–Dep–3 and **C**–Dep–4, five positions always correspond to crystals among the first ten to be detected but in a random order ($r = -0.03$).

Deposition nucleation seem to occur regularly on the same ice nucleating active sites, but the order in which the ice crystals are created in this experiment is random.

4.2.4 Correlation with immersion freezing

We have concluded in the previous section that deposition nucleation occurred on preferred ice nucleating active sites. We now address the question for which the experiment was designed: "*Does being a good immersion freezing ice nucleus imply being a good deposition nucleation ice nucleus?*"

In the previous chapter, we observed a high correlation between consecutive freezing experiments for suspensions **A** and **B**, showing that the droplets froze in the same order, proof of heterogeneous nucleation by immersion freezing; whereas for suspension **C**, the correlation was rather low, indicating a small number of INP in the droplets as most of the droplets froze in a random order.
However, it was noticed, that the first droplets to freeze in experiment **C**–Imm–1 were incidentally also the droplets for which the residual particles were responsible of ice nucleation at a frost point temperature of -22.1°C (experiment **C**–Dep–2, $1\,\mathrm{K.min^{-1}}$).

Suspensions A and B

We first look into the correlation between the freezing order for immersion freezing and deposition nucleation for the two concentrated suspensions. For suspension **A**, the mean correlation coefficient is $r = 0.24$, with a minimum of -0.15 and a maximum of 0.45; and for suspension **B**, the mean correlation coefficient is $r = 0.15$, with a minimum of -0.24 and a maximum of 0.44.

There is absolutely no correlation between the freezing ranks and deposition nucleation ranks for those suspensions. However, we noticed in a previous section that for those concentrated suspensions, there were multiple ice nucleating active sites per droplet. Therefore, we cannot draw any conclusion on the link between immersion freezing and deposition nucleation from those two suspensions.

Suspension C

For suspension **C**, the correlation coefficients were only computed for cases with more than 10 individual crystals formed and therefore exclude the cooling rates of 0.5 and 0.2 K.min^{-1} for experiment **C**–Dep–2. The mean correlation coefficient is $r = 0.52$, with a minimum of 0.20 and a maximum of 0.84. There seems to be a correlation, however, not for all experiments.

We focus on the correlation between the immersion freezing experiments and the deposition nucleation experiment for a frost point temperature of −21.9°C and a cooling rate of 1 K.min^{-1}. The mean correlation in this case is $r = 0.72$ (0.66; 0.78) over the 15 considered nucleated crystals. Not only is there a correlation for the considered droplets, but more importantly, 10 of the 15 considered positions belong to the first 18 frozen droplets in each of the immersion freezing experiments and the five most ice active positions identified for experiments **C**–Imm–1 through 3 are also among the most active for the immersion freezing experiments:

```
C-Imm-1:[ 46, 15, 13, 37, 77,103,138,136,124, 58, 52, 82, 96, 33, 89]
C-Imm-2:[ 15, 46, 13,138, 77, 76, 37,103, 58, 96, 16,132, 33, 26,136]
C-Imm-3:[ 46, 15, 13, 77,136, 37, 58,138, 96, 74, 82, 39, 99, 88,103]
C-Dep-2 :[ 15, 13, 46, 37, 42, 58, 96,103,136,133, 77, 33, 82,104,132]
C-Dep-3 :[116, 42, 46, 60, 77, 15, 53, 13,104,103, 87, 96, 78, 37,138]...58
C-Dep-4 :[ 77, 13, 49, 46,116, 96,103, 15, 18, 95, 32, 60, 58, 90, 87]...37
```

The same sites of ice nucleation are involved for the different experiments, but in different orders. This in itself doesn't necessary indicate a link between immersion freezing and deposition nucleation: the fact that the active sites for immersion freezing are the same as those for deposition nucleation could result from a preactivation of the sites during the immersion freezing cycles.

However, Figure 3.2 shows that for the first frozen droplets in each of the **C**–Imm experiments have a very similar freezing behavior as well as correlated freezing ranks (Figure 3.3) which invalidates a preactivation hypothesis.

Therefore, the presence of the same sites between the two types of experiments points towards a strong link between very ice active aerosol particles in the immersion freezing and deposition nucleation modes. However, this is only noticeable when considering the lower concentrated suspension.

Marcolli (2014) suggested that deposition nucleation was actually immersion freezing or homogeneous nucleation taking place in asperities of the aerosol particles. The results from this study come in good agreement with this assertion as the correlation between

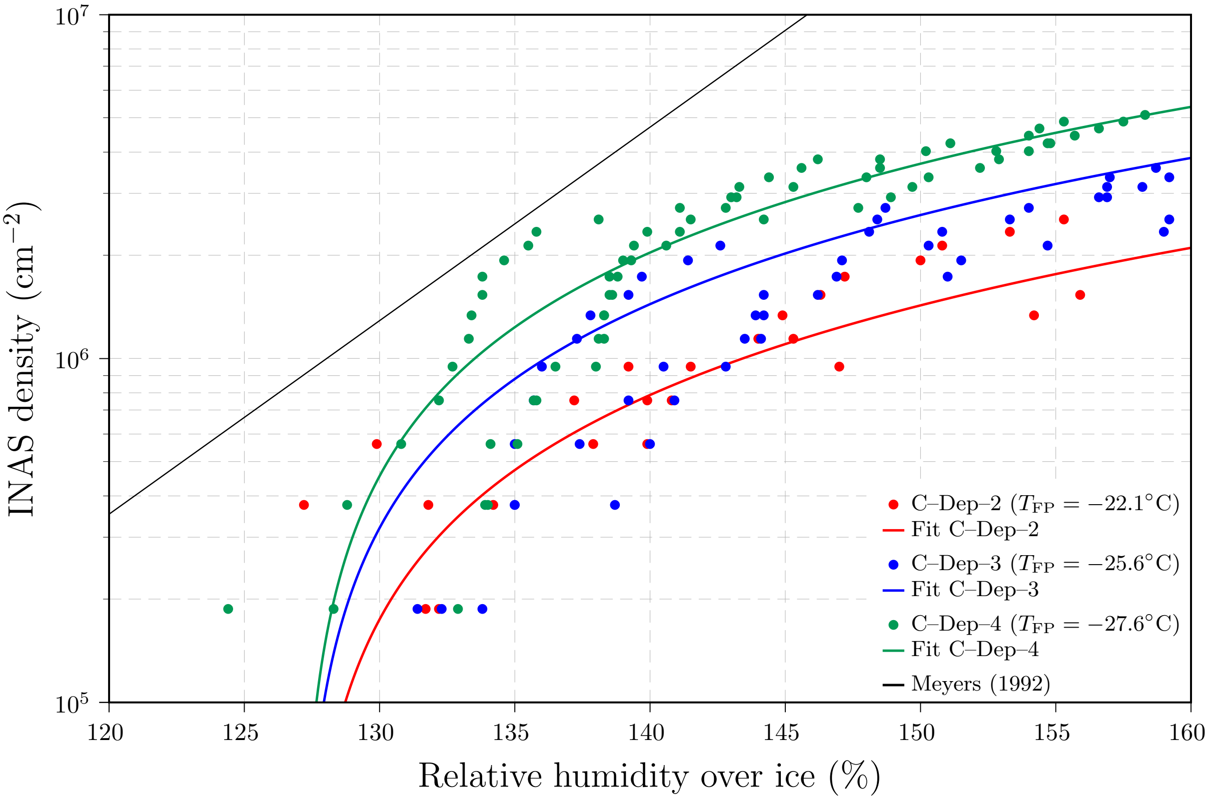

Figure 4.7 – Ice nucleating active site (INAS) density as a function of the relative humidity for the three deposition nucleation experiments using suspension **C**: **C**–Dep–2 in red, **C**–Dep–3 in blue and **C**–Dep–4 in green. In colored solid lines are represented the fit curves for each of these experiments with the fit function defined as: $n_{s,\mathrm{dep}}(T, RH_i) = \exp(10.5 - 0.18 \cdot T) \cdot [1 - \exp(0.02 \cdot (127 - RH_i))]$. The black solid line corresponds the Meyers parameterization with the assumption of an aerosol surface concentration of $S_{\mathrm{aer}} = 2 \cdot 10^{-2} \mathrm{cm.m}^{-3}$.

the experiments for both heterogeneous nucleation mechanisms for suspension **C** indicate similar physical processes responsible for ice nucleation.

However, for the more concentrated suspensions, the cracks, pits and other asperities at the surface of the aerosol particles might come in competition with more "*open*" and more efficient ice nucleating active sites which translates into a lack of correlation between the experiments for immersion freezing and deposition nucleation.

4.3 Ice Nucleating Active Sites density: Parameterization

As previously for immersion freezing, we derive a parameterization for deposition nucleation from the glsinas densities. Because of the multiplicity of active sites on the residual particles for suspensions **A** and **B**, only the results from experiments **C**–Dep are used here to compute INAS densities.

The results are presented along the non–aerosol–specific deposition nucleation parameterization from Meyers et al. (1992) in Figure 4.7. This parameterization provides a number of ice nuclei per unit of volume solely depending on the supersaturation with respect to ice; therefore, in order to compare our results with this parameterization, it is assumed that the aerosol population on which this parameterization is based has an aerosol surface concentration of $S_{\text{aer}} = 2 \cdot 10^{-2}\text{cm.m}^{-3}$ as proposed by Phillips et al. (2012).

For a constant relative humidity, the INAS density increases with decreasing frost point temperature. However, the rather small number of experiments, nucleated ice crystals and residual particles considered in this experiment, there is a rather large scattering of the data, and the determining of a parameterization from these results is therefore quite difficult.
We propose the following fit function, presented in Figure 4.7 in colored solid lines:

$$n_{s,\text{dep}}(T, RH_i) = \exp(10.5 - 0.18 \cdot T) \cdot [1 - \exp(0.02 \cdot (127 - RH_i))] \quad [\text{cm}^{-2}] \tag{4.2}$$

with $T \in [-22; -30°\text{C}]$ the Celsius temperature of the silicon wafer and $RH_i \in [127; 160\%]$ the relative humidity over ice measured on the wafer.
This function follows the exponential temperature dependence of the INAS density proposed for example in Steinke et al. (2015). However, the exponential supersaturation dependence from this same parameterization cannot be applied to the present set of data for a relative humidity below 140%.

The chosen fit function comes in good coherence with the experimental INAS densities at high relative humidity. For a relative humidity below 135%, there is too large a variation of the INAS densities for the consecutive experiments to obtain a precise fit for each frost point temperature investigated. The limit of 127% for the relative humidity was chosen as it corresponds to the relative humidity at which the first ice crystals are detected in experiment **C**–Dep–4, corresponding to the critical relative humidity measured by Yakobi-Hancock et al. (2013) for K–feldspar.

4.4 Summary for deposition nucleation experiments

The second part of the experiments conducted in this thesis on K–feldspar particles consisted in a succession of cooling experiments with a controlled humidity in the flow cell. This method provided both condensation freezing and deposition nucleation experiments. Condensation freezing experiments showed a behavior very similar to that of immersion freezing, even though the order in which the droplets froze in both types of experiments were not the same.
Deposition nucleation experiments didn't show any dependence towards the cooling rate. Contrary to immersion freezing experiments, the ice nucleation order of the residual particles was not the same in consecutive experiments. However, the experiments on the sample using the highly diluted suspension **C** showed that the same residual particles were involved in ice nucleation.
Particularly, the droplets involved in heterogeneous nucleation for this last suspension correspond to the most ice active residual particles for deposition nucleation, indicating that the same ice nucleating active sites are involved in both types of mechanisms.

Finally, a parameterization is proposed for deposition nucleation on K–feldspar particles. No such parameterization was found in the literature to be compared with the results

from the present study. The proposed parameterization is a preliminary result as only a small number of experiments for three different frost point temperatures with a low number of residual particles is available; some more experiments are needed to improve the reliability of the parameterization.
Furthermore, the correspondence between dew point mirror and cold stage frost point temperatures must be addressed and improved.

This new setup for cold stage experiments at the IMK–AAF provides new insights on the mechanistic similarities between the different heterogeneous nucleation mechanisms and the results presented in this thesis indicate that *good ice nucleating active sites in the immersion freezing mode are also good active sites in the deposition nucleation mode.*

Part II

Modeling Study of the Impact of Mineral Particles on a Convective Cloud: The DESCAM Model

Chapter 5

The DESCAM Model: Parameterization of Homogeneous and Heterogeneous Ice Nucleation for Modeling

The impact of clouds on the climate is dependent on the generated precipitations (Flossmann and Wobrock, 2010) as well as on the phase of the hydrometeors constituting the clouds, as it determines its radiative properties (Sun and Shine, 1994). To determine how ice crystals form in the atmosphere (whether in or out of cloud), models use ice nucleation parameterizations based on experimental results (*e.g.* Koop et al., 2000; Hoose and Möhler, 2012). This chapter aims to improve the simulation of ice formation through appropriate parameterization of ice nucleation and study its potential impact on the development of a convective cloud and the resulting precipitations.

5.1 The DESCAM model

The model used in the following study is the Detailed Scavenging Model (DESCAM), Flossmann et al., 1985; Flossmann and Wobrock, 2010), a bin–detailed microphysics scheme — simulating the evolution of a cloud in the atmosphere — coupled with a 1.5–D dynamics model.

5.1.1 Atmosphere representation

The atmosphere is modeled based on four main equations: the continuity equation, Newton's second law of motion, the conservation of energy (first thermodynamics principle) and the conservation of water vapor (Leroy, 2007). These four equations, coupled with the equation of state of the air determines the evolution of the main thermodynamics variables: the temperature T (or potential temperature θ), pressure p, humidity q_v, wind speed $\vec{V}$ and density ρ of the air mass.

DESCAM, in addition to these thermodynamic variables, follows explicitly the populations of aerosol particles on which the water vapor condensate to form clouds droplets and ice crystals.

5.1.2 Ice nucleation

Different ice nucleation mechanisms occur under different thermodynamics conditions (water vapor supersaturation, temperature, presence of activated or unactivated aerosol particles). In the literature, there has been discussion on the origin of the ice crystals in different types of clouds with respect to these different mechanisms. For example, it has been inferred that cirrus clouds resulted in a combination of heterogeneous and homogeneous nucleation processes (DeMott et al., 1997) but recent studies showed that heterogeneous nucleation and particularly deposition nucleation seems to dominate the formation of ice crystals in the upper atmosphere (*e.g.* Cziczo et al., 2013).

The work of this thesis aims to better understand the importance of the different ice nucleation mechanisms on the evolution and life cycle of a convective cloud. It also assesses the conditions in which the different mechanisms influence the evolution of the cloud.

Aerosol particles and hydrometeors size distributions

The aerosol particles, as well as the droplets and ice crystals (hydrometeors), are represented in a bin–resolved fashion: they are distributed on a mass grid and each value at the grid points is then evaluated separately during the evolution of the atmospheric system.

In the version of Descam used in the following studies, aerosol particles and hydrometeors are described using a 39–bin mass grid with equivalent radii ranging from 1 nm to 7 µm for the aerosol particles and 1 µm to 7 mm for the cloud droplets. The grid for the ice crystals is defined in order to have a mass equivalence between two corresponding grid points of cloud droplets and ice crystals. The different grid points are computed with the radius of bin $\mathtt{j}$ defined as follows:

$$r(\mathtt{j}) = r(\mathtt{1}) \cdot 2^{\frac{\mathtt{j}-1}{3}}$$

The particularity of Descam is that it follows explicitly the mass of aerosol particles inside the different reservoirs (aerosol particles, cloud droplets and ice crystals). Therefore, Descam uses six different size distributions: number concentrations of aerosol particles $[\mathcal{N}_a(r_a)]$, cloud droplets $[N_d(r_d)]$ and ice crystals $[N_i(r_i)]$ as well as the mass of aerosol particles in each of these categories ($\mathcal{M}_a(r_a)$ in the the aerosol particles, $\mathcal{M}_d(r_d)$ in the cloud droplets and $\mathcal{M}_i(r_i)$ in the ice crystals).
The mean mass of one aerosol particle in the aerosol particles reservoir can be obtained as follows:

$$\overline{m}(r_a) = \frac{\mathcal{M}_a(r_a)}{\mathcal{N}_a(r_a)}$$

a similar equation can be used for the mean mass of aerosol particles in one cloud droplet or one ice crystal.

The size distributions correspond to conservative variables and therefore follow also a conservation equation, similar to that of water vapor:

$$\frac{\mathrm{d}\varphi(r)}{\mathrm{d}t} = \left.\frac{\partial\varphi(r)}{\partial t}\right|_{\mathrm{dyn}} + \left.\frac{\partial\varphi(r)}{\partial t}\right|_{\mathrm{mic}} \tag{5.1}$$

5.1.3 Dynamical frame

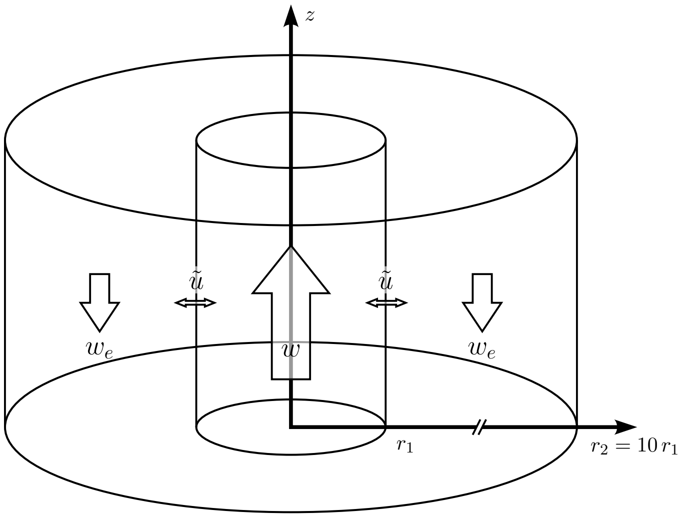

The dynamic equations are resolved in the 1.5–dimension dynamical frame presented by Asai and Kasahara (1967): *the model consists of two concentric cylindrical air columns, the inside column corresponding to an updraft (cloud) region and the outside concentric annular column for the surrounding compensating downward motion (cloudless) region.* The radius of the outer cylinder is ten times larger than the inner cylinder, which allows to consider the environment as constant.
The set of dynamical equations (Monier et al., 2006) resulting from this dynamical frame is detailed in §A.3.2.

5.1.4 Microphysics equations

The microphysical evolution of the different size distributions follow the scheme described in Figure 5.1 which leads to the following equations:

$$\left.\frac{\partial \mathcal{N}_a(r_a)}{\partial t}\right|_{\text{mic}} = \left.\frac{\partial \mathcal{N}_a(r_a)}{\partial t}\right|_{\text{act/deact}} + \left.\frac{\partial \mathcal{N}_a(r_a)}{\partial t}\right|_{\text{con/eva}} + \left.\frac{\partial \mathcal{N}_a(r_a)}{\partial t}\right|_{\text{coll}} + \left.\frac{\partial \mathcal{N}_a(r_a)}{\partial t}\right|_{\text{nucl}} \tag{5.2}$$

$$\begin{aligned}\left.\frac{\partial N_d(r_d)}{\partial t}\right|_{\text{mic}} = {} & \left.\frac{\partial N_d(r_d)}{\partial t}\right|_{\text{act/deact}} + \left.\frac{\partial N_d(r_d)}{\partial t}\right|_{\text{con/eva}} + \left.\frac{\partial N_d(r_d)}{\partial t}\right|_{\text{coll,cont}} + \left.\frac{\partial N_d(r_d)}{\partial t}\right|_{\text{coal}} \\ & + \left.\frac{\partial N_d(r_d)}{\partial t}\right|_{\text{break}} + \left.\frac{\partial N_d(r_d)}{\partial t}\right|_{\text{nucl}} + \left.\frac{\partial N_d(r_d)}{\partial t}\right|_{\text{rim}} + \left.\frac{\partial N_d(r_d)}{\partial t}\right|_{\text{melt}}\end{aligned} \tag{5.3}$$

$$\left.\frac{\partial N_i(r_i)}{\partial t}\right|_{\text{mic}} = \left.\frac{\partial N_i(r_i)}{\partial t}\right|_{\text{dep/sub}} + \left.\frac{\partial N_i(r_i)}{\partial t}\right|_{\text{coll,cont}} + \left.\frac{\partial N_i(r_i)}{\partial t}\right|_{\text{nucl}} + \left.\frac{\partial N_i(r_i)}{\partial t}\right|_{\text{rim}} + \left.\frac{\partial N_i(r_i)}{\partial t}\right|_{\text{melt}} \tag{5.4}$$

The different terms treat the different microphysical processes of the atmosphere: the activation and deactivation of cloud droplets ($|_{\text{act/deact}}$), the condensation and evaporation of water vapor on the aerosol particles and droplets ($|_{\text{con/eva}}$) and the deposition and sublimation on the ice crystals ($|_{\text{dep/sub}}$), the ice nucleation ($|_{\text{nucl}}$), the collection of aerosol particles by the droplets and subsequent contact freezing ($|_{\text{coll,cont}}$), the collision coalescence between droplets ($|_{\text{coal}}$) and subsequent break–up of large droplets ($|_{\text{break}}$) and the collision between droplets and ice crystals and subsequent freezing ($|_{\text{rim}}$) and the instantaneous melting of the ice crystals when crossing the iso–zero level ($|_{\text{melt}}$).

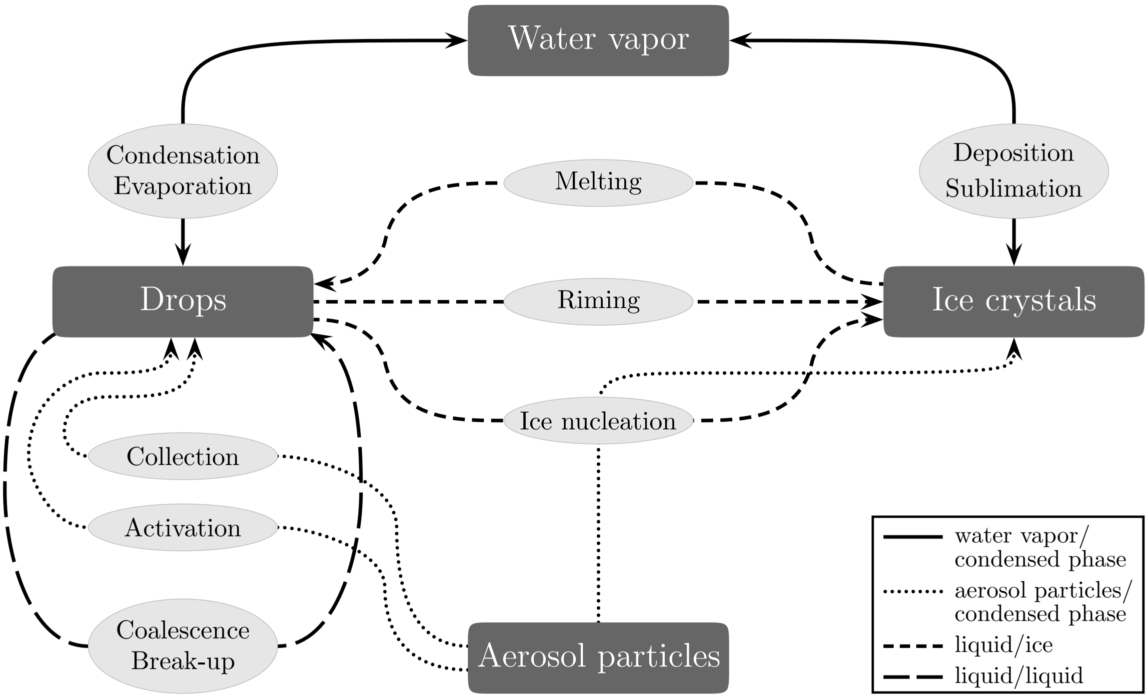

Figure 5.1 – Microphysical scheme in DESCAM

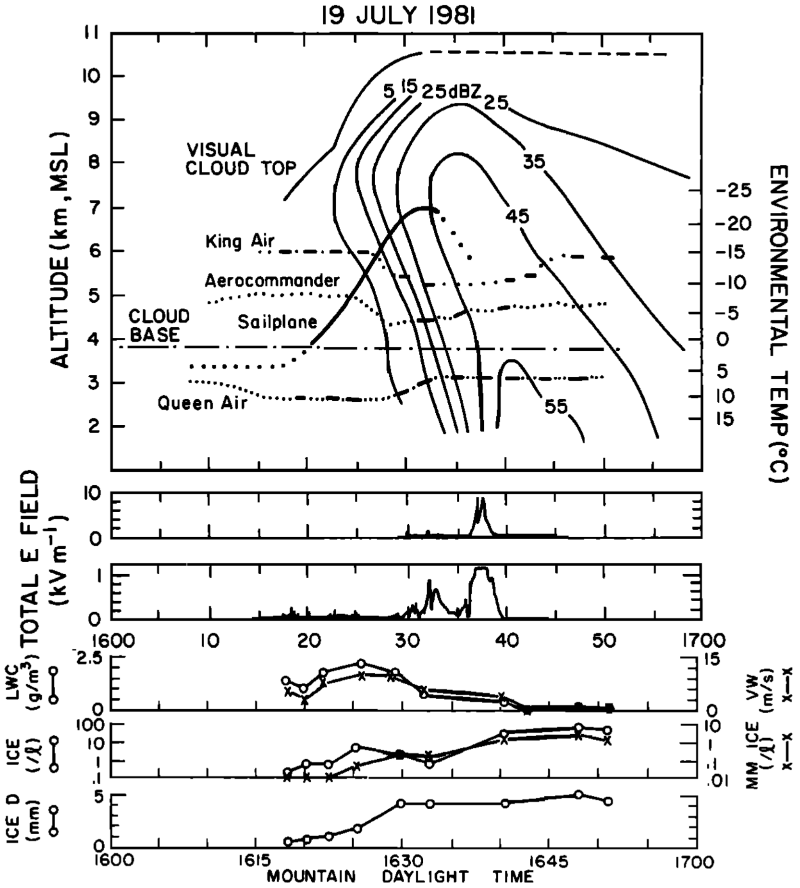

Figure 5.2 – Time–altitude history of the development of the CCOPE cloud represented by the radar reflectivity reflectivity with the times and altitudes of the in–cloud penetrations of the aircraft superimposed, fourth and fifth panel show the liquid water content (LWC), the vertical wind (VW) and ice particle concentration (ICE) measured by the King Air plane, from Dye et al. (1986)

	Size mode		
Mode i	$i = 1$	$i = 2$	$i = 3$
R_i (µm)	$1.00 \cdot 10^{-3}$	$2.18 \cdot 10^{-2}$	6.24
σ_i	2.218	3.199	1.892
n_i (cm^{-3})	$9.97 \cdot 10^2$	$8.42 \cdot 10^2$	$7.10 \cdot 10^{-4}$

Table 5.1 – Aerosol log–normal distributions parameters for a continental air mass from Jaenicke (1988)

This work focuses on the ice nucleation term ($|_{\mathrm{nucl}}$) and its impact on the evolution of the cloud, the detail of the mechanisms and parameterizations of ice nucleation will be detailed later.

5.1.5 Dynamical initialization: CCOPE

The dynamical framework is initialized using the well documented reference case of Cooperative COnvective Precipitation Experiment (CCOPE, Dye et al., 1986; Leroy et al., 2006), a strong convective cloud observed on July 19th 1981 in Montana (USA).

Three aircraft and a sailplane made *in situ* measurements during the small storm and two Doppler radars provided reflectivity and motion of the storm (Figure 5.2).
The development of the cloud can be divided in three parts: first some week updraft before developing an organized structure with stronger updrafts between 1617 and 1630 (as can be seen by the ascent of the sailplane on Figure 5.2) and finally strong precipitations from 1630 on.
The thermodynamic parameters necessary to the dynamical initialization of the model (temperature, pressure, humidity) are taken from radiosonding profiles measured shortly before the beginning of the CCOPE storm (Leroy et al., 2006).

5.1.6 Aerosol particle size distribution

The aerosol particle size distribution is initialized using a superposition of three log–normal number distributions:

$$\mathcal{N}_a(r_a) = \sum_i \frac{n_i}{\sqrt{2\pi}\ln 10 \log \sigma_i} \exp\left(-\frac{\log^2(r_a/R_i)}{2\log^2 \sigma_i}\right) \tag{5.5}$$

with R_i the mean particle radius (µm), n_i the integral of the i^{th} log–normal function (cm^{-3}) and σ_i a measure of the spectrum width as proposed by Jaenicke (1988), values are to be found in Table 5.1.

5.2 Ice nucleation processes and parameterizations

The phase transition from liquid water (either on aerosol particles or cloud droplets) to ice occurs when the ice embryo reach a critical germ size which will then grow spontaneously and lead to the phase change of all the liquid water (Chapter 1, *see* also Pruppacher and

Klett, 1997, Chapter 7). This phase transition mechanism is called ice nucleation.
The ice embryo can either grow directly in the liquid phase (homogeneous nucleation, $|_{\text{nucl,hom}}$) or on a solid substrate acting as pattern for the embryo formation (heterogeneous nucleation, $|_{\text{nucl,het}}$). These mechanisms have been introduced previously in Chapter 1.

5.2.1 Homogeneous nucleation

In Descam, homogeneous nucleation is treated using the parameterization of Koop et al. (2000, *see* Monier et al., 2006 for details):

$$\log(J_{\text{hom}}) = -906.7 + 8\,502 \cdot \Delta a_w - 26\,924 \cdot \Delta a_w^2 + 29\,180 \cdot \Delta a_w^3 \tag{5.6}$$

where J_{hom} is the homogeneous nucleation rate ($\text{cm}^{-3}.\text{s}^{-1}$) and $\Delta a_w(c, T) = a_w(c^{\text{eff}}, T) - a_w^i(T)$, with $0.26 < \Delta a_w < 0.34$, is the 'water–activity criterion' for homogeneous ice nucleation with:

$$a_w^i(T) = \exp\left[\left(210\,368 + 13.438 \cdot T - \frac{3\,323\,730}{T} - 41\,729.1 \cdot \ln T\right) \cdot \frac{10^7}{RT}\right] \tag{5.7}$$

the water activity of the solution in equilibrium with the ice phase. R is the universal gas constant and the water activity of the solution $a_w(c^{\text{eff}}, T)$ can be assimilated to the ambient relative humidity over water.

This yields the variation of N_d and N_i, for a droplet containing a water volume of $V_w = V_d - V_{a,\text{dry}}$:

$$\left.\frac{\partial N_d}{\partial t}\right|_{\text{nucl,hom}} = -J_{\text{hom}} \cdot V_w \cdot N_d = -\left.\frac{\partial N_i}{\partial t}\right|_{\text{nucl,hom}} \tag{5.8}$$

the same formulation applies to unactivated aerosol particles where homogeneous ice nucleation is considered on the small layer of water surrounding the droplet.

5.2.2 Heterogeneous nucleation

Heterogeneous nucleation is generally associated to four different modes (Hiron and Flossmann, 2015) separated in two groups: freezing nucleation, where the ice crystal originated in the liquid phase and deposition nucleation ($|_{\text{nucl,dep}}$), where the ice crystal developed directly from the vapor phase.

Freezing nucleation includes several processes, with the three following processes being well defined and studied: contact freezing, immersion freezing ($|_{\text{nucl,imm}}$) and condensation freezing ($|_{\text{nucl,cond}}$).

5.2.2.1 Immersion freezing

Bigg (1953) pointed out that larger droplets have a larger probability of ice embryos reaching the critical size to initiate the freezing of the droplet. Also, larger droplets have a larger probability of having captured aerosol particles through impaction scavenging, leading to an increased number of aerosol particles available to serve as ice nuclei (Diehl and Wurzler, 2004).

Therefore, the general formula describing these effects shows a dependence on droplet volume (Pruppacher and Klett, 1997):

$$-\frac{1}{N_u}\left(\frac{\mathrm{d}N_u}{\mathrm{d}t}\right)=\frac{1}{N_u}\left(\frac{\mathrm{d}N_f}{\mathrm{d}t}\right)=B\cdot V_d\cdot\left[\exp(aT_s)-1\right] \tag{5.9}$$

with N_u and N_f the number of unfrozen and frozen droplets respectively, $T_s = 273.15 - T_d$ where T_d is the mean cloud drop temperature which is here assumed to be identical to the air temperature and V_d the volume of the water droplet.

Generally, for temperatures below $-5°\mathrm{C}$, $\exp(aT_s) \gg 1$ and the variations on N_d and N_i can be computed by:

$$\left.\frac{\partial N_d}{\partial t}\right|_{\text{nucl,imm}} = -N_d\cdot B\cdot V_d\cdot\exp(aT_s) = -\left.\frac{\partial N_i}{\partial t}\right|_{\text{nucl,imm}} \tag{5.10}$$

Different proposed values of a and B can be found in the literature. The original values suggested by Bigg (1953) ($a = 0.82\,K^{-1}$ and $B = 2.9\cdot10^{-8}\,\mathrm{cm}^{-3}.s^{-1}$) initiate droplet freezing at temperatures up to $-15°\mathrm{C}$. However, the laboratory results on which these values are based were obtained using contaminated water droplets thought to be pure and therefore strongly underestimate the influence of aerosol particles on ice nucleation.
The 100–times–larger value of $B = 2.9\cdot10^{-6}\,\mathrm{cm}^{-3}.s^{-1}$ corresponds to the orders of magnitude of recent observations (*e.g.* Diehl and Wurzler, 2004) and will be used in this chapter to compute immersion freezing. A sensitivity test, using the original values of Bigg (1953), completes this study of immersion freezing.

5.2.2.2 Contact freezing

This freezing mechanism occurs during the collection of aerosol particles by cloud droplets (*e.g.* impaction scavenging). The number concentration of ice nucleating particle (INP) in the contact freezing modes is given by the parameterization of Meyers et al. (1992):

$$n_{\text{IN,cont}} = \exp\left[0.262\cdot(273.15 - T_d) - 2.80\right] \tag{5.11}$$

The algorithm involved in contact freezing has been revised and improved between Hiron and Flossmann (2015) and the present thesis. The potential number concentration of ice nucleation particles given by Meyers et al. (1992) doesn't account for actual ice condensation nuclei behavior. In order to take those aerosol particles into account, the maximal number of aerosol particles available to act as ice nuclei (IN) includes the number of hydrometeors. Following Pruppacher and Klett (1997) and DeMott et al. (2010), a lower limit on the size of aerosol particles that can act as ice nuclei is set to $r_{\text{IN},lim} = 0.1\,\mu\mathrm{m}$. Which leads to a total number of:

$$n_{\text{IN},max} = \sum_{r_a > r_{\text{IN},lim}} \mathcal{N}_a(r_a) + \sum N_d(r_d) + \sum N_i(r_i) \tag{5.12}$$

The implications and limits of this new computation of $n_{\text{IN},max}$ are discussed in §5.4.1.3. The portion of collected aerosol particles that are INP is given by:

$$\Gamma_{\text{cont}} = \frac{n_{\text{IN,cont}}}{n_{\text{IN},max}} \tag{5.13}$$

The variations of $\mathcal{N}_a$, N_d and N_i are expressed as follows (for complete set of equations, *see* Hiron and Flossmann (2015) and §A.3.5.1):

$$\left.\frac{\partial \mathcal{N}_a}{\partial t}\right|_{\text{coll}} = -\mathcal{N}_a \int N_d K_{a,d}\, \mathrm{d}m_d \tag{5.14}$$

where $K_{a,d}$ gives the collection kernel for droplet/particle collection

$$\left.\frac{\partial N_d}{\partial t}\right|_{\text{coll,cont}} = -\frac{\partial}{\partial m_d}\left[\left(\frac{\mathrm{d}m_d}{\mathrm{d}t}\right)_{\text{collec,cont}} N_d\right] - N_d \int \mathcal{N}_a \cdot \Gamma_{\text{cont}} \cdot K_{a,d}\, \mathrm{d}m_a \tag{5.15}$$

$$\left.\frac{\partial N_i}{\partial t}\right|_{\text{coll,cont}} = -\frac{\partial}{\partial m_i}\left[\left(\frac{\mathrm{d}m_i}{\mathrm{d}t}\right)_{\text{collec,cont}} N_i\right] + N_d \int \mathcal{N}_a \cdot \Gamma_{\text{cont}} \cdot K_{a,d}\, \mathrm{d}m_a \tag{5.16}$$

with $\left(\frac{\mathrm{d}m_d}{\mathrm{d}t}\right)_{\text{coll,cont}}$ and $\left(\frac{\mathrm{d}m_i}{\mathrm{d}t}\right)_{\text{coll,cont}}$ the growth speeds of the hydrometeors by collection of aerosol particles (expressions in §A.3.5.1).

5.2.2.3 Meyers et al. (1992) parameterization

The heterogeneous ice nucleation parameterization by Meyers et al. (1992) is based on continuous flow chamber measurements. During these experiments, unactivated aerosol particles enter the chamber and the number of ice crystals coming out of the chamber are counted. This *modus operandi* leads to an indistiction between the deposition nucleation and freezing nucleation, as the experiment does not show whether the aerosol particles were activated before freezing. Therefore, the resulting parameterization regroups the deposition nucleation and condensation freezing modes.

However, the distinction exists in DESCAM through the following distinction: condensation freezing applies to droplets (aerosol particles activated before ice nucleation) and deposition nucleation applies to unactivated aerosol particles.

The Meyers et al. (1992) parameterization gives a number of INP ($n_{\text{IN,Meyers}}$) per liter only as function of the supersaturation over ice $s_{v,i}$:

$$n_{\text{IN,Meyers}} = \exp(12.96 \cdot s_{v,i} - 0.639) \tag{5.17}$$

We can compute a maximal number of INP, corresponding to the total number of aerosol particles in both the reservoir of aerosol particles and droplets:

$$n_{\text{IN},max} = \sum_{r_a} \mathcal{N}_a(r_a) + \sum_{r_d} N_d(r_d) \tag{5.18}$$

If the number of INP prognosed by Meyers et al. (1992) is larger than that of already formed crystals, the excess gives the total number of new INP:

$$n_{\text{IN,nucl},new} = n_{\text{IN,Meyers}} - N_i \tag{5.19}$$

From this we obtain variations of $\mathcal{N}_a$, N_d due to condensation freezing and deposition nucleation:

$$\left.\frac{\partial N_i}{\partial t}\right|_{\text{nucl,Meyers}} = -\left.\frac{\partial \mathcal{N}_a}{\partial t}\right|_{\text{nucl,dep}} - \left.\frac{\partial N_d}{\partial t}\right|_{\text{nucl,cond}} \tag{5.20}$$

Deposition nucleation

As was the case for contact freezing, a lower limit on the size of aerosol particles acting as deposition nucleation ice nuclei is set to $r_{\text{IN},lim} = 0.1\,\mu\text{m}$. Which yields the following variation on $\mathcal{N}_a$:

$$\left.\frac{\partial \mathcal{N}_a}{\partial t}\right|_{\text{nucl,dep}} = -\mathcal{N}_a(r_a)\frac{n_{\text{IN,nucl},new}}{n_{\text{IN},max}} \cdot \frac{1}{\Delta t} \quad \text{if} \quad r_a > 0.1\,\mu\text{m} \tag{5.21}$$

with Δt the time step.

Condensation freezing

To limit condensation freezing in the model to the mechanism described by Vali et al. (2015; *see* Chapter 1), an upper limit on the size of the cloud droplets participating to condensation freezing is set to 16 µm. Furthermore, considering that the droplets involved in condensation freezing are all freshly formed, we can assume that the number of droplets smaller than 16 µm is equal to the number of aerosol particles in the droplets. This yields the variation on N_d for condensation freezing:

$$\left.\frac{\partial N_d}{\partial t}\right|_{\text{nucl,cond}} = -N_d(r_d)\frac{n_{\text{IN,nucl},new}}{n_{\text{IN},max}} \cdot \frac{1}{\Delta t} \quad \text{if} \quad r_d < 16\,\mu\text{m} \tag{5.22}$$

In order to discriminate immersion from condensation freezing, a minimal radius on the droplets considered for immersion freezing is set to 16 µm.

The implementation of this parameterization leads to a uniform freezing fraction over all aerosol particles larger than 0.1 µm, and cloud droplets smaller than 16 µm.

5.3 Method

In order to differentiate the impact of the different mechanisms, a series of sensitivity studies are performed in which each ice nucleation mechanisms have been considered separately as the only source of pristine ice crystals (cases 3 to 7, Table 5.2). Then, all mechanisms are considered together in a single simulation, to study the role of their competition (case 2). Finally these cases are compared with a '*reference*' case where no ice nucleation mechanism is considered (only–liquid case 1).

Case	Description	Rain	± Var.	First rain peak	
				Intensity (mm.h^{-1})	Time (min)
Case 1	No ice nucleation mechanisms active	7.52	—	103.4	42.9
Case 2	All ice nucleation mechanisms active	8.78	+ 17 %	18.0	45.9
Case 3	Only homogeneous nucleation active	5.27	− 30 %	72.3	43.1
Case 4	Only immersion freezing active	7.39	− 2 %	21.3	44.9
	4* — $B = 2.9 \cdot 10^{-8}\,\mathrm{cm^{-3}.s^{-1}}$	10.77	+ 43 %	47.4	43.6
Case 5	Only contact freezing active	15.97	+ 113 %	94.9	43.2
	5* — $r_{\mathrm{IN},lim} = 0.5\,\mu\mathrm{m}$	5.80	− 23 %	103.8	42.9
Case 6	Only deposition nucleation active	12.48	+ 70 %	88.7	43.1
	6* — $r_{\mathrm{IN},lim} = 0.5\,\mu\mathrm{m}$	5.61	− 25 %	107.0	43.0
Case 7	Only condensation freezing active	17.53	+ 133 %	30.1	45.6

Table 5.2 – List of case studies and the results for the cumulative rain (mm) on the ground as well as the properties of the first peak in the rainfall rate (intensity in mm.h^{-1} and the time of simulation at which it occurs).

The importance of the minimal radius of aerosol particles to act as ice nuclei in deposition nucleation and contact freezing mode is discussed through a sensitivity study using two values: a generally assumed value of 0.1 µm and a sensitivity study using 0.5 µm. For immersion freezing, both the original values suggested by Bigg (1953) ($a = 0.82\,K^{-1}$ and $B = 2.9 \cdot 10^{-8}\,\mathrm{cm^{-3}.s^{-1}}$) and a larger value of $B = 2.9 \cdot 10^{-6}\,\mathrm{cm^{-3}.s^{-1}}$ are tested (§5.2.2.1). The different cases are listed in table 5.2.

This methodology was already used in Hiron and Flossmann (2015) and the results presented in this chapter are in agreement with those presented in the publication, taking into account some recent model improvements (*e.g.* aforementioned changes to the contact freezing algorithm, restructuration of the order in which subroutines are called, calculations in double precision). However, the qualitative results, and the conclusions from Hiron and Flossmann (2015) regarding the determining factors with regard to the importance of an ice nucleation mechanism remain valid.

A '*reference*' case: no ice nucleation mechanism — case 1

A '*reference*' case in this study is the entire liquid cloud against which the impact of each mechanism of ice formation is studied. Therefore, in this case 1, only the mechanisms on the left side of Figure 5.1 are taken into account. The liquid water content (LWC in g.m^{-3}) as a function of time (min) and altitude (km) is displayed in Figure 5.3a. The initial levels for 0°C (later referred to as iso–zero level) and −32°C (later referred to as homogeneous nucleation line[1], §5.4.1.1) are also represented in the graph to help analyze the results. The cloud starts forming around 3 km altitude after 8 min of simulation and quickly develops over 27 min to reach an altitude of 9.5 km, at which point the updraft has weakened. The precipitation is initiated at altitudes between 8 and 8.7 km after 23 min of

---

[1] in this case study, homogeneous nucleation is first encountered when the cloud top reaches an altitude of 7.5 km, corresponding to an initial temperature of −32°C, such high homogeneous nucleation threshold temperatures have been also noticed by Herbert et al. (2015)

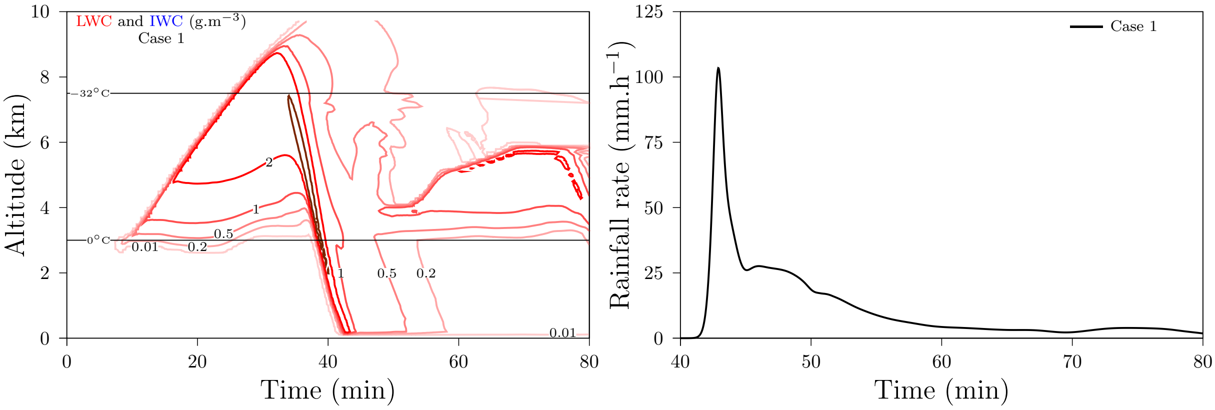

Figure 5.3 – (**a**, left) Liquid water content (g.m^{-3}, red) simulated by DESCAM as a function of altitude and time for the case with no nucleation active (case 1). (**b**, right) Time evolution of the rainfall rate (mm.h^{-1}) for the '*reference*' only–liquid case (case 1, black).

cloud life time, as is shown by the precipitating liquid water content (RWC, Figure 5.5a). The precipitation system can be divided into two distinctive parts:

'*Warm*' rainfall peak: the rainfall reaches the ground after 41.5 min of simulation time with the precipitation peak occurring at 42.9 min with a rainfall rate of 103 mm.h^{-1} (Figure 5.3b, black and Table 5.2), with precipitating liquid water content values exceeding 5 g.m^{-3} (dark red contour Figure 5.3b with a maximum liquid water content of 9.0 g.m^{-3}, Table 5.3). This first precipitation regime corresponds to the first droplets that initiated the rainfall at high altitude in the updraft (wind speeds above 10 m.s^{-1}, Figure 5.7a) and collected the droplets from the lower layers yielding large droplets (when the rainfall crosses the iso–zero level, the liquid water content reaches locally 7.1 g.m^{-3}).

Steadier regime: the precipitation system then enters a steadier regime with rainfall rates between 7.6 and 27.6 mm.h^{-1} from 45 min to 56 min, which corresponds to remaining droplets of smaller sizes associated to a downdraft; the liquid water content at the iso–zero level for this part of the precipitations lies between 0.2 and 1 g.m^{-3}. In this period of the precipitation system, a small downdraft (around 1 m.s^{-1}) in the lower 500 m of the atmosphere increases the rainfall rate.

The remaining 25 min of simulation represent a smaller amount of precipitation (22%) with a moderate rainfall rate (below 7.6 mm.h^{-1}). There is a quite steady dynamics below the iso–zero level (wind speeds below 2 m.s^{-1}) and low liquid water contents (below 0.2 g.m^{-3}), only a few water droplets sedimenting down to the ground level.

The cumulative rain for this '*reference*' case is of 7.52 mm.

5.4 Results from the ice nucleation case studies

In this section, we will focus on the different ice nucleation mechanisms when active alone and compare them among each other and with respect to the '*reference*' case 1 (§5.4.1).

Case	Precipitation onset (WC> $0.2 g.m^{-3}$)				Maximal water contents		
	Droplets		Ice crystals				
	Altitude (km)	Time (min)	Altitude (km)	Time (min)	RWC ($g.m^{-3}$)	SWC ($g.m^{-3}$)	TPWC ($g.m^{-3}$)
Case 1	8.5	31.3	—	—	9.0	—	9.0
Case 2	5.9	35.0	6.6	33.7	1.3	2.3	2.6
Case 3	7.0	32.6	7.3	32.7	4.6	1.9	5.5
Case 4	5.9	34.5	6.5	33.5	1.6	2.2	2.8
Case 4*	6.7	34.0	7.0	33.0	2.4	2.6	4.0
Case 5	7.5	32.2	8.2	31.3	3.8	5.1	6.6
Case 5*	8.5	31.3	—	—	7.4	5.4	8.6
Case 6	7.9	32.0	8.3	31.3	5.5	6.9	7.5
Case 6*	8.5	31.3	—	—	7.7	7.5	8.7
Case 7	6.0	35.0	7.1	33.0	1.3	2.9	3.1

Table 5.3 – Properties of the precipitation system for different cases: the altitude (in km) and time (in min) at which the precipitation starts (the arbitrary reference point chosen is a precipitating liquid, respectively ice, water content larger than $0.2\,g.m^{-3}$) and the maximal water contents (in $g.m^{-3}$) in the precipitation system above the iso–zero level.

The mechanisms are then considered all together, and comparing with the results from §5.4.1, to allow to identify the role of each of them for the evolution of the dynamics of the cloud (§5.4.2).

5.4.1 Only one ice forming mechanism active

5.4.1.1 Homogeneous nucleation — case 3

In Figure 5.4a are displayed the liquid and ice water content (IWC) for the case 3 where only homogeneous nucleation is taken into account (Table 5.2). The dynamics of the cloud during the early cloud life is quite similar to the one of case 1 (Figure 5.3a) until the cloud top reaches the level where homogeneous nucleation starts (the number of ice nucleation events jumps directly from 0 to more than $1\,000\,m^{-3}.min^{-1}$) at 7.5 km (−32°C). From this altitude on, the water droplets start freezing rapidly, leading to a high cloud ice water content (up to $2.3\,g.m^{-3}$) and a strengthened updraft due to the latent heat release, so that most of the pristine ice crystals formed by homogeneous nucleation do not take part in the precipitation at first. The rainfall is being initiated in the liquid phase a little below the freezing limit (at 32.6 min for an altitude of 7.0 km, corresponding to a temperature of −30°C; red contour lines, Figure 5.5b, Table 5.3); therefore, only a small part of the cloud, containing mainly small droplets, is glaciated (Table 5.3, maximal water contents).

'*Warm*' rainfall peak: as in '*reference*' case 1, this first rainfall period corresponds to droplets that initiated the rainfall in the updraft (wind speeds above $6\,m.s^{-1}$, graph not shown) and a few large ice crystals that froze close to the homogeneous nucleation line (blue contours, Figure 5.5b, Table 5.3). The collection processes (collision–coalescence and riming) are then responsible for the increase of the liquid and ice water content in the rainfall. The riming process results in a latent heat release, reducing slightly the intensity of the downdraft and therefore leading to a delay in the peak of rainfall intensity.

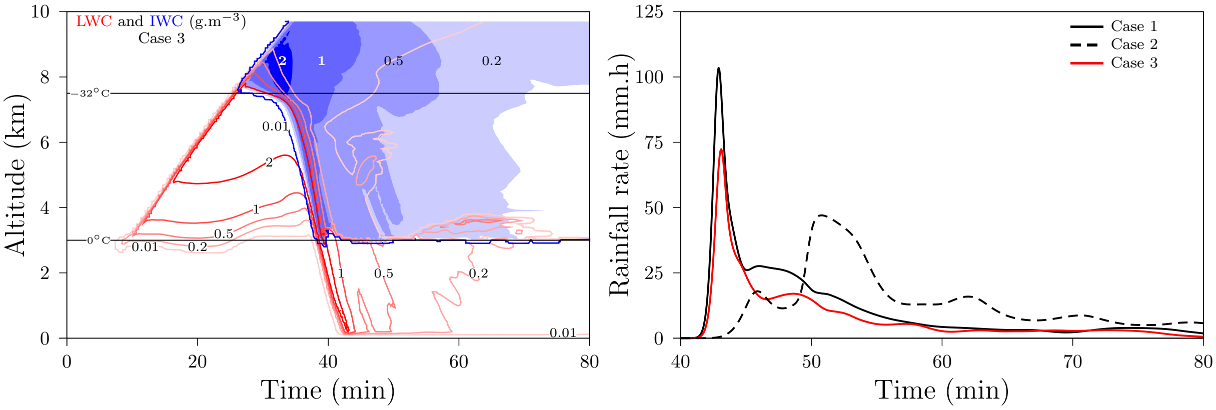

Figure 5.4 – (**a**, left) Liquid water content (g.m^{-3}, red) and ice water content (g.m^{-3}, blue) simulated by DESCAM as a function of altitude and time for the case with only homogeneous nucleation active (case 3). (**b**, right) Time evolution of the rainfall rate (mm.h^{-1}) for the only–liquid case (case 1, black continuous), the all ice processes, all minerals case (case 2, black dashed) and the homogeneous only case (case 3, red continuous).

When crossing the iso–zero level, the total water content reaches locally 4.3 g.m^{-3}, a 40% reduction when compared to the total water content in '*reference*' case 1. This leads to a first rain peak of 72.3 mm.h^{-1} at 43.1 min (Figure 5.4b, Table 5.2).

Steadier regime: the rest of the precipitation system (after 46.5 min) follows a dynamic very similar to that of '*reference*' case 1 with the difference that all droplets involved in the late rainfall went through the ice phase during their fall and a lower total water content (Figure 5.5b).

Overall, homogeneous nucleation is responsible for the freezing of the entire cloud at temperatures below −32°C (altitudes above 7.5 km) and reduces by 30% the total amount of precipitation of the only–liquid case 1 (Table 5.2) but has a small impact on the overall dynamics of the cloud, due to its late onset in the cloud development and therefore doesn't lead to a delay in the precipitation formation as could be expected when ice formation

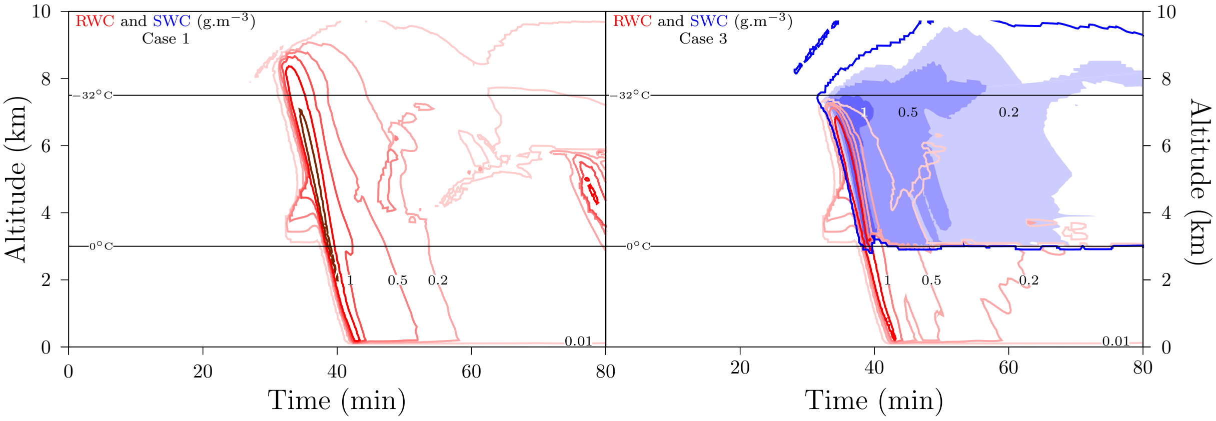

Figure 5.5 – Precipitating liquid water content (g.m^{-3}, red) and precipitating ice water content (g.m^{-3}, blue) simulated by DESCAM as a function of altitude and time for the case with no ice nucleation mechanisms (**a**, left — case 1) and for the case with only homogeneous nucleation active (**b**, right — case 3).

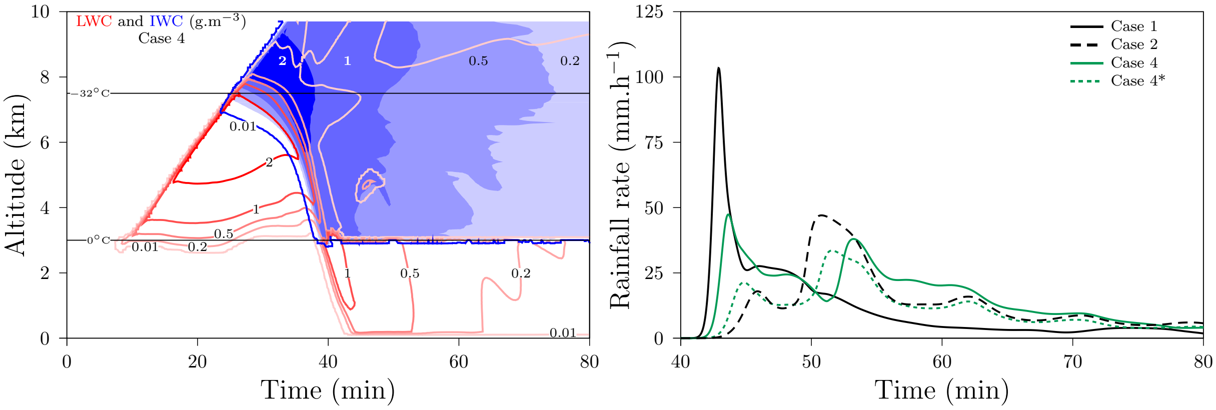

Figure 5.6 – (**a**, left) Liquid water content (g.m^{-3}, red) and ice water content (g.m^{-3}, blue) simulated by DESCAM as a function of altitude and time for the case with only immersion freezing active (case 4). (**b**, right) Time evolution of the rainfall rate (mm.h^{-1}) for the only–liquid case (case 1, black continuous), the all ice processes case (case 2, black dashed) and for immersion freezing with $B = 2.9 \cdot 10^{-6}$cm^{-3}.s^{-1} (case 4, green continuous) and with original Bigg values (case 4*, green dashed).

takes place (Respondek et al., 1995).

5.4.1.2 Immersion freezing — case 4

In Figure 5.6a are displayed the liquid and ice water content for the case where only immersion freezing is taken into account (case 4). As was the case for homogeneous nucleation, the vertical development of the cloud is little impacted by ice nucleation: the cloud top reaches the homogeneous nucleation level after 26 min in case 4 as in case 3. However, ice nucleation comes significant earlier in the cloud development and therefore on smaller droplets than when homogeneous nucleation was considered: from 5.3 km of altitude on, the number of ice nucleation events exceeds 1 m^{-3}.min^{-1} and exceeds 1 000 m^{-3}.min^{-1} for altitudes above 6.2 km. This enhanced ice nucleation rate in the early development of the cloud leads to an increase of the latent heat release, strengthening the updraft at high altitudes and produces a higher cloud ice water content. This strengthened updraft in the higher altitudes of the atmosphere delays the onset of the precipitation in the liquid phase (Table 5.3). Contrary to the homogeneous nucleation case 3, the precipitation is initiated in the ice phase at an altitude of 6.5 km after 33.5 min, prior to the precipitation onset in the liquid phase (Table 5.3).

‘*Warm*’ rainfall peak: as was already observed in case 3, the riming process in the rainfall leads to a delay of the first rain peak. As there are more ice crystals in the precipitation, the riming process is of larger importance which leads to an increased delay of the peak. Further more, as the freezing occurs earlier in the cloud development, the volume of the droplets as they freeze is reduced and only a smaller portion of the droplets reaches the critical size necessary to form the precipitation. As a result, the total water content in the precipitation is reduced (Table 5.3), generating a smaller downdraft, even though the amount of latent heat released through riming is smaller than in case 3. When crossing the iso–zero level, the total water content reaches 2.1 g.m^{-3} after 39.9 min. This results in an increase of the delay at which a much smaller ‘*warm*’ rainfall peak is observed (−80%, Figure 5.6b, Table 5.2).

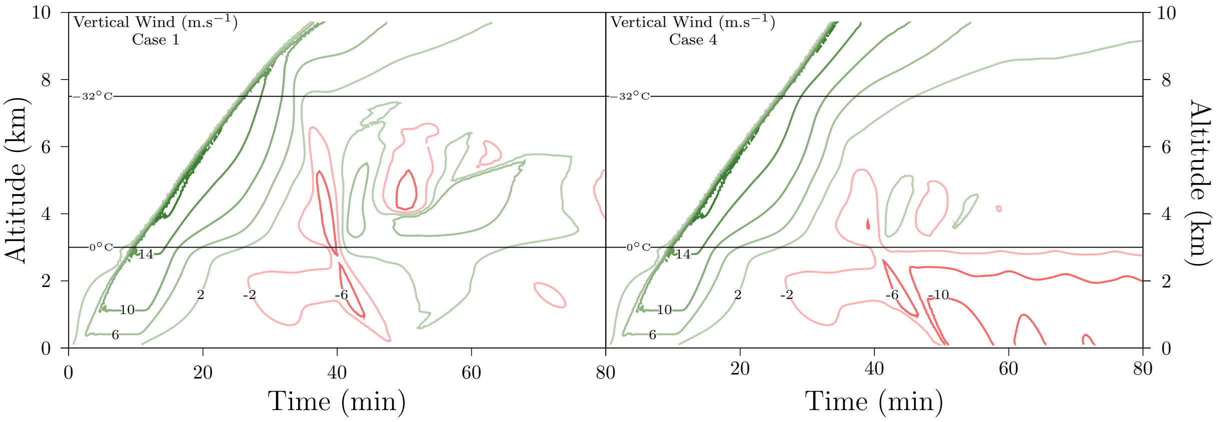

Figure 5.7 – Vertical wind speeds (m.s^{-1}, upward in green and downward in red) simulated by DESCAM as a function of altitude and time for the case with no ice nucleation mechanisms (**a**, left — case 1) and for the case with only immersion freezing active (**b**, right — case 4).

Steadier regime: the second part in the precipitation system starts at 47.6 min as a strong downdraft starts to develop below the iso–zero level. In this regime, the iso–zero level marks also the separation between a downdraft (below the iso–zero level) and an updraft (above the iso–zero level) so that only large ice crystals can sediment and form rain. The smaller crystals, on the other hand, are kept below 0°C in a subsaturated environment and steadily sublimate. The downdraft is caused by the mixing of dry air from higher layers of the atmosphere which leads to a drop in potential temperature[2]. As the drops evaporate rather slowly, the imbalance in virtual potential temperature between the inner and outer cylinder persists and this dynamical state is maintained (between 51 and 80 min, the wind speeds are higher than 6 m.s^{-1}, Figure 5.7). Therefore, even though the total water content at the iso–zero level is much lower in this part of the precipitation system as it was during the peak (below 1 g.m^{-3}, a reduction of 63%), there is a second peak in the rainfall rate of 33.6 mm.h^{-1} at 51.6 min because of the strong downdraft (the liquid water content at ground level reaches 0.5 g.m^{-3} with a wind speed of 12.6 m.s^{-1}).

Overall, immersion freezing is responsible for the freezing of rather large droplets at temperatures below −15°C and decreases by 2% the total amount of precipitation with respect to the only–liquid case 1 (Table 5.2) but with a very different time evolution of the precipitation system. It has a moderate impact on the overall dynamics of the cloud: its relatively late onset in the cloud development doesn't change the dynamics of the updraft, but the freezing of a large amount of large droplets leads to a significant decrease in the '*warm*' rainfall intensity. The downdraft below the cloud base after '*warm*' rainfall peak balances the decrease of the peak, which leads to almost the same total amount of precipitation.

Sensitivity study (case 4* — $B = 2.9 \cdot 10^{-8}\,\mathrm{cm}^{-3}.\mathrm{s}^{-1}$): The sensitivity study done on immersion freezing consists in an decrease of the value of the B parameter by a factor 100 ($B = 2.9 \cdot 10^{-8}\,\mathrm{cm}^{-3}.s^{-1}$), using the original values of (Bigg, 1953, §5.2.2.1). This variation increases, at constant temperature, the volume at which droplets can be frozen

---

[2] One of the term in the dynamical evolution of the vertical wind speed is expressed as $\dfrac{\theta_v - \theta_{v,e}}{\theta_{v,e}}$, *see* Monier (2003)

by immersion freezing. Therefore, ice nucleation is initiated later in the cloud development and on larger droplets (the ice nucleation rates from case 4 are met 500 m higher), the updraft in the higher levels of the atmosphere is weaker and the cloud ice water content above the homogeneous nucleation level is smaller. The total water content in the precipitation is increased, which means a higher downdraft between 6 and 3 km of altitude (wind speeds higher than 6 m.s^{-1}, graph not shown). This results in a '*warm*' rainfall peak between the ones observed in case 3 and case 4 (Table 5.2). During the rest of the precipitation event, the dynamics is similar in the sensitivity case to that of case 4 with the second peak reaching slightly larger intensity a little later.
As the hydrometeors reach larger sizes in the cloud, the total amount of water available for the rainfall is increased, therefore, the total amount of precipitation in case 4* shows an increase of 46% when compared to case 4 (Table 5.2).

In the rest of this chapter, the immersion freezing parameterization uses the value of case 4: $B = 2.9 \cdot 10^{-6}\text{cm}^{-3}.\text{s}^{-1}$.

5.4.1.3 Contact freezing — case 5

In Figure 5.8a are displayed the liquid and ice water content for the case where only contact freezing is taken into account (case 5). The cloud development during the first 28 min is identical to that of only–liquid '*reference*' case 1. As large droplets reach altitudes between 7 and 8 km, the contact freezing rate exceed 1 m^{-3}.min^{-1} with rates up to 1 000 m^{-3}.min^{-1} which lead to a high cloud ice water content in the updraft (up to 2.4 g.m^{-3}). Therefore, the precipitation in the liquid phase is initiated later and lower than in case 1 (Table 5.3). The larger droplets that were frozen through contact freezing at higher altitudes initiate the precipitation in the ice phase approximately after the same time of simulation and at the same altitude as in case 1 (Table 5.3), so that the total precipitation system is very close, in the early development, to that of case 1. However, two different processes change the dynamics of the precipitation in the lower altitudes: first, as both droplets and ice crystals are in presence, the riming process increases the ice water content and releases latent heat. Secondly, in the downdraft, there is an entrainment of dry aerosol particles from the environmental cylinder, which are collected by the precipitating droplets. This leads to ice nucleation with a rate up to 100 m^{-3}.min^{-1} meaning an increase of the ice water content and additional latent heat release.

'*Warm*' rainfall peak: the combination of those characteristics (same precipitation onset as case 1 but latent heat release in the downdraft) leads to a delay of the first peak in the rainfall close to that of case 3 but with a greater intensity (+29%, Table 5.2 and Figure 5.8b).

Steadier regime: as was noticed in case 4, after the first peak in rainfall, a strong downdraft develops below the iso–zero level (49.2 min) to the difference that in case 5, it remains a relatively high liquid water content (larger than 0.5 g.m^{-3}) below 3 km of altitude until 53 min of simulation. The second high intensity peak in the rainfall (81.2 mm.h^{-1} at 51.8 min) is due to this combination of a strong downdraft and a large liquid water content (1 g.m^{-3} at the peak).

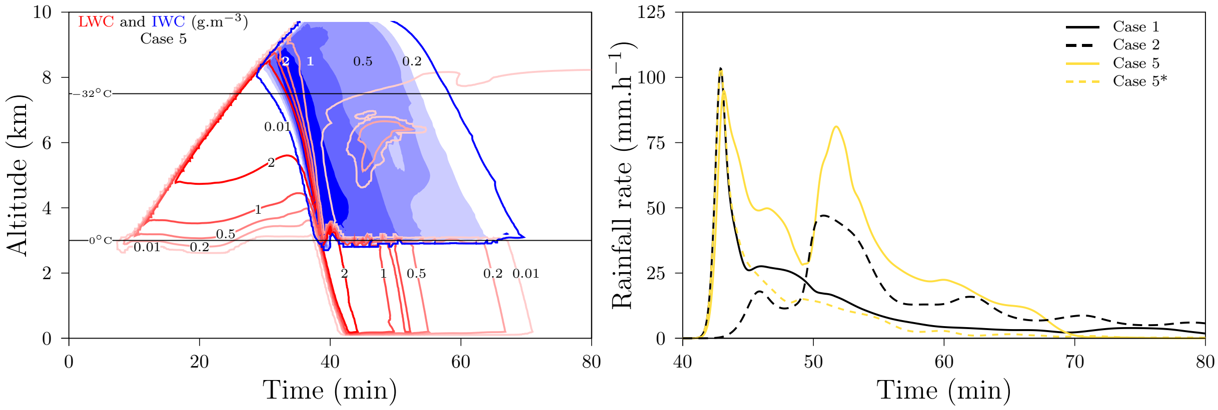

Figure 5.8 – (**a**, left) Liquid water content (g.m^{-3}, red) and ice water content (g.m^{-3}, blue) simulated by DESCAM as a function of altitude and time for the case with only contact freezing active (case 5). (**b**, right) Time evolution of the rainfall rate (mm.h^{-1}) for the only–liquid case (case 1, black continuous), the all ice processes case (case 2, black dashed) and for contact freezing with $r_{\mathrm{IN},lim} = 0.1\,\mu\mathrm{m}$ (case 5, yellow continuous) and with $r_{\mathrm{IN},lim} = 0.5\,\mu\mathrm{m}$ (case 5*, yellow dashed).

The total amount of precipitation in case 5 is larger than in case 1 by 113% (Table 5.2), mainly because of the strong downdraft after the first peak of rainfall and the subsequent second peak of high intentsity.

Sensitivity study (case 5* — $r_{\mathrm{IN},lim} = 0.5\,\mu\mathrm{m}$): The increase of the minimal radius for an aerosol particle to act as an ice nuclei from 0.1 to 0.5 µm doesn't make a difference on the development of the cloud, but as the cloud top reaches altitudes above the homogeneous nucleation level, there is no ice nucleation taking place, so that the precipitation onset is the same as in case 1. It is only in the downdraft, at altitudes with a relative humidity with respect to water lower than 100% that, as unactivated particles are entrained from the environmental cylinder, contact freezing occurs with a relatively low rate (less than $100\,\mathrm{m}^{-3}.\mathrm{min}^{-1}$). However, this small amount of (rather large) pristine ice crystals contributes to a large ice water content in the downdraft through riming (Table 5.3). This onset of ice nucleation only in the downdraft implies a minimal impact of contact freezing on the first peak in the rainfall. The total amount of precipitation in case 5* is reduced with respect to case 1 due to a weaker dynamic and lower water contents (Figure 5.8 and Table 5.2).

The large difference in behavior between cases 5 and 5* is due to the particular dynamics of the studied cloud: the activation radius for the aerosol particles is between 0.1 and 0.5 µm, which means that in case 5, there are some aerosol particles remaining that can act as ice nuclei whereas in case 5*, all potential ice nuclei have been activated into droplets and it is therefore only in the downdraft, as entrained aerosol particles remain unactivated, that some ice nuclei are available for contact freezing.
Also, the computation method used for $n_{\mathrm{IN},max}$ assumes that each of the droplets only contain one aerosol particle larger than $r_{\mathrm{IN},lim}$, which is necessarily an underestimation of the reality because of the collection and collision–coalescence processes involved in the evolution of the cloud. But this allows us to make an estimation of the maximal impact that contact freezing using the (Meyers et al., 1992) parameterization can have on the evolution of the CCOPE cloud.

A sensitivity study was also done using $n_{\mathrm{IN},max} = \sum \mathcal{N}_a(r_a \geq 0.1\,\mu\mathrm{m})$, not taking into account the activated aerosol particles (results not shown). As a major part of the aerosol particles are activated during the development of the cloud with an activation radius larger than 0.1 µm, the number of free aerosol particles is drastically reduced, the value of $n_{\mathrm{IN},max}$ drops and the ratio $n_{\mathrm{IN,cont}}/n_{\mathrm{IN},max}$ increases artificially (in total in one layer of the atmosphere, the number of aerosol particles hasn't changed by a large factor as did $n_{\mathrm{IN},max}$). Therefore, ice nucleation starts earlier in the cloud development (the ice nucleation rate reaches $1\,\mathrm{m}^{-3}.\mathrm{min}^{-1}$ when the cloud top reaches 7 km). This leads to a dramatic variation in the total amount of precipitation (264% increase, rainfall rates larger than $125\,\mathrm{mm.h}^{-1}$ over 15 min).
This computation method was the one used in Hiron and Flossmann (2015).

This major impact of contact freezing when considered alone is contrary to what had been obtained in Hiron and Flossmann (2015), this difference is due to the major modifications implemented into the collection algorithm since the paper was published.

5.4.1.4 Deposition nucleation — case 6

The other ice nucleation mechanism that depends on the number of unactivated aerosol particles is deposition nucleation, for which the liquid and ice water content are displayed in Figure 5.9a. The development of the cloud until the top reaches the homogeneous nucleation level is unchanged by deposition nucleation. However, an early out–of–cloud ice formation becomes noticeable at 8.3 km after 13.4 min. Due to the supersaturation with respect to ice in the initial humidity profile of the model between 7.2 and 8.6 km, some deposition nucleation occurs in those levels in the first time step (between 100 and $5\,000\,\mathrm{m}^{-3}$). This cirrus–like cloud spreads slowly as larger crystal sediment to lower levels, until the cloud top reaches the homogeneous nucleation level.
After 24 min of simulation, in–cloud aerosol particles act as ice nuclei under the very high relative humidity with respect to ice. In the updraft, the ice nucleation rate increases to values as high as $10^5\,\mathrm{m}^{-3}.\mathrm{min}^{-1}$ leading to a high cloud ice water content. However, precipitation is initiated at altitudes close to those of cases 1 and 6 and the total water content in the downdraft is only slightly reduced (Table 5.3).

'*Warm*' rainfall peak: This onset of the precipitation at high altitudes and the total water content close to that of case 1 lead to an only slightly reduced and delayed first rainfall peak (Table 5.2), but the very high ice water content obtained mainly through riming leads to a very large amount of latent heat release at iso–zero level, which is responsible for the increased length of the first rainfall peak (Figure 5.9b).

Steadier regime: This large latent heat release and the mixing of dry air, as was the case in cases 4 and 5 lead to an increased downdraft below the iso–zero level. Therefore, a second peak in the rainfall rate appears at a similar time as in case 4 (51.5 min) but with a greater intensity ($52.8\,\mathrm{mm.h}^{-1}$) because of the higher water content in the downdraft.

The combination of the enlarged and strong first rainfall peak and of the second dynamically induced rainfall peak lead to an increase in the total amount of precipitation to the

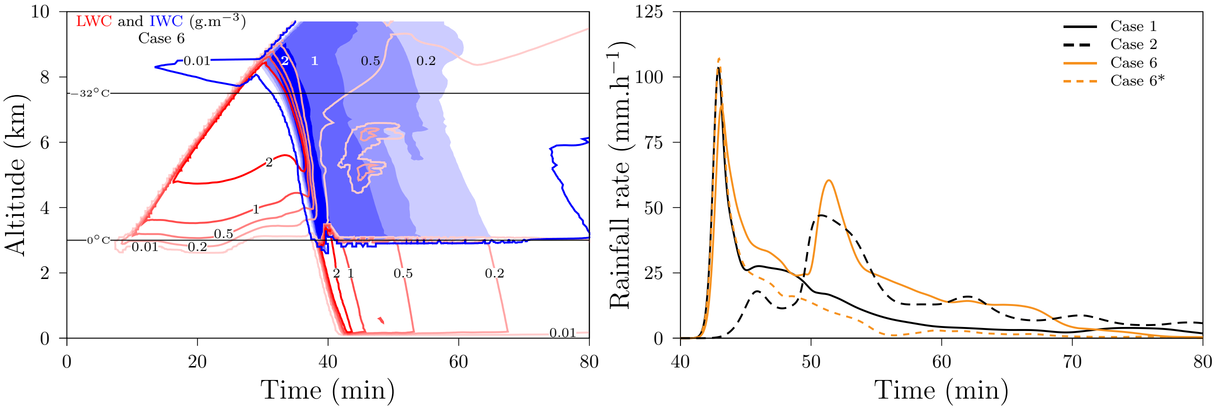

Figure 5.9 – (**a**, left) Liquid water content (g.m^{-3}, red) and ice water content (g.m^{-3}, blue) simulated by DESCAM as a function of altitude and time for the case with only deposition nucleation active (case 6). (**b**, right) Time evolution of the rainfall rate (mm.h^{-1}) for the only–liquid case (case 1, black continuous), the all ice processes case (case 2, black dashed) and for deposition nucleation with $r_{\mathrm{IN}} \geq 0.1\,\mu\mathrm{m}$ (case 5, orange continuous) and with $r_{\mathrm{IN}} \geq 0.5\,\mu\mathrm{m}$ (case 5*, orange dashed).

ground by 70% (Table 5.2).

Sensitivity study (case 6* — $r_{\mathrm{IN},lim} = 0.5\,\mu\mathrm{m}$): When the minimal radius for an aerosol particle to act as an ice nuclei is increased from 0.1 to 0.5 µm, the cirrus–like cloud formed early on isn't impacted. As the number of ice nuclei is predicted solely as a function of relative humidity by the parameterization of Meyers et al. (1992), it is the same in both cases and only the frozen fraction of the aerosol particles with a radius larger than $r_{\mathrm{IN},lim}$ is changed. Therefore the number of nucleation events due to deposition nucleation is the same in cases 6 and 6* and the growth of the ice crystals by vapor diffusion in the same manner. Contrary to this, we notice a large impact on the dynamics of the cloud. It was already noticed for contact freezing (§5.4.1.3) that in the cloud, the aerosol particles activation radius is smaller than 0.5 µm, therefore, there are no aerosol particles available to act as ice nuclei in the higher altitudes and the precipitation is initialized only in the liquid phase at the same time and altitude as for the only–liquid case 1. It is only when the downdraft reaches altitudes subsaturated with respect to water that deposition nucleation takes place, freezing a large part of the cloud through the riming process (the ice water content reaches 6.4 g.m^{-3}, Table 5.3) but with little impact on the precipitation: the total water content in the downdraft varies by about 3%. The first peak in the rainfall is increased by 3% because of the large amount of latent heat release when the precipitation crosses the iso–zero level but isn't delayed as the ice nucleation occurred late in the precipitation system. In the second regime of the precipitation system, the amount of rainfall is reduced with respect to case 1 as there is a slightly stronger updraft below 2.5 km of altitude, immediately after the first rainfall peak.

Deposition nucleation, when considered alone is responsible for an early cirrus–like formation at high altitudes (around 8 km) and leads to a high ice water content in the precipitation system. The impact on the dynamics is highly dependent on the minimal radius of the aerosol particles that can serve as ice nuclei. In the case of deposition nucleation, the variation of this minimal radius plays an important role as it determines where in–cloud deposition nucleation will be significant: either at high altitude, before the

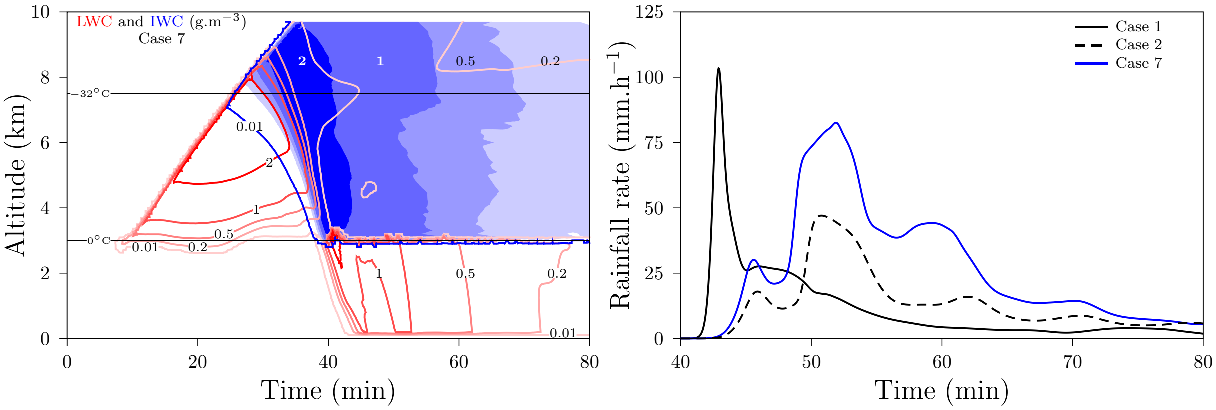

Figure 5.10 – (**a**, left) Liquid water content (g.m^{-3}, red) and ice water content (g.m^{-3}, blue) simulated by DESCAM as a function of altitude and time for the case with only condensation freezing active (case 7). (**b**, right) Time evolution of the rainfall rate (mm.h^{-1}) for the only–liquid case (case 1, black continuous), the all ice processes case (case 2, black dashed) and for condensation freezing (case 7, blue).

precipitation onset or late in the downdraft, when the atmosphere becomes subsaturated with respect to water.

Because of the shared parameterization between deposition nucleation and condensation freezing and the renormalization of the number of ice nuclei upon unactivated aerosol particles and freshly formed droplets (§5.2.2.3), the impact of deposition nucleation is dependent on the limit radius introduced for the droplets. Removing the size limit on the droplets that are considered for condensation freezing reduces the number of ice nuclei in the unactivated particles reservoir and therefore reduces the impact of deposition nucleation on the dynamics of the cloud.

5.4.1.5 Condensation freezing — case 7

The evolution of liquid and ice water contents for condensation freezing considered as only ice nucleation mechanism indicates a significant impact on the dynamics of the cloud (Figure 5.10a). Ice nucleation starts early in the development of the cloud: from 4.2 km of altitude on with a nucleation rate exceeding 1 000 m^{-3}.min^{-1}. However, the ice water content reaches 0.01 g.m^{-3} only when the cloud top reaches 7.1 km., slightly higher than in case 4. Also, as immersion freeing in case 4 only treats droplets larger than 16 µm and condensation freezing only treats droplets smaller than this radius, for a same number of ice nucleating events, the amount of latent heat release in case 4 is larger than in case 7. Therefore, the updraft weakens earlier in the latter case. Also, as the ice crystals were formed at low altitudes, because of the Bergeron–Findeisen process, the hydrometeors participating in the precipitation are larger in case 7 than in cse 4. The combination of those two effects yields a higher ice water content in the downdraft, with an onset of the precipitation in the ice phase at a higher altitude and a 0.5 min earlier (Table 5.3). Furthermore, as some droplets froze at low altitude, because of the riming and Bergeron–Findeisen processes, the droplets in the updraft are smaller, which delays the onset of the precipitation in the liquid phase and reduces the precipitating liquid water content (Table 5.3).

'*Warm*' rainfall peak: The precipitation in the ice phase is initiated earlier in case 7 as in case 4 (0.5 min) but as it occurs at a higher altitude (0.7 km), the first peak of intensity in the rainfall is further delayed[3] (Table 5.2). The higher total water content along the downdraft yields a larger intensity of the first peak of rainfall (Table 5.2 and Figure 5.10b).

Steadier regime: After 48 min of simulation, as was already noticed in case 4, there is a strong downdraft below the iso–zero level (wind speeds up to 15.6 $\mathrm{m.s^{-1}}$), combined with a high liquid water content (up to 1.1 $\mathrm{g.m^{-3}}$) which results in a very high rainfall intensity over 6 minutes (with a peak of 82.7 $\mathrm{mm.h^{-1}}$ at 51.9 min).

Overall, condensation freezing is responsible of the earliest ice nucleation (1 km above cloud base) but at a relatively low rate, so that the ice water content remains lower than 0.01 $\mathrm{g.m^{-3}}$ until the cloud top reaches 7 km. This early nucleation of ice causes a major impact of condensation freezing on precipitation (17.53 mm of rain, +133% with respect to case 1) even though the amount of latent heat release is rather small and has a minimal impact on the dynamics of the updraft.

5.4.2 Mechanisms in competition — case 2

In case 2, all the previously studied mechanisms are considered as active with $r_{\mathrm{IN},lim} = 0.1\,\mu\mathrm{m}$ and $B = 2.9 \cdot 10^{-8}\,\mathrm{cm^{-3}.s^{-1}}$. In Figure 5.11a, the evolution of the cloud in case 2 is a combination of the cases 4, 6 and 7: we observe the cirrus–like ice formation at high altitudes and out of the cloud. In the updraft, the cloud liquid and ice water contents replicate both cases 4 and 7 in two different region: below 6 km, the case 2 cloud water contents are identical to those of case 7 and above 6 km, the cloud water contents are similar to those of case 4 (Table 5.3). This translates also in the onset of precipitation at the altitudes and times indicating an initiation of the precipitation in the liquid phase similar to case 2 and case 7 and in the ice phase, the initiation is similar to that of case 4. In the downdraft, the liquid water content reaches the same value in case 2 as in case 7, whereas the ice water content reaches a value close to that of case 4 (Table 5.3).

'*warm*' rainfall peak: The total water content in case 2 reaches values lower as in both cases 4 and 7, which is a consequence of the low liquid water content of case 7 and the lower ice water content of case 4. As a result, the first peak of intensity in the rainfall is weaker in case 2 than in both cases 4 and 7 and a with a larger delay (Table 5.2) which reflects the later onset of the precipitations.

Steadier regime: Both cases 4 and 7 show a strong second peak of intensity in the rainfall because of the strong downdraft present below the iso–zero line after the first peak of intensity. This second peak is also noticible in case 2. After 47 min of simulation, the liquid water content, as well as the wind below the iso–zero level in case 2 is following closely those of case 4, with a slight increase. However, until 55 min, the liquid water

---

[3] To '*catch up*' on the precipitation of case 4, the fall speed of the hydrometeors would need to be approximately 23 $\mathrm{m.s^{-1}}$, but the terminal velocity of the largest ice particles reaches only 17 $\mathrm{m.s^{-1}}$ and the precipitation starts in a region with an updraft larger than 2 $\mathrm{m.s^{-1}}$.

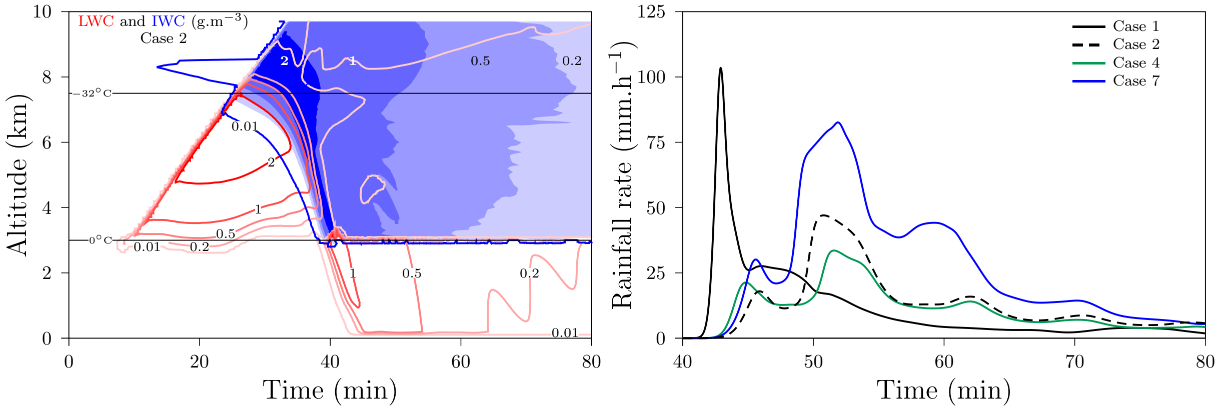

Figure 5.11 – (**a**, left) Liquid water content (g.m^{-3}, red) and ice water content (g.m^{-3}, blue) simulated by DESCAM as a function of altitude and time for the case with all ice nucleation mechanisms active (case 2). (**b**, right) Time evolution of the rainfall rate (mm.h^{-1}) for the only–liquid case (case 1, black continuous), for the all ice processes case (case 2, black dashed), for immersion freezing alone with $B = 2.9 \cdot 10^{-6}\text{cm}^{-3}.\text{s}^{-1}$ (case 4, green) and for condensation freezing alone (case 7, blue).

content in case 2 exceeds by 0.2 g.m^{-3} the liquid water content of case 4. This leads to a higher intensity of the second rainfall peak 47.0 mm.h^{-1}, +40%). The remaining precipitations are very close to that of case 4.

The combination of all the ice nucleation processes lets appear different zones of influence for the different mechanisms: in out–of–cloud regions, deposition nucleation is responsible for a cirrus–like cloud formation at high altitude, condensation freezing dictates the evolution of the cloud at low altitudes, before immersion freezing becomes dominant above 6 km. In the precipitation, the first peak of intensity corresponds to a combination of the effects of condensation and immersion freezing, but the remaining precipitations follow closely those simulated for immersion freezing. Contact freezing and homogeneous nucleation do not seem to be of large importance in the dynamical evolution of the cloud and the resulting precipitations.

These first conclusions will now be addressed and further investigated.

5.5 Analysis & Discussion

In figure 5.12 are displayed the integrated number of ice nucleation events (INNE)[4] as a function of time for the cases 3 to 7 (a) and 2 (b).

Contact freezing is by far the least important of the mechanisms in terms of pristine ice particle formation (Figure 5.12). It becomes active first just above the cloud top during the cloud development in the mixing layer, where the aerosol particles are being activated: some droplets are advected to upper layers and collide with unactivated particles. But in these levels, the ice nucleation rates remain quite small, and it is only as the cloud top reaches higher altitudes that ice nucleation rates become larger than 100 m^{-3}.min^{-1}

---

[4] In the model, for each time step, the number of new ice crystals obtained by ice nucleation for each of the different mechanisms in all the levels is computed and integrated over altitude and time.

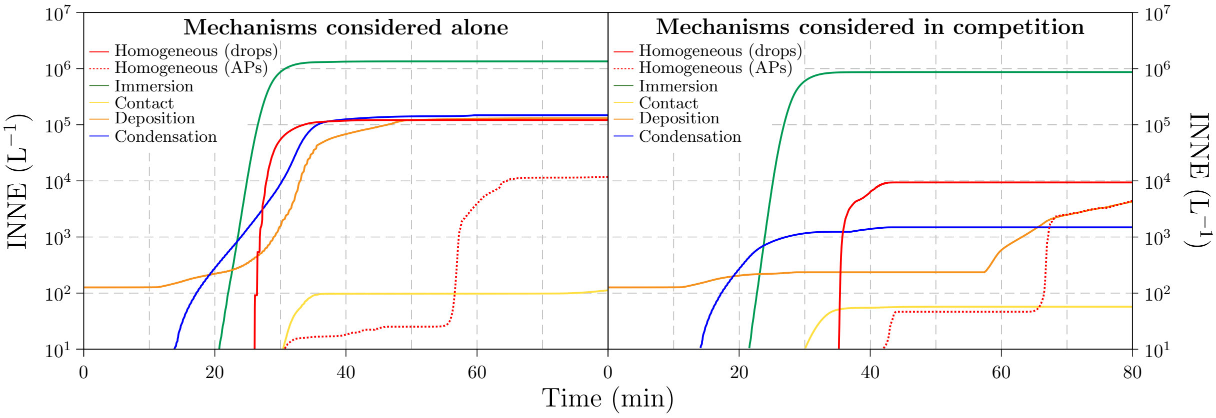

Figure 5.12 – INNE in the column for the different mechanisms taken alone (**a**, left) and in competition (**b**, right), for homogeneous nucleation (red — *on droplets* continuous, on *aerosol particles* dotted), immersion freezing (green), contact freezing (yellow), deposition nucleation (orange) and condensation freezing (blue).

(Figure 5.13b and 5.14b). The high activity of contact freezing in the upper layers of the atmosphere (particularly above 9 km in case 2) is due to the exponential in the parameterization for the number of ice nuclei and the absence of lower limit for the temperature at which it is valid in Meyers et al. (1992). Therefore, at temperatures below −40°C, there are over 2 000 ice nuclei per liter, which means that all aerosol particles larger than 0.1 µm act as an ice nuclei. This might lead to a strong over estimation of the impact of contact freezing and on the number of pristine ice crystals created through this process.
However, this high activity in the very high levels of the atmosphere doesn't translate into any kind of impact of contact freezing on the precipitations system, when considered in competition with other ice nucleation mechanisms: the ice crystals created by contact freezing are produced in the updraft above the precipitation onset level.

The mechanism active the earliest is deposition nucleation: in both cases 2 and 6, this mechanism is responsible for ice nucleation in the first time step (an integrated value of 126.5 L^{-1}). There is little to no ice nucleation in the following 11 min (0.9 L^{-1} new ice crystals, Figure 5.12). This corresponds to the pristine ice formation due to the initial conditions at high altitude in the model (between 7.2 and 8.8 km, some supersaturation with respect to ice is encountered). The ice crystals created account for the number of ice nuclei in the deposition mode according to the Meyers et al. (1992) parameterization over the next time steps as they slowly grow by diffusion of water vapor. When the ice crystals reach a critical size, they sediment to lower levels, allowing for new ice nucleation events in the upper levels. This appears clearly between 11 and 29 min on Figure 5.13b at altitudes between 8.4 and 8.7 km with ice nucleation rates larger than 1 000 m^{-3}.min^{-1}.
When deposition nucleation is considered alone, ice nucleation occurs just above the cloud top during the cloud development in the mixing layer, as was the case for contact freezing. After 24 min, in–cloud deposition nucleation occurs at higher altitudes (above 6.5 km) as the supersaturation with respect to ice increases and high nucleation rates (larger than 10^5 m^{-3}.min^{-1} in the upper levels of the atmosphere). This in–cloud ice nucleation is not to be noticed when all processes are considered. As the number of new ice crystals is calculated by taking into account the number of preexisting ice crystals (5.19), when more than one process is creating ice crystals, $n_{\mathrm{IN,Meyers}}$ becomes smaller than N_i which

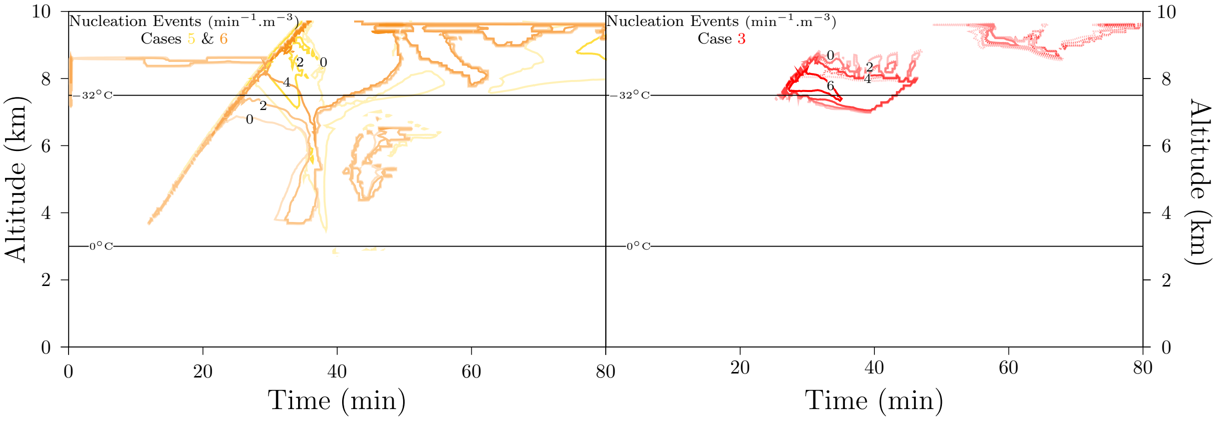

Figure 5.13 – Ice nucleation rate (decimal logarithm of the number of events per cubic meter and per minute) simulated by Descam as a function of altitude and time (**a**, left) for the cases with only deposition nucleation active (orange contours) and only contact freezing active (yellow contours), and (**b**, right) for the case with only homogeneous nucleation active (red contours) on droplets (continuous) and on aerosol particles (dotted).

blocks deposition nucleation (Figures 5.12b and 5.14b).

Homogeneous nucleation acts both on the water contained in the cloud droplets and on the thin water layer of unactivated aerosol particles. This ice nucleation mechanisms becomes active at low temperatures (it is usually assumed that at −38°C all micrometer–sized droplets are frozen, Koop et al., 2000). As the dynamical frame used in this study leads to large droplets in the updraft (up to 1 mm in radius), ice nucleation starts on those large droplets at higher temperatures. In Figure 5.13b, we notice that homogeneous nucleation starts around −32°C (ice nucleation rate larger than $10^6\,\mathrm{min}^{-1}.\mathrm{m}^{-3}$) on these large droplets and freezes rapidly the entire cloud above this level (red continuous curve in Figure 5.12a). As the relative humidity in the cloud at this altitude reaches high values ($RH_w > 102.5\%$), unactivated aerosol particles also take part in homogeneous ice nucleation at temperatures around −40°C (dotted red curve between 30 and 45 min in Figure 5.12a). After 50 min at high altitudes (above 8.5 km) the large aerosol particles entrained from the environmental cylinder freeze homogeneously (dotted red curve between 50 and 65 min in Figure 5.12a).
However, when put in competition with the other ice nucleation mechanisms, homogeneous nucleation doesn't impact the dynamics of the clouds anymore. Its role in the formation of ice is also diminished: the total number of ice crystals due to homogeneous nucleation on droplets is reduced by a factor 13 (Figure 5.12b). This is indicated in Figure 5.14b, where homogeneous nucleation only acts after 35 min on the remaining droplets at altitudes above 6.8 km. Homogeneous nucleation in this part of the cloud acts on all sizes of cloud droplets (as it is also active on aerosol particles) because of the high humidity present ($RH_w > 105\%$). Finally, as was the case when homogeneous nucleation was considered alone, there is some late ice nucleation at high altitude on aerosol particles (after 58 min) but with a limited ice nucleation rate as it is competing with deposition nucleation.

The other droplet–volume dependent parameterization corresponds to immersion freezing. Its efficiency increases with colder temperature and larger droplets, it therefore becomes significant in the higher levels of the atmosphere. In Figure 5.14a, is represented the ice

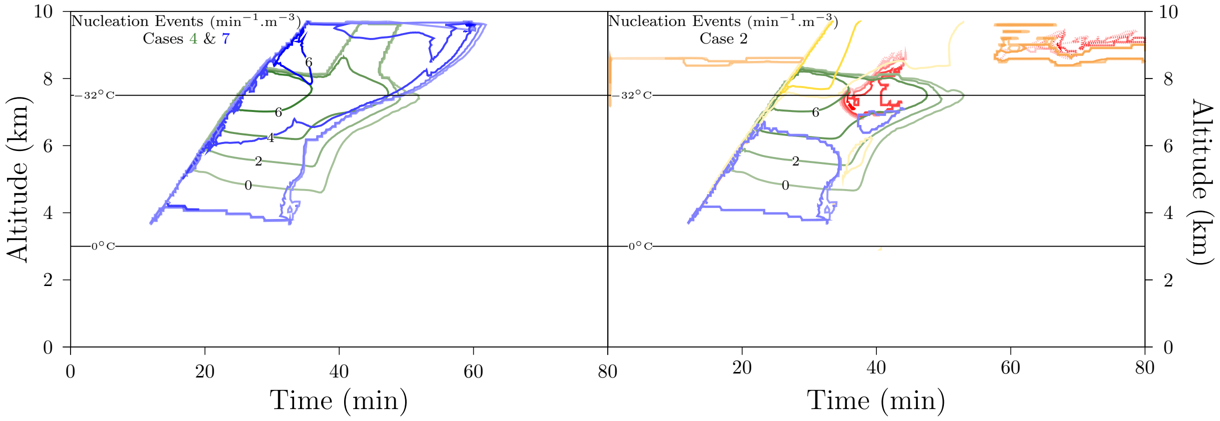

Figure 5.14 – Ice nucleation rate (decimal logarithm of the number of events per cubic meter and per minute) simulated by DESCAM as a function of altitude and time (**a**, left) for the cases with only immersion freezing active (green contours) and condensation freezing active (blue contours) and (**b**, right) for the case with all ice nucleation active (same contours as in Figures 5.13 and 5.14a).

nucleation rate as a function of altitude and time (green contours). Immersion freezing starts around 5.3 km and its intensity steadily increases until the cloud reaches 8 km, at which point the cloud is almost entirely frozen (Figure 5.6a). Also, as the updraft slightly decreases in intensity with time at a constant altitude (Figure 5.7b), the droplets are larger as they reach a same altitude and therefore, the intensity of immersion freezing increases (after 38 min, the 1 min^{-1}.m^{-3} contour is found at 4.6 km).
When considered among the other ice nucleation processes, there is no change in the ice nucleation rates of immersion freezing until the cloud top reaches 8.5 km and immersion freezing clearly dominates ice nucleation in the cloud (Figure 5.12b).

Condensation freezing (blue contours in Figure 5.14) acts on forming droplets and only needs little supersaturation to be active (for a relative humidity with respect to ice of 105% — humidity reached at 4 km, there is 1 ice nuclei per liter) and therefore starts quite early in the cloud development (nucleation rate of 1 000 min^{-1}.m^{-3} at 4.4 km). This early formation of ice in the cloud development plays a major role on the global dynamics of the rainfall (§5.4.1.5), however, even though the ice nucleation rate is quite high at high temperatures, where the other ice nucleation mechanisms based on droplets — immersion freezing and homogeneous nucleation — have very low ice nucleation rates, the impact of condensation freezing on the dynamics in the cloud development is fairly limited. As condensation freezing concentrates on droplets with a radius smaller than 16 µm, the latent heat release due to ice nucleation is very small. Also, even though the riming process immediately starts, the collision between small hydrometeors is rather inefficient (after 20 min of simulation, at 5 km, the spectrum of cloud droplets — Figure not shown — is the same as in the case with no ice nucleation, which indicates a lack of growth of the crystals by riming). Therefore, the latent heat release in the early development of the cloud does not impact the dynamics: it is first after 28 min that the wind speeds in case 7 differ from those of case 1. However, the Bergeron–Findeisen process reduces strongly the growth of the cloud droplets in the updraft which explains the delay in the precipitations, as droplets do not reach the critical size to form the rainfall (in case 1 the precipitations are initiated despite a wind speed larger than 12 m.s^{-1} whereas in case 7, the precipitations are initiated with a wind speed of 8 m.s^{-1}).

When all processes are taken into account, condensation freezing is only active in the lower levels of the cloud (below 6.5 km, Figure 5.14b). As was already noticed for deposition nucleation, the number of new ice crystals is calculated by taking into account the number of preexisting ice crystals, therefore, as immersion freezing starts being very active (nucleation rate larger than $10^4\,\mathrm{min}^{-1}.\mathrm{m}^{-3}$), the maximal number of ice crystals, according to Meyers et al. (1992), is reached. Nevertheless, condensation freezing has a major impact on the precipitation system: as was already the case when condensation freezing is considered as only ice nucleation mechanism, the early formation of ice reduces the growth of the cloud droplets by the Bergeron–Findeisen effect, yielding smaller droplets at the initialization of '*warm*' rainfall (5.9 km and 35 min in case 1 as in case 7 instead of 34.5 min in case 4). But as immersion freezing takes over for the higher altitudes, condensation freezing has very little impact on the initialization of the precipitations in the ice phase.

5.6 Conclusion

In this chapter, we investigated the impact of generic standard ice nucleation parameterizations from the literature for the different ice nucleation mechanisms. These parameterizations do not take into account different types of aerosol particles present in the atmosphere, but as was reported in Hiron and Flossmann (2015) some particularly ice active aerosol populations can play an important role on the development of this type of cloud and on the resulting precipitations.

The results from this chapter show a major importance of heterogeneous ice nucleation, particularly when all ice nucleation mechanisms are taken into account. Unactivated aerosol particles dependent parameterizations (*ie* deposition nucleation and contact freezing) have shown a minimal impact on the dynamics of the cloud and the resulting precipitations when considered in competition with the other ice nucleation mechanisms. They therefore could be neglected in models with less complexity when considering convective clouds.

Homogeneous nucleation does not play a major role in this cloud because of the particular dynamics of the cloud: this mechanism only becomes active at low temperatures and high humidity, at altitudes where heterogeneous nucleation mechanisms have already been significantly active earlier in the cloud development yielding a lower droplet count and a lower relative humidity.

Finally, condensation and immersion freezing are the determining ice nucleation mechanisms. Condensation freezing because of its activity at early in the cloud development, impacting the droplets and ice crystals spectra through the Bergeron–Findeisen process. Immersion freezing because of the high ice nucleation rate and therefore freezing the entire cloud before the homogeneous nucleation level. These results now need to be further investigated, using more recent aerosol–specific parameterizations. Also, there have been discussions in the literature on whether the notion of condensation freezing and its separation from immersion freezing was relevant. Particularly, in experimental literature, immersion freezing and condensation freezing are treated together Hoose and Möhler (2012).

Chapter 6

The DESCAM Model: Explicit Study of Mineral Particles; Ice Nucleating Active Sites Density Representation of Heterogeneous Ice Nucleation

In the previous chapter, the predominant ice nucleation process in the model was linked to the Meyers parameterization. It is commonly used in meso–scale models as it reproduces quite well the observed ice formation at high temperatures and is easy to implement as the parameterization gives directly a number of nucleated ice crystals per unit of volume as a function of supersaturation only. But the parameterization doesn't take into account the aerosol populations providing the ice nuclei, which can be a weakness when discussing future behavior of clouds, formed in a changed atmospheric composition. It is, therefore, useful to change the model in order to use aerosol–dependent ice parameterizations. As was discussed in Part I, there has been a wide focus on ice nucleation by mineral aerosols over the last decade (Hoose and Möhler, 2012).
Also, the most recent studies on ice nucleation use extensively the notion of ice nucleating active sites (INAS) density (DeMott, 1995), an aerosol surface dependent representation of ice nucleation, to account for the properties of the different aerosol particles.
The following chapter focuses on mineral particles and their impact on the CCOPE cloud in DESCAM using INAS density parameterizations.

6.1 Mineral aerosol distributions

Given the wide variability in the studied mineral ice nuclei, the consideration in the model of different mineral aerosol populations is appropriate. Most of the aerosol population measurements offer a global size distribution combined with a number or mass ratio per aerosol type (mineral, soot, biological, ...). As DESCAM uses a bin–detailed microphysics scheme, the choice was made to include specific size distributions for each of the different minerals, which implies that a size specific proportion of the different mineral aerosols is necessary.

	Size mode		
Parameter	Fine ($i = 1$)	Fine ($i = 2$)	Medium ($i = 3$)
R_i (µm)	$4.27 \cdot 10^{-2}$	$1.77 \cdot 10^{-2}$	$3.67 \cdot 10^{-1}$
σ_i	1.898	5.208	1.749
n_i (cm^{-3})			
K–feldspar	65.0	18.0	4.20
Illite	74.5	19.0	4.80
Kaolinite	14.5	3.7	0.95
Quartz	12.2	8.0	2.10

Table 6.1 – Aerosol log–normal distributions parameters for medium to low dust conditions, from Kandler et al. (2009) with R_i the mean particle radius (µm), σ_i a measure of the spectrum width (Jaenicke, 1988) and n_i the integral of the ith log–normal function (cm^{-3})

6.1.1 Observed mineral aerosol distributions

Kandler et al. (2009) studied mineral aerosols in the Atlas mountains in different atmospheric conditions (high and medium to low dust) and measured the total aerosol size distribution, fitted by a combination of log–normal functions, as well as the daily average of the size–resolved volume composition for 10 different minerals in 10 different size bins. The three atmospherically most relevant minerals according to their results are K–feldspar, illite and quartz. kaolinite was also included in this study, despite its lesser abundance in the Kandler et al. (2009) study, because of its importance in different ice nucleation experimental studies (Hoose and Möhler, 2012).

6.1.2 Implementation in DESCAM

Given the size of the largest bin of the aerosol reservoir in DESCAM (7 µm), the largest log–normal function from Kandler et al. (2009) isn't implemented into the model (mean particle radius of 31 µm). The three remaining functions have been adapted for each of the minerals with log–normal distributions (eq. 5.5).

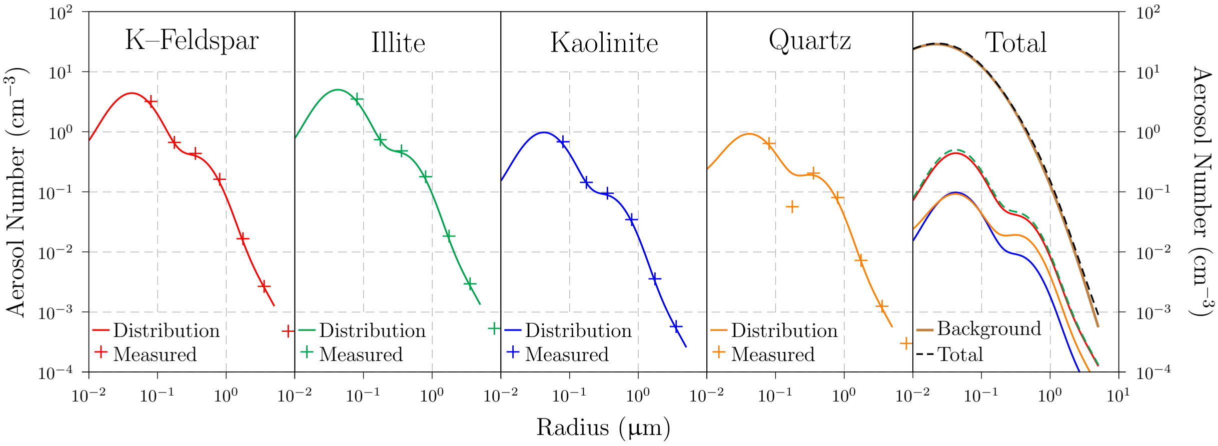

Figure 6.1 – Mineral aerosol size distributions for K–feldspar (red), illite (green), kaolinite (blue) and quartz (orange), crosses corresponding to *in situ* measurements and continuous lines to the log–normal distributions of Table 6.1.

Aerosol particle	κ–value	Source
Background $[(NH_4)_2SO_4]$	$6.1 \cdot 10^{-1}$	Petters and Kreidenweis (2007)
K–feldspar [ATD]	$4.1 \cdot 10^{-3}$	Garimella et al. (2014)
Illite	$7.2 \cdot 10^{-3}$	Garimella et al. (2014)
Kaolinite	$3.3 \cdot 10^{-3}$	Gibson et al. (2007)
Quartz [ATD]	$4.1 \cdot 10^{-3}$	Garimella et al. (2014)

Table 6.2 – κ–values used in DESCAM for the different aerosol particles considered.

The parameter values are presented in Table 6.1 and correspond to the following calculation: the size distributions from medium to low dust conditions found in (Kandler et al., 2009, Table 4) were multiplied by the proportions of each of the four minerals at given particles diameters from Table 1. This yielded number concentrations for each of the minerals (crosses in Figure 6.1) which were used to determine the n_i parameters for each mode and each mineral fitting at best the *in situ* measurements, R_i and σ_i being left unchanged. The size distribution was extrapolated to aerosol radii smaller than 0.5µm.

The high concentration of mineral particles resulting from the *in situ* measurement yield a very high impact of ice nucleation on the cloud development (§6.4.2.2). To allow for a discussion on the relative impact of each mechanism and a comparison with the results from the preliminary study, the results presented in this chapter correspond to mineral concentrations c_0 where the parameters n_i from Table 6.1 where multiplied by a factor 0.1.
This yields a number concentration of mineral aerosols of 22 cm^{-3}. While such a concentration of mineral aerosols can be reached over Europe during large Saharan dust outbreaks (Bangert et al., 2012), the number of mineral aerosol particles are generally rather around 0.1 cm^{-3} (Hande et al., 2015). Such a concentration as well as the implications of changed number concentrations of mineral aerosol particles will be discussed in section 6.4.2.2.

6.1.3 Kappa–Köhler Theory

The interaction of cloud droplets and aerosol particles with water vapor is described by the Köhler theory where both the effects of a curved surface on the saturation vapor pressure (Kelvin effect) and the presence of a solute (Raoult's Law) are taken into account (Köhler, 1936). The term corresponding to Raoult's Law is expressed as follows (Pruppacher and Klett, 1997, eq. 13–27):

$$\alpha_2 = \nu \Phi_a \varepsilon_a \frac{m_a}{\rho_s'' V_d - m_a} \cdot \frac{M_w}{M_a} \simeq \nu \Phi_a \varepsilon_a \frac{m_a}{M_a} \cdot \frac{M_w}{m_w} \tag{6.1}$$

with ν is the total number of ions per dissociating molecule, Φ_a the aerosol molal osmotic coefficient, ε_a the solubility, m_a and m_w the masses of the aerosol particle and of water in the drop respectively, ρ_s'' the density of the aqueous solution drop, V_d the volume of the drop, and M_a and M_w the molar mass of the aerosol particle and of water respectively.
The large number of variables used in this equation makes it difficult to apply when considering several types of aerosol particles. The κ–Köhler Theory (Petters and Kreidenweis, 2007) offers a solution, as it parameterizes Raoult's Law using a single parameter κ called

hygroscopicity parameter, defined through its effect on the water activity of the solution, a_w:

$$\frac{1}{a_w} = 1 + \kappa \frac{V_a}{V_w} \tag{6.2}$$

where V_a is the volume of the dry aerosol particle and V_w the volume of the water in the drop ($V_w = V_d - V_a$).
Also, in the Köhler theory, the water activity is defined by:

$$\frac{1}{a_w} \simeq 1 + \nu \Phi_a \varepsilon_a \frac{n_a}{n_w} \tag{6.3}$$

where n_a and n_w represent the moles of aerosol particles and water respectively. Finally, (6.2)−(6.3) yields:

$$\nu \Phi_a \varepsilon_a \frac{n_a}{n_w} = \kappa \frac{V_a}{V_w} \tag{6.4}$$

Therefore, Raoult's Law (eq. 6.1), using (6.4) becomes:

$$\alpha_2 = \nu \Phi_a \varepsilon_a \frac{m_a}{M_a} \cdot \frac{M_w}{m_w} = \kappa \frac{V_a}{V_w} \tag{6.5}$$

The κ–values for the different minerals were directly taken from the literature when available and are compiled in table 6.2. The κ–values for the background aerosols were assimilated to ammonium sulfate, those for K–feldspar and quartz were assimilated to Arizona Test Dust (ATD).

6.2 INAS densities and nucleation parameterization

The preliminary study of ice nucleation presented in Chapter 5 was using non–aerosol–specific parameterizations for heterogeneous nucleation.
The Meyers et al. (1992) parameterizations used for condensation and contact freezing and for deposition nucleation assumed the number of ice nuclei as a function exclusively of temperature (for contact freezing) or of supersaturation (for condensation freezing and deposition nucleation) and the Bigg (1953) parameterization for immersion freezing was dependent of the temperature and of the droplet volume.
This chapter moves towards aerosol–dependent representations with INAS density parameterizations for the four types of mineral aerosol introduced to DESCAM in section 6.1.

In this study, the parameterizations for immersion and deposition freezing determined in Part I using the cold stage setup are implemented in the model.
As the parameterization from Atkinson et al. (2013) is determined for a wider temperature range and on a larger number of experiments and therefore more reliable than the parameterization proposed in Chapter 3; the Atkinson et al. (2013) parameterization will be used for immersion freezing on K–feldspar in the reference cases.
No parameterization of deposition nucleation on K–feldspar was found in the literature to be implemented. Therefore, the parameterization proposed in Chapter 4 is used for deposition nucleation on K–feldspar in the reference cases. Because of the limitations of this

parameterization pointed out in Chapter 4, the conclusions for deposition nucleation are to consider with caution. For this reason, a sensitivity study using an Arizona Test Dust parameterization (Steinke et al., 2015) is conducted to look into deposition nucleation for dust particles taken as a whole.

6.2.1 New size distributions: Aerosol surface in DESCAM

The original version of DESCAM describes aerosol particles and hydrometeors using six bin–resolved size distributions (*see* Chapter 5): $\mathcal{N}_a$, N_d and N_i representing the number of aerosol particles, droplets and ice crystals respectively (in cm^{-3}) and $\mathcal{M}_a$, $\mathcal{M}_d$ and $\mathcal{M}_i$ representing the total mass of aerosol (in $\mathrm{g.cm}^{-3}$) in the aerosol particles, droplets and ice crystals respectively.

In order to use the INAS density parameterizations for ice nucleation, five new size distributions are necessary: $\mathcal{S}_a$, $\mathcal{S}_d$ and $\mathcal{S}_i$, which represent the total surface of aerosol particles in the aerosol particles, droplets and ice crystals respectively (in $\mu\mathrm{m}^2.\mathrm{cm}^{-1}$) and $\mathcal{N}_d$ and $\mathcal{N}_i$ which represent the total number of aerosol particles in each class of droplets and ice crystals respectively (in cm^{-3}).

Each of the new distributions follows equations similar to those presented in Chapter 5.

6.2.2 Heterogeneous nucleation: INAS densities

The concept of INAS density, defined originally by DeMott (1995), is used extensively in experimental studies to obtain size–independent parameterizations for ice nucleation.

"*The INAS density describes the number of ice nucleating active sites at a certain temperature and supersaturation, normalized by the aerosol surface area. The approach is based on the assumption that the investigated aerosol sample is of uniform composition. Time dependence is not taken into account.*" (Hoose and Möhler, 2012)

The INAS density n_s is defined as follows:

$$f_i = 1 - \exp(-n_s \cdot S_p) \tag{6.6}$$

with f_i the frozen fraction and S_p the mean surface of aerosol particle per hydrometeor (*see* Chapter 1). Therefore the total number of frozen hydrometeors n_{IN} is defined as:

$$n_{\mathrm{IN}} = (N_d + N_i) \cdot [1 - \exp(-n_s \cdot S_p)]$$

This yields the following nucleation rate:

$$\left.\frac{\partial N_i}{\partial t}\right|_{\mathrm{nucl,het}} = \max(0, n_{\mathrm{IN}} - N_i) \cdot \frac{1}{\Delta t} \tag{6.7}$$

6.2.3 Immersion freezing

In the previous chapter, the mechanisms of immersion and condensation freezing were separated and two different parameterizations were used. However, in Part I, it was concluded that immersion and condensation freezing yielded similar results when considered at similar temperatures, therefore, in this modeling study, the same parameterization will be used for the two mechanisms and be only referred to as immersion freezing.

Mineral	Source	$n_{s,imm}(T)$ [μm^{-2}]	T^o range (K)
K–feldspar	Atkinson et al. (2013)	$10^{-8} \cdot \exp\left[-1.038 \cdot \max(T, 248) + 275.26\right]$	$T < 268$
	This work, Chapter 3	$10^{-8} \cdot \exp[10.5 \cdot \exp(-\exp[0.345 \cdot (T - 251.95)]) + 6.05]$	$T \leq 253$
Illite	Hiranuma et al. (2015)	$10^{-12} \cdot \exp[25.75 \cdot \exp(-\exp[0.13 \cdot \max(-37, T - 255.98) + 17.17]) + 3.34]$	$T \leq 262.15$
Kaolinite	Wex et al. (2014)	$10^{-12} \cdot \exp\left[-0.91 \cdot \max(-35, T - 273.15) - 6.67\right]$	$T \leq 247.15$
Quartz	Atkinson et al. (2013)	$10^{-2} \cdot \exp[-0.7676 \cdot (T - 244)]$	$T \in [244, 247]$
		$10^{-2} \cdot \exp[1.792 - .5973 \cdot (T - 241)]$	$T \in [241, 244]$
		$10^{-2} \cdot \exp[3.689 - .3162 \cdot (T - 235)]$	$T \in [235, 241]$
		$10^{-2} \cdot \exp[3.689]$	$T < 235$

Table 6.3 – Ice nucleating active site density $n_{s,\mathrm{imm}}$ (in μm^{-2}) parameterizations for immersion freezing for K–feldspar, illite, kaolinite and quartz. The Atkinson et al. (2013) parameterization for K–feldspar is used as main parameterization and the parameterization derived from Chapter 3 is used later in a sensitivity study.

In the preliminary study, the size limit to separate condensation from immersion freezing was set to 16 µm as it reflects the separation of the cloud drop category in bulk microphysics models.

To implement INAS densities for ice nucleation in DESCAM, new size distributions for the number of aerosol particle per droplet have been added (§6.2.1).

In Figure 6.2, is represented the number of aerosol particles per droplet as a function of the droplet radius for different time steps of the updraft (every minute from 17 to 34 min) at the altitude of 5 km. We observe here two very distinct regimes: one for droplets smaller than 16 µm, freshly formed droplets where there is only one aerosol particle per droplet and one for droplets larger than 16 µm, coalesced droplets where the number of aerosol particles per droplet is proportional to the droplet volume.

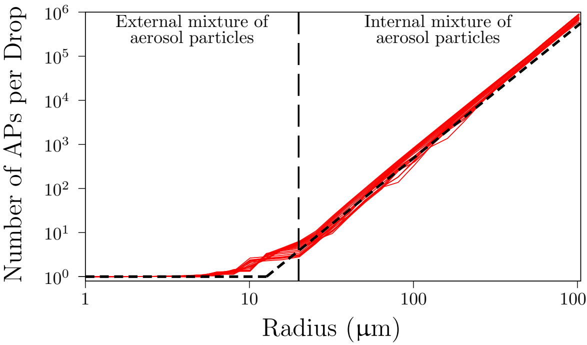

Figure 6.2 – Number of aerosols particles per droplet as a function of the radius at 5 km altitude for integration times between 17 and 34 min

We can divide the immersion freezing mechanism into two different computing schemes with the separation radius being the same as between condensation and immersion freezing in the previous chapter: for droplets smaller than 16 µm, we assume an external mixture of the different mineral components, the aerosol surface is therefore counted per aerosol particles, whereas for droplets larger than 16 µm, we assume en internal mixture, the aerosol surface is therefore counted per droplet and assumed evenly distributed among all droplets in the considered size bin. In the following sections, the two computing schemes will be presented as a whole.

Finally, the choice was made to treat each of the different size bins separately: the frozen fraction predicted by the INAS density parameterization is only computed on droplets and ice crystals of equal masses. The immersion freezing mechanism is therefore treated

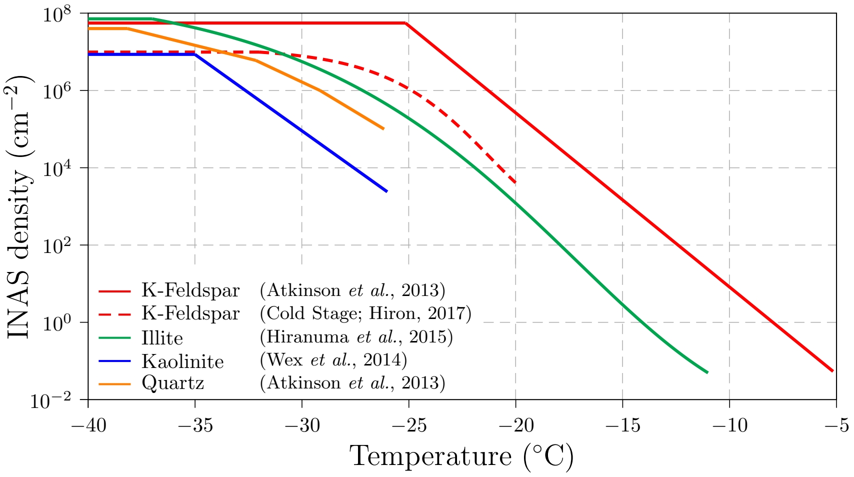

Figure 6.3 – INAS density parameterizations as a function of temperature for immersion freezing for K–feldspar (red), illite (green), kaolinite (blue) and quartz (orange).

as follows:

$$\begin{cases} n_{\text{IN,imm}}(j,kt) = [\mathcal{N}_d(j,kt) + \mathcal{N}_i(j,kt)] \cdot [1 - \alpha_{\text{imm}}(j,kt)] & \text{if} \quad j(r_d) \leq 16\,\mu\text{m} \\ n^{\dagger}_{\text{IN,imm}}(j) \quad = [N_d(j) + N_i(j)] \cdot \left[1 - \prod_{kt} \alpha^{\dagger}_{\text{imm}}(j,kt)\right] & \text{otherwise} \end{cases} \tag{6.8}$$

where j and kt correspond to the size bin and considered aerosol type respectively, and α_{imm} the nucleation ratio, which is defined as:

$$\begin{cases} \alpha_{\text{imm}}(j,kt) = \exp\left(-n_{s,\text{imm}}(T,kt) \cdot \dfrac{\mathcal{S}_d(j,kt) + \mathcal{S}_i(j,kt)}{\mathcal{N}_d(j,kt) + \mathcal{N}_i(j,kt)}\right) & \text{if} \quad j(r_d) \leq 16\,\mu\text{m} \\ \alpha^{\dagger}_{\text{imm}}(j,kt) = \exp\left(-n_{s,\text{imm}}(T,kt) \cdot \dfrac{\mathcal{S}_d(j,kt) + \mathcal{S}_i(j,kt)}{N_d(j) + N_i(j)}\right) & \text{otherwise} \end{cases} \tag{6.9}$$

with $n_{s,\text{imm}}$ the INAS density in the immersion mode for aerosol type kt at the temperature T. The parameterizations of $n_{s,\text{imm}}$ used for immersion freezing are found in Table 6.3. This yields the number of new ice crystals:

$$\left.\frac{\partial N_i}{\partial t}\right|_{\text{nucl,imm}}(j) = \begin{cases} \max\left[0, \sum_{kt} n_{IN,\text{imm}}(j,kt) - N_i(j)\right] \cdot \dfrac{1}{\Delta t} & \text{if} \quad j(r_d) \leq 16\,\mu\text{m} \\ \max\left[0, n^{\dagger}_{IN,\text{imm}}(j) - N_i(j)\right] \cdot \dfrac{1}{\Delta t} & \text{otherwise} \end{cases} \tag{6.10}$$

The mass and surface size distributions are treated using the similar equations. The impact of the assumptions in the treatment of immersion freezing on the dynamical evolution of the cloud will be discussed in §6.4.2.3.

6.2.4 Contact freezing

The contact freezing rate is calculated using contact ice nucleating active sites (CINAS) densities (Hoffmann, 2015), the combination of equations 4.7, 4.10 and 5.11 therein yield:

$$\ln[1 - f_i(t)] = -n_c \cdot e_c \cdot t = -n_c \cdot n_{s,\text{cont}} \cdot S_p \cdot t \tag{6.11}$$

Mineral	Source	$n_{s,cont}(T)$ [µm^{-2}]	T^o range (K)
K–feldspar	Hoffmann (2015)	$0.8174 \cdot \exp[(250.52 - T)/1.61]$	$T \in [250.52, 254.06]$
		$0.8174 \cdot \exp[\max(-7.78, 250.52 - T)/21.73]$	$T < 250.52$
Illite	Hoffmann (2015)	$0.0269 \cdot \exp[-\max(0, T - 238.83)/1.94]$	$T < 243.22$
Kaolinite	Hoffmann (2015)	$0.3900 \cdot \exp[-\max(0, T - 239.25)/2.10]$	$T < 242.02$

Table 6.4 – Ice nucleating active site density parameterizations $n_{s,\mathrm{cont}}$ (in µm^{-2}) for contact freezing for K–feldspar, illite and kaolinite.

with n_c the collection rate of aerosol particles by the droplets, e_c the probability of freezing, $n_{s,\mathrm{cont}}$ the CINAS density.
When deriving this equation by the time t, and with $f_i \ll 1$, this yields an INP portion of:

$$\Gamma_{\mathrm{cont}}(r_a, kt) = n_{s,\mathrm{cont}}(T, kt) \cdot \frac{\mathcal{S}_a(r_a, kt)}{\mathcal{N}_a(r_a, kt)} \cdot \tag{6.12}$$

The parameterizations used for $n_{s,\mathrm{cont}}$ are summarized in Table 6.4.

6.2.5 Deposition nucleation

For the parameterization of deposition nucleation, a bin separated treatment is difficult given that there is no mass equivalence between aerosol particles and ice crystals bins. Therefore, the calculation of the fraction ratio is taking into account the whole aerosol particles and ice crystals spectra. This yields:

$$\mathrm{d}n_{i,\mathrm{dep}}(kt) = \max\left[0, \left(\sum_{r_a > r_{lim}} \mathcal{N}_a(r_a, kt) + \sum_{r_i} \mathcal{N}_i(r_i, kt)\right) \cdot [1 - \widetilde{\alpha}_{\mathrm{dep}}(kt)] - \sum_{r_i} \mathcal{N}_i(r_i, kt)\right] \tag{6.13}$$

where $\widetilde{\alpha}_{\mathrm{dep}}$ is given by the INAS density:

$$\widetilde{\alpha}_{\mathrm{dep}}(kt) = \exp\left(-n_{s,\mathrm{dep}}(kt) \cdot \frac{\sum\limits_{r_a > r_{lim}} \mathcal{S}_a(r_a, kt) + \sum\limits_{r_i} \mathcal{S}_i(r_i, kt)}{\sum\limits_{r_a > r_{lim}} \mathcal{N}_a(r_a, kt) + \sum\limits_{r_i} \mathcal{N}_i(r_i, kt)}\right) \tag{6.14}$$

The number of new ice crystals for each aerosol type $\mathrm{d}n_{\mathrm{IN,dep}}(kt)$ is then redistributed upon the different aerosol particle bins. To keep the size dependence of the INAS density approach, the repartitioning is weighted using the surface per aerosol particle in each of the aerosol particle bins:

$$\mathrm{d}n^*_{i,\mathrm{dep}}(r_a, kt) = \mathcal{N}_a(r_a, kt) \cdot \left[1 - \exp\left(-n_{s,\mathrm{dep}}(kt) \cdot \frac{\mathcal{S}_a(r_a, kt)}{\mathcal{N}_a(r_a, kt)}\right)\right] \tag{6.15}$$

which yields:

$$\left.\frac{\partial N_i}{\partial t}\right|_{\mathrm{nucl,dep}}(r_{i,eq}) = \sum_{kt} \mathcal{N}_{i,\mathrm{dep}}(r_{i,eq}, kt) = \sum_{kt} \mathrm{d}n_{i,dep}(kt) \cdot \frac{\mathrm{d}n^*_{i,\mathrm{dep}}(r_a, kt)}{\sum\limits_{r_a > r_{lim}} \mathrm{d}n^*_{i,\mathrm{dep}}(r_a, kt)} \cdot \frac{1}{\Delta t} \tag{6.16}$$

where $r_{i,eq} = 1$ µm if $r_a < 1$µm and $r_{i,eq} = \sqrt[3]{\rho_i} r_a$ otherwise.

Mineral	Source	$n_{s,dep}(T, s_{v,i})$ [μm^{-2}]	T^o range (K)
K–feldspar	This work, Chapter 4	$10^{-8} \cdot \exp[10.5 - 0.18 \cdot \max(-30, T - 273.15)]$ $\cdot [1 - \exp(-2 \cdot (s_{v,i} - 1.27))]$	$T < 253, s_{v,i} \geq 127\%$
Illite	Wheeler and Bertram (2012)	$1.46 \cdot 10^{-2} \cdot (s_{v,i} + 0.0585)^2$	$T < 246,\ s_{v,i} \geq 100\%$
Kaolinite	Wex et al. (2014)	$1.27 \cdot 10^{-15} \cdot \exp\left[-0.91 \cdot (T - 273.15 + \Delta T_{\text{het}}(a_w))\right]$ where $\Delta T_{\text{het}}(a_w) = 3.162 \cdot \left(-\frac{\ln[a_w^i(T)]}{M_w}\right)$	$T < 240,\ s_{v,w} \geq 85\%$
ATD	Steinke et al. (2015)	$1.88 \cdot 10^{-7} \cdot \exp\left[-0.2659 \cdot (273 - T) + 100 \cdot s_{v,i}\right]$	$T < 250,\ s_{v,i} \geq 100\%$

Table 6.5 – Ice nucleating active site density parameterizations $n_{s,\text{dep}}$ (in μm^{-2}) for deposition nucleation for K–feldspar, illite, kaolinite and Arizona Test Dust, which is used in a sensitivity study.

This calculation method causes some artificial ice nucleation. As the ice fraction ratio is calculated for all the aerosol particles contained in the ice crystals in the model, there is no differentiation between pristine deposition nucleation ice crystals and ice crystals formed through other ice formation processes or riming, this means that in–cloud computation of deposition nucleation is disturbed by the increased number of ice crystals (if all processes are taken into account).

The large aerosol particles being easily activated, the mean aerosol surface per particle in–cloud is larger than the mean aerosol surface per particle out–of–cloud leading to a decreased value of α and therefore an increased value of $\mathrm{d}\mathcal{N}_{i,\text{dep}}(r_a, kt)$ as a function of particle size.

The chosen solution here is to exclude in–cloud deposition nucleation, with in–cloud being defined as:

$$\begin{cases} LWC + IWC > 0.1\,\text{g.cm}^{-3} \\ N_d > 10\,\text{L}^{-1} \end{cases}$$

The impact of the in–cloud assumption is discussed in §6.11.

The parameterizations used for deposition nucleation are summarized in Table 6.5.

6.3 Results

The same principles as for the preliminary study from the previous chapter are used here. In order to assess the importance of the different mechanisms and of the different minerals on the dynamics of the cloud, the total amount of ice produced and the resulting precipitation, six cases were taken into account, with the same referencing as in the preliminary study: no ice nucleation (case 1), all ice nucleation mechanisms active (case 2) and the different mechanisms considered separately: homogeneous nucleation only (case 3), immersion freezing only (case 4), contact freezing only (case 5) and deposition nucleation only (case 6).

Each of the heterogeneous cases was tested in two different configurations: with only one mineral as INP (cases A [K–feldspar], B [illite], C [kaolinite] and D [quartz]) and when all minerals were considered together (case E).

The list of the case studies, the results for the cumulative rain and the properties of the first peak of intensities of the rainfall can be found in Table 6.6.

Case	Description	Rain	± Var.	First rain peak	
				Int. (mm.h^{-1})	Time (min)
Case 1	No ice nucleation mechanisms active	7.57	—	103.2	43.0
Case 2	All ice nucleation mechanisms active:				
	2–A — INP: K–feldspar	6.25	− 17 %	22.3	44.7
	2–B — INP: Illite	8.47	+ 15 %	50.5	43.6
	2–C — INP: Kaolinite	5.37	− 29 %	71.6	43.2
	2–D — INP: Quartz	6.12	− 19 %	65.1	43.3
	2–E — INP: All minerals	6.25	− 17 %	22.3	44.7
Case 3	Only homogeneous nucleation active	5.33	− 30 %	71.7	43.2
Case 4	Only immersion freezing active:				
	4–A — INP: K–feldspar	6.65	− 12 %	22.3	44.7
	4–B — INP: Illite	12.69	+ 6 %	50.6	43.6
	4–C — INP: Kaolinite	9.62	+ 27 %	83.7	43.2
	4–D — INP: Quartz	12.34	+ 63 %	67.2	43.3
	4–E — INP: All minerals	6.62	− 13 %	22.3	44.7
Case 5	Only contact freezing active:				
	5–A — INP: K–feldspar	8.64	+ 14 %	106.6	43.1
	5–B — INP: Illite	7.81	+ 3 %	104.5	43.0
	5–C — INP: Kaolinite	8.07	+ 7 %	105.8	43.0
	5–E — INP: All minerals	8.62	+ 14 %	106.4	43.1
Case 6	Only deposition nucleation active:				
	6–A — INP: K–feldspar	7.57	± 0 %	103.2	43.0
	6–B — INP: Illite	7.52	− 1 %	103.3	43.0
	6–C — INP: Kaolinite	7.57	± 0 %	103.2	43.0
	6–E — INP: All minerals	7.54	− 0 %	103.2	43.0

Table 6.6 – List of case studies and the results for the cumulative rain on the ground (mm) on the ground as well as the properties of the first peak in the rainfall rate (intensity — Int. — in mm.h^{-1} and the time of simulation at which it occurs).

6.3.1 ‘*Reference*’ case: no ice nucleation mechanism — case 1

Following the same methodology as in the previous chapter, in order to assess the impact of ice nucleation by minerals on the development of a convective cloud and on the precipitations, the results are compared to a ‘*reference*’ case where only warm microphysics processes are taken into account. The inclusion of the mineral aerosol particles to the modeled atmosphere has a minimal impact on the results observed in this ‘*reference*’ case 1 when compared to the *no ice nucleation mechanisms active* from the previous chapter: the first peak of intensity in the rainfall is almost identical (103.2 mm.h^{-1} after 43 min instead of 103.4 mm.h^{-1} after 42.9 min) and the final amount of precipitations to the ground is increased by 1% (7.57 mm instead of 7.52 mm). The dynamics of the cloud and its visualizations presented in the previous chapter (total water content, precipitation water content and vertical wind) reflect these close similarities between the two cases and are therefore not reproduced here. The impact of the concentration of aerosol particles will be further discussed in §6.9.

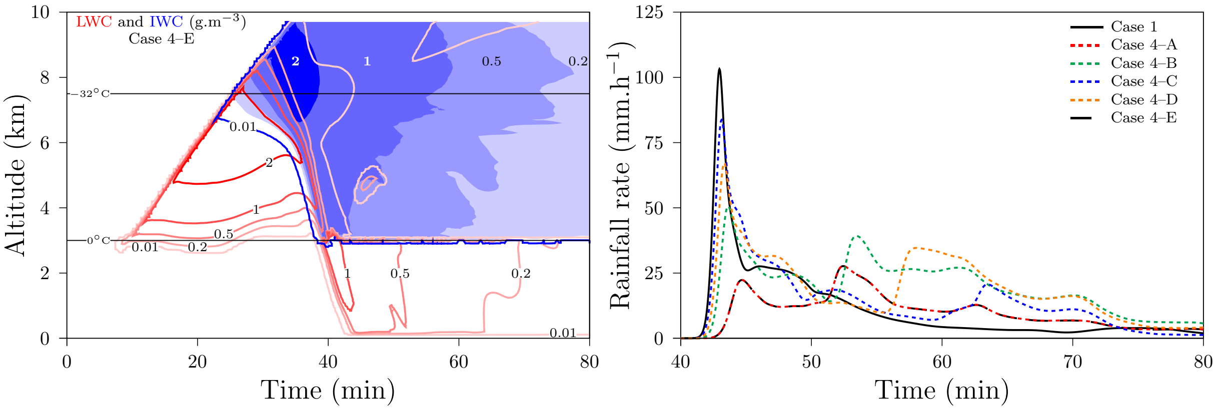

Figure 6.4 – (**a**, left) Liquid water content (g.m^{-3}, red) and ice water content (g.m^{-3}, blue) simulated by DESCAM as a function of altitude and time for the case with only immersion freezing active with all minerals as INP (case 4–E). (**b**, right) Time evolution of the rainfall rate (mm.h^{-1}) for the only–liquid case (case 1, black continuous) and the immersion freezing only cases for K–feldspar (case 4–A, red short dashed), illite (case 4–B, green short dashed), kaolinite (case 4–C, blue short dashed), quartz (case 4–D, orange short dashed) and all minerals (case 4–E, black long dashed).

6.3.2 Independently studied mechanisms

6.3.2.1 Homogeneous Nucleation — case 3

As for case 1, the results for homogeneous nucleation when mineral aerosol particles are taken into account are only slightly different from those of the previous chapter (1% decrease in the total amount of rain and 1% increase in intensity of the first peak of rainfall, Table 6.6).

6.3.2.2 Immersion Freezing — case 4

In Figure 6.4a are displayed the liquid and ice water contents for the case where only immersion freezing is active with K–feldspar, illite, kaolinite and quartz considered as INP (case 4–E). As was previously the case in the preliminary study from Chapter 5, the vertical development is marginally impacted by ice nucleation: the cloud top reaches the homogeneous nucleation level after 25.3 min in case 4–E, as was the case for case 1. The ice nucleation process starts after 17.3 min of simulation ice nucleation rate above 1 min^{-1}.m^{-3}), when the cloud top reaches an altitude of 4.9 km at temperatures around −13°C and steadily intensifies as the cloud develops (ice nucleation rate above 1 000 min^{-1}.m^{-3} at altitudes above 5.8 km). Through the ice nucleation, latent heat is released and the updraft is strengthened at higher altitudes. Furthermore, as more ice crystals are created early in the cloud development, the hydrometeors reach smaller sizes as in case 3. The combination of the increased latent heat release and smaller ice crystals lead to a delay of the precipitation onset in the liquid as well as in the ice phase as had already been pointed out in the preliminary study.

‘*Warm*’ rainfall peak: the delay in precipitation onset leads to a delay of 1.7 min on the ‘*warm*’ rainfall peak. Furthermore, as the hydrometeors reach smaller sizes and the updraft is strengthened, the downward motion of the hydrometeors is spread over a longer time. Therefore, the total precipitation water content reach much lower values than

Case	Precipitation onset (WC> 0.2g.m^{-3})				Maximal water contents		
	Droplets		Ice crystals				
	Altitude (km)	Time (min)	Altitude (km)	Time (min)	LWC (g.m^{-3})	IWC (g.m^{-3})	TWC (g.m^{-3})
Case 1	8.3	31.3	—	—	8.9	—	8.9
Case 2–E	5.9	34.4	6.6	33.9	1.8	1.9	2.8
Case 3	7.2	32.7	7.4	32.5	4.6	1.8	5.4
Case 4–E	5.9	34.4	6.6	33.9	1.8	1.9	2.8
Case 5–E	8.3	31.6	8.3	31.5	5.5	5.3	7.5
Case 6–E	8.3	31.3	—	—	8.9	$3 \cdot 10^{-3}$	8.9

Table 6.7 – Properties of the precipitation system for different cases: the altitude (in km) and time (in min) at which the precipitation starts (the arbitrary reference point chosen is a precipitating liquid, respectively ice, water content larger than 0.2 g.m^{-3}) and the maximal water contents (in g.m^{-3}) in the precipitation system above the iso–zero level.

in cases 1 and 3 yielding a largely reduced '*warm*' rainfall peak (78%, Figure 6.4b, Table 6.6).

Steadier regime: after 47.7 min, a strong downdraft starts to develop below the iso–zero level as had already been noticed in the preliminary study (*see* §5.4.1.2 for the analysis of this downdraft). This downdraft yields a second peak of 27.7 mm.h^{-1} in the rainfall rate after 52.4 min of simulation.

Even though the mechanistic principle in the parameterization used in this study (INAS density representation of ice nucleation on droplets of all sizes, time independent parameterization) is different from that of the preliminary study (volume and time dependence of ice nucleation on droplets larger than 16 µm), the results obtained in both studies for immersion freezing are quite similar: same maximal total precipitation water contents, similar peaks in the precipitations and similar overall dynamics.

Minerals considered separately: When K–feldspar is considered alone (case 4–A),the results are comparable to those of case 4–E: there is a variation of less than 1% in the total amount of precipitation and the two rainfall rates are almost identical (red continuous and black long dashed curves in Figure 6.4b). K–feldspar dominates the immersion freezing mechanism, as was expected after the conclusions of the preliminary study: this mineral is ice active at the warmest temperature among the four mineral considered and is the most present of the minerals in the initial size distributions of aerosol particles.
The other three minerals are responsible for less ice formation during the updraft, yielding an earlier onset of the precipitations and an earlier '*warm*' rainfall peak (Table 6.6. Therefore, for cases 4–B, C and D, as the considered minerals (illite, kaolinite and quartz) have lower ice nucleation efficiencies, the lower number of ice crystals with respect to cases 4–A and 4–E lead to higher total water contents in the downdraft (values up to 4.1 g.m^{-3}, 6.2 g.m^{-3} and 5.0 g.m^{-3} for illite, kaolinite and quartz respectively).
It is noteworthy that as the ice nucleation starts at warmer temperatures, the intensity of the '*warm*' rainfall peak decreases: K–feldspar provides the warmest ice nucleation and

yields the smallest peak whereas kaolinite starts forming ice crystals at the highest altitude (7 km) and has therefore the largest '*warm*' rainfall peak.
The total amount of precipitation shows an increase in all three cases with a higher rainfall rate after the first '*warm*' rainfall peak (12.69 mm for illite, 9.62 mm for kaolinite and 12.34 mm for quartz). This increase is the combination of two factors: the '*warm*' rainfall peak is not as reduced as in case 4–A and E (particularly for case 4–C) and a longer and stronger '*cold*' rainfall part of the precipitation

6.3.2.3 Contact Freezing — case 5

In Figure 6.5a are displayed the liquid and ice water contents for the case where only contact freezing ($r_{lim} = 0.1$ µm) is active with K–feldspar, illite and kaolinite considered as INP (case 5–E). The initial development of the cloud is not modified by the ice nucleation process: only a small amount of ice crystals are nucleated in the updraft at the cloud top in the mixing layer where unactivated aerosol particles are in presence of droplets. This ice formation has a minimal impact on the dynamics of the cloud as the precipitations onset is found at the same altitude, only slightly delayed (by about 15 seconds, Table 6.7). It is only in the downdraft that ice nucleation becomes significant in the cloud: at the precipitation onset (at an altitude of 8.3 km after 31.5 min), the ice nucleation rate reaches 100 $\text{min}^{-1}.\text{m}^{-3}$, mainly concentrated on the large droplets. Indeed, in this region where both cloud and precipitating hydrometeors coexist, the precipitating ice water content increases much more rapidly than the cloud ice water content. The large precipitating ice crystal formed collect large amount of droplets in the downdraft which leads to a large ice water content through the riming process (5.3 g.m^{-3}, the highest precipitating ice water content of all considered cases).

'*Warm*' rainfall peak: as there was only a slight delay in the precipitation onset, there is also a very small delay in the observation of the first peak in the rainfall rate. Furthermore, the melting of the large precipitating ice water content at the iso–zero level is responsible for an increased downdraft in the lower altitudes of the modeled atmosphere with respect to the '*reference*' case 1. Therefore, even though there is a smaller total precipitating water content in case 5–E, the intensity of the first peak is slightly larger than in case 1 and takes place over a larger time span (Figure 6.5b).

Steadier regime: after the first peak in rainfall, a small downdraft develops below the iso–zero level, weaker (by 2 m.s^{-1}) than what had been noticed in the preliminary study. More importantly, in the lower levels of the modeled atmosphere (below 2 km of altitude), there is rather a slight updraft (wind speeds around 2 m.s^{-1}), as in case 1. Therefore, after 50 min of simulation, the rainfall rate in case 5–E is similar to that of case 1, with no second peak of intensity.

The total amount of precipitation in case 5–E shows an increase of 14% with respect to case 1. This increase is mainly due to the higher intensity and time span of the precipitation peak.
In the preliminary study, the Meyers et al. (1992) parameterization for contact freezing was extrapolated for temperatures below −2°C, increasing exponentially with decreasing

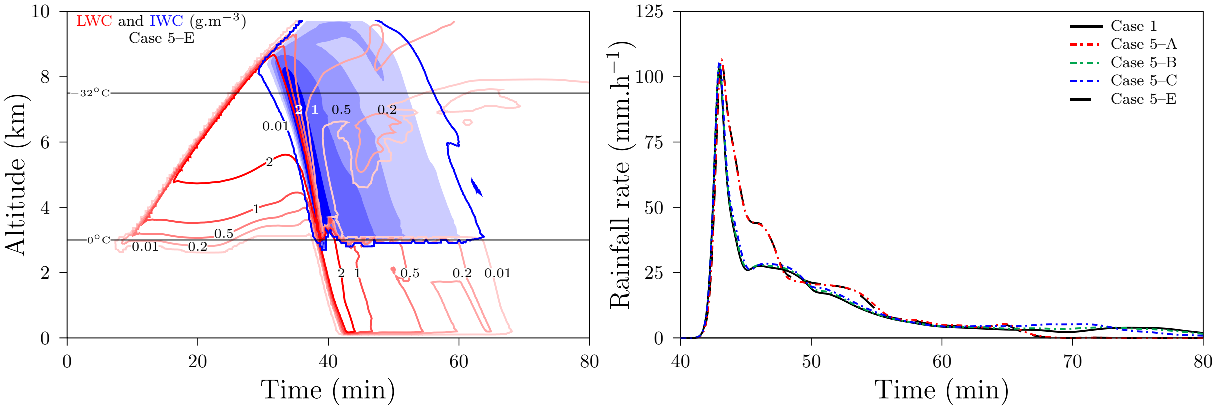

Figure 6.5 – (**a**, left) Liquid water content (g.m^{-3}, red) and ice water content (g.m^{-3}, blue) simulated by DESCAM as a function of altitude and time for the case with only contact freezing active with all minerals as INP (case 5–E). (**b**, right) Time evolution of the rainfall rate (mm.h^{-1}) for the only–liquid case (case 1, continuous), the contact freezing only cases with $r_{\mathrm{IN},lim} = 0.1\mu$m for K–feldspar (case 5–A, red dotted–dashed), illite (case 5–B, green dotted–dashed), kaolinite (case 5–C, blue dotted–dashed) and all minerals (case 5–E, black long dashed).

temperature. The results of Hoffmann (2015) have shown that for lower temperatures, the contact freezing probability — and therefore the INAS density — tends to reach a plateau. Therefore, for temperatures below the last experimental point of each of the experiments used to determine the INAS density parameterization for contact freezing, $n_{s,\mathrm{cont}}$ was assumed constant. Further more, the maximum temperature for contact freezing in the current study is of −19°C, limiting the range of altitudes at which contact freezing can impact the evolution of the cloud.

The smaller impact of the contact freezing mechanism in this chapter when compared to the preliminary study of Chapter 5 is in large parts due to those limitations.

The increase of the lower limit on the size of aerosol particles that can act as ice nuclei from 0.1 µm to 0.5 µm reduces the impact of contact freezing with a cumulative rain of 7.0 mm and an intensity of the first peak in rainfall rate of 101 mm.h^{-1} after 43.0 min. This decrease in the impact of contact freezing with a larger $r_{\mathrm{IN},lim}$ had already been pointed out in the preliminary study and was to be expected with the INAS density representation of ice nucleation. However, the difference between the two values of $r_{\mathrm{IN},lim}$ is smaller than was the case in Chapter 5 as the larger aerosol particles have a larger surface and therefore a higher ice nucleating efficiency: by increasing $r_{\mathrm{IN},lim}$, only the less ice active particles have been eliminated from the contact freezing mechanism.

Minerals considered separately: as was already the case for immersion freezing, the sensitivity study in which K–feldspar is the only ice active mineral shows a result very close to those of case 5–E (same precipitation onset, maximal precipitating water contents and rainfall rate). Here again, K–feldspar is the most ice active of the three considered minerals (no parameterization was found for quartz) in the contact freezing mode, and therefore dominates the ice nucleation by this mechanism.

The sensitivity studies for illite and kaolinite showed lower maximal precipitating ice water contents (0.7 and 1.7 g.m^{-3} respectively) in coherence with their lower ice nucleation efficiency, yielding higher maximal precipitating total water contents, with values closer to that of case 1 (8.8 and 8.6 g.m^{-3} respectively), which results in smaller intensities in the

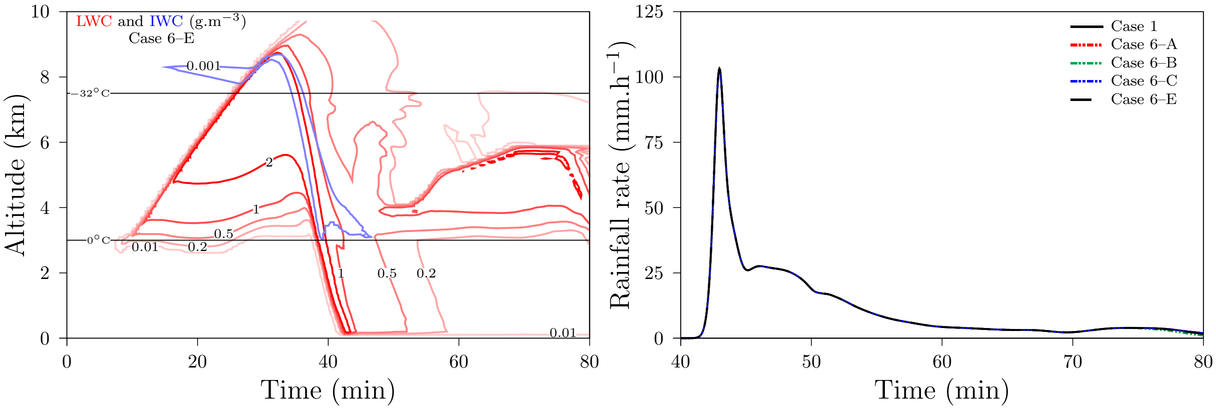

Figure 6.6 – (**a**, left) Liquid water content (g.m^{-3}, red) and ice water content (g.m^{-3}, blue) simulated by DESCAM as a function of altitude and time for the case with only deposition nucleation active with all minerals as INP (case 6–E). (**b**, right) Time evolution of the rainfall rate (mm.h^{-1}) for the only–liquid case (case 1, continuous) and the deposition only cases for K–feldspar (case 6–A, red double dotted–dashed), illite (case 6–B, green double dotted–dashed), kaolinite (case 6–C, blue double dotted–dashed) and all minerals (case 6–E, black long dashed) on top of each other.

first '*warm*' rainfall peak and more importantly, shorter peaks (over the same time span as for case 1, Figure 6.5b). Therefore, the variation in terms of total amount of precipitation is minimal for these two cases: 1% for case 5–B and 0% for case 5–C.

6.3.2.4 Deposition nucleation — case 6

In Figure 6.6a are displayed the liquid and ice water contents for the case where only deposition nucleation ($r_{\mathrm{IN},lim} = 0.1\,\mu\mathrm{m}$) is active with K–feldspar, illite and kaolinite considered as INP (case 6–E). The overall dynamics of the cloud is identical to the one of case 1 to the slight difference of a very small ice water content, reaching values up to 0.003 g.m^{-3}, forming out of cloud at high altitude (around 8 km, Figure 6.6a) with ice nucleation rates reaching 100 m^{-3}.min^{-1}. This early out–of–cloud ice formation corresponds to deposition nucleation on mineral particles, as observed during *in situ* measurement by Cziczo et al. (2013). The formed crystals are present in small amounts and are later integrated to the cloud but their number concentration is too low to observe an intense riming process along the downdraft. The precipitation onset and maximal precipitating water contents in this case 6–E are the same as for case 1.
In this case study, no deposition ice nucleation occurs in–cloud, which might diminish the impact of this mechanism on the dynamics. This will be discussed, using the Arizona Test Dust parameterization from Steinke et al. (2015) in §6.4.2.4.

Precipitations to the ground: the negligible impact of deposition nucleation on the dynamics of the cloud and the very small precipitating ice water content results in an almost unchanged rainfall rate with respect to the only–liquid case 1 (Figure 6.6b, Table 6.6) in the first '*warm*' rainfall peak as well as in the steadier regime.

Minerals considered separately: in this mechanism, none of the considered minerals (K–feldspar, illite and kaolinite) have an impact on the dynamics of the cloud. The variation in the '*warm*' rainfall peak intensity is anecdotic and there is almost no variation in the rainfall rate for each of the cases 6–A, B and C until 63 min of simulation. In this latter part, in the case 6–A, where only K–feldspar is considered as INP, the rainfall rate drops to values close to 0, as in this case, opposite to case 1 and the other deposition nucleation cases, there is no small downdraft (wind speeds around $-2\,\mathrm{m.s^{-1}}$). Therefore, even though the liquid water content in the lower levels of the modeled atmosphere are similar, less precipitation is obtained at the ground. This yields a non negligible variation of 8% for the cumulative rain on the ground in case 6–A with respect to case 1 (Table 6.6). Such a behavior is also noticeable for case 6–B, but in a much narrower manner.

These variations in the late evolution of the cloud are not reproduced by the all minerals case 6–E as they seem to take part in a butterfly effect: a very small variations in the dynamics in the first part of the downdraft linked to small ice water contents have a larger effect on the last 20 min of simulation.

The parameterization for the three minerals considered have rather low INAS densities. In this nucleation mechanism again, K–feldspar is the most active of all minerals, but as was shown in the final Figure of Chapter 4, the parameterization derived from the cold stage experiments and used in this case study yield rather low INAS densities. Particularly, the INAS densities obtained by this parameterization are at least two orders of magnitude lower than the Steinke et al. (2015) parameterization for Arizona Test Dust.

6.3.3 Mechanisms in competition — case 2

In Figure 6.7a are displayed the liquid and ice water contents for the case where only kaolinite is considered as an INP with all the ice formation processes active (case 2–C).

Ice nucleation cloud starts very late in the cloud, when the cloud top reaches 7 km after 24.5 min (temperature of −28°C), altitudes close to those of homogeneous nucleation. At such temperatures, the active ice nucleation mechanism can only be heterogeneous, but because of the low ice nucleating efficiency of kaolinite, after only 1 min, as the cloud top reaches the homogeneous nucleation line, homogeneous nucleation becomes dominant. The precipitation system is however still set below the homogeneous nucleation line: the liquid precipitation onset occurs after 32.7 min at an altitude of 7.2 km and the ice precipitation onset occurs after 32.5 min at an altitude of 7.4 km, This results in an increased maximal precipitating total water content, reaching $5.4\,\mathrm{g.m^{-3}}$. The precipitation onset and the maximal precipitating total water content in this case 2–C are identical to those for homogeneous nucleation as only ice nucleation mechanism (case 3, Table 6.7).

Naturally, the evolution of the rainfall rate follows closely that of homogeneous nucleation, yielding a similar cumulative rain.

It was pointed out in §6.3.2.2 that the warmer ice nucleation starts in the cloud, the more impact the considered mineral has on the dynamical evolution of the cloud. This remains true when all ice nucleation mechanisms are considered together. This was detailed for kaolinite in the previous paragraph, and from Figure 6.7, it is clear that in case 2–D, homogeneous nucleation has an important role in the dynamical evolution of the cloud. The '*warm*' rainfall peak is similar to that of case 4–D, but the precipitation system is largely modified after 55 min as the large peak of intensity is not to be noticed, resulting in a cumulative rain strongly reduced and closer to that of case 3.

The same observation applies to illite in case 2–B: the '*warm*' rainfall peak, with respect to case 4–B, is not impacted by the competition among the ice nucleation mechanisms, but the intensity of the second peak around 55 min is diminished. The reduction of the

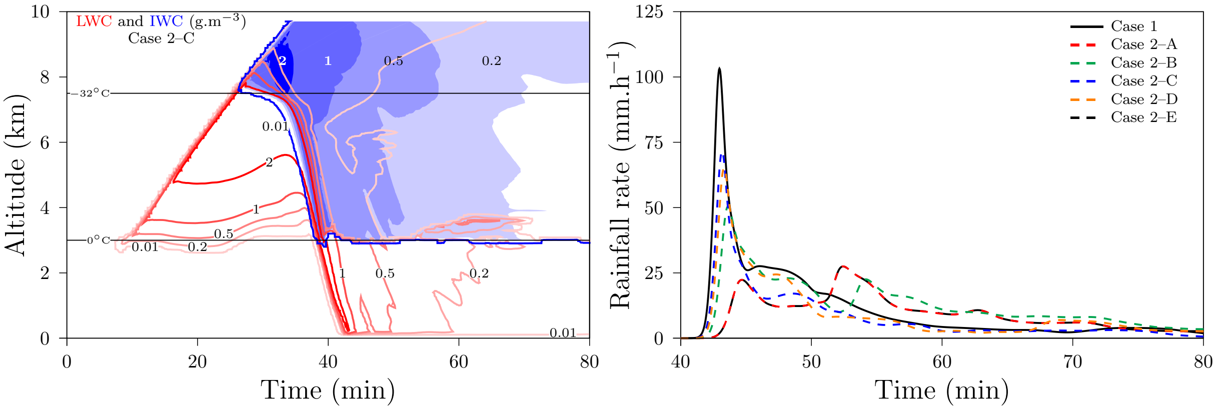

Figure 6.7 – (**a**, left) Liquid water content (g.m^{-3}, red) and ice water content (g.m^{-3}, blue) simulated by DESCAM as a function of altitude and time for the case with only kaolinite active as INP and all ice nucleation mechanisms active (case 2–C). (**b**, right) Time evolution of the rainfall rate (mm.h^{-1}) for the only–liquid case (case 1, black continuous) and the all ice nucleation mechanisms cases for K–feldspar (case 2–A, red dashed), illite (case 2–B, green dashed), kaolinite (case 2–C, blue dashed), quartz (case 2–D, orange dashed) and all minerals (case 2–E, black long dashed).

cumulative rain is not as large as in case 2–D with a total amount of precipitations reduced to 8.47 mm.

Contrary to this, when K–feldspar is considered as the only INP, the resulting cloud and precipitations are very similar to those of case 4–A, as K–feldspar starts forming ice crystals early in the cloud development. Therefore, as had already been pointed out for the various ice nucleation mechanisms considered separately, when all mechanisms are considered together, the resulting cloud follows closely that of case 2–A.

Contact freezing and deposition nucleation showed a fairly limited impact on the cloud dynamics when considered alone (§6.3.2.3 and 6.3.2.4) so quite logically, they do not play a role in the dynamical evolution of the cloud.

Homogeneous nucleation is responsible for the large differences between cases 2 and 4 observed for illite, kaolinite and quartz. As a smaller portion, compared to case 2–A, of the cloud is frozen, the remaining large droplets freeze when they reach the homogeneous nucleation altitudes. This releases quite large amounts of additional latent heat and thereby reduces the amount of hydrometeors taking part in the precipitation. Furthermore, as the ice water content in the downdraft is lower, the below–cloud downdraft is smaller, as has already been pointed out in previous sections.

6.3.4 Summary of the reference cases with all minerals as INP

In Figure 6.8a are displayed the liquid and ice water contents for the case where K–feldspar, illite, kaolinite and quartz together are considered as INP (case 2–E). This case summarizes the results from the previous sections 6.3.2 and 6.3.3.

As has been pointed out for each of the different heterogeneous ice nucleation mechanism, K–feldspar is the most active of the mineral particles in each of the ice nucleation modes and dictates the evolution of the cloud when considered among the other minerals. In each of the 'E' cases for individually considered ice nucleation mechanism, the dynamical evolution of the cloud and the precipitations show a very similar behavior to that of the corresponding 'A' case. This is also true for case 2–E which closely follows the evolution

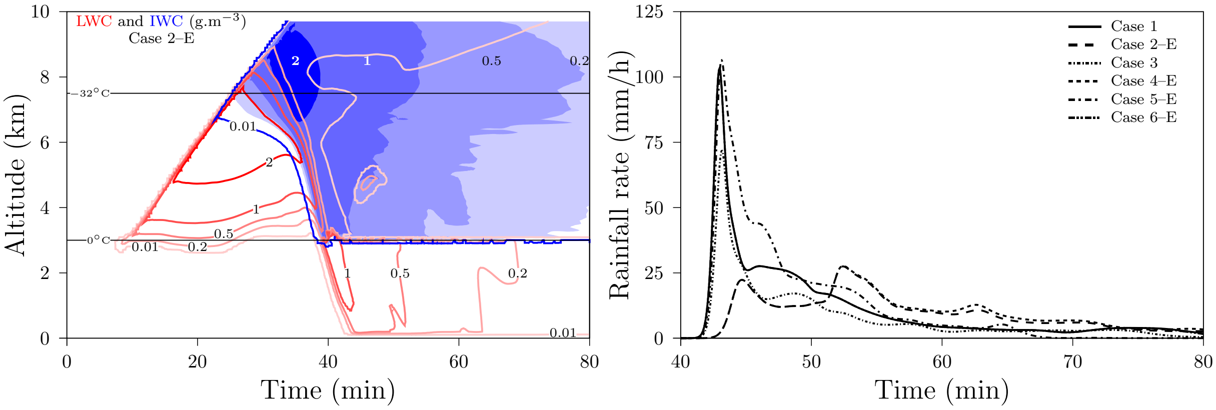

Figure 6.8 – (**a**, left) Liquid water content (g.m^{-3}, red) and ice water content (g.m^{-3}, blue) simulated by Descam as a function of altitude and time for the case with all minerals active as INP and all ice nucleation mechanisms active (case 2–E). (**b**, right) Time evolution of the rainfall rate (mm.h^{-1}) for the only-liquid case (case 1, continuous), homogeneous nucleation (case 3, short dashed–dotted) and all minerals cases for all ice processes (case 2–E, dashed), immersion freezing (case 4–E, short dashed), contact freezing (case 5–E, dotted–dashed) and deposition nucleation (case 6–E, double dotted–dashed).

of case 2–A.

6.4 Analysis

6.4.1 Ice nucleation rates

To better understand the role of the different ice nucleation mechanisms, we look into the ice nucleation rate evolution for the presented cases as was done in the preliminary study's analysis section. Even though freezing of droplets based on immersed particles is considered as a whole in the model, the ice nucleation rates for droplets smaller and larger than 16 µm are differentiated in the nucleation rate output.

When considering deposition nucleation as the only ice nucleation mechanism, the total number of ice crystals nucleated when all minerals are considered as ice active corresponds to the sum of the ice crystals nucleated when the minerals are considered separately (Figure 6.9a). There is no influence on the total number of ice crystals as there is no competition among deposition nucleation by the different minerals. As the ice nucleation efficiencies are rather low, there are not enough ice crystals growing by vapor diffusion to reduce locally the relative humidity. Therefore, all mineral aerosol particles remain in the same environment both when considered as only ice active mineral and when all minerals are considered as ice active.

Even though the integrated number of ice nucleation events (INNE) for contact freezing is of the same order of magnitude as that of deposition nucleation, the INNE when all mineral particles are taken into account does not correspond to the addition of the isolated cases: the INNE of case 5–E is close to that of cas 5–A with only a slight increase (Figure 6.9b).
Deposition nucleation occurs only on unactivated aerosol particles and creates small crystals, whereas contact freezing corresponds to the collection of unactivated particles by

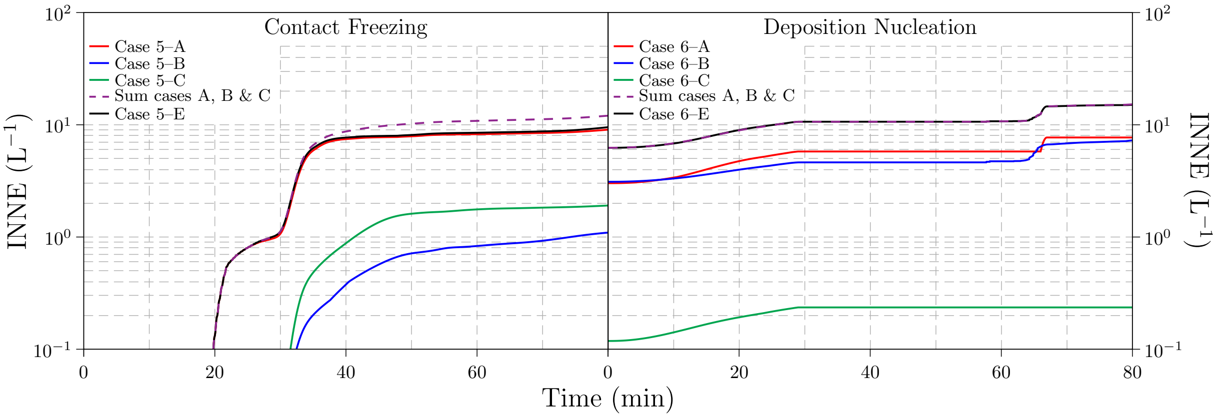

Figure 6.9 – Integrated number of nucleation events as a function of simulation time for cases 5 (**a**, left) and 6 (**b**, right) for the different minerals: K–feldspar (cases A, red colored lines), illite (cases B, green colored lines) and kaolinite (cases C, blue colored lines). In black lines are respectively the cases for all minerals active at one (cases E, continuous) and the sum of the integrated number of nucleation events for the three individual cases (purple dashed).

rather large droplets. Furthermore, in this case study, contact freezing mainly takes place during the downdraft, where the obtained ice crystals rapidly freeze large amounts of the liquid water in the cloud through the riming process. As K–feldspar is the most ice active of the minerals, the first droplets to be frozen by contact freezing involved K–feldspar particles. This depletes the large droplets which would otherwise interact with illite and kaolinite.

Because of their reduced ice nucleation efficiency, illite and kaolinite contribute less to the freezing of the cloud in case 5–E than in cases 5–B and C (INNE reduced by one order of magnitude).

In Figure 6.10 are represented the nucleation rates as a function of time and altitude for immersion freezing on droplets larger than 16 µm and for homogeneous nucleation when kaolinite is the only ice active mineral.

The immersion freezing mechanism starts at an altitude of 7 km, as was the case when immersion freezing on droplets smaller than 16 µm were also taken into account. The ice nucleation intensifies as the cloud top reaches higher altitudes with ice nucleation rates up to $6 \cdot 10^4\,\mathrm{min}^{-1}.\mathrm{m}^{-3}$ around 8 km of altitude. The ice nucleation rate then decreases over time as the precipitation starts.

Homogeneous ice nucleation starts when the cloud top reaches 7.5 km, corresponding to the identified homogeneous nucleation line in the preliminary study. Already at this altitude, this mechanism is very ice active with ice nucleation rates larger than $10^6\,\mathrm{min}^{-1}.\mathrm{m}^{-3}$. As was to be expected from the characteristics of the cloud and precipitations in case 3, the homogeneous ice nucleation rates are identical in this study to those of Chapter 5.

When all ice nucleation mechanisms are taken into account, the ice nucleation rates for deposition nucleation and immersion freezing on droplets smaller than 16 µm are not largely impacted (graphs not shown). For droplets larger than 16 µm, there is a large difference: as was suggested in §6.3.3, the homogeneous nucleation dominates at higher altitudes. As soon as the cloud top reaches 7.5 km, the immersion freezing ice nucleation

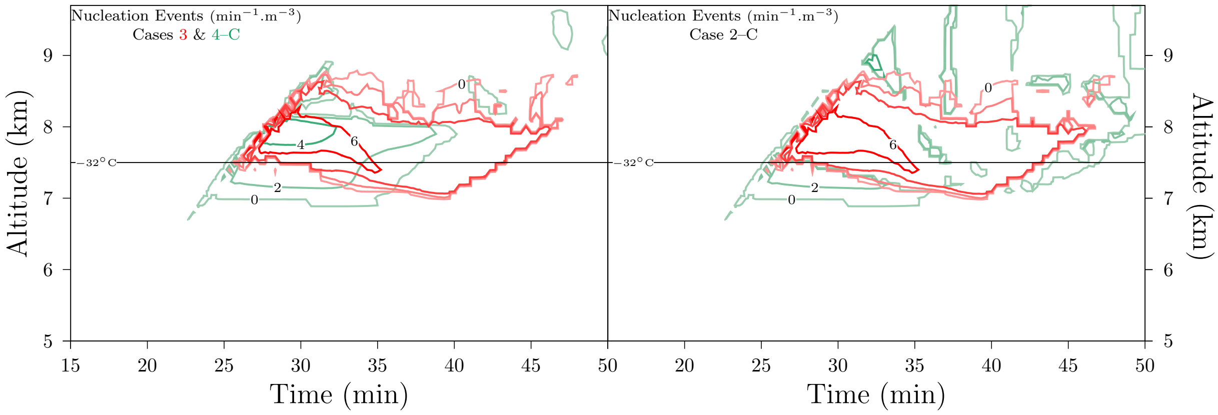

Figure 6.10 – Ice nucleation rate (decimal logarithm of the number of events per cubic meter and per minute) simulated by DESCAM as a function of altitude and time (**a**, left) for the cases with only immersion freezing active (case 4–C, green contours) and homogeneous nucleation active (case 3, red contours) and (**b**, right) for the case with all ice nucleation active (case 2–C, same color codes) when only kaolinite is considered as ice active.

rates sinks and only homogeneous nucleation remains, with the homogeneous nucleation rate being almost identical to that of case 3.

Given that homogeneous nucleation is volume dependent, it is mostly efficient on the large droplets, as is the case for immersion freezing, and is therefore responsible for a steep increase in the frozen fraction in the larger size bins. As the ice nucleation rate of immersion freezing in the INAS density representation directly depends on the frozen fraction in each of the size bins, the increase due to homogeneous nucleation implies that the maximal frozen fraction predicted by the INAS density parameterization is exceeded and therefore, no new ice crystals are formed by the mechanism. Therefore, the simulated cloud in case 2–C is very similar to that of case 3.

In Figure 6.11 are presented the same ice nucleation rates as in Figure 6.10 with all minerals considered as ice active (cases E).

Immersion freezing on droplets larger than 16 μm starts when the cloud top reaches 5.8 km (Figure 6.11a), when immersion freezing on droplets smaller than 16 μm starts one kilometer below (same altitude as in case 4–A). The ice nucleation rate for this mechanism reaches much larger values than in case 4–C (up to $1.4 \cdot 10^6\,\text{min}^{-1}.\text{m}^{-3}$), the maximum being reach 700 m below the homogeneous nucleation line. As was pointed out in case 4–C, the ice nucleation rate then decreases over time as the precipitation starts.

When all ice nucleation mechanisms are active (Figure 6.11), the competition between immersion freezing and homogeneous nucleation is quite balanced: homogeneous nucleation becomes gradually more significant from 7.5 km on, reaching $10^6\,\text{min}^{-1}.\text{m}^{-3}$. When the homogeneous ice nucleation rate reaches this last value, the immersion freezing rate sinks as was observed in case 2–C; between 27 and 37 min of simulation, the lower contour for an homogeneous ice nucleation rate of $10^6\,\text{min}^{-1}.\text{m}^{-3}$ follows the upper contour for an immersion freezing rate of $1\,\text{min}^{-1}.\text{m}^{-3}$.

This sinking of the immersion freezing rate has the same origin as in case 2–C: homogeneous nucleation increases the frozen fraction which then exceeds the value predicted by the INAS density parameterization. However, in case 2–E, homogeneous nucleation dom-

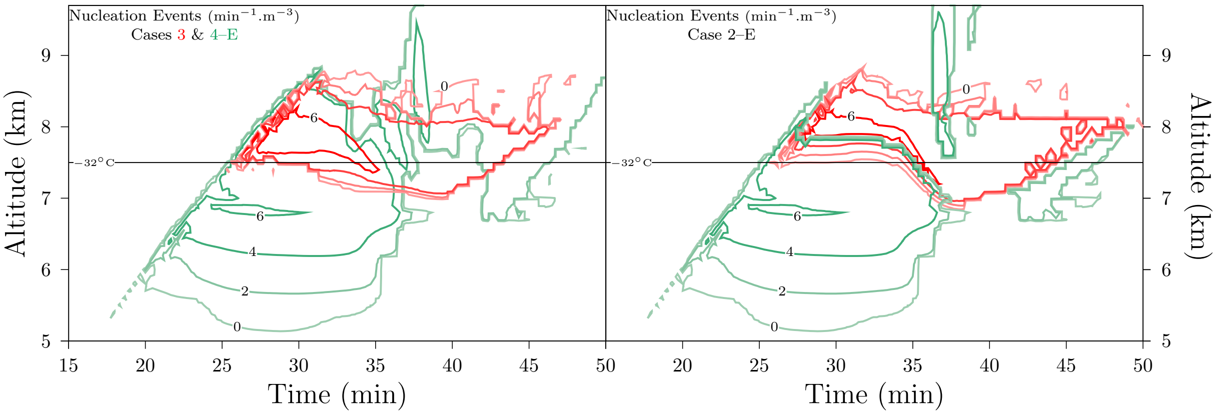

Figure 6.11 – Ice nucleation rate (decimal logarithm of the number of events per cubic meter and per minute) simulated by DESCAM as a function of altitude and time (**a**, left) for the cases with only immersion freezing active (case 4–E, green contours) and homogeneous nucleation active (case 3, red contours) and (**b**, right) for the case with all ice nucleation active (case 2–E, same color codes) when all minerals are considered as ice active.

inates at higher altitudes than in case 2–B: it is a volume dependent parameterization, and it was pointed out previously that because the ice nucleation started around 5 km in the cloud, the droplets reach smaller sizes than in case 3 (and also case 2–B), therefore, the cloud needs to reach colder temperature for the smaller droplets to be frozen. From this moment on, homogeneous nucleation dominates and immersion freezing does not contribute to pristine ice formation.

Overall, when all mechanisms are considered in competition, deposition nucleation and immersion freezing on droplets smaller than 16 µm are only marginally impacted: both mechanism do not have ‘competitors’. This had already been noticed for deposition nucleation in the preliminary study, where on the other hand, condensation freezing stopped when immersion freezing was becoming significant. This depletion of the condensation freezing rate was however due to the computation method of the Meyers et al. (1992) parameterization as it takes into account the ice crystals in all size bins. As, for INAS density representation, each size bin is treated separately, immersion freezing on the smaller droplets is not affected by homogeneous nucleation which is particularly efficient on large droplets.

Finally, contact freezing is significant only at the higher altitudes (above 8 km), as was the case in the preliminary study: with all ice nucleation mechanisms active, there are no droplets in the downdraft to collect unactivated aerosol particles with subsequent contact freezing.

6.4.2 Sensitivity studies

In order to check the independence of the modeled relative importance of the different mechanisms with regards to the background aerosol populations, in a first sensitivity study, the type of aerosol particles in the model is modified in number and nature. Furthermore, in order evaluate the importance of the different choices made for the basic cases presented in sections 6.3.1, 6.3.2 and 6.3.3, sensitivity studies on the impact of the number concentration of mineral aerosol particles, on the ice nucleation schemes and

Case	Description	Rain	±	Var.	First rain peak	
					Intensity (mm.h^{-1})	Time (min)
Case α_1	Marine bkgd AP (Jaenicke, 1988)					
	1–α_1 — No ice nucleation	7.00	–	7 %	125.1	40.1
	2–α_1 — All ice nucleation	13.70	+	119 %	70.0	40.6
Case α_2	Agricultural area bkgd AP (Jaenicke, 1988)					
	1–α_2 — No ice nucleation	8.30	+	10 %	115.5	44.7
	2–α_2 — All ice nucleation	4.61	–	26 %	10.5	47.3
Case α_3	Changed bkgd AP κ–value ($6.1 \cdot 10^{-2}$)					
	1–α_3 — No ice nucleation	7.63	–	1 %	106.3	42.8
	2–α_3 — All ice nucleation	6.43	–	3 %	25.3	44.3
Case α_4	Changed bkgd AP κ–value ($6.1 \cdot 10^{-3}$)					
	1–α_4 — No ice nucleation	7.62	–	1 %	106.7	42.8
	2–α_4 — All ice nucleation	6.41	–	4 %	25.5	44.3

Table 6.8 – List of cases for the sensitivity study on the background aerosol particles and the results for the cumulative rain on the ground. The indicated variation corresponds to the variation with respect to the associated reference case (either case 1 or case 2–E).

parameterizations are now presented.

6.4.2.1 Modifications of the background aerosols — cases α_i

In the cases presented previously, the background aerosol population taken into account was based on the continental aerosol size distribution (total concentration of $1\,839\,\mathrm{cm}^{-3}$) from Jaenicke (1988) with the assumption that the aerosols have the chemical properties of ammonium sulfate. In two case studies, this background aerosol population was changed for a cleaner marine aerosol size distribution (total concentration of $202\,\mathrm{cm}^{-3}$, case α_1) and a more polluted agricultural area size distribution (total concentration of $8\,787\,\mathrm{cm}^{-3}$, case α_2), both based on Jaenicke (1988). All three size distributions provide comparable number concentrations of aerosol particles larger than 1 µm however, in the submicronic range, the marine aerosol size distribution yields number concentrations lower by about three orders of magnitude than the two other size distributions. In this range, it is only for aerosol particles smaller than 0.2 µm that the polluted size distribution contains more particles than the continental one, but given the low limit activation radius in the studied CCOPE cloud (around 0.1 µm), the agricultural area size distribution provides three times the number of cloud condensation nuclei (CCN) the continental size distribution provided. This results in a delayed precipitation onset with a larger '*warm*' rainfall peak (114.9 mm.h^{-1} after 44.7 min) for case 1–α_2, whereas for case 1–α_1, the variation on the background aerosol size distribution leads to a larger increase of the '*warm*' rainfall peak, but this time noticeable earlier (125.1 mm.h^{-1} after 40.1 min).

In two additional case studies, the chemical properties of the background aerosol population (in a continental aerosol size distribution from Jaenicke (1988), as in case 2) were changed to simulate more hydrophobic aerosol particles, with κ–values of $6.1 \cdot 10^{-2}$ (case α_3) and $6.1 \cdot 10^{-3}$ (case α_4). This increased hydrophobic behaviors of the background aerosol population imply a smaller amount of activated aerosol particles, the results for

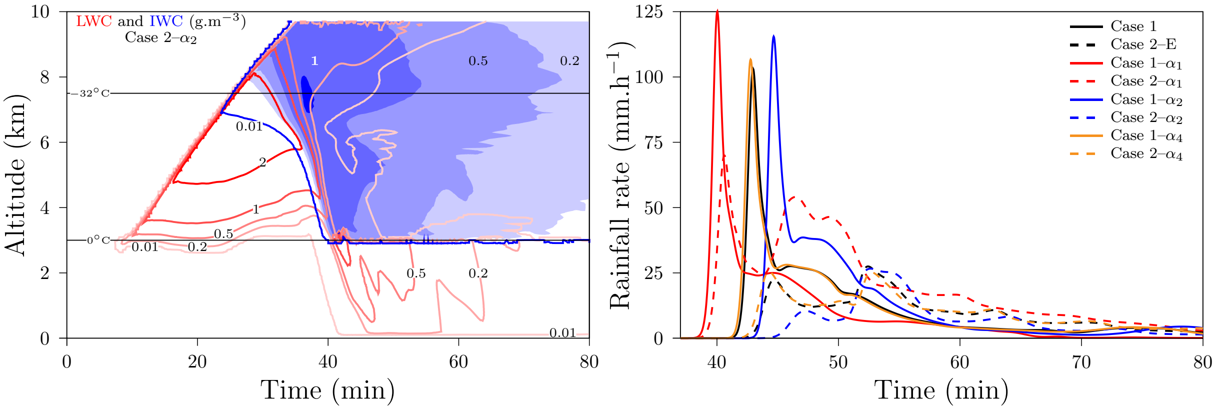

Figure 6.12 – (**a**, left) Liquid water content (g.m^{-3}, red) and ice water content (g.m^{-3}, blue) simulated by DESCAM as a function of altitude and time for the case 2–α_2 with all minerals active as INP and all ice nucleation mechanisms active, with agricultural area (polluted) background aerosol distribution (Jaenicke, 1988). (**b**, right) Time evolution of the rainfall rate (mm.h^{-1}) for the only–liquid case (cases 1, continuous) and all minerals cases for all ice processes (cases 2, dashed) for the reference study (black), marine background aerosols (α_1, red) and agricultural area background aerosols (α_2, blue) according to Jaenicke (1988), and hydrophobic background aerosols (α_4, orange).

those cases therefore tend towards an increased and anticipated main '*warm*' rainfall peak, but this impact of hygroscopicity on the precipitations is very small : in case 1–α_3, the main peak reaches 106.3 mm.h^{-1} after 42.8 min and in case 1–α_4, the main peak reaches 106.7 mm.h^{-1} after 42.8 min also. On the final amount of precipitations, the variation due to a change in hygroscopicity of the background aerosols is of 1% for both case 1–α_3 and α_4, a minimal impact when compared to the variations obtained through a change of the background aerosol size distributions

For a discussion on the influence of different background aerosol particle spectra on the evolution of the simulated 1.5–D CCOPE convective cloud, *see* Leroy et al. (2006).

When considering the ice nucleation mechanisms (cases 2–α_i), the variations on the number of cloud droplets observed in the different case studies impact the absolute values of the integrated number of nucleation events, the total amount of precipitations and the precipitation dynamics (Figure 6.12) as they impact the early development of the cloud; but the comparative results for each of the studied ice nucleation mechanisms remain the same. As immersion freezing in the mechanism the most active at warm temperatures, it has the most impact and drives the dynamics of the precipitation system, even though in both cases α_1 and α_2, homogeneous nucleation produces the most pristine ice crystals. The variation on the hygroscopicity of the background aerosol particles do not imply large changes in the results from the reference cases.

Therefore, in all four cases α_i, the dynamics of the cloud and of the precipitation is dictated by immersion freezing, homogeneous nucleation is responsible for the freezing of the remaining droplets above the homogeneous nucleation line and deposition nucleation and contact freezing have little impact on the global dynamics of the cloud; finally K–feldspar is the most significant of the different mineral ice nuclei.

Case	Description	Rain	± Var.	First rain peak	
				Intensity (mm.h^{-1})	Time (min)
Case β_1	Mineral aerosols concentration: $10\,c_0$				
	1–β_1 — No ice nucleation	7.82	+ 3 %	105.8	43.3
	2–β_1 — All ice nucleation	3.90	− 38 %	11.2	46.3
Case β_2	Mineral aerosols concentration: $2\,c_0$				
	1–β_2 — No ice nucleation	7.55	− 0 %	103.3	43.0
	2–β_2 — All ice nucleation	5.60	− 10 %	19.2	45.0
Case β_3	Mineral aerosols concentration: $0.1\,c_0$				
	1–β_3 — No ice nucleation	7.56	− 0 %	103.3	42.9
	2–β_3 — All ice nucleation	8.85	+ 42 %	34.2	44.0
Case β_4	Mineral aerosols concentration: $0.01\,c_0$				
	1–β_4 — No ice nucleation	7.57	− 0 %	103.3	43.0
	2–β_4 — All ice nucleation	10.44	+ 67 %	50.3	43.6

Table 6.9 – List of cases for the sensitivity study on the mineral aerosol particles concentration and the results for the cumulative rain on the ground. The indicated variation corresponds to the variation with respect to the associated reference case (either case 1 or case 2–E).

6.4.2.2 Modifications of the mineral aerosols concentration — cases β_i

In the reference cases from section 6.3, the number concentrations of mineral aerosol particles were fixed to 10% of the values found in Kandler et al. (2009). This sensitivity study looks into the impact of a variation of these concentrations with four additional concentrations tested: original Kandler et al. (2009) mineral number concentrations ($10\,c_0$, cases β_1), number concentrations reduced to 20% ($2\,c_0$, cases β_2), number concentrations reduced to 1% ($0.1\,c_0$, cases β_3) and number concentrations close to the mean mineral aerosol particles concentration over Europe ($0.01\,c_0$, cases β_4).
When considering only the warm microphysics (no ice nucleation), the cloud and precipitations dynamics are not changed by much. The increase of large aerosol particles (larger than 0.1 µm) has the same impact on the cloud development as seen in the previous section: in case 1–β_1, the '*warm*' rainfall peak is slightly increased to 105.8 mm.h^{-1} after 43.3 min, corresponding to a delay of 20 s with respect to the '*reference*' case 1 (figure 6.13b). The variations in the number concentrations in cases 1–β_2, 1–β_3 and 1–β_4 have even less impact on the '*warm*' rainfall peak: less than 0.1 mm.h^{-1} and a shift of less than 5 s; with precipitations tending further towards those obtained for case 1 from the previous chapter as the added minerals concentration decreases. The total amount of precipitation at the end of the simulations reflects on those light variations.

In the different cases 2–β_i, the impact of the mineral aerosol number concentrations is much more noticeable: the structure of the precipitation remains the same (a first peak of intensity corresponding to '*warm*' rainfall remains followed by a stronger second peak) but the precipitation rates, and therefore the total amount of rain, strongly depend on the mineral aerosol number concentration.

In case 2–β_1, the '*warm*' rainfall peak reaches only 11.2 mm.h^{-1} after 46.3 min (a variation of 50% with respect to the 22.3 mm.h^{-1} after 44.7 min obtained in case 2–E, Table 6.9)

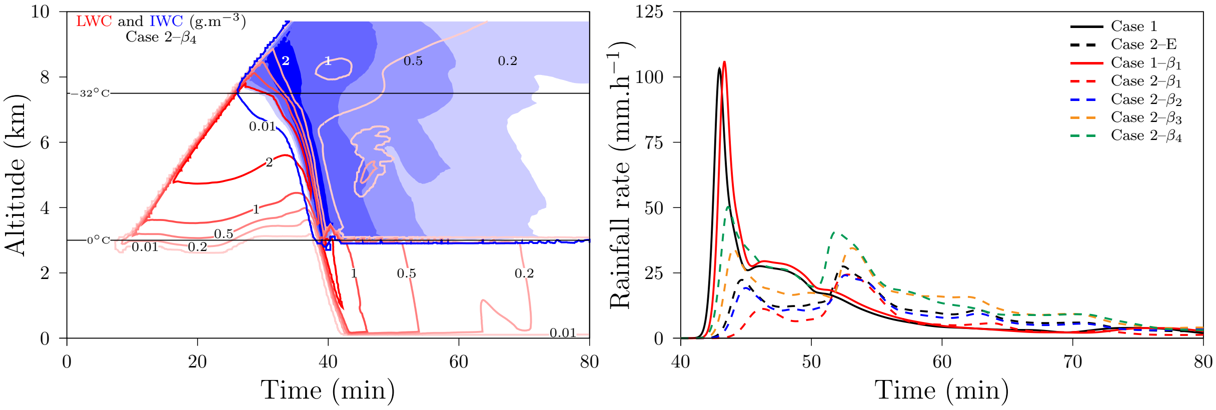

Figure 6.13 – (**a**, left) Liquid water content (g.m^{-3}, red) and ice water content (g.m^{-3}, blue) simulated by DESCAM as a function of altitude and time for the case with all minerals active as INP and all ice nucleation mechanisms active for an increased mineral aerosol particles number concentration (case 2–β_4). (**b**, right) Time evolution of the rainfall rate (mm.h^{-1} for the only–liquid case (cases 1, continuous) and all minerals cases for all ice processes (cases 2, dashed) for the reference study (black), a mineral aerosols concentration of $10\,c_0$ (β_1, red), $2\,c_0$ (β_2, blue) and $0.1\,c_0$ (β_3, orange) and $0.01\,c_0$ (β_4, green).

and the second peak reaches 24.4 mm after 52.8 min (a variation of 11% with regard to the 27.5 mm.h^{-1} after 52.4 min obtained in case 2–E).
Overall, the precipitations in case 2–β_1 start later with the total amount of precipitation reduced by 38%. The early cirrus–like cloud is noticeable with ice water contents larger than in case 2–E (up to $1.5 \cdot 10^{-2}$ g.m^{-3}, an increase of one order of magnitude), as was to be expected because of the increase of one order of magnitude of the number of ice nuclei. In the convective cloud, the total water content in the downdraft reaches only 2.4 g.m^{-3} where in case 2–E, the total water content reaches 2.8 g.m^{-3}. The increased number of ice nuclei implies more ice crystals formed, which then grow less in case 2–β_1 than in case 2–E, so that even though the basic dynamics of the cloud remain the same (as seen previously in this section) and the ice nucleation processes occur in the same conditions, there are less large hydrometeors available to form the precipitations.

In case 2–β_2, the global dynamics of the cloud and the ice and liquid water contents are only marginally modified.
In case 2–β_3, the '*warm*' rainfall peak shows an increase of about 53% with respect to case 2–E, and a stronger '*cold*' rainfall peak (36.5 mm.h^{-1} after 53.1 min, a variation of 33%) which was to be expected as the importance of immersion freezing on the global dynamics of the cloud has weakened due to the decreased number of ice nuclei. However, it is still heterogeneous freezing that dictates the precipitation system.

In figure 6.13a are represented the liquid and ice water content for this case 2–β_4. In this case, the ice nucleation becomes significant much later. The higher ice water contents (< 0.2 g.m^{-3}) appear when the cloud top reaches altitudes similar to those of case 3. However, due to the riming process, the early frozen ice crystals, even though in small amounts, yield an increase of the ice water content and anticipated depletion of cloud droplets when compared to the case 3. Therefore, even though homogeneous nucleation dominates the ice nucleation (INNE 200 times larger than that of immersion freezing), there is a large contribution of heterogeneous nucleation to the dynamics of the cloud (case 3–β_4 yields a cumulative rain of 5.33 mm whereas case 4–β_4 yields a cumulative rain of 23.52 mm, for a cumulative rain in case 2–β_4 of 10.44 mm).

Overall, even though there are some changes in the dynamics of the cloud and in the rainfall rates, the relative behaviors of the different heterogeneous ice nucleation mechanisms as described in sections 6.3.2 and 6.3.3 and subsequent conclusions are independent from the mineral aerosol particles concentration.
Homogeneous nucleation becomes dominant for the lowest concentration but heterogeneous nucleation still plays a major role in the dynamical evolution of the cloud, even though it yields only a small fraction of the pristine ice crystals obtained.

6.4.2.3 Modifications in immersion freezing computation — cases γ_i

The reference cases presented in section 6.3.2.2 are based on strong assumptions on the immersion freezing mechanisms: independence of the different bins and separate representation of the surface (per aerosol particle or per droplet) depending on the size of the considered bin. In this section, five additional sensitivity studies are presented in order to assess the importance of the technical choices made in defining immersion freezing using INAS densities.

In cases γ_1 and γ_2, only one size range is considered: either ice nucleation on smaller droplets ('*condensation*' freezing, γ_1) or on larger droplets ('*immersion*' freezing, γ_2).
In cases γ_3 and γ_4, a single computation algorithm is used regardless of the size of the droplets, either considering an internal mixture of the aerosol particle (case γ_3):

$$\left.\frac{\partial N_i}{\partial t}\right|_{\text{nucl,imm},\gamma_3}(j) = \max\left[0, \sum_{kt}[\mathcal{N}_d(j,kt) + \mathcal{N}_i(j,kt)]\cdot[1-\alpha_{\text{imm}}(j,kt)] - N_i(j)\right]\cdot\frac{1}{\Delta t} \tag{6.17}$$

or an internal mixture (case γ_4):

$$\left.\frac{\partial N_i}{\partial t}\right|_{\text{nucl,imm},\gamma_4}(j) = \max\left[0[(N_d(j) + N_i(j)]\cdot\left[1-\prod_{kt}\alpha^{\dagger}_{\text{imm}}(j,kt)\right] - N_i(j)\right]\cdot\frac{1}{\Delta t} \tag{6.18}$$

with α_{imm} and $\alpha^{\dagger}_{\text{imm}}$ as defined in equation 6.9.
Finally, in case γ_5, immersion freezing is computed over all size bins as is done for deposition nucleation:

$$\mathrm{d}n_{i,\text{imm},\gamma_5}(kt) = \max\left[0, \left(\sum_{r_d} N_d(r_d) + \sum_{r_i} N_i(r_i)\right)\cdot[1-\widetilde{\alpha}_{\gamma_5}(kt)] - \sum_{r_i} N_i(r_i)\right] \tag{6.19}$$

where $\widetilde{\alpha}_{\gamma_5}$ is determined using the same equation as in equation 6.14. The repartitioning for this case γ_5 is then determined using:

$$\mathrm{d}n^*_{i,\text{imm},\gamma_5}(j,kt) = \mathcal{N}_d(j,kt)\cdot\left[1-\exp\left(-n_{s,\text{imm}}(kt)\cdot\frac{\mathcal{S}_d(j,kt)}{\mathcal{N}_d(j,kt)}\right)\right] \tag{6.20}$$

Case	Description	Rain	± Var.	First rain peak	
				Intensity ($\mathrm{mm.h^{-1}}$)	Time (min)
Case γ_1	Condensation freezing only				
	2–γ_1 — All ice nucleation	8.51	+ 36 %	26.2	44.5
	4–γ_1 — Immersion freezing only	9.56	+ 44 %	26.2	44.5
Case γ_2	Immersion freezing only				
	2–γ_2 — All ice nucleation	6.40	– 2 %	22.6	44.7
	4–γ_2 — Immersion freezing only	7.04	– 6 %	22.6	44.7
Case γ_3	All condensation freezing				
	2–γ_3 — All ice nucleation	7.13	– 14 %	24.4	44.5
	4–γ_3 — Immersion freezing only	7.45	– 13 %	24.4	44.7
Case γ_4	All immersion freezing				
	2–γ_4 — All ice nucleation	6.27	– 0 %	22.3	44.7
	4–γ_4 — Immersion freezing only	6.54	– 1 %	22.3	44.6
Case γ_5	Immersion freezing bulk computation				
	2–γ_5 — All ice nucleation	5.04	– 20 %	20.4	44.8
	4–γ_5 — Immersion freezing only	5.04	– 24 %	20.4	44.8

Table 6.10 – List of cases for the sensitivity study on the immersion freezing computation and the results for the cumulative rain on the ground. The indicated variation corresponds to the variation with respect to the associated reference case (either case 2–E or case 4–E).

yielding the variation of the ice crystals:

$$\left.\frac{\partial N_i}{\partial t}\right|_{\mathrm{nucl,imm},\gamma_5}(j) = \sum_{kt} \mathrm{d}\mathcal{N}_{i,\mathrm{imm},\gamma_5}(j,kt) \tag{6.21}$$

where $\mathrm{d}\mathcal{N}_{i,\mathrm{imm},\gamma_5}$ is computed in the same fashion as in equation 6.16.
In Figure 6.14b are displayed the rainfall rates for the sensitivity cases listed in Table 6.10 and in Figure 6.15a are displayed the INNE for immersion freezing for the different 4–γ_i cases.

All five sensitivity cases yield precipitation systems similar to that of case 2–E: a '*warm*' rainfall peak of intensity around 44.6 ± 02 min with a maximal rainfall rate around 23 $\mathrm{mm.h^{-1}}$, followed by a second peak of intensity around 53 min, and finally a gradual decrease with an intensity of 5 $\mathrm{mm.h^{-1}}$ after 80 min of simulation (Figure 6.14). In all cases, immersion freezing determines the precipitation onset: the first peak of intensity in the rainfall rate is the same between a case 4–γ_i and the corresponding 2–γ_i.

In case γ_1, immersion freezing only occurs on the smaller droplets, therefore, the precipitation onset in the liquid phase is left unchanged as the large droplets remain liquid in comparable amounts to case 2–E (the onset in this case takes place at an altitude of 5.8 km, where immersion freezing on large droplets remains quite inefficient — ice nucleation rate below 100 $\mathrm{min^{-1}.m^{-3}}$). The precipitation onset in the ice phase on the other hand is slightly anticipated as the updraft weakens earlier as in case 2–E.
The rainfall rate in the '*warm*' rainfall peak is identical in both cases. Is is only after 50 minutes that the two differ: in case 2–γ_1, homogeneous nucleation took place at the

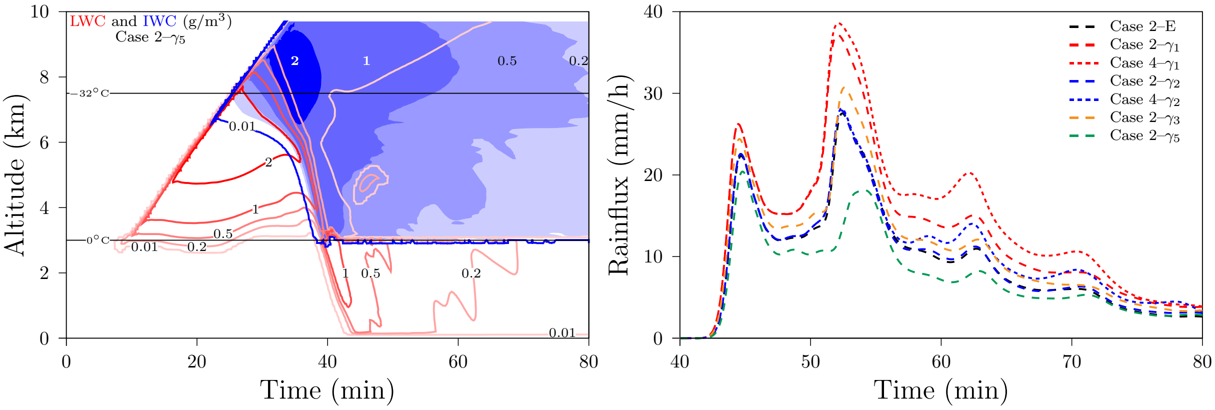

Figure 6.14 – (**a**, left) Liquid water content (g.m^{-3}, red) and ice water content (g.m^{-3}, blue) simulated by DESCAM as a function of altitude and time for the case with all ice nucleation mechanisms active and immersion freezing computed over the entire spectra of droplets and ice crystals (case 2–γ_5). (**b**, right) Time evolution of the rainfall rate (mm.h^{-1}) for the sensitivity cases 2–γ_1 and 4–γ_1 (in red) where immersion freezing is only active on droplets with radii smaller than 16 µm, the sensitivity cases 2–γ_2 and 4–γ_2 (in blue) where immersion freezing is only active on large droplets, the sensitivity case 2–γ_3 (in orange) where immersion freezing is computed considering the surface per aerosol particles and the sensitivity case 2–γ_5 (in green) where immersion freezing is computed by averaging over all the size bins, as is done for deposition nucleation (§6.2.5).

higher altitudes in the cloud development, yielding a larger updraft. The precipitating total water content and rainfall rate are therefore smaller.

In case γ_2, the immersion freezing mechanism starts later in the cloud development as in case 2–E. However, this delay is rather small (about 200 m) and immersion freezing in case γ_2 occurs on the larger droplets, therefore releasing a larger amount of latent heat than in case γ_1. Therefore, the onsets of the precipitation in the ice phase in cases γ_2 replicate those of cases 2 and 4–E, yielding similar '*warm*' rainfall peaks.
As was pointed out in case γ_1, the rainfall rates between case 2 and 4–γ_2 differ after 50 min, because of the dominance of homogeneous nucleation at the higher altitudes. Its impact is however much smaller, as some of the larger droplets were already frozen when they reached the homogeneous nucleation altitudes.

To the difference of the preliminary study, immersion freezing on freshly formed cloud droplets (condensation freezing) plays a much reduced role on the dynamics of the cloud. The ice nucleation mechanism occurs on too small droplets to impact the dynamical development of the cloud (as was already the case for condensation freezing in Chapter 5), but also, it is not efficient enough at high temperatures to impact the development of the droplets. Therefore, when put in competition with immersion freezing on the larger droplets (case 4–E), the dynamics and precipitations are mainly determined by the latter ice nucleation mechanism, as is shown by the smaller variation between case 4–γ_2 and case 4–E than between case 4–γ_1 and case 4–E (Table 6.10).

In case γ_3, the frozen fraction in each bin is predicted by considering the aerosol surface per aerosol particle inside the droplets. This necessarily minimizes the ice nucleation efficiency: it was shown in Figure 6.2 that the number of aerosol particle per droplet grows

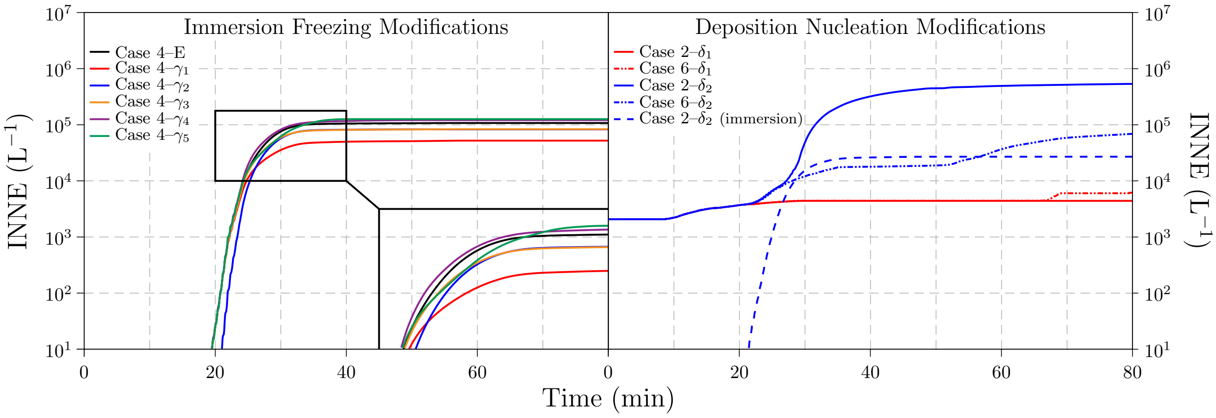

Figure 6.15 – (**a**, left)integrated number of ice nucleation events (INNE) for immersion freezing considered as only active ice nucleation mechanism for the reference case (black) and the sensitivity cases γ_1 (red), γ_2 (blue), γ_3 (orange), γ_4 (purple) and γ_5 (green).(**b**, right) INNE for deposition nucleation when considered alone (case 6, double dotted–dashed lines) and in competition (case 2, continuous) for cases δ_1 (red) and δ_2 (blue). The INNE for immersion freezing in case 2–δ_2 (short dashed) is shown as indicator of in–cloud freezing.

with the droplet volume for radii larger than 16 µm. The assumption made in this case assumes practically that there is only one aerosol particle in each droplet, and therefore the combination of multiple ice nucleating active sites belonging to the different collected aerosol particles inside a droplet is negated.

Immersion freezing in this representation yields ice nucleation rates between case γ_1 and case E: the initial development on freshly formed droplets (smaller than 16 µm) is not changed and the ice nucleation on larger droplets is gradually diminished (the INNE is reduced by 23% in case 4–γ_3 with respect to case 4–E, Figure 6.15a). This results in an evolution of the precipitation for case 2–γ_3 between those of cases 2–γ_1 and 2–E (Figure 6.14).

The case γ_4 makes the opposite assumption of case γ_3: all droplets are constituted of the same mix of aerosol particles. This is true when considering large droplets (for a radius of 100 µm, there are 1 000 aerosol particles per droplet — Figure 6.2, so it is safe to assume that statistically, all droplets contain the same amount of each type of aerosol particle), but it is largely exaggerated for the smaller droplets, as for radii smaller than 10 µm, there is only one aerosol particle per droplet. This assumption therefore reduces the predicted frozen fraction (as $\mathcal{N}_d(kt) < N_d$ for a single type of aerosol particles). However, the frozen fraction is now computed using the number of droplets and not the number of aerosol particles in the droplets, which balances the reduction of the predicted frozen fraction. This is confirmed by the INNE for immersion freezing in case 4–E and 4–γ_4: the algorithm in case 4–γ_4 generates 10 to 20% more ice crystals than the original algorithm from case 4–E (purple curve Figure 6.15a).

However, this overestimation occurs mainly on the smaller droplets, and as was pointed out following cases γ_1 and γ_4, immersion freezing on the smaller droplets does not have a major impact on the development of the cloud, particularly when considered with immersion freezing on the larger droplets. Therefore, in case γ_4, the dynamics as well as the precipitations replicate very closely those of the reference cases E.

The correct description of ice nucleation on the larger droplets is essential to correctly predict the evolution of the cloud. An overestimation in the ice nucleation efficiency of small droplets has almost no impact on the overall evolution, but the underestimation of ice nucleation on the larger droplets leads to large variations in the life and resulting precipitations of the cloud.

Finally, the cases γ_5 assess the influence of the choice of the immersion freezing computation scheme by opting for a computation of $S(kt)$ and therefore of $\alpha_{\mathrm{imm}}(kt)$ over the entire droplets and ice crystals spectra instead of a separated bin treatment. The evolution of the modeled cloud in case 2–γ_5 is represented in Figure 6.14a.
In the early development of the cloud (below 7 km and for integration times below 30 min), the bulk computation of immersion freezing makes little difference with respect to the reference case with similar nucleation rates in case 4–E and 4–γ_5. The precipitation onset in the liquid phase is not changed and only the onset in the ice phase is slightly anticipated and occurs at an altitude 200 m lower. However, when the cloud top reaches 7 km, the ice nucleation rate suddenly drops to values below 1 $\mathrm{min}^{-1}.\mathrm{m}^{-3}$: the temperature at altitudes higher than 7 km are below 248 K. Below this temperature, a plateau of the INAS density for immersion freezing on K–feldspar particles is assumed. Therefore, as the frozen fraction is computed over the entire spectra of droplets and ice crystals and when the temperature decreases, the predicted frozen fraction remains constant, no new ice crystals are to be formed. This is not the case with the bin–treatment of immersion freezing because of the Bergeron–Findeisen effect: the formed ice crystals grow faster than the droplets and do not correspond to the same bin anymore.
This stopped ice nucleation results in a smaller ice water content in the downdraft, and therefore less latent heat collection through the melting, yielding a smaller downdraft in the below cloud altitudes. The rainfall rate after 50 min reflects this smaller downdraft with a smaller second peak of intensity.

The lack of difference in the ice nucleation rates in the first part of the cloud development validates the chosen reference algorithm as it does not artificially overestimate the total number of ice crystals.

6.4.2.4 Modifications on the parameterizations — cases δ_i

In this chapter, deposition nucleation was computed on three different mineral types, based on rather inefficient parameterizations. Steinke et al. (2015) determined an INAS density parameterization for Arizona Test Dust based on cloud chamber measurements. This parameterization offers INAS densities at least two order of magnitude higher than the parameterization derived from the cold stage experiments in Chapter 4. Furthermore, it is active as soon as the relative humidity over ice reaches 100%. To test a '*best case scenario*' for deposition nucleation on mineral particles, cases δ_1 and δ_2 use this parameterization with all four minerals considered as ATD particles for this mechanism.
In the development of the ice nucleation algorithm for deposition nucleation, a limitation to out–of–cloud conditions was set. This limitation is lifted in case δ_2 to look into its implications.
Finally, case δ_3 implements the K–feldspar parameterization for immersion freezing derived from the cold stage experiment.

Case	Description	Rain	±	Var.	First rain peak	
					Int. (mm.h^{-1})	Time (min)
Case δ_1	Deposition nucleation on ATD					
	2–δ_1 — All ice nucleation	6.24	–	0 %	22.3	44.7
	6–δ_1 — Deposition nucleation only	6.66	–	12 %	104.4	43.0
Case δ_2	In–cloud deposition nucleation on ATD					
	2–δ_2 — All ice nucleation	6.20	–	1 %	22.3	44.7
	6–δ_2 — Deposition nucleation only	8.93	+	18 %	83.04	43.1
Case δ_3	Immersion freezing with Chapter 3 K–feldspar parameterization					
	All ice nucleation:					
	2–δ_3–A — INP: K–feldspar	9.29	+	49 %	41.1	43.8
	2–δ_3–E — INP: All minerals	8.21	+	31 %	39.6	43.8
	Only immersion freezing active:					
	4–δ_3–A — INP: K–feldspar	13.39	–	101 %	39.9	43.9
	4–δ_3–E — INP: All minerals	11.64	–	76 %	39.9	43.9

Table 6.11 – List of cases for the sensitivity study on the parameterizations and the results for the cumulative rain on the ground. The indicated variation corresponds to the variation with respect to the associated reference case

In case δ_1, an early cirrus–like cloud formation is to be noticed between 8 and 9 km of altitude (similar to Figure 6.16a). As the deposition nucleation parameterization is more efficient than those used in the reference cases 6–A, B and C, this early formation of ice is easier noticeable.

However, in spite of this increased efficiency, the impact of deposition nucleation on the cloud dynamics and resulting precipitations remains minimal: the precipitating ice water content only reaches 0.17 g.m^{-3} with a maximal precipitating total water content of 8.9 g.m^{-3} as in cases 1 and 6–E. As a result, the '*warm*' rainfall is almost unchanged; but as was the case for case 6–A (K–feldspar as only mineral in the deposition nucleation mode), a small updraft develops below the cloud base after 50 min of simulation, stopping the rainfall earlier than in case 1 and reducing the cumulative rain by 12%.

When all ice nucleation processes are considered in competition, deposition plays as little a role in case 2–δ_1 as in case 2–E.

This little role of deposition nucleation might originate in the limitation imposed. Indeed, in the preliminary study of Chapter 5, it was shown that some deposition nucleation occurred at high altitudes inside the cloud.

In Figure 6.16a is represented the evolution of the simulated cloud when deposition nucleation on ATD is the only ice mechanism considered. Beside the aforementioned cirrus–like cloud, it is noticeable that in this case, the ice water content reaches values larger than 2 g.m^{-3} at high altitudes as well as in the downdraft. The high precipitating ice water content is a consequence of the riming process along the downdraft and is not of interest in the current discussion.

At higher altitudes, this high ice water content is drive originally by ice nucleation on unactivated aerosol particles: the in–cloud deposition nucleation rate is larger than 1 000 min^{-1}.m^{-3} when the cloud top reaches an altitude of 7.4 km. In the light of the results from cases γ_3 and γ_5, we know that this ice nucleation rate cannot be overestimated

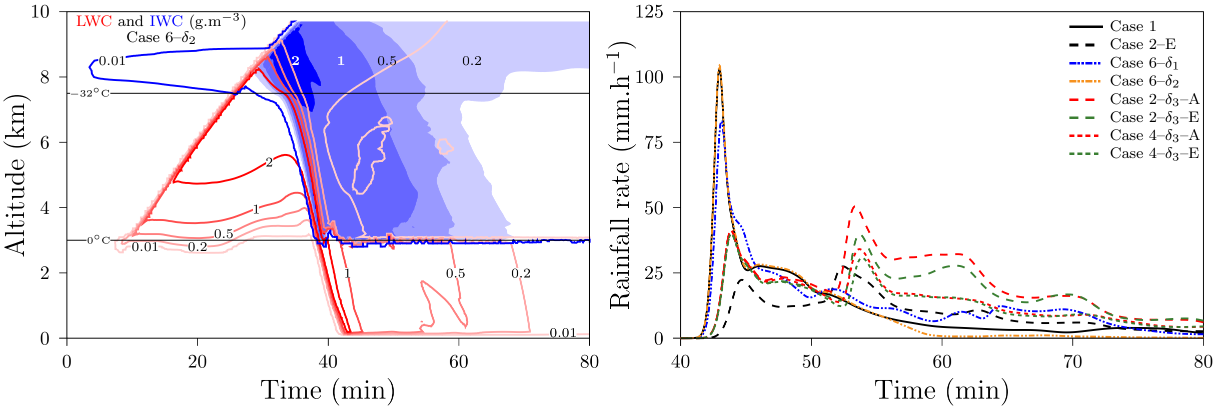

Figure 6.16 – (**a**, left) Liquid water content (g.m^{-3}, red) and ice water content (g.m^{-3}, blue) simulated by Descam as a function of altitude and time for the case with only unrestricted deposition nucleation active with all minerals active as INP with ATD deposition nucleation parameterization from Steinke et al. (2015; case 2–δ_2). (**b**, right) Time evolution of the rainfall rate (mm.h^{-1}) for the sensitivity cases 6–δ_1 (in blue) and 6–δ_2 (in orange) where deposition nucleation is the only active ice nucleation mechanism respectively without and with in–cloud nucleation parameterized with ATD parameterization from Steinke et al. (2015), the sensitivity cases 2–δ_3–A (in red) and 2–δ_3–E (in green) where all ice nucleation mechanisms are considered active and immersion freezing on K–feldspar parameterized using the results from Chapter 3 with K–feldspar and all minerals considered active respectively, and the sensitivity cases 4–δ_3–A (in red) and 4–δ_3–E (in green) where only immersion freezing is considered active.

by the algorithm even if riming is involved: the surface is calculated per aerosol particle and the predicted frozen fraction for deposition nucleation is calculated over the entire aerosol particles and ice crystals spectra.

This results in a delayed onset of the precipitation similar to that of case 3, yielding a slightly delayed and smaller '*warm*' rainfall peak with respect to case 6–E and 6–δ_1 (Table 6.11). Over the steadier regime of the precipitation system, the rainfall rate follows somewhat that of case 1 with a quite higher intensity between 60 and 72 min produced by a small downdraft below the cloud base. Overall, the cumulative rain for this case 6–δ_2 shows an increase of 18% with respect to case 6–E.

When considered among the other ice nucleation mechanism, unrestricted deposition nucleation has a more limited impact on the global dynamics of the cloud and the resulting cumulative rain only varies by less than 1%. (Table 6.11, rainfall rate not represented on Figure 6.16b). In spite of this lack of impact, the INNE from case 2–δ_2 increases faster than the INNE from case 6–δ_2 by a factor of about 50 (Figure 6.15b), when the opposite would be expected: with all ice nucleation mechanisms active, there are more ice crystals formed and therefore a smaller relative humidity over ice, reducing the number of new ice crystals formed on unactivated particles.

In case 6–δ_2, most of the in–cloud ice nucleation took place around the homogeneous nucleation line, in a region where immersion freezing and homogeneous nucleation coexist when all mechanisms are considered together (Figure 6.11b). In case 2–δ_2, no deposition nucleation takes place in this region. The strong deposition nucleation (ice nucleation rate larger than 10^6 min^{-1}.m^{-3}) occurs at altitudes higher than 8 km, where homogeneous nucleation dominates the pristine ice formation.

This extreme deposition nucleation rates is the results of the freezing of all large droplets by homogeneous nucleation: each of these droplets contain a large amount of aerosol parti-

cles which increases the computed number of frozen crystals. This yields a high deposition nucleation rate in order to have a good agreement between the predicted and the computed frozen fraction.
In cloud deposition nucleation does not have a large impact on the overall cloud dynamics and precipitations when all ice nucleation mechanisms are considered in competition. However, the extreme deposition nucleation rate obtained because of the freezing of large droplets by homogeneous nucleation might be a problem in other cloud dynamics.

Finally, in case δ_3, the parameterization for immersion freezing on K–feldspar derived from the cold stage experiment in Chapter 3 is implemented in replacement of the Atkinson et al. (2013) parameterization.
The Chapter 3 parameterization has a narrower temperature range and is less efficient, therefore, ice nucleation starts later in the cloud development (the immersion freezing starts when the cloud top reaches 6.3 km) which yields an earlier precipitation onset both in the liquid (6.3 km at 33.9 min) and in the ice phase (6.7 km at 33.4 min). This results in an increased intensity of the '*warm*' rainfall peak.
The low efficiency of the parameterization of K–feldspar results in an increased impact of homogeneous nucleation, as was the case for illite (cases 2 and 4–B).

Overall, the Chapter 3 parameterization of immersion freezing on K–feldspar particles leads to an impact of K–feldspar on the cloud development similar to that of illite, whereas the Atkinson et al. (2013) parameterization yields a dominating behavior of K–feldspar.

6.4.3 Simplification of heterogeneous nucleation computation — cases ϵ_i

The implementation of INAS densities into DESCAM implied adding five additional size distributions: three for the total aerosol surface and two for the number of aerosol particles in the hydrometeors. Such a development is expensive in terms of computing time and memory use and cannot be done for models using more complex representations of the atmosphere, as for example the 3–D version of DESCAM, which furthermore cannot treat more than one aerosol particles type.
This sensitivity study contains two cases: in case ϵ_1, the added size distributions $\mathcal{N}$ and $\mathcal{S}$ are eliminated from the computation; in case ϵ_2, the size distributions for mineral particles are eliminated and ice nucleation is considered on the background aerosol particles only.

6.4.3.1 Modification of the model

Suppression of $\mathcal{N}$ and $\mathcal{S}$ (case ϵ_1)

In Figure 6.2, two very distinct regimes in the number of aerosol particles per drop were pointed out: for droplets smaller than 16 µm, freshly formed droplets where there is only one aerosol particle per droplet and for droplets larger than 16 µm, coalesced droplets where the number of aerosol particles per droplet is proportional to the droplet volume.
These two regimes are also to be observed when looking into the evolution of the total

Mineral	A_1	A_2	B_1	B_2	B_3
K–feldspar	0.5	20	$4.0 \cdot 10^{-2}$	5	$6.5 \cdot 10^{-2}$
Illite	0.5	20	$4.5 \cdot 10^{-2}$	5	$7.0 \cdot 10^{-2}$
Kaolinite	0.3	20	$9.0 \cdot 10^{-3}$	6	$1.4 \cdot 10^{-2}$
Quartz	0.4	20	$2.0 \cdot 10^{-2}$	6	$3.0 \cdot 10^{-2}$

Table 6.12 – Values for the fit of total surface and mass of aerosol particles in droplets (*see* equations 6.22 and 6.24).

surface as a function of the total mass of the aerosol particles for the '*reference*' case 1, then extrapolated to the cases where ice nucleation is considered:

$$\begin{cases} \mathcal{S}_d(j,kt) = A_1(kt) \cdot \exp(\frac{r_d(j)}{10}) \cdot \mathcal{M}_d^{\frac{2}{3}}(j,kt) & \text{if} \quad R_d \leq 16\,\mu\text{m} \\ \mathcal{S}_d(j,kt) = A_2(kt) \cdot \mathcal{M}_d(kt) & \text{otherwise} \end{cases} \tag{6.22}$$

where $A_i(kt)$ are the fit factors for the total surface in the droplets in bin j, for aerosol particles of type kt; values of A_i are listed in Table 6.12.
For the computation of immersion freezing, as the size distribution for the number of aerosol particles per droplet is eliminated, all size bins are computed using the total surface of aerosol particles per droplet, as was done in the case study γ_4.

The fit for $\mathcal{S}_d$ only applies to immersion freezing; for the unactivated aerosol particles dependent mechanisms (deposition nucleation and contact freezing), another simplification was chosen, based on the geometric relations between radius, surface and volume of an aerosol particle:

$$\mathcal{S}_a(j,kt) = 4\pi \cdot \mathcal{N}_a(j,kt) \cdot \left(\frac{3}{4\pi\rho_a} \cdot \frac{\mathcal{M}_a(j,kt)}{\mathcal{N}_a(j,kt)} \right)^{\frac{2}{3}} \tag{6.23}$$

where ρ_a represents the aerosol particles density; the same relation applies to the aerosol particles in ice crystals with $\mathcal{N}_i(j,kt) = \frac{\mathcal{M}_i(j,kt)}{\sum\limits_{kt} \mathcal{M}_i(j,kt)} \cdot N_i(j)$.

Suppression of the mineral size distributions (case ϵ_2)

In a second step of simplification, the mass of each aerosol particle types relatively to the total mass of aerosol particles was fitted using the following equation:

$$\begin{cases} \mathcal{M}_d(kt) = B_1 \cdot \sqrt[B_2]{r_d} \cdot \sum\limits_{kt} \mathcal{M}_d(kt) & \text{if} \quad r_d \leq 16\,\mu\text{m} \\ \mathcal{M}_d(kt) = B_3 \cdot \sum\limits_{kt} \mathcal{M}_d(kt) & \text{otherwise} \end{cases} \tag{6.24}$$

where $B_i(kt)$ are the fit factors for the total mass, for aerosol particles of type kt; values of B_i are listed in Table 6.12.

Case	Description	Rain	± Var.	First rain peak	
				Int. (mm.h^{-1})	Time (min)
Case ϵ_1	Simplified representation of $\mathcal{S}$				
	2–ϵ_1 — All ice nucleation	5.31	– 15 %	17.4	45.1
	4–ϵ_1 — Immersion freezing only	5.31	– 24 %	17.4	45.1
	5–ϵ_1 — Contact freezing only	8.58	– 0 %	106.5	43.1
	6–ϵ_1 — Deposition nucleation only	7.55	– 0 %	103.2	43.0
Case ϵ_2	Ice nucleation on a single aerosol type				
	2–ϵ_2 — All ice nucleation	5.39	+ 2 %	17.9	45.0
	4–ϵ_2 — Immersion freezing only	5.38	+ 1 %	17.9	45.0
	5–ϵ_2 — Contact freezing only	8.81	+ 3 %	104.1	43.1
	6–ϵ_2 — Deposition nucleation only	7.60	+ 1 %	103.4	42.9

Table 6.13 – List of sensitivity case studies on the simplification of heterogeneous ice nucleation computation and the results for the cumulative rain on the ground. The indicated variation corresponds to the variation with respect to the associated reference case for case ϵ_1 and to case ϵ_1 for case ϵ_2.

As was the case for the first simplification, this fit only applies to immersion freezing where the aerosol particles are activated into droplets. The simplification for deposition nucleation and contact freezing presents further challenges: for these two mechanisms, it is not possible to considered an homogeneous mixture of background and mineral aerosol particles.

For contact freezing, the number and mass of the different mineral aerosol particles are computed as follows:

$$\mathcal{N}_{a,\mathrm{mrl}}(i,kt) = \frac{\mathcal{N}_{a,\mathrm{bkg}}(i)}{\mathcal{F}_{\mathrm{bkg}}(i)} \cdot \mathcal{F}_{\mathrm{mrl}}(i,kt) \tag{6.25}$$

with $\mathcal{F}_{\mathrm{mrl}}(i)$ the original number concentration of the mineral aerosol particles in size bin i as presented in Figure 6.1 and $\mathcal{F}_{\mathrm{bkg}}(i)$ the original number concentration of the background aerosol particles.

The same calculation is applied to deposition nucleation for the number and mass of unactivated aerosol particles. But deposition nucleation computes a frozen fraction on the aerosol particles. As the information on the mass of aerosol particles of each type in the ice crystals is not available this frozen fraction cannot be properly computed without introducing another size distribution.
Furthermore, as all the fits regarding mineral aerosol particles in the model are determined with respect to the background aerosol particles, it is not possible to parameterize the surface and number of mineral aerosol particles in the ice crystals due to the passivity of the background aerosol particles in the ice nucleation; and a parameterization based on case 6–E is not an option as it would be dependent on the deposition nucleation INAS density parameterizations of each of the minerals.
The most simple and efficient solution found was to consider that all the aerosol mass in the ice crystal corresponded simultaneously to all mineral aerosol types. This assumption systematically overestimates the amount of mineral aerosol particles in the ice crystals and therefore minimizes the deposition nucleation efficiency.

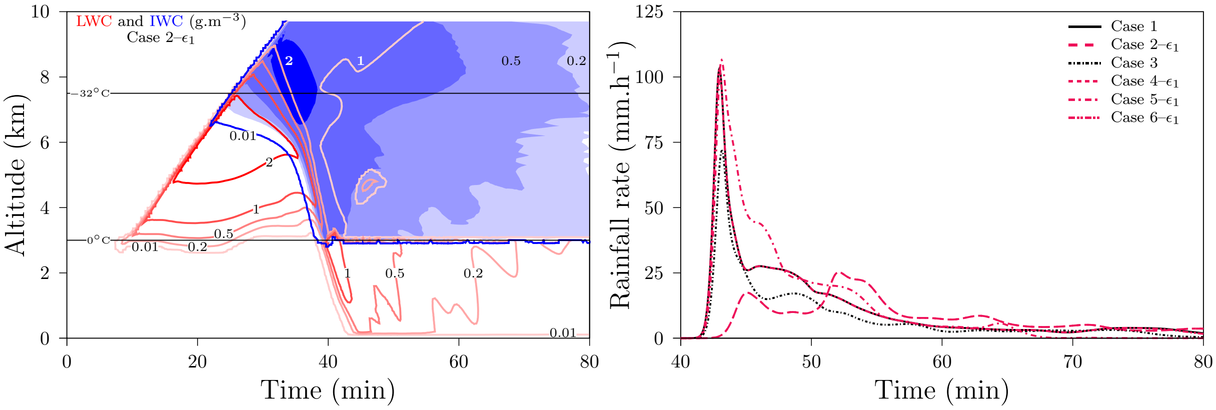

Figure 6.17 – (**a**, left) Liquid water content (g.m^{-3}, red) and ice water content (g.m^{-3}, blue) simulated by DESCAM as a function of altitude and time for the case with all minerals active as INP and all ice nucleation mechanisms active with a simplified representation of $\mathcal{S}$ (case 2–ϵ_1). (**b**, right) Time evolution of the rainfall rate (mm.h^{-1}) for the only–liquid case (case 1, continuous), for simplified representation of $\mathcal{S}$ with all minerals ice active for all ice processes (case 2–ϵ_1, pink dashed), homogeneous nucleation (case 3, black short dashed–dotted), immersion freezing (case 4–ϵ_1, pink short dashed), contact freezing (case 5–ϵ_1, pink dotted–dashed) and deposition nucleation (case 6–ϵ_1, pink double dotted–dashed).

6.4.3.2 Results

The cumulative precipitations and rainfall characteristics of the different ϵ cases are listed in Table 6.13.

Case ϵ_1

In Figure 6.17a is presented the evolution of the cloud in with all ice nucleation mechanisms and aerosol particles considered as active and a simplified representation of the total surface of aerosol particles in the model.

The dynamics of the cloud is similar in case 2–ϵ_1 to that of case 2–E. Ice nucleation through immersion freezing starts at 5 km as for case 2–E and gradually intensifies until the cloud top reaches 6.8 km. To the difference of case 2–E, the ice nucleation rate remains at a high level until the cloud top reaches 8.2 km. All the ice nucleation at high altitude occurs through the immersion freezing mechanism and homogeneous nucleation does not contribute to the pristine ice formation: the large droplets are already frozen by the immersion freezing mechanism as they reach the homogeneous nucleation level.

The precipitation onset is delayed with respect to case 2–E and occurs at lower altitudes, as can be expected from the increased immersion freezing rate on large droplets, yielding a stronger updraft. As was pointed out in every case where more ice crystals were formed in the updraft, there is a decrease in the precipitating total water content. These two factors result in a more delayed and reduced '*warm*' rainfall peak. Furthermore, as the crystals reach smaller sizes due to the increased competition for depositional growth, the remaining rainfall also has a smaller intensity than in case 2–E. The cumulative precipitation reflects this, with a decrease of 20%.

The immersion freezing only case 4–ϵ_1 is identical to case 2–ϵ_1: the deposition nucleation and contact freezing mechanism have the exact same impact as in the reference cases and as mentioned in the previous paragraph, homogeneous nucleation does not contribute to the pristine ice formation.

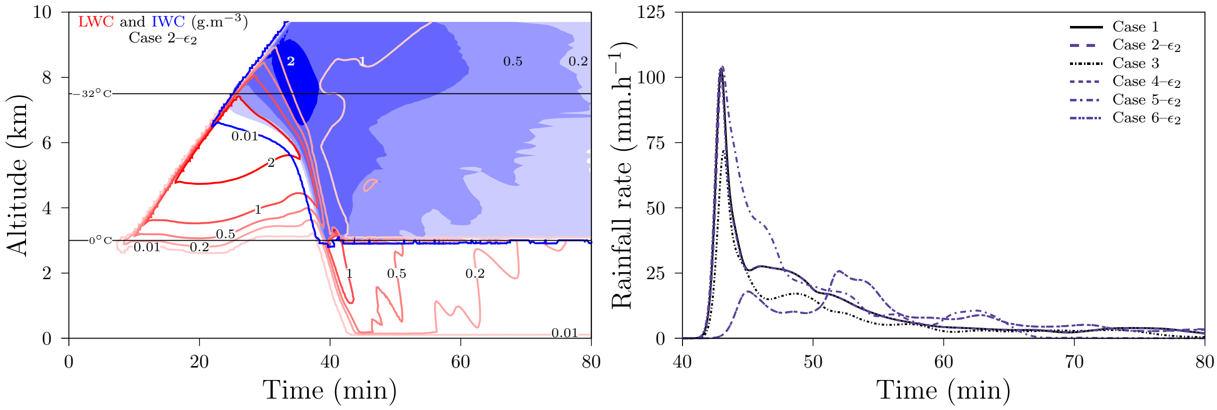

Figure 6.18 – (**a**, left) Liquid water content (g.m^{-3}, red) and ice water content (g.m^{-3}, blue) simulated by DESCAM as a function of altitude and time for the case with all minerals active as INP and all ice nucleation mechanisms active with a simplified representation of $\mathcal{S}$ with only one type of aerosol particles (case 2–ϵ_2). (**b**, right) Time evolution of the rainfall rate (mm.h^{-1}) for the only–liquid case (case 1, continuous), for simplified representation of $\mathcal{S}$ and only one type of aerosol particles with all minerals ice active for all ice processes (case 2–ϵ_2, purple dashed), homogeneous nucleation (case 3, short dashed–dotted), immersion freezing (case 4–ϵ_2, purple short dashed), contact freezing (case 5–ϵ_2, purple dotted–dashed) and deposition nucleation (case 6–ϵ_2, purple double dotted–dashed).

The integrated number of ice nucleation events for immersion freezing is increased by a factor 3.5 with respect to case 4–E and a factor 3 with respect to case 4–γ_4 (Figures 6.15a and 6.19a, with the INNE for case 4–ϵ_1 identical to that of case 2–ϵ_1). This increase is due to the high ice nucleation rates found at high altitudes that are particular to the cases ϵ_1, which indicate an overestimation of the total surface of aerosol particle per droplet for the larger droplets.

Case ϵ_2

In figure 6.18a is displayed the evolution of the cloud in with all ice nucleation mechanisms with a simplified representation of the total surface of aerosol particles in the model; only the background aerosol particle size distribution is considered in the model and the mineral particles on which heterogeneous ice nucleation occurs are represented as a function of the background aerosol number and mass size distributions.

The dynamical evolution of the cloud is almost identical to that of case ϵ_1. There is only marginal changes in the in–cloud nucleation rates in case 2–ϵ_2, at altitudes above 7 km and after 35 min of simulation and does not impact the cloud evolution and the precipitations. The differences in the cumulative rain and precipitation structure between cases 2–ϵ_1 and 2–ϵ_2 originate in the concentration of the mineral aerosol particles which is set to $0 \cdot c_0$.

There are larger differences between cases ϵ_1 and ϵ_2 for contact freezing and deposition nucleation. For the former mechanism, the approximation made in case ϵ_2 increases the contact freezing efficiency. At the beginning of the downdraft, between 6 and 7 km of altitude, there is over a couple of minutes an increased ice nucleation rate when some unactivated aerosol particles are entrained from the environmental cylinder. This results in an overall increase of the INNE by a factor 8 (Figure 6.19). As this high ice nucleation rate occurs along the downdraft as the precipitations are already formed, it has very little impact on the total cumulative rain.

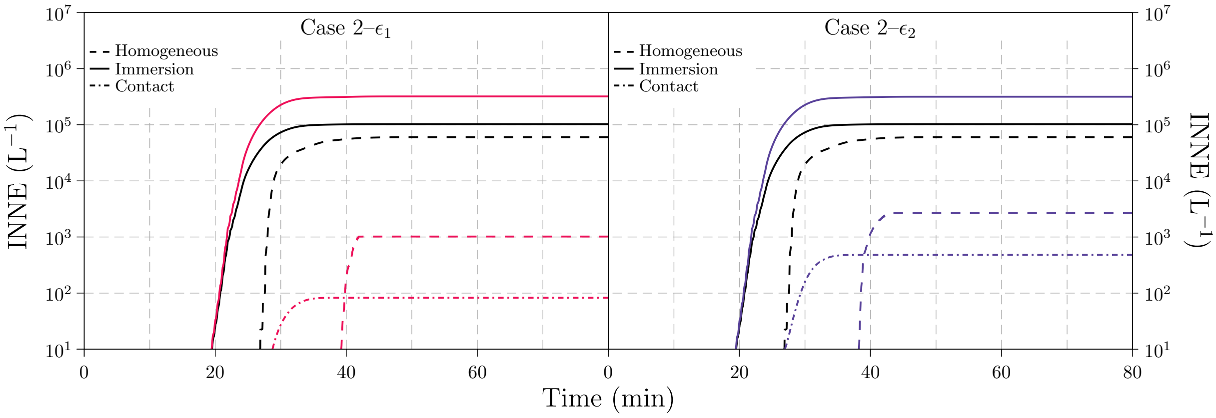

Figure 6.19 – (**a**, left)Integrated number of ice nucleation events (INNE) for immersion freezing (continuous) and homogeneous nucleation (dashed) when all ice nucleation mechanisms are considered as active for cases 2–ϵ_1 (pink) and 2–E (black); the contact freezing INNE is shown for case 2–ϵ_1 (dotted–dashed pink), the other ice nucleation mechanism don't yield enough pristine ice to appear. (**b**, right) INNE integrated number of ice nucleation events (INNE) for immersion freezing (continuous) and homogeneous nucleation (dashed) when all ice nucleation mechanisms are considered as active for cases 2–ϵ_2 (purple) and 2–E (black); the contact freezing (dotted–dashed purple) is also shown for case 2–ϵ_2.

Deposition nucleation in case ϵ_2 evolves in a different manner from cases E and ϵ_1: as it is assumed that all formed ice crystal contain one particle of each mineral, the frozen fraction is systematically overestimated, therefore, after the first ice crystals have been nucleated, no ice nucleation occurs until the larger crystals sediment out of the 'complete' altitudes. This yields a decrease in the INNE for deposition nucleation by a factor 2 with respect to case ϵ_1.

The results obtained when simplifying the representation of heterogeneous nucleation on mineral particles in cases ϵ_1 and ϵ_2 are consistent between them and with the results obtained with the complete representation of the reference cases (§6.3.2). There are some differences in the ice nucleation efficiencies obtained in the different cases, but except for contact freezing, they imply a variation of the integrated number of heterogeneous nucleation events by less than a factor 4 resulting in variations on the cumulative rain of less than 20%. More importantly, those variation reflect only uncertainties in the intensity of the rain but not on the structure of the precipitation event.
The variation in cumulative rain due to the simplification of the representation of heterogeneous nucleation on mineral particles is equivalent to the variation obtained when the concentration of the mineral particles is decreased by a factor 3.

6.5 Summary

Aerosol–specific heterogeneous ice nucleation parameterization were implemented into DESCAM to further investigate the importance of the different ice nucleation mechanisms studied in Chapter 5. Focus was brought to mineral aerosol particles, using recent parameterizations derived from laboratory experiments.

The results using aerosol specific parameterization for heterogeneous nucleation showed the robustness of the conclusions from Hiron and Flossmann (2015). Because of dynamics of the cloud and the small activation radius for the aerosol particles in the CCOPE cloud, ice nucleation mechanisms based on unactivated aerosol particles only play a minor role in the evolution of the cloud. They have an impact when considered as only ice nucleation mechanism (case 5–E and 6–δ_2) but are dominated by the droplet–based mechanisms when considered all together. However, in out–of–cloud conditions, it is heterogeneous ice nucleation that is responsible for the formation of the cirrus–like cloud at high altitudes. Immersion freezing — corresponding to both immersion and condensation freezing in Chapter 5 and Hiron and Flossmann (2015) — dictates the dynamics of the cloud as it is active early in the development. The large droplets freeze through homogeneous nucleation when they reach temperatures below −32°C when the mechanism is considered alone, but when all mechanisms are active, the impact of homogeneous nucleation is reduced as the larger droplets freeze with a higher efficiency through immersion freezing.

It was postulated in Chapter 5, that condensation freezing — immersion freezing on droplets smaller than 16 µm, parameterized using the Meyers et al. (1992) parameterization — had a large impact on the dynamics of the cloud because of its ability to form ice crystals early in the cloud development, slowing the growth of the cloud droplets. This has been confirmed by the current study (cases 2 and 4–γ_1), even though the effect was not as important as in Chapter 5, as immersion freezing is less active at low altitudes. The temperature independence of Meyers et al. (1992) allows for high ice nucleation rates at high temperatures, where mineral particles are rather inactive. Aerosols of biological origin could replicate this efficiency at high temperature but were out of scope for the current study.

As it is the most present mineral in the model (with mineral size distributions based on *in situ* measurements from Kandler et al., 2009) and the most ice active mineral in all modes of heterogeneous nucleation, K–feldspar naturally has the largest impact on the development of the cloud. When all minerals are considered together as ice active, the high nucleation efficiency of K–feldspar reduces ice nucleation by the other minerals for contact and immersion freezing on large droplets. For deposition nucleation and immersion freezing on freshly formed small droplets, each mineral forms pristine ice independently as they are considered as separate elements.

The impact of ice nucleation on the dynamics and on the precipitations, with respect to a reference case where no ice nucleation mechanism is active, varies depending on the mineral aerosols concentration or the characteristics of the background aerosol particles (chemical properties and size distribution). However, the conclusions on the relative impact of each mechanism and its role in the evolution of the cloud are rather independent of these parameters.

The parameterizations determined for K–feldspar in the Part I on cold stage experiments were implement into the model. The deposition nucleation parameterization (Chapter 4) as primary parameterization, given that no publication on the matter was found; the immersion freezing parameterization (Chapter 3) as a sensitivity study, because the temperature range in which the experiments were conducted do not cover the warm temperatures obtained by Atkinson et al. (2013). Both parameterizations confirmed the relevance of K–feldspar for ice nucleation in a convective cloud.

Finally, a first step towards the adaptation of INAS density representation for dynamically more complex models (*e.g.* the 3–D version of DESCAM) was made by simplifying the computation through parameterizations of the surface of aerosol particles as a function of their masses in the bins of the different reservoirs (aerosol particles, droplets or ice crystals) and a parameterization of the mass of mineral aerosol particles as a function of the mass of background aerosol particles.
These simplifications implied some variations in the integrated number of ice nucleation events by a factor up to 4. But those variations do not change the relative importance of the different heterogeneous ice nucleation mechanisms.

Overall, the results from Hiron and Flossmann (2015) have been further investigated and confirmed for a convective cloud. The adaptation of this study for different types of dynamics have been prepared through a simplified representation of aerosol–specific heterogeneous ice nucleation and will be investigated in later studies.

Conclusion

Summary and Outlook

The understanding of the formation of ice crystals in the atmosphere, called ice nucleation, is of crucial importance to both climate modeling and weather prediction. Ice nucleation comprises two different types of mechanisms: homogeneous nucleation, where ice develops within the liquid water phase; and heterogeneous nucleation, where ice develops on the surface of a solid aerosol particle. This thesis aimed at providing a better understanding of heterogeneous nucleation and its impact on cloud development through experiment and modeling.

The experimental work relied on the development of a flow cell for a cold stage experiment previously developed at the Institute for Meteorology — Atmospheric Aerosol Research division (IMK–AAF) in Karlsruhe, in order to broaden the range of ice nucleation mechanisms that could be investigated.
Using this new setup, a series of cooling experiments have been conducted to investigate immersion freezing and deposition nucleation on K–feldspar, an atmospherically relevant mineral aerosol particle identified as one of the most ice active minerals. These experiments were conducted to achieve two goals: explore the relationship between immersion freezing and deposition nucleation induced by mineral dust particles and to provide ice nucleating active sites (INAS) density parameterizations for both ice nucleation mechanisms as input for models.

The experimental study extended the work of Peckhaus et al. (2016) who used the same cold stage setup but without the flow cell. Three suspensions containing K–feldspar particles were prepared with concentrations between $2.5 \cdot 10^{-1}$ and $2.5 \cdot 10^{-3}\,\mathrm{g.L^{-1}}$. The results obtained for immersion freezing were found to be in agreement with those of Peckhaus et al. (2016) for the lower temperature range investigated, as the low aerosol particle concentration used in this study limited the investigation to temperatures below −20°C. As has been already suggested by other studies (Peckhaus et al., 2016; Steinke, 2013), a high correlation in the freezing ranks between successive immersion freezing experiments was observed.
The droplets containing the K–feldspar were then evaporated, leaving residual particles on the silicon substrate that have been exposed to humidified gas flow held at a constant frost point temperature. The dew point temperatures investigated ranged between −20 and −33°C. At temperatures above −24°C, droplet condensation on the residual particles have been observed, allowing to explore condensation freezing. At lower temperatures, deposition nucleation was observed.
The condensation freezing experiments showed a very good agreement with the immersion freezing experiments in the temperature evolution of the frozen fraction.

No clear trend in the order of crystal appearance was observed for consecutive deposition nucleation experiments. However, the analysis of the order of appearance correlation for the two more concentrated solutions was rendered difficult as more than one ice nucleating active site for deposition nucleation was identified per evaporated droplet. The less concentrated suspension offered only one ice nucleating active site per evaporated droplet, allowing to compare ice nucleation of individual residual particles between immersion freezing and deposition nucleation experiments.
These experiments have shown that droplets frozen heterogeneously at higher temperatures contained feldspar particles responsible for deposition nucleation of ice at lowest on–set supersaturations.

This indicated that *the good ice nucleating active sites in the immersion freezing mode are also good active sites in the deposition nucleation mode.*
This could imply that the two ice nucleation mechanisms are competing over dominating ice nucleation. For example, particles that served as ice nuclei in the immersion freezing mode in a precipitating cloud would not be available for deposition nucleation at a later stage or in a different cloud because of the wet removal of the particles by the precipitation.

The modeling work was aimed at generalizing the experimental work and at gaining a broader insight into the ice formation mechanisms. It used the Detailed Scavenging Model (DESCAM) developed at the Laboratoire de Méréorologie Physique (LaMP) by Flossmann et al. and her colleagues since 1985. DESCAM is a bin–resolved cloud–resolving model, coupled in this thesis to a 1.5–D dynamical frame work simulating the well documented convective cloud of the Cooperative COnvective Precipitation Experiment (CCOPE). In this frame work, the response of a strong convective cloud system to the different heterogeneous ice nucleation mechanisms was investigated.
In a first step, non–aerosol–specific parameterizations were implemented into DESCAM and their respective impact on the dynamic of the cloud was assessed by first considering each mechanism as the only ice formation pathway and then by considering their respective role in ice formation when all mechanisms were contributing to the pristine ice formation. Heterogeneous nucleation on freshly formed droplets (condensation freezing) had the most impact on the cloud because of its efficiency at warm temperatures: ice nucleation starts early in the cloud development which changes slightly the dynamics through the latent heat release of freezing, increasing the buoyancy in the updraft and more importantly, the Bergeron process reduces the maximal size of the droplets in the cloud. This delays the formation of the precipitations on the ground and largely impacts the cumulative rain.
But these non–aerosol–specific parameterizations have some limitations in their usefulness as the heterogeneous nucleation processes depend the number concentration and size as well as physicochemical properties of the aerosol particles that serve as ice nucleating particle (INP) in the atmosphere.

Therefore, the INAS density approach to heterogeneous nucleation was implemented into DESCAM.
The same ice nucleation mechanisms as in the non–aerosol–specific modeling study were considered and mineral particles were chosen as the INP, because of their well documented atmospheric relevance and their important ice nucleating properties, documented

in laboratory and field measurements. Four types of minerals were implemented into DESCAM with number concentration size distributions derived from *in–situ* measurements: K–feldspar (*ca* 20% of the original mineral number concentration in Kandler et al., 2009, representing *ca* 35% of the total number of mineral particles implemented to DESCAM), illite (*ca* 40% of the implemented minerals), kaolinite (*ca* 8%) and quartz (*ca* 17%). INAS density parameterizations were taken from the literature with the exception of deposition nucleation on K–feldspar and quartz, for which no parameterizations have been found.
Based on the data obtained in the cold stage experiment, also a parameterization for immersion freezing and one for deposition nucleation on K–feldspar particles were derived. The deposition nucleation parameterization was based on a small number of experiments containing a rather small number of crystals and need to be confirmed by further experiments in the future. However, being the only existing parameterization for deposition nucleation on K–feldspar, it was implemented as the default parameterization in DESCAM. To ensure robustness of the conclusions, a sensitivity study using an Arizona Test Dust based parameterization was also conducted.

The implementation of INAS densitiy parameterizations into the model ensured a better representation of heterogeneous ice nucleation: the mechanisms now depend on the size of the aerosol particles, which was not the case *e.g.* in the Meyers et al. (1992) parameterization. Previous experimental studies (*see e.g.* Hoffmann, 2015) have already shown a size dependence of ice nucleating efficiency: the larger the aerosol particle, the higher the frozen fraction; therefore, replacing non–aerosol–specific parameterizations by INAS density reprensentations of ice nucleation improves the robustness of the conclusions from those modeling studies.
In this thesis, the results for the study using the INAS density representation for heterogeneous nucleation confirmed those from the non–aerosol–specific study: immersion freezing has the most impact on the cloud development because of its activity early in the cloud development. However, the immersion freezing on freshly formed droplets did not have as much impact on the convective cloud dynamics as in the first study because it was not active at as warm temperatures, reducing the influence of the Bergeron process.
The two mechanisms dependent on unactivated aerosol particles (contact freezing and deposition nucleation) played a negligible role in the dynamical evolution of the cloud, as had already been observed in the first part of the study. However, this conclusion might be biased by the cloud studied: the strong convective case used in these thesis yields an activation radius slightly larger than 100 nm, which is considered as the minimal radius for potential INP (Pruppacher and Klett, 1997). Therefore, there are only a few potential candidates for ice nucleation by contact freezing and deposition left inside the cloud, as all others have already served as cloud condensation nuclei.

Extensive sensitivity studies were conducted to test the influence of various parameters (*e.g.* aerosol distribution, computation algorithm).

Among the considered minerals, K–feldspar was found to have the strongest impact on the development of the cloud, both because of its high nucleation activity (immersion freezing was observed in laboratory experiments for temperatures as warm as −5°C) and

of its relatively high number concentration with respect to other minerals.
Kaolinite was found to have the least impact due to its low abundance and ice nucleating properties.

Outlook

The new cold stage setup proved to be efficient to gain theoretical knowledge on ice nucleation in immersion freezing and deposition nucleation modes. However, the sample on which the study was conducted was rather small. More experiments are needed to further investigate the underlying question of the thesis: *does being a good immersion freezing ice nucleus mean being a good deposition nucleation ice nucleus?*.
The experimental methodology needs to be improved in order to increase the range of dew point temperatures achievable in the flow cell chamber.

Furthermore, an improved methodology with adapted residual particle counts are needed to obtain a more reliable parameterization for deposition nucleation using this setup: a larger number of deposited droplets with only one ice nucleating active site would yield a better statistical analysis of deposition nucleation and a more reliable calculation of INAS densities.
The combination of the cold stage experiments to environmental electron microscopy (ESEM) would provide further information on the structure of the most active INP.

Such improvement would increase the level of confidence for a deposition nucleation parameterization based on the experimental data. Furthermore, even though the results presented in this thesis are robust, they only apply to a certain type of dynamics. It is necessary to look into the impact of the different ice nucleation mechanisms on the cloud development for other dynamics as well (*e.g.* stratiform clouds).

Furthermore, a more complex dynamics, for example in 3–D models should be privileged. The parameterization of the number and mass concentration of mineral aerosol particles as a function of the background aerosol number and mass concentration as well as a simplification of the heterogeneous ice nucleation computation schemes have already been proposed in Chapter 6.

It was indicated in this thesis that immersion freezing and deposition nucleation were probably occurring on the same active sites. Possible improvements in the experimental procedure should ideally yield a parameterization linking immersion freezing and deposition nucleation, in a relationship of the following type:

$$n_{s,\mathrm{dep}}(T, RH_i) = n_{s,\mathrm{imm}}(T) \cdot f(T, RH_i)$$

Such a parameterization can then be tested in a modeling study.

Bibliography

Asai, T., and A. Kasahara, 1967: A theoretical study of the compensating downward motions associated with cumulus clouds. *Journal of the Atmospheric Sciences*, **24 (5)**, 487–496, doi:10.1175/1520-0469(1967)024<0487:atsotc>2.0.co;2.

Atkinson, J. D., B. J. Murray, M. T. Woodhouse, and Coauthors, 2013: The importance of feldspar for ice nucleation by mineral dust in mixed–phase clouds. *Nature*, **498 (7454)**, 355–358, doi:10.1038/nature12278.

Ault, T. R., J. E. Cole, J. T. Overpeck, G. T. Pederson, and D. M. Meko, 2014: Assessing the risk of persistent drought using climate model simulations and paleoclimate data. *Journal of Climate*, **27 (20)**, 7529–7549, doi:10.1175/jcli-d-12-00282.1.

Bangert, M., A. Nenes, B. Vogel, and Coauthors, 2012: Saharan dust event impacts on cloud formation and radiation over western europe. *Atmospheric Chemistry and Physics*, **12 (9)**, 4045, doi:10.5194/acp-12-4045-2012.

Bergeron, T., 1935: On the physics of cloud and precipitation. *Proc. 5th Assembly IUGG Lisbon*, Vol. 2, 156.

Bigg, E., 1953: The formation of atmospheric ice crystals by the freezing of droplets. *Quarterly Journal of the Royal Meteorological Society*, **79 (342)**, 510–519, doi:10.1002/qj.49707934207.

Boose, Y., B. Siereau, M. I. García, and Coauthors, 2016: Ice nucleating particles in the saharan air layer. *Atmospheric Chemistry and Physics*, **16 (14)**, 9067–9087, doi:10.5194/acp-16-9067-2016.

Bott, A., 1989: A positive definite advection scheme obtained by nonlinear renormalization of the advective fluxes. *Monthly Weather Review*, **117 (5)**, 1006–1016, doi:10.1175/1520-0493(1989)117<1006:apdaso>2.0.co;2.

Bott, A., 1998: A flux method for the numerical solution of the stochastic collection equation. *Journal of the Atmospheric Sciences*, **55 (13)**, 2284–2293, doi:10.1175/1520-0469(1998)055<2284:afmftn>2.0.co;2.

Bourges-Monnier, C., and M. Shanahan, 1995: Influence of evaporation on contact angle. *Langmuir*, **11 (7)**, 2820–2829, doi:10.1021/la00007a076.

Brunauer, S., P. H. Emmett, and E. Teller, 1938: Adsorption of gases in multimolecular layers. *Journal of the American Chemical Society*, **60 (2)**, 309–319, doi:10.1021/ja01269a023.

Burrows, S. M., W. Elbert, M. Lawrence, and U. Pöschl, 2009: Bacteria in the global atmosphere — Part 1: Review and synthesis of literature data for different ecosystems. *Atmospheric Chemistry and Physics*, **9 (23)**, 9263–9280, doi:10.5194/acpd-9-10777-2009.

Cardwell, J., P. Field, and T. Choularton, 2003: A modelling study of ice–spectrum modes in deep frontal clouds. *Quarterly Journal of the Royal Meteorological Society*, **129 (591)**, 1873–1890, doi:10.1256/qj.01.133.

Chauvigné, A., K. Sellegri, M. Hervo, and Coauthors, 2016: Comparison of the aerosol optical properties and size distribution retrieved by sun photometer with in situ measurements at midlatitude. *Atmospheric Measurement Techniques*, **9 (9)**, 4569, doi:10.5194/amt-9-4569-2016.

Choobari, O. A., P. Zawar-Reza, and A. Sturman, 2014: The global distribution of mineral dust and its impacts on the climate system: A review. *Atmospheric Research*, **138**, 152–165, doi:10.1016/j.atmosres.2013.11.007.

Cotton, W. R., R. Pielke Sr, R. Walko, and Coauthors, 2003: RAMS 2001: Current status and future directions. *Meteorology and Atmospheric Physics*, **82 (1-4)**, 5–29, doi:10.1007/s00703-001-0584-9.

Cziczo, D. J., K. D. Froyd, C. Hoose, and Coauthors, 2013: Clarifying the dominant sources and mechanisms of cirrus cloud formation. *Science*, **340 (6138)**, 1320–1324, doi:10.1126/science.1234145.

DeMott, P. J., 1995: Quantitative descriptions of ice formation mechanisms of silver iodide–type aerosols. *Atmospheric Research*, **38 (1)**, 63–99, doi:10.1016/0169-8095(94)00088-u.

DeMott, P. J., D. C. Rogers, and S. M. Kreidenweis, 1997: The susceptibility of ice formation in upper tropospheric clouds to insoluble aerosol components. *Journal of Geophysical Research: Atmospheres*, **102 (D16)**, 19 575–19 584, doi:10.1029/97jd01138.

DeMott, P. J., A. J. Prenni, X. Liu, and Coauthors, 2010: Predicting global atmospheric ice nuclei distributions and their impacts on climate. *Proceedings of the National Academy of Sciences*, **107 (25)**, 11 217–11 222, doi:10.1073/pnas.0910818107.

DeMott, P. J., O. Möhler, O. Stetzer, and Coauthors, 2011: Resurgence in ice nuclei measurement research. *Bulletin of the American Meteorological Society*, **92 (12)**, 1623–1635, doi:10.1175/2011bams3119.1.

Diehl, K., and S. Wurzler, 2004: Heterogeneous drop freezing in the immersion mode: Model calculations considering soluble and insoluble particles in the drops. *Journal of the Atmospheric Sciences*, **61 (16)**, 2063–2072, doi:10.1175/1520-0469(2004)061<2063:hdfiti>2.0.co;2.

Duft, D., and T. Leisner, 2004: Laboratory evidence for volume–dominated nucleation of ice in supercooled water microdroplets. *Atmospheric Chemistry and Physics*, **4 (7)**, 1997–2000, doi:10.5194/acpd-4-3077-2004.

Dye, J., J. Jones, W. Winn, and Coauthors, 1986: Early electrification and precipitation development in a small, isolated montana cumulonimbus. *Journal of Geophysical Research: Atmospheres*, **91 (D1)**, 1231–1247, doi:10.1029/jd091id01p01231.

Eastwood, M. L., S. Cremel, C. Gehrke, E. Girard, and A. K. Bertram, 2008: Ice nucleation on mineral dust particles: Onset conditions, nucleation rates and contact angles. *Journal of Geophysical Research: Atmospheres*, **113 (D22)**, doi:10.1029/2008jd010639.

Emde, K., and P. Kahlig, 1989: Comparison of the observed 19th july 1981, Montana thunderstorm with results of a one–dimensional cloud model using Kessler parameterized microphysics. *Annales Geophysicae*, Vol. 7, 405–414.

Flossmann, A. I., 1987: A theoretical investigation of the removal of atmospheric trace constituents by means of a dynamic model. Ph.D. thesis, Johannes-Gutenberg Universität, Mainz.

Flossmann, A. I., W. Hall, and H. R. Pruppacher, 1985: Theoretical study of the wet removal of atmospheric pollutants. Part I: The redistribution of aerosol particles captured through nucleation and impaction scavenging by growing cloud drops. *Journal of the Atmospheric Sciences*, **42 (6)**, doi:10.1175/1520-0469(1985)042<0583:atsotw>2.0.co;2.

Flossmann, A. I., and W. Wobrock, 2010: A review of our understanding of the aerosol–cloud interaction from the perspective of a bin resolved cloud scale modelling. *Atmospheric Research*, **97 (4)**, 478–497, doi:10.1016/j.atmosres.2010.05.008.

Flossmann, A. I., and W. Wobrock, 2012: Will pollution reduce precipitations? *Air Pollution Modeling and its Application XXI*, 949–957.

Fujikawa, S., T. Akamatsu, J. Yahara, and H. Fujioka, 1982: Studies of liquid–vapour phase change by a shock tube. *Applied Scientific Research*, **38 (1)**, 363–372, doi:10.1007/bf00385966.

Garimella, S., Y.-W. Huang, J. S. Seewald, and D. J. Cziczo, 2014: Cloud condensation nucleus activity comparison of dry– and wet–generated mineral dust aerosol: the significance of soluble material. *Atmospheric Chemistry and Physics*, **14 (12)**, 6003–6019, doi:10.5194/acp-14-6003-2014.

GESIM, 2014: Nanolitre dosage piezoelectric microdispensers.

Gibson, E. R., K. M. Gierlus, P. K. Hudson, and V. H. Grassian, 2007: Generation of internally mixed insoluble and soluble aerosol particles to investigate the impact of atmospheric aging and heterogeneous processing on the CCN activity of mineral dust aerosol. *Aerosol Science and Technology*, **41 (10)**, 914–924, doi:10.1080/02786820701557222.

Halder, M., A. Hazra, P. Mukhopadhyay, and D. Siingh, 2015: Effect of the better representation of the cloud ice–nucleation in WRF microphysics schemes: A case study of a severe storm in India. *Atmospheric Research*, **154**, 155–174, doi:10.1016/j.atmosres.2014.10.022.

Hall, W. D., 1980: A detailed microphysical model within a two–dimensional dynamic framework: Model description and preliminary results. *Journal of the Atmospheric Sciences*, **37 (11)**, 2486–2507, doi:10.1175/1520-0469(1980)037<2486:admmwa>2.0.co;2.

Hallett, J., and S. Mossop, 1974: Production of secondary ice particles during the riming process. *Nature*, **249 (5452)**, 26, doi:10.1038/249026a0.

Hande, L., C. Engler, C. Hoose, and I. Tegen, 2015: Seasonal variability of saharan desert dust and ice nucleating particles over europe. *Atmospheric Chemistry and Physics*, **15 (8)**, 4389–4397, doi:10.5194/acp-15-4389-2015.

Harrison, A. D., T. F. Whale, M. A. Carpenter, and Coauthors, 2016: Not all feldspars are equal: a survey of ice nucleating properties across the feldspar group of minerals. *Atmospheric Chemistry and Physics*, **16 (17)**, 10 927–10 940, doi:10.5194/acp-16-10927-2016.

Herbert, R. J., B. J. Murray, S. J. Dobbie, and T. Koop, 2015: Sensitivity of liquid clouds to homogenous freezing parameterizations. *Geophysical research letters*, **42 (5)**, 1599–1605.

Hirabayashi, Y., R. Mahendran, S. Koirala, and Coauthors, 2013: Global flood risk under climate change. *Nature Climate Change*, **3 (9)**, 816–821, doi:10.1038/nclimate1911.

Hiranuma, N., S. Augustin-Bauditz, H. Bingemer, and Coauthors, 2015: A comprehensive laboratory study on the immersion freezing behavior of illite NX particles: a comparison of 17 ice nucleation measurement techniques. *Atmospheric Chemistry and Physics*, **15 (5)**, 2489–2518, doi:10.5194/acp-15-2489-2015.

Hiron, T., 2011: Experimentelle beobachtung des heterogenen gefrierens von wolkentropfen und numerische modellierung der gefrierdynamik. M.S. thesis, Département de Physique, École Normale Supérieure de Cachan.

Hiron, T., 2013: Étude de la formation des cristaux de glace sur les bioaérosols pour améliorer l'initiation d'événements pluvieux. M.S. thesis, Laboratoire de Météorologie Physique, Université Blaise Pascal.

Hiron, T., and A. I. Flossmann, 2015: A Study of the Role of the Parameterization of Heterogeneous Ice Nucleation for the Modeling of Microphysics and Precipitation of a Convective Cloud. *Journal of the Atmospheric Sciences*, **72 (9)**, 3322–3339, doi:10.1175/jas-d-15-0026.1.

Hoffmann, N., 2015: Experimental Study on the Contact Freezing of Supercooled Micro–Droplets in Electrodynamic Balance. Ph.D. thesis, Ruprecht-Karls-Universität Heidelberg, doi:10.11588/heidok.00018744.

Hoose, C., J. E. Kristjánsson, and S. M. Burrows, 2010: How important is biological ice nucleation in clouds on a global scale? *Environmental Research Letters*, **5**, 024 009, doi:10.1088/1748-9326/5/2/024009.

Hoose, C., and O. Möhler, 2012: Heterogeneous ice nucleation on atmospheric aerosols: a review of results from laboratory experiments. *Atmospheric Chemistry and Physics*, **12 (20)**, 9817–9854, doi:10.5194/acpd-12-12531-2012.

IPCC, 2013: *The Physical Science Basis. Working Group I Contribution to the Fifth Assessment Report of the Intergovernmental Panel on Climate Change*. Cambridge University Press. [Available online at http://www.ipcc.ch/report/ar5/wg1/.]

Jaenicke, R., 1988: Aerosol physics and chemistry. *Numerical Data and Functional Relationships in Science and Technology*, G. Fischer, Ed., Vol. 4b, 391–457.

Kandler, K., L. Schütz, C. Deutscher, and Coauthors, 2009: Size distribution, mass concentration, chemical and mineralogical composition and derived optical parameters of te boundary layer aerosol at Tinfou, Morocco, during SAMUM 2006. *Tellus B*, **61 (1)**, 32–50, doi:10.3402/tellusb.v61i1.16798.

Kärcher, B., and U. Lohmann, 2003: A parameterization of cirrus cloud formation: Heterogeneous freezing. *Journal of Geophysical Research: Atmospheres*, **108 (D14)**, doi:10.1029/2002jd003220.

Karydis, V., P. Kumar, D. Barahona, I. Sokolik, and A. Nenes, 2011: On the effect of dust particles on global cloud condensation nuclei and cloud droplet number. *Journal of Geophysical Research: Atmospheres*, **116 (D23)**, doi:10.1029/2011jd016283.

Kaufmann, L., C. Marcolli, B. Luo, and T. Peter, 2017: Refreeze experiments with water droplets containing different types of ice nuclei interpreted by classical nucleation theory. *Atmospheric Chemistry and Physics*, **17 (5)**, 3525–3552, doi:10.5194/acp-17-3525-2017.

Kessler, E., 1969: *On the Distribution and Continuity of Water Substance in Atmospheric Circulations*. Springer, 1–84 pp., doi:10.1007/978-1-935704-36-2_1.

Kiselev, A., F. Bachmann, P. Pedevilla, and Coauthors, 2017: Active sites in heterogeneous ice nucleation — the example of K–rich feldspars. *Science*, **355 (6323)**, 367–371, doi:10.1126/science.aai8034.

Koehler, K. A., S. M. Kreidenweis, P. J. DeMott, and Coauthors, 2009: Hygroscopicity and cloud droplet activation of mineral dust aerosol. *Geophysical Research Letters*, **36 (8)**, doi:10.1029/2009gl037348.

Köhler, H., 1936: The nucleus in and the growth of hygroscopic droplets. *Trans. Faraday Soc.*, **32**, 1152–1161, doi:10.1039/tf9363201152.

Koop, T., B. Luo, A. Tsias, and T. Peter, 2000: Water activity as the determinant for homogeneous ice nucleation in aqueous solutions. *Nature*, **406 (6796)**, 611–614, doi:10.1038/35020537.

Ladino Moreno, L., O. Stetzer, and U. Lohmann, 2013: Contact freezing: a review of experimental studies. *Atmospheric Chemistry and Physics*, **13 (19)**, 9745–9769, doi:10.5194/acp-13-9745-2013.

Lauber, A., 2016: Potential ice multiplication mechanisms associated with the freezing process of drizzle droplets. M.S. thesis, Meteorology, Karlsruhe Institute of Technology.

Leroy, D., 2007: Développement d'un modèle de nuage tridimensionnel à microphysique détaillée — application à la simulation de cas de convection moyenne et profonde. Ph.D. thesis, Université Blaise Pascal, Clermont-Ferrand. [Available online at http://wwwobs.univ-bpclermont.fr/atmos/fr/Theses/Th_Leroy.pdf.]

Leroy, D., M. Monier, W. Wobrock, and A. I. Flossmann, 2006: A numerical study of the effects of the aerosol particle spectrum on the development of the ice phase and precipitation formation. *Atmospheric Research*, **80 (1)**, 15–45, doi:10.1016/j.atmosres.2005.06.007.

Marcolli, C., 2014: Deposition nucleation viewed as homogeneous or immersion freezing in pores and cavities. *Atmospheric Chemistry and Physics*, **14 (4)**, 2071–2104, doi:10.5194/acp-14-2071-2014.

Mason, B., 1971: *The Physics of Clouds*. Clarendon Press.

MBW calibration, 373 Dew Point Mirror. Tech. rep. [Available online at http://www.mbw.ch/products/humidity-measurement/373-dew-point-mirror/.]

Meyers, M. P., P. J. DeMott, and W. R. Cotton, 1992: New Primary Ice–Nucleation Parametrizations in an Explicit Cloud Model. *Journal of Applied Meteorology*, **31**, 708–721, doi:10.1175/1520-0450(1992)031<0708:npinpi>2.0.co;2.

Möhler, O., O. Stetzer, S. Schaefers, and Coauthors, 2003: Experimental investigation of homogeneous freezing of sulphuric acid particles in the aerosol chamber AIDA. *Atmospheric Chemistry and Physics*, **3 (1)**, 211–223, doi:10.5194/acp-3-211-2003.

Monier, M., 2003: Développement d'un modèle de cirrus à microphysique détaillée. Ph.D. thesis, Université Blaise Pascal, Clermont-Ferrand.

Monier, M., W. Wobrock, J.-F. Gayet, and A. I. Flossmann, 2006: Development of a detailed microphysics cirrus model tracking aerosol particles' histories for interpretation of the recent INCA campaign. *Journal of the Atmospheric Sciences*, **63 (2)**, 504–525, doi:10.1175/jas3656.1.

Murray, B. J., S. Broadley, T. Wilson, J. D. Atkinson, and R. Wills, 2011: Heterogeneous freezing of water droplets containing kaolinite particles. *Atmospheric Chemistry and Physics*, **11 (9)**, 4191–4207, doi:10.5194/acp-11-4191-2011.

Nickovic, S., A. Vukovic, M. Vujadinovic, V. Djudjevic, and G. Pejanovic, 2012: Technical Note: High–resolution mineralogical database of dust–productive soils for atmospheric dust modeling. *Atmospheric Chemistry and Physics*, **12 (2)**, 845–855, doi:10.5194/acp-12-845-2012.

Niedermeier, D., B. Ervens, T. Clauss, and Coauthors, 2014: A computationally efficient description of heterogeneous freezing: A simplified version of the Soccer Ball Model. *Geophysical Research Letters*, **41 (2)**, 736–741, doi:10.1002/grl.51242.

NOAA National Centers for Environmental Information, State of the Climate: Global Climate Report for Annual 2016, published online January 2017. [Available online at https://www.ncdc.noaa.gov/sotc/global/201613.]

Pander, T., 2015: Laboratory ice multiplication experiments in levitated microdroplets. Ph.D. thesis, Ruprecht-Karls-Universität Heidelberg, doi:10.11588/heidok.00018784.

Peckhaus, A., 2016: Study of phase transitions in atmospheric aerosols: freezing and efflorescence of complex aqueous mixtures. Ph.D. thesis, Ruprecht-Karls-Universität Heidelberg, doi:10.11588/heidok.00021653.

Peckhaus, A., A. Kiselev, T. Hiron, M. Ebert, and T. Leisner, 2016: A comparative study of K–rich and Na/Ca–rich feldspar ice nucleating particles in a nanoliter droplet freezing assay. *Atmospheric Chemistry and Physics*, **16 (18)**, 11 477–11 496, doi:10.5194/acp-16-11477-2016.

Pedevilla, P., S. J. Cox, B. Slater, and A. Michaelides, 2016: Can ice–like structures form on non–ice–like substrates? The example of the K–feldspar microcline. *The Journal of Physical Chemistry C*, **120 (12)**, 6704–6713, doi:10.1021/acs.jpcc.6b01155.

Persad, A. H., and C. A. Ward, 2016: Expressions for the evaporation and condensation coefficients in the hertz–knudsen relation. *Chemical reviews*, **116 (14)**, 7727–7767, doi:10.1021/acs.chemrev.5b00511.

Petters, M. D., and S. M. Kreidenweis, 2007: A single parameter representation of hygroscopic growth and cloud condensation nucleus activity. *Atmospheric Chemistry and Physics*, **7 (8)**, 1961–1971, doi:10.5194/acp-7-1961-2007.

Phillips, V. T., P. J. DeMott, C. Andronache, and Coauthors, 2012: Improvements to an empirical parameterization of heterogeneous ice nucleation and its comparison with observations. *Journal of the Atmospheric Sciences*, **70 (2)**, 378–409, doi:10.1175/jas-d-12-080.1.

Planche, C., W. Wobrock, and A. I. Flossmann, 2014: The continuous melting process in a cloud–scale model using a bin microphysics scheme. *Quarterly Journal of the Royal Meteorological Society*, **140 (683)**, 1986–1996, doi:10.1002/qj.2265.

Planche, C., W. Wobrock, A. I. Flossmann, and Coauthors, 2010: The influence of aerosol particle number and hygroscopicity on the evolution of convective cloud systems and their precipitation: A numerical study based on the cops observations on 12 august 2007. *Atmospheric Research*, **98 (1)**, 40–56, doi:10.1016/j.atmosres.2010.05.003.

Pruppacher, H. R., and J. D. Klett, 1997: *Microphysics of Clouds and Precipitation*. 2nd ed., Atmospheric and Oceanographic Sciences Library, Kluwer Academic Publishers, doi:10.1080/02786829808965531.

Quérel, A., M. Monier, A. I. Flossmann, P. Lemaitre, and E. Porcheron, 2014: The importance of new collection efficiency values including the effect of rear capture for the below–cloud scavenging of aerosol particles. *Atmospheric Research*, **142**, 57–66, doi:10.1016/j.atmosres.2013.06.008.

Ramanathan, V., and G. Carmichael, 2008: Global and regional climate changes due to black carbon. *Nature geoscience*, **1 (4)**, 221–227, doi:10.1038/ngeo156.

Respondek, P. S., A. I. Flossmann, R. R. W. Alheit, and H. R. Pruppacher, 1995: A theoretical study of the wet removal of atmospheric pollutants. Part V: the uptake, redistribution, and deposition of $(NH_4)_2SO_4$ by a convective cloud containing ice. *Journal of the Atmospheric Sciences*, **52 (11)**, 2121–2132, doi:10.1175/1520-0469(1995)052<2121:ATSOTW>2.0.CO;2.

Rose, C., 2014: Nucléation et formation de nouvelles particules à haute altitude. Ph.D. thesis, Université Blaise Pascal, Clermont-Ferrand. [Available online at https://tel.archives-ouvertes.fr/tel-01162629.]

Schill, G. P., K. Genareau, and M. A. Tolbert, 2015: Deposition and immersion-mode nucleation of ice by three distinct samples of volcanic ash. *Atmospheric Chemistry and Physics*, **15 (13)**, 7523–7536, doi:10.5194/acp-15-7523-2015.

Shaw, R. A., A. J. Durant, and Y. Mi, 2005: Heterogeneous surface crystallization observed in undercooled water. *The Journal of Physical Chemistry B*, **109 (20)**, 9865–9868, doi:10.1021/jp0506336.

Smolarkievicz, P. K., 1983: A simple positive definite advection scheme with small implicit diffusion. *Monthly Weather Review*, **111 (3)**, 479–486, doi:10.1175/1520-0493(1983)111<0479:aspdas>2.0.co;2.

Steinke, I., 2013: Ice nucleation properties of mineral dusts. Ph.D. thesis, Ruprecht-Karls-Universität Heidelberg, doi:10.11588/heidok.00015967.

Steinke, I., C. Hoose, O. Möhler, P. Connolly, and T. Leisner, 2015: A new temperature– and humidity–dependent surface site density approach for deposition ice nucleation. *Atmospheric Chemistry and Physics*, **15 (7)**, 3703–3717, doi:10.5194/acp-15-3703-2015.

Sun, Z., and K. P. Shine, 1994: Studies of the radiative properties of ice and mixed–phase clouds. *Quarterly Journal of the Royal Meteorological Society*, **120 (515)**, 111–137, doi:10.1256/smsqj.51506.

Tabezadeh, A., S. T. Martin, and J.-S. Lin, 2000: The effect of particle size and nitric acid uptake on the homogeneous freezing of aqueous sulfuric acid particles. *Geophysical Research Letters*, **27 (8)**, 1111–1114, doi:10.1029/1999gl010966.

Ullrich, R., C. Hoose, O. Möhler, and Coauthors, 2017: A new ice nucleation active site parameterization for desert dust and soot. *Journal of the Atmospheric Sciences*, **74 (3)**, 699–717, doi:10.1175/jas-d-16-0074.1.

Vali, G., P. J. DeMott, O. Möhler, and T. F. Whale, 2015: Technical Note: A proposal for ice nucleation terminology. *Atmospheric Chemistry and Physics*, **15 (18)**, 10 263–10 270, doi:10.5194/acp-15-10263-2015.

Walko, R. L., W. R. Cotton, M. Meyers, and J. Harrington, 1995: New RAMS cloud microphysics parameterization part I: the single–moment scheme. *Atmospheric Research*, **38 (1-4)**, 29–62, doi:10.1016/0169-8095(94)00087-t.

Welti, A., F. Lüönd, O. Stetzer, and U. Lohmann, 2009: Influence of particle size on the ice nucleating ability of mineral dusts. *Atmospheric Chemistry and Physics*, **9 (18)**, 6705–6715, doi:10.5194/acpd-9-6929-2009.

Wex, H., P. J. DeMott, Y. Tobo, and Coauthors, 2014: Kaolinite particles as ice nuclei: learning from the use of different kaolinite samples and different coatings. *Atmospheric Chemistry and Physics*, **14 (11)**, 5529–5546, doi:10.5194/acp-14-5529-2014.

Wheeler, M., and A. K. Bertram, 2012: Deposition nucleation on mineral dust particles: a case against classical nucleation theory with the assumption of a single contact angle. *Atmospheric Chemistry and Physics*, **12 (2)**, 1189–1201, doi:10.5194/acp-12-1189-2012.

Wobrock, W., 1986: Numerische modellsimulation von stralhlungsnebelsituation unter berucksichtinggung spektraler wolkenmikrophysik. Ph.D. thesis, Johannes-Gutenberg Universität, Frankfurt.

Yakobi-Hancock, J., L. Ladino Moreno, and J. P. Abbatt, 2013: Feldspar minerals as efficient deposition ice nuclei. *Atmospheric Chemistry and Physics*, **13 (22)**, 11 175–11 185, doi:10.5194/acpd-13-17299-2013.

Yu, H., Y. Kaufman, M. Chin, and Coauthors, 2006: A review of measurement–based assessments of the aerosol direct radiative effect and forcing. *Atmospheric Chemistry and Physics*, **6 (3)**, 613–666, doi:10.5194/acp-6-613-2006.

Zender, C. S., R. Miller, and I. Tegen, 2004: Quantifying mineral dust mass budgets: Terminology, constraints, and current estimates. *Eos, Transactions American Geophysical Union*, **85 (48)**, doi:10.1029/2004eo480002.

Zimmermann, F., M. Ebert, A. Worringen, L. Schütz, and S. Weinbruch, 2007: Environmental scanning electron microscopy (ESEM) as a new technique to determine the ice nucleation capability of individual atmospheric aerosol particles. *Atmospheric Environment*, **41 (37)**, 8219–8227, doi:10.1016/j.atmosenv.2007.06.023.

Zobrist, B., T. Koop, B. Luo, C. Marcolli, and T. Peter, 2007: Heterogeneous ice nucleation rate coefficient of water droplets coated by a nonadecanol monolayer. *The Journal of Physical Chemistry C*, **111 (5)**, 2149–2155, doi:10.1021/jp066080w.

Zwiebel, J., 2015: Etude de l'impact orographique sur la structure microphysique horizontale et verticale des précipitations. Ph.D. thesis, Université Blaise Pascal, Clermont-Ferrand. [Available online at https://tel.archives-ouvertes.fr/tel-01343430.]

Appendices

Appendix A

DESCAM Handbook

The Detailed Scavenging Model (DESCAM) is a bin–detailed microphysics model that has been developed by Flossmann and her colleagues, mainly at the Laboratoire de Méréorologie Physique (LaMP).
DESCAM is written in Fortran 77 and has been recently extensively commented.

In the following text, most of the model's features are detailed. However, in the main program, the initialization is quite simple and is not hereafter heavily detailed.

A.1 Model structure

DESCAM in its 1.5–D version[1] is divided in three main parts:

1. Modules declaration
2. Main program
3. Subroutines:
    - (a) Initialization
    - (b) Dynamical advection
    - (c) Vapor exchange
    - (d) Ice nucleation
    - (e) Collection/collision
    - (f) Technical subroutines
    - (g) Balance sheet

The modules declarations are described precisely in section A.2 and the subroutines in section A.3. The main program in DESCAM has the following structure:

I — Preambule
1. Call modules
2. Declare local variables
3. Read input/output parameters
4. Open output files

II — Initialization
1. Create vertical grid
2. Initialize thermodynamical variables
3. Initialize microphysics
4. Initialize collection processes
5. Write labels and initial state in files
6. Warm start

---

[1] Vertical definition of the dynamics (1D) on two co-axial cylinders, the inner cylinder corresponding to the convective cloud with full microphysics calculation, the outer cylinder corresponding to the environment with only thermodynamical updates.

III — Integration
A — Thermodynamics
0. Diabatic heating and buffer strip
1. Advection of thermodynamical variables
2. Update of the thermodynamical variables
3. Advection of the size distributions
4. Balance sheet before microphysics

B — Microphysics
1. Exchanges vapor/condensed phase
2. Ice nucleation processes
3. Collision–coalescence processes
C — Balance sheet and update
D — Write results

Details for the parts I and III-D are to be found in sections A.2 and A.4. The part II is quite self–explanatory as it calls the initialization subroutines described in section A.3 and sets the original values without particular computation.

III — Integration

The integration section of the source code solves the equations schematized in Figure A.1 and expressed as:

$$\begin{aligned}\frac{\mathrm{d}\mathcal{N}_a(r_a)}{\mathrm{d}t} &= \left.\frac{\partial\mathcal{N}_a(r_a)}{\partial t}\right|_{\mathrm{dyn}} + \left.\frac{\partial\mathcal{N}_a(r_a)}{\partial t}\right|_{\mathrm{mic}} \\ &= \left.\frac{\partial\mathcal{N}_a(r_a)}{\partial t}\right|_{\mathrm{dyn}} + \left.\frac{\partial\mathcal{N}_a(r_a)}{\partial t}\right|_{\mathrm{act/deact}} + \left.\frac{\partial\mathcal{N}_a(r_a)}{\partial t}\right|_{\mathrm{con/eva}} + \left.\frac{\partial\mathcal{N}_a(r_a)}{\partial t}\right|_{\mathrm{coll}} + \left.\frac{\partial\mathcal{N}_a(r_a)}{\partial t}\right|_{\mathrm{nucl}}\end{aligned} \tag{A.1}$$

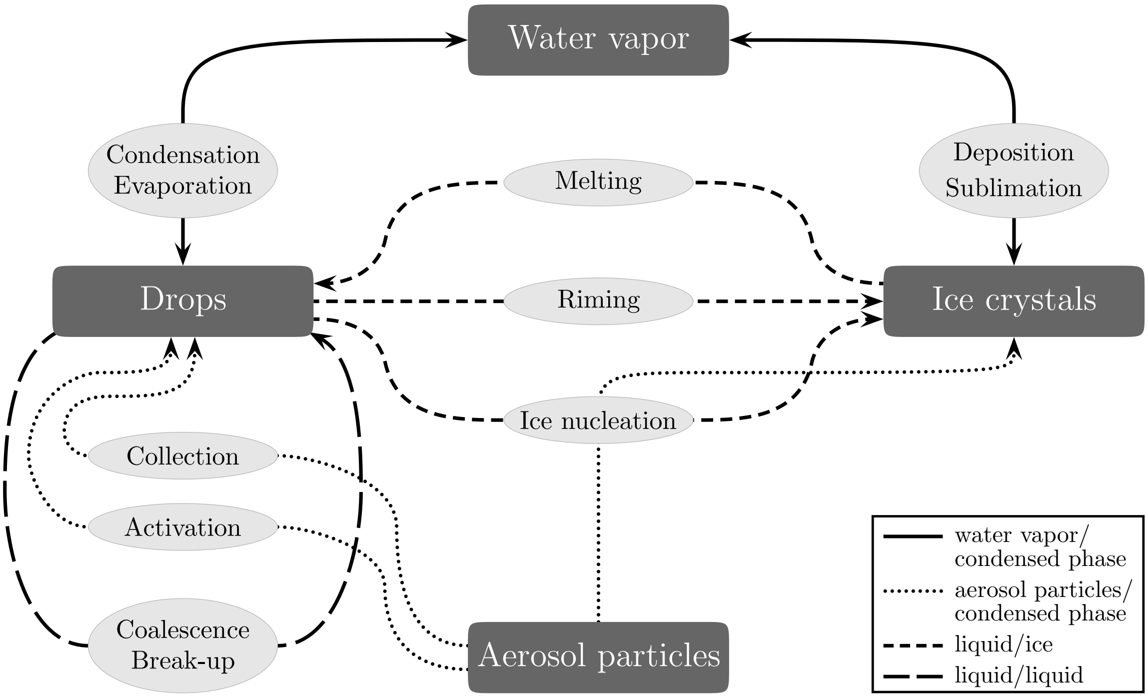

Figure A.1 – Microphysical scheme in DESCAM

$$\begin{aligned}\frac{\mathrm{d}N_d(r_d)}{\mathrm{d}t} &= \left.\frac{\partial N_d(r_d)}{\partial t}\right|_{\text{dyn}} + \left.\frac{\partial N_d(r_d)}{\partial t}\right|_{\text{mic}} \qquad \text{(A.2)} \\ &= \left.\frac{\partial N_d(r_d)}{\partial t}\right|_{\text{dyn}} + \left.\frac{\partial N_d(r_d)}{\partial t}\right|_{\text{act/deact}} + \left.\frac{\partial N_d(r_d)}{\partial t}\right|_{\text{con/eva}} + \left.\frac{\partial N_d(r_d)}{\partial t}\right|_{\text{coll,cont}} + \left.\frac{\partial N_d(r_d)}{\partial t}\right|_{\text{coal}} \\ &\quad + \left.\frac{\partial N_d(r_d)}{\partial t}\right|_{\text{break}} + \left.\frac{\partial N_d(r_d)}{\partial t}\right|_{\text{nucl}} + \left.\frac{\partial N_d(r_d)}{\partial t}\right|_{\text{rim}} + \left.\frac{\partial N_d(r_d)}{\partial t}\right|_{\text{melt}}\end{aligned}$$

$$\begin{aligned}\frac{\mathrm{d}N_i(r_i)}{\mathrm{d}t} &= \left.\frac{\partial N_i(r_i)}{\partial t}\right|_{\text{dyn}} + \left.\frac{\partial N_i(r_i)}{\partial t}\right|_{\text{mic}} \qquad \text{(A.3)} \\ &= \left.\frac{\partial N_i(r_i)}{\partial t}\right|_{\text{dyn}} + \left.\frac{\partial N_i(r_i)}{\partial t}\right|_{\text{dep/sub}} + \left.\frac{\partial N_i(r_i)}{\partial t}\right|_{\text{coll,cont}} + \left.\frac{\partial N_i(r_i)}{\partial t}\right|_{\text{nucl}} \\ &\quad + \left.\frac{\partial N_i(r_i)}{\partial t}\right|_{\text{rim}} + \left.\frac{\partial N_i(r_i)}{\partial t}\right|_{\text{melt}}\end{aligned}$$

The different terms treat the different microphysical processes of the atmosphere: the activation and deactivation of cloud droplets ($|_{\text{act/deact}}$, §A.3.3.1), the condensation and evaporation of water vapor on the aerosol particles and droplets ($|_{\text{con/eva}}$, §A.3.3.1) and the deposition and sublimation on the ice crystals ($|_{\text{dep/sub}}$, §A.3.3.2), the ice nucleation ($|_{\text{nucl}}$, §A.3.4), the collection of aerosol particles by the droplets and subsequent contact freezing ($|_{\text{coll,cont}}$, §A.3.5.1), the collision coalescence between droplets ($|_{\text{coal}}$, §A.3.5.2) and subsequent break–up of large droplets ($|_{\text{break}}$) and the collision between droplets and ice crystals and subsequent freezing ($|_{\text{rim}}$, §A.3.5.3) and the instantaneous melting of the ice crystals when crossing the iso–zero level ($|_{\text{melt}}$).

The integration is done using the variable `itt` with a time step dt (usually fixed to 2 s), yielding the integration time variable $t = \mathtt{itt} \cdot \mathrm{d}t$. In the current version, the integration is calculated over 2400 time steps as after 80 min the precipitations in all studied cases have stopped (rainfall rates below 0.5 mm.h^{-1}).

A — thermodynamics

0. Diabatic heating and buffer layer

To start the dynamics of the convective cloud, we need a heat source to increase the buoyancy of the air mass to generate an updraft. To do so, over the first 10 min, the first layer (`zmean` = 100 m) is heated with an increase of 2.3°C with respect to the external cylinder temperature, corresponding to the radiosounding measurements.
The last three layer (`zmean` $\in$ [9800 : 10000] m) are taken as buffer: they are used to compute the evolution of the dynamics of the cloud, but not that of thermodynamics. Their temperatures are always considered as equal to those of the external cylinder (and therefore of the radiosounding measurements).

1. Advection of the conservative thermodynamical variables

In this section, the advection of potential temperature (`subroutine evtheta`), water vapor content (`subroutine evrhoqv`) and vertical momentum (`subroutine evw`) are calculated using the Smolarkievicz (1983) advection scheme A.3.2.

2. Update of the remaining thermodynamical variables

Using the advected potential temperature and water vapor content, we update the remaining thermodynamical variables:

$$T(\mathtt{k}) = \theta(\mathtt{k}) \cdot \left(\frac{p(\mathtt{k})}{1\,000}\right)^{0.286} \tag{A.4}$$

$$\rho_{air}(\mathtt{k}) = 1\,000 \cdot \frac{p(\mathtt{k})}{R_d \cdot T(\mathtt{k})} \cdot (1 - x_w(\mathtt{k}))\left(1 - \frac{R_d}{R_v}\right) \tag{A.5}$$

$$r(\mathtt{k}) = \frac{q_v(\mathtt{k})}{\rho_{air}(\mathtt{k})} \tag{A.6}$$

The order in which those calculations are done is of large importance on the conservation of water quantity in the model. If the update of r is done before that of ρ then there is a large variation in the integrated total water content (TWC): from an original value of $235.5\,\mathrm{g.cm^{-3}}$, the TWC rises up to $251.5\,\mathrm{g.cm^{-3}}$ during the updraft and then lowers to a final value of $249\,\mathrm{g.cm^{-3}}$. The variation of the integrated TWC in the model is larger than 5% when in comparison, with the equation order presented previously (ρ update before that of r), the integrated TWC varies from $235.5\,\mathrm{g.cm^{-3}}$ to $235.6\,\mathrm{g.cm^{-3}}$, a variation below 0.1%.

There is also an update for the relative humidities and the recalculation of the terminal velocities of droplets and ice crystals (`subroutine vterm`, A.3.2.3).

3. Advection of the size distribution

As was already the case in the section III–A–1, we use the Smolarkievicz advection scheme to advect the different size distributions.

`subroutine advectap` advects the aerosol particles with the third variable corresponding to the type of size distribution (1 for aerosol particles number, 2 for the total surface and 3 for the total mass). This precision doesn't affect the way the advection is calculated but is used in the balance sheet calculation A.3.7.

`subroutine advectn` advects the number of hydrometeors with the third variable corresponding to the nature of hydrometeor (1 for droplets and 2 for ice crystals). This precision affects the way the advection is calculated as it is used to choose which terminal velocities are used.

`subroutine advectm` advects the aerosol particles contained by the hydrometeors, with the third variable corresponding to the nature of hydrometeor and the fourth variable corresponding to the type of size distribution.

Finally, `subroutine corr_neg_val` is called to ensure that after the advection there are no negative values in the size distributions.

4. Balance sheet before the microphysics

`subroutine integre` calculates the liquid water content (LWC) and ice water content (IWC) as well as the total number of droplets and ice crystals in each layer, parameters that will be needed during the computation of the microphysics processes.

The balance sheet after the advection is done using the `bal_***` subroutines to check on the integrated TWC and total number, surface and mass of aerosol particles.

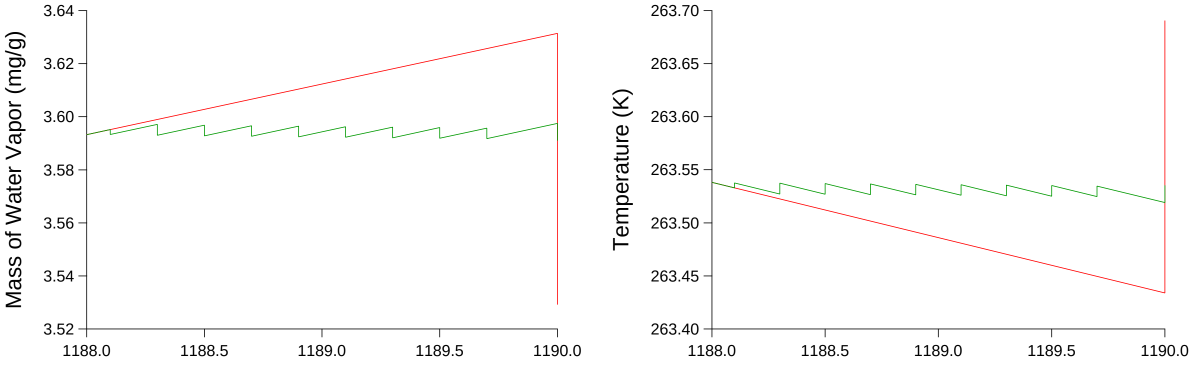

Figure A.2 – Evolution of the variable `qv(k)` (mass of water vapor, left) and of the variable `T(k)` (temperature, right) as a function of time between the beginning of the time step and the end of the vapor exchanges. In red are represented the evolution for normal time steps ($\mathrm{d}t$) and in green are represented the evolution for split time steps ($\delta \mathrm{d}t$). The vertical lines correspond to the vapor exchange processes (time not updated).

B — Microphysics

1a. Vapor/condensed phase exchanges

First we store the LWC and IWC as well as the different size distributions (no explicit loops here, using the array equality available in Fortran 90).

Then the deposition/sublimation on ice crystals is calculated using `subroutine descatice` and `subroutine advctice2` shortly followed by the consensation/evaporation on aerosol particles and cloud droplets using `subroutine condupkappa` (see A.3.3). Whether the deposition/sublimation or condensation/evaporation is calculated first in DESCAM makes no difference as there is no update of the relative humidity nor calculation of the latent heat release between both calculations meaning that both processes are computed in the same conditions.

After the two processes, the new LWC and IWC are calculated yielding the quantity of water vapor exchanged (`cph` and `cphi`).

1b. Devided time step for Vapor/condensed phase exchanges if too much condensation in 1a.

If the calculation of deposition/sublimation and condensation/evaporation processes lead to a large amount of vapor exchanged ($\texttt{cph} + \texttt{cphi} > \texttt{cdmax}$) then the exchanges are recalculated over splitted time steps (between 3 and 10 depending on the previous amount of vapor exchanged), using the results stored in the previous section in order to prevent too strong variations in temperature and humidity (Figure A.2)[2].

The principle of the split time step for condensation is as follows: the variation of r and T due to the advection is used to compute moistening and heating rates ($\Delta_{\mathrm{cond}}T$ and $\Delta_{\mathrm{cond}}r$ respectively). Then the model starts again with the values found at the beginning of the time step and only a smaller portion of the advected humidity and temperature are added

---

[2] This scheme was developed by Delphine Leroy, for more details on this, see Leroy (2007) appendix C.

before the condensation/deposition calculation:

$$T_2 = T_2 + \Delta_{\text{cond}} T \cdot \delta \mathrm{d}t \tag{A.7}$$

$$q_{v,2} = q_{v,2} + \Delta_{\text{cond}} r \cdot \delta \mathrm{d}t \tag{A.8}$$

After the vapor exchange calculation, the new values of r_2 and T_2 are computed based on latent heat release and variation of LWC and IWC:

$$T(\mathtt{k}) = T(\mathtt{k}) + \frac{\Delta q_c(\mathtt{k})}{\rho(\mathtt{k})} \cdot \frac{\mathcal{L}_e[T(\mathtt{k})]}{C_{p,air}} + \frac{\Delta q_i(\mathtt{k})}{\rho(\mathtt{k})} \cdot \frac{\mathcal{L}_s[T(\mathtt{k})]}{C_{p,air}} \tag{A.9}$$

1c. Update thermodynamical variables after condensation/deposition

Temperature and humidity are update after the condensation/deposition calculation. It is necessary to do the update at this point, even though it has an impact on ice nucleation larger than the order in which the microphysics processes are computed in the model (do we want to let the hydrometeors grow first or first undergo ice nucleation or even collection and collision–coalescence processes?).

If no update of the humidity is done here, in some cases the homogeneous nucleation will be strongly increased which can lead to numerical oscillations!

2. Ice nucleation processes

The IWC from the layer is stored in `qiold` to compute the latent heat release at the end of the ice nucleation processes and the contact freezing INAS densities are reset[3] to 0. Then, if the temperature is negative and if some ice nucleation processes are activated (`code` $\neq 0$), the `subroutine INAS_densities` is called and returns the INAS densities for immersion and contact freezing and for deposition nucleation which are used in the different subroutines:

- `subroutine INAS_freezing` for immersion freezing (see A.3.4.2)
- `subroutine INAS_deposition` for deposition nucleation (see A.3.4.3)
- `subroutine nuclhom` for homogeneous nucleation (see A.3.4.1)

Finally the balance sheets upon the current layer are calculated.

3. Collision–coalescence processes

First, the `subroutine lwciwc` is called to update the number of droplets present in the layer and if they are in sufficient number, the processes are computed. The variable `dmir`, used for the calculation of splintering, is initialized with the mass of ice in each size bin, with the presence of aerosol particles inside the ice crystals being neglected.

The `subroutine APCOLLDR_cntctfreez` calculates the capture of aerosol particles by droplets and subsequent contact freezing based on the contact freezing INAS density `nsc` (see A.3.5.1). Then, if the number of ice crystals is sufficient (call of `lwciwc`) the riming is calulated with `subroutine riming` (A.3.5.3), using the collection efficiencies computed in `subroutine hall` (A.3.5.4). Finally, after riming, the variation of the mass of ice in each size bin is calculated through the update of `dmir` and used to compute splintering

---

[3] The `subroutine INAS_densities` is only called if the temperature is negative, so an independent reset is necessary as the subroutine for contact freezing is called as soon as droplets are present in the layer.

through the Hallett and Mossop (1974) process based on the parameterization of Cardwell et al. (2003), with `splintering` as defined in A.2.3.8:

$$\mathrm{d}N_i|_{HM} = \sum_j \texttt{splintering}[T(\texttt{k})] \cdot N_i(\texttt{k},\texttt{j}) \cdot \texttt{dmir}(j) \tag{A.10}$$

Once all ice nucleation processes are computed, there is an update of the IWC in the layer and the latent heat release and temperature are updated:

$$T(\texttt{k}) = T(\texttt{k}) + \frac{\Delta q_i(\texttt{k})}{\rho(\texttt{k})} \cdot \frac{\mathcal{L}_f[T(\texttt{k})]}{C_{p,air}} \tag{A.11}$$

and if the temperature reaches positive temperatures, because of the latent heat release or due to the other processes computed earlier, all ice melts, with a final latent heat and temperature update.

After the ice phase has been delt with, the collision–coalescence of droplets is computed using the Bott (1989) scheme (`subroutine coalsbott`, A.3.5.2), using the collection efficiencies computed in `subroutine hall`.

C —Balance sheet and update after microphysics

After a recalculation of all integrated variables, there is an update of the thermodynamical variables over the entire column:

$$\theta(\texttt{k}) = T(\texttt{k}) \cdot \left(\frac{1\,000}{p(\texttt{k})}\right)^{0.286} \tag{A.12}$$

$$q_v = \rho(\texttt{k}) \cdot r(\texttt{k}) \tag{A.13}$$

$$\rho(\texttt{k}) = 1\,000 \cdot \frac{p(\texttt{k})}{R_d \cdot T(\texttt{k})} \cdot (1 - x_w(\texttt{k}))\left(1 - \frac{R_d}{R_v}\right) \tag{A.14}$$

$$r(\texttt{k}) = \frac{q_v(\texttt{k})}{\rho(\texttt{k})} \tag{A.15}$$

D — Write the results in files

Before all results are written in the different files, some integral values have to be computed.

1a. Calculation of radar reflectivities

The radar reflectivities are defined as follows:

$$\texttt{xdbza} = \mathrm{d}BZ_a = 10\log\left[10^{-12}\sum_{\texttt{kt}=1}^{\texttt{ktyp}}\sum_{\texttt{j}=1}^{\texttt{nac}}\mathcal{N}_a(\texttt{j},\texttt{kt}) \cdot [2 \cdot r_a(\texttt{j})]^6\right] \tag{A.16}$$

$$\texttt{xdbzd} = \mathrm{d}BZ_d = 10\log\left[10^{-12}\sum_{\texttt{j}=1}^{\texttt{nrp}} N_d(\texttt{j}) \cdot [2 \cdot r_d(\texttt{j})]^6\right] \tag{A.17}$$

$$\texttt{xdbzi} = \mathrm{d}BZ_i = 10\log\left[10^{-12}\sum_{\texttt{i}=1}^{\texttt{nic}} N_i(\texttt{i}) \cdot [2 \cdot r_i(\texttt{i})]^6\right] \tag{A.18}$$

with the total radar reflectivity `xdbz` defined as the sum of those three reflectivities.

1d. Calculation of mixing ratios
This section computes the proportion of cloud (non precipitant, $r_{d/i} < r_{d/i,\text{fall}}$) and rain (precipitant, $r_{d/i} \geq r_{d/i,\text{fall}}$) water contents (in g.m^{-3}). In this current version, $r_{d/i,\text{fall}}$ is calculated in the section **1b. Calculation of critic falling sizes** but can be set back to the 40 µm class by commenting the two lines in **1b**.

1e. Calculation of particles and rain fluxes and cumuls
The particles and rain fluxes to the ground are calculated as follows:

$$\texttt{rainflux} = \frac{4}{3}\pi\rho_w \cdot 3600.10^{-9} \sum_{\texttt{j=1}}^{\texttt{nrp}} \left(r_d^3(\texttt{j}) N_d(200\,\text{m},\texttt{j}) \cdot \max[0, w_{d,\infty}(200\,\text{m},\texttt{j}) - w(150\,\text{m})]\right) \tag{A.19}$$

$$\texttt{apflux} = \frac{4}{3}\pi\rho_w \cdot 3600.10^{-12} \sum_{\texttt{j=1}}^{\texttt{nrp}} \left(r_d^3(\texttt{j}) \mathcal{M}_d(200\,\text{m},\texttt{j}) \cdot \max[0, w_{d,\infty}(200\,\text{m},\texttt{j}) - w(150\,\text{m})]\right) \tag{A.20}$$

With this end all calculations in the main program of DESCAM, the other blocks from the source code (modules and subroutines) will now be presented in details.

A.2 The modules

A.2.1 Parameters

The versions of DESCAM prior to 2013 used extensively common blocks to deal with global variables, following the standard Fortran 77 norms. Compilers now allow a mix of Fortran 77 and Fortran 90 in `.f` programs, with notabily the advantage of using modules instead of the common blocks. This has the advantage of reducing the compiling errors as modules are declared once and for all, ensuring an homogeneity of the variables name all over the source code, and are much more evolutive than common blocks. Also, with the backgroung intention of suppressing implicit variables in DESCAM, the use of modules allowed a systematic precise declaration of variables. The modules `functions` and `filenames` will be presented in an independant section.

A.2.1.1 `parameters`

This module is the mother of all modules and variables in the DESCAM source code. It contains the (integer)-parameters used to structure the model:

- `NLVL`: the number of vertical layers;
- `NAC,NRP,NIC`: the number of bins for the size grid of aerosol particles, droplets and ice crystals respectively;
- `NCO`: number of classes used for coalescence calculation;
- `JRS,KRS,IRS`: the resolution parameter for the size grid of aerosol particles, droplets and ice crystals respectively;
- `ktyp`: the number of different types of aerosol particles.

A.2.1.2 `constants`

This module contains the main constants used in descam, now declared as parameters, that were previously mostly locally declared. It ensures a better unity in the calculation of physical processes.

- `pi,cc1`: the geometrical parameters $\pi = \arccos(-1)$ and $\frac{4}{3}\pi$;
- `grav`: the standard gravity $g = 980.665\,\mathrm{cm.s^{-2}}$;
- `T0,p0`: the melting point of water ($T_0 = 273.15\,\mathrm{K}$) and normal atmospheric pressure ($p_0 = 1013\,\mathrm{hPa}$);
- `Rd,Rv,Rg`: the individual gas constant of dry air ($R_d = 2.87.10^6\,\mathrm{erg.K^{-1}.g^{-1}}$) and water vapor ($R_v = 4.615.10^6\,\mathrm{erg.K^{-1}.g^{-1}}$) and the universal gas constant ($R_g = 8.314.10^7\,\mathrm{erg.K^{-1}.g^{-1}}$);
- `Cp`: the thermal capacity of dry air ($C_p = 1.005.10^7\,\mathrm{erg.K^{-1}.g^{-1}}$);
- `Hlat,Hfus`: latent heat of evaporation ($\mathcal{H}_{vap} = 2.5.10^5\,\mathrm{erg.g^{-1}}$) and of fusion ($\mathcal{H}_{fus} = 3.331.10^9\,\mathrm{erg.g^{-1}}$) at 0°C.

A.2.2 Variables

A.2.2.1 `grids`

This module contains the variables and parameters defining the size grids for aerosol particles, droplets and ice crystals, with the following important variables:

- `RAP,RAPS,RAP3`: the mean bin radius (µm), the logarithmic mean radius between two consecutive bins (µm) and the mean bin radius to the third ($\mu\mathrm{m}^3$) for aerosol particles;
- `RADC,RADCS,RADC3`: the mean bin radius (µm), the logarithmic mean radius between two consecutive bins (µm) and the mean bin radius to the third ($\mu\mathrm{m}^3$) for droplets;
- `RICE,RICES,EMIC`: mean bin radius (µm) for ice crystals, the logarithmic mean radius between two consecutive bins (µm) and mean bin mass (g);
- `dlnrp`: logarithmic scale parameter ($\mathtt{dnlrp} = \dfrac{\ln 2}{3\,\mathtt{krs}}$)

A.2.2.2 `microphysics`

This module contains the main microphysics variables used in Descam:

- `CAP,SCAP,GCAP`: the number ($\mathrm{cm^{-3}}$), total surface ($\mu\mathrm{m^2.cm^{-3}}$) and total mass[4] ($\mathrm{pg.cm^{-3}}$) of aerosol particles in a layer for one size bin and one type of aerosols;
- `TANP,TNIC`: the number of droplets ($\mathrm{cm^{-3}}$) and ice crystals ($\mathrm{cm^{-3}}$) in a layer for one size bin;
- `TFAP,TFIC`: the number ($\mathrm{cm^{-3}}$) of aerosol particles in the droplets and ice crystals reservoirs in a layer for one size bin and one type of aerosols;
- `TSAP,TSIC`: the total surface ($\mu\mathrm{m^2.cm^{-3}}$) of aerosol particles in the droplets and ice crystals reservoirs in a layer for one size bin and one type of aerosols;
- `TMAP,TMIC`: the total mass ($\mathrm{pg.cm^{-3}}$) of aerosol particles in the droplets and ice crystals reservoirs in a layer for one size bin and one type of aerosols;

---

[4] mind that all aerosol particle masses are calculated without taking into account the $\frac{4}{3}\pi$ factor, this is always done locally.

- `ECAP,ESCAP,EGCAP`: the number (cm^{-3}), total surface ($\mu m^2.cm^{-3}$) and total mass ($pg.cm^{-3}$) of aerosol particles in the environmental cylinder in a layer for one size bin and one type of aerosols;
- `qc,qi`: liquid water content ($g.cm^{-3}$) and ice water content ($g.cm^{-3}$) in a layer;
- `xmeap,xmed`: the liquid water content contained by aerosol particles and water droplets ($g.cm^{-3}$) in a layer;
- `xnap,xnd,xni`: the number total number (cm^{-3}) of aerosol particles, droplets and ice crystals in a layer.

A.2.2.3 `dynamics`

This module contains the variables used for the dynamics and thermodynamics of the cloud:

- `dt,dz,time,itt`: time step (s), vertical resolution (m), integration time (s) and iteration counter;
- `p,t,told,rho`: pressure (hPa), temperature (K) and volumic mass ($g.cm^{-3}$) of the atmosphere of a given layer;
- `w,wm,theta,qv,qvold,rhoqv,zmean`: vertical wind speed ($m.s^{-1}$) in the layer, vertical wind speed ($m.s^{-1}$) at the upper interface of the layer, potential temperature (K), mass of water vapor ($g_{wv}.g_{air}^{-1}$), vapor water content ($g.cm^{-3}$) and altitude (m) at the top of the layer;
- `rfd,rfold,rfi,rfiold`: relative humidities in respect to liquid water and ice (in units, *i.e.* saturation is obained for `rfd` $= 1$);
- `te,we,thethae,qve,rhoqve`: vertical wind speed ($m.s^{-1}$) at the upper interface of the layer, temperature (K), potential temperature (K), mass of water vapor ($g_{wv}.g_{air}^{-1}$) and vapor water content ($g.cm^{-3}$) in the layer for the environmental cylinder;
- `uhor,bh,bv,rcyl1,rcyl2,alcar`: horizontal wind speed at the interface between the two cylinders ($m.s^{-1}$), air fluxes through the horizontal interface of the layer and in the layer respectively ($m^3.s^{-1}$), the radii of the inner and outer cyclinders ($R_1 = 3.8\,km$, $R_1 = 38\,km$) and turbulence coefficient (s^{-1});
- `winf`: relative terminal velocity of hydrometeors ($m.s^{-1}$).

A.2.2.4 `icenucleation`

This modules contains the input parameters for ice nucleation case studies and the counter for created ice crystals:

- `immersion,deposition,contact,homogeneous,code`: on/off switches for ice nucleation and the resulting code used in the output files (`code` $=$ `immersion` $+ 2 \cdot$ `deposition` $+ 4 \cdot$ `contact` $+ 8 \cdot$ `homogeneous`);
- `KFS,kao,ill,ATD,codeIN`: on/off switches for ice nucleating particles (Feldspar, Kaolinite, Illite, Quartz) and the resulting code used in the output files (`codeIN` $=$ `KFS` $+ 2 \cdot$ `kao` $+ 4 \cdot$ `ill` $+ 8 \cdot$ `ATD`);
- `rlim,toPS`: minimal aerosol particle radius (μm) to contribute to deposition and contact freezing and concentration factor for ice nucleation particles;
- `frozcryst,frozen`: counters for the number of ice crystals created by the different ice nucleation mechanisms in each layer and overall respectively (arbitrary units homogeneous to cm^{-3}).

A.2.2.5 `growth`

This modules contains the variables and parameter used to compute the diffusional growth of aerosol particles, droplets and ice crystals (Pruppacher and Klett, 1997, Chapter 13):

- `rhoap,rhos,rhoi,xmw`: volumic mass of aerosol particles, water and ice (g.cm^{-3}) and molar mass of water (g.mol^{-1})
- `kappa`: hygroscopicity parameter for the different aerosol types (no unit).
- `cph,cphi,cdmax` mass of water vapor exchanged with aerosol particles and dropets or with ice crystals per gram of air ($g_w.g_a^{-1}$) and maximal allowed exchange (`cdmax` $= 10^{-5}\,g_w.g_a^{-1}$)

A.2.2.6 `collection`

This module contains the variables used to compute the different collection processes (aerosol particles collection, droplets coalescence and riming):

- `CKE,CEF1`: collection kernel for aerosol particle collection and hydrometeor collision kernel (cm^3.s^{-1});
- `radco,em`: radius (µm) and mass (pg) of droplets;
- `pcent`: redistribution ratio through the break-up of large droplets.

A.2.2.7 `exchanges`

This module contains the variables used to compute the balance sheets of water mass and aerosol particles number, surface and mass.
The variables starting with
`from`: correspond to the fluxes through the lower interface of the layer;
`to` : correspond to the fluxes through the upper interface of the layer;
`side`: correspond to the fluxes through the lateral interface of the layer;
The variables ending with
`ap` : correspond to the fluxes of aerosol particles ($\mathcal{N}$, $\mathcal{S}$, $\mathcal{M}$, cm^{-3}) for on size bin in one layer for one type of particles, they are reinitialized after each flux calculation (`im`=1 for $\mathcal{N}$, 2 for $\mathcal{S}$ and 3 for $\mathcal{M}$);
`layerap`: correspond to the total fluxes of aerosol particles in one layer for one type of particles;
`n` : correspond to the fluxes of hydrometeors (N_d, N_i, cm^{-3}) for one size bin in one layer, they are reinitialized after each flux calculation;
`layer` : correspond to the fluxes of water (g.m^{-3}) in one layer.

A.2.3 Functions

The module `functions` contains pieces of code frequently used throughout the source.

A.2.3.1 For the Smolarkievicz advection scheme: `smolar(phi1,phi2,u)` and `cievic(phi1,phi2,u)`

Those two functions execute two consecutive parts from the Smolarkievicz advection scheme:

$$\texttt{smolar} = \begin{cases} \dfrac{1}{2}u\varphi_1\dfrac{\delta \mathrm{d}t}{\mathrm{d}z} & \text{if} \quad u \leq 0 \\ \dfrac{1}{2}u\varphi_2\dfrac{\delta \mathrm{d}t}{\mathrm{d}z} & \text{if} \quad u > 0 \end{cases} \qquad \text{and} \qquad \texttt{cievic} = \left[|u| - u^2\frac{\delta \mathrm{d}t}{\mathrm{d}z}\right] \cdot \frac{(\varphi_2 - \varphi_1)}{(\varphi_1 + \varphi_2)} \tag{A.21}$$

A.2.3.2 `cvmgm(a,b,c)`

This function is used to choose between two different values depending on the sign of `c`:

$$\texttt{cvmgm} = \begin{cases} a & \text{if} \quad c < 0 \\ b & \text{if} \quad c \geq 0 \end{cases} \tag{A.22}$$

A.2.3.3 Water droplets surface tension: `sigma(T)`

This function is used to compute the water surface tension of droplets as a function of temperature:

$$\texttt{sigma} = 76.1 - 0.155 \cdot (T - T_0) \tag{A.23}$$

A.2.3.4 Latent heats: `slwv(T)`, `sliv(T)` & `sliw(T)`

Those three functions are used to compute the latent heat realease/absorbtion respectively for condensation/evaporation, deposition/sublimation and freezing/melting as a function of temperature:

$$\texttt{slwv} = \mathcal{L}_e = \mathcal{H}_{\text{evap}} \quad -2.36.10^7 \cdot (T - T_0) + 1.6.10^4 \cdot (T - T_0)^2 - 6.10^2 \cdot (T - T_0)^3 \tag{A.24}$$

$$\texttt{sliv} = \mathcal{L}_s = \mathcal{H}_{\text{evap}} + \mathcal{H}_{fus} - 2.90.10^6 \cdot (T - T_0) + 4.0.10^4 \cdot (T - T_0)^2 \tag{A.25}$$

$$\texttt{sliw} = \mathcal{L}_v = \quad \mathcal{H}_{fus} + 1.93.10^7 \cdot (T - T_0) - 1.3.10^5 \cdot (T - T_0)^2 \tag{A.26}$$

A.2.3.5 Water and ice saturation vapor pressures & relative humidity: `p21(T)`, `p31(T)` & `RH(qv,p,psat)`

Those three functions are used to compute the saturation vapor pressures ($p_{\text{sat},w}$ and $p_{\text{sat},i}$) using Buck (1981) equations and the resulting relative humidity:

$$p_{\text{sat},w} = 6.1121 \cdot \exp\left[\left(18.678 - \frac{T - T_0}{234.5}\right)\left(\frac{T - T_0}{257.14 + T - T_0}\right)\right] \tag{A.27}$$

$$p_{\text{sat},i} = 6.1115 \cdot \exp\left[\left(23.036 - \frac{T - T_0}{333.7}\right)\left(\frac{T - T_0}{279.82 + T - T_0}\right)\right] \tag{A.28}$$

$$RH_{w/i} = \frac{r}{0.622 + r} \cdot \frac{p}{p_{\text{sat},w/i}} \tag{A.29}$$

A.2.3.6 Water molar fraction: `xv(qv)`

This function is used to compute the water molar fraction x_w, used mainly to calculate ρ:

$$x_w = \frac{r}{r + \frac{\mathcal{R}_d}{\mathcal{R}_v}} \tag{A.30}$$

A.2.3.7 Water activity: `aiw(T)`

This function is used to compute the water activity as a function of temperature. It is based on Koop et al. (2000)

$$\texttt{aiw} = \exp\left[\left(210\,368 + 131.438 \cdot T - \frac{3\,323\,730}{T} - 41\,729.1 \cdot \log T\right) \cdot \frac{10^7}{\mathcal{R} \cdot T}\right] \tag{A.31}$$

A.2.3.8 Hallett–Mossop process: `spintering(T)`

This function is used to compute the splintering following the Hallett–Mossop process (Hallett and Mossop, 1974)

$$\texttt{splintering} = \begin{cases} -(T+3) \cdot 10^{-8} & \text{if} \quad T \in \,]268.15; 270.15]\,\mathrm{K} \\ -(T+8) \cdot 2.10^{-8} & \text{if} \quad T \in [265.15; 268.15]\,\mathrm{K} \\ 0 & \text{else} \end{cases} \tag{A.32}$$

A.2.3.9 Implicit diffusion: `wr2implicit(n,w,j)`

This function is used to compute the implicit diffusion correction in an upstream advection scheme (A.3.6.2):

$$\texttt{wr2implicit} = (|w(\texttt{j})| - w(\texttt{j})^2)\frac{N(\texttt{j+1}) - N(\texttt{j})}{|N(\texttt{j})| + |N(\texttt{j+1})|} - \frac{w(\texttt{j}) \cdot (w(\texttt{j+1}) - w(\texttt{j-1}))}{4} \tag{A.33}$$

if $|N(\texttt{j})| + |N(\texttt{j+1})| < 10^{-15}$, only the second term is taken into account.

A.3 Subroutines

The subroutines in DESCAM have been rearranged in the source code to be ordered by their role in the model and regrouped in different sections.

A.3.1 Initalization subroutines

A.3.1.1 Initialization of the dynamics: `ccope`

This subroutine initalizes the thermodynamics in the model based on the CCOPE cloud (Dye et al., 1986).
The data loaded by the subroutine correspond to the 90 points of radiosounding available in CCOPE with four measures: `zc` the altitude (z_r in m), `pc` the pressure (p_r in hPa), `tc` the temperature (T_r in °C) and `dc` the dew point temperature ($T_{dp,r}$ in °C).

A. Interpolation between the different sounding points
First, the radiosounding altitudes are shifted so that the first measure point corresponds to the base of the module, then the program enters two loops: one on `k` for the levels of the model and one on `kr` for the radiosounding measurement points.
The thermodynamics in the model are initialized as follows (for $z_r(\texttt{kr-1}) < z(\texttt{k}) < z_r(\texttt{kr})$) and with $\Delta z_r = z_r(\texttt{kr}) - z_r(\texttt{kr-1})$:

$$p(\mathtt{k}) = \frac{p_r(\mathtt{kr}) - p_r(\mathtt{kr\text{-}1})}{\Delta z_r} \cdot z(\mathtt{k}) + \frac{p_r(\mathtt{kr\text{-}1}) \cdot z_r(\mathtt{kr}) - p_r(\mathtt{kr}) \cdot z_r(\mathtt{kr\text{-}1})}{\Delta z_r} \tag{A.34}$$

$$T(\mathtt{k}) = T_0 + \frac{T_r(\mathtt{kr}) - T_r(\mathtt{kr\text{-}1})}{\Delta z_r} \cdot z(\mathtt{k}) + \frac{T_r(\mathtt{kr\text{-}1}) \cdot z_r(\mathtt{kr}) - T_r(\mathtt{kr}) \cdot z_r(\mathtt{kr\text{-}1})}{\Delta z_r} \tag{A.35}$$

$$T_{dp}(\mathtt{k}) = \frac{T_{dp,r}(\mathtt{kr}) - T_{dp,r}(\mathtt{kr\text{-}1})}{\Delta z_r} \cdot z(\mathtt{k}) + \frac{T_{dp,r}(\mathtt{kr\text{-}1}) \cdot z_r(\mathtt{kr}) - T_{dp,r}(\mathtt{kr}) \cdot z_r(\mathtt{kr\text{-}1})}{\Delta z_r} \tag{A.36}$$

The mass of water vapor ($r(\mathtt{k})$ or `qv` in DESCAM , expressed in $\mathrm{g}_w.\mathrm{g}_{air}^{-3}$) is defined by:

$$r(\mathtt{k}) = \begin{cases} \dfrac{6.11}{p(\mathtt{k})} \cdot \dfrac{R_d}{R_v} \cdot \exp\left[\dfrac{\mathcal{H}_{\text{evap}}}{T_0 \cdot R_v} \cdot \dfrac{T_{dp}(\mathtt{k})}{(T_{dp}(\mathtt{k}) + T_0)}\right] & \text{if} \quad p(\mathtt{k}) \leq 685.1\,\text{hPa} \\ 7 \cdot 10^{-3} & \text{else} \end{cases} \tag{A.37}$$

Also, if $p(\mathtt{k}) \leq 685.1\,\text{hPa}$, then the rpogram calls `subroutine thetaw`[5] to compute the pseudo-adiabatic temperature for $p(\mathtt{k})$.
This section ends with an update of ρ, `rhoqv` as well as the thermodynamics parameters of the external cylinder and the calculation of the relative humidities.

B. Realization of heating
The heating of the lower atmosphere in the model is done by assigning a constant potential temperature for all layers for which $p(\mathtt{k}) > 685.1\,\text{hPa}$ and creating an instability between the inner and the outer cylinder:

$$T_{\text{ext}}(\mathtt{k}) = T(\mathtt{k}) - \frac{p(\mathtt{k}) - 685.1}{921 - 685.1} \tag{A.38}$$

$$r(\mathtt{k}) = r_{\text{ext}}(\mathtt{k}) + 2.10^{-4} \tag{A.39}$$

Also, in the layers 24 to 31, the potential temperature us kept constant and equal to $\theta(24)$.

A.3.1.2 Set grids: `cldint`

This subroutine creates the grids in radius for aerosol particles and droplets. They are defined as:

$$r_d(\mathtt{j}) = r_d(1) \cdot 2^{\frac{\mathtt{j\text{-}1}}{\mathtt{3krs}}} \quad \text{with} \quad r_d(1) = 1\,\mu\text{m} \tag{A.40}$$

$$r_a(\mathtt{j}) = r_a(1) \cdot 2^{\frac{\mathtt{j\text{-}1}}{\mathtt{3krs}}} \quad \text{with} \quad r_a(\mathtt{kshift}) = r_d(1) \tag{A.41}$$

The variables `radcs` and `raps` correspond to the logarithmic mean value between two different classes:

$$\ln[\mathtt{radcs}(\mathtt{j})] = \frac{\ln[r_d(\mathtt{j})] + \ln[r_d(\mathtt{j+1})]}{2} \tag{A.42}$$

A.3.1.3 Initizalization of the warm microphysics: `cldstr`

This subroutine inializes the droplets size distributions and the aerosol particles size distributions.

---

[5] The equation used to calculate p_{sat} in `subroutine thetaw` is not the same as in the rest of DESCAM. If we homogenize the equations, it yields a 10% variation in the warm rain peak for the all liquid case.

A. Chemical characteristics of aerosol particles

This short section initializes the kappa values for the different aerosol particles types (for definition of kappa values, see Chapter 6).

B. Calculation of the dry AP spectra

The size distributions of the aerosol particles are based on three lognormal functions as presented in Chapter 5 with the following final superposition[6] (in DESCAM, `S` corresponds to $\log\sigma$):

$$\mathcal{N}_a(\texttt{j},\texttt{kt}) = \sum_{i=1}^{3} \frac{n_i(\texttt{kt})}{\sqrt{2\pi}\ln(10)\log[\sigma_i(\texttt{kt})]} \exp\left[-\frac{1}{2}\left(\frac{\log[r_a(\texttt{j})/R_i(\texttt{kt})]}{\log[\sigma_i(\texttt{kt})]}\right)^2\right] \tag{A.43}$$

This size distribution is then applied to the entire column with an exponential decrease of the number of particles when the altitude is higher than 1 000 m, with a typical length of 3 000 m.

The total surface and mass size distributions are calculated from this number size distribution:

$$\mathcal{S}_a(\texttt{j}) = \mathcal{N}_a(\texttt{j}) \cdot 4\pi \cdot r_a(\texttt{j})^2 \tag{A.44}$$

$$\mathcal{M}_a(\texttt{j}) = \mathcal{N}_a(\texttt{j}) \cdot \rho_a \cdot r_a(\texttt{j})^3 \tag{A.45}$$

One must remember that throughout the entire source code, the mass grids (for aerosol particles as well as for water droplets and ice crystals) are always defined to a factor $\texttt{cc1} = \frac{4}{3}\pi$

At initialization, all functions relative to droplets (N_d, $\mathcal{N}_d$, $\mathcal{S}_d$ and $\mathcal{M}_d$) are set to 0.

C. Calculation of the AP spectra at 99% RH

The calculated spectra are then brought to an equilibrium for a relative humidity of 99%. First the equilibrium radii are calculated using `subroutine scritic` and `subroutine koehler`. Then, based on those equilibrium radii, the condensational growth of the aerosol particles are calculated on an upstream advection scheme (A.3.6.2) with a growth speed:

$$w_r = \frac{\log[\texttt{apr}] - \log[\texttt{arax}]}{\texttt{dlnrp}}$$

A.3.1.4 Initizalization of the cold microphysics: `iceini`

A. Creation of the ice crystals size and mass grids

The ice crystals size grids is created to ensure mass equivalence between the different droplets and ice crystals classes (this version of descam imposes `irs`=`jrs`). Therefore:

$$r_i(\texttt{j}) = \sqrt[3]{\frac{r_d(\texttt{j})^3}{\rho_i}} \tag{A.46}$$

B. Initialization of the ice crystals size distributions

The ice phase in DESCAM is initialized with all size distributions equal to 0. Then if there is ice supersaturation, deposition nucleation and homogeneous nucleation are activated, calling the following `subroutines`: `INAS_densities`, `INAS_deposition` and `nuclhom` (A.3.4).

---

[6] This distribution is multiplied by the factor `dlnrp` in order to take into account the size bins' width.

A.3.2 Dynamical advection subroutines

The dynamical advection in this version of DESCAM is based on the equations presented in the appendix A of Monier (2003), adapted in the same dynamical frame (Emde and Kahlig, 1989).

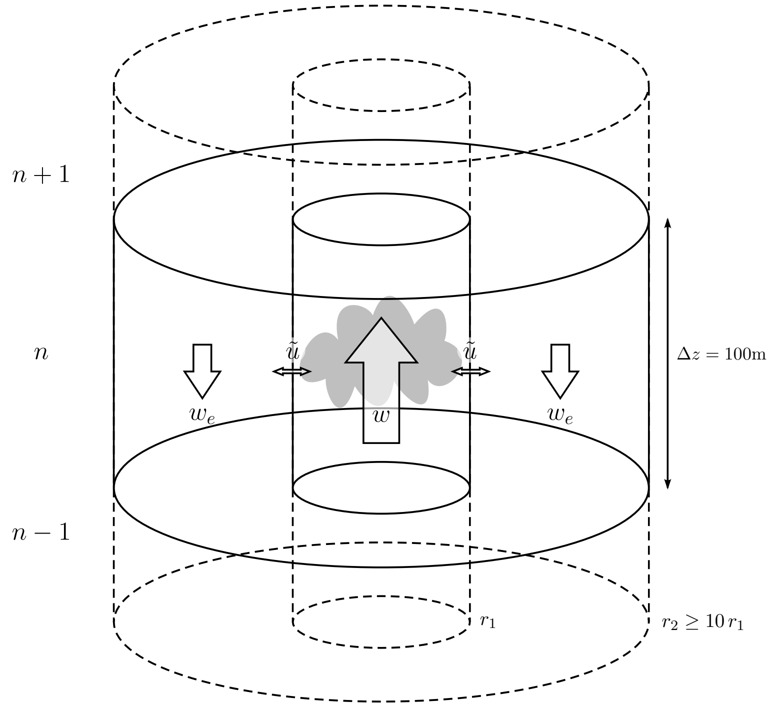

The formation and dynamical evolution of the cloud is considered with the help of two cylinders. The cloud develops in the inner cylinder where all microphysical parameters are updated. The outer cylinder corresponds to the environment and is used for subsidence and only the vertical wind (w_e) and volumic mass of air ($\rho_e = \rho$) are updated.
Therefore, in the outer cylinder, the size distributions for aerosol particles ($\mathcal{N}_{a,e}$, $\mathcal{S}_{a,e}$ and $\mathcal{M}_{a,e}$), as well as the quantity of water vapor (r_e) and the temperature (T_e) are considered as constants.

Under those conditions, based on the continuity equation (found also in Emde and Kahlig, 1989), we can write the following relationship defining the lateral wind $\tilde{u}$ in the model:

$$\frac{2}{R_{\text{int}}}\tilde{u} = -\frac{1}{\rho}\frac{\partial \rho w}{\partial z} \tag{A.47}$$

Also, the model is conservative in term of mass of air, therefore, the flux of air through an horizontal section of both cylinders must be zero, which means that the flux through the section of the inner cylinder must be compensated by an opposite flux of air through the section the outer cylinder: $\rho \cdot w_m A_{\text{int}} = \rho \cdot w_e A_{\text{ext}}$ where A is the area of each cylinder. This yields the following relation for the external vertical speed:

$$w_e = -w_m \cdot \frac{R_{\text{int}}^2}{R_{\text{ext}}^2 - R_{\text{int}}^2} \tag{A.48}$$

with w_m the vertical wind in the middle of the given layer ($w_m(\mathtt{k}) = (w(\mathtt{k}) + w(\mathtt{k+1}))/2$). Finally, for a conservative quantity ψ, the dynamical advection is expressed as follows (adapted from Monier, 2003):

$$\left.\frac{\partial \psi}{\partial t}\right|_{\text{dyn}} = \left.\frac{\partial \psi}{\partial t}\right|_{\text{vert}} + \left.\frac{\partial \psi}{\partial t}\right|_{\text{lat}} \tag{A.49}$$

with

$$\begin{cases} \left.\dfrac{\partial \psi}{\partial t}\right|_{\text{vert}} & = -\dfrac{\partial w\psi}{\partial z} \\ \left.\dfrac{\partial \psi}{\partial t}\right|_{\text{lat}} & = \dfrac{2}{R_{\text{int}}}\alpha^2 \left|w_e - w_m\right| (\psi_e - \psi) - \dfrac{2}{R_{\text{int}}}\tilde{\psi}\tilde{u} \end{cases} \tag{A.50}$$

where ψ_e is the value of ψ in the outer cylinder and $\tilde{\psi}$ its value at the interface between both cylinders, which is defined as (Emde and Kahlig, 1989):

$$\tilde{\psi} = \begin{cases} \dfrac{B_h\psi_e + B_v\psi^{\uparrow}}{B_h + B_v} & \text{if} \quad \tilde{u} \leq 0 \\ \dfrac{B_h\psi + B_v\psi^{\uparrow}}{B_h + B_v} & \text{else} \end{cases} \quad \text{with} \quad \begin{cases} B_h = 2\pi R_{\text{int}} \mathrm{d}z \, |\tilde{u}| \\ B_v = R_{\text{int}}^2 \pi \left| w^{\uparrow} \right| \end{cases} \tag{A.51}$$

B_h corresponds to the volume ($\mathrm{m}^3.\mathrm{s}^{-1}$) passing through the lateral surface of the cylinder and B_v corresponds to the incoming volume passing through the horizontal surface of the cylinder. $\psi^{\uparrow}$ and $w^{\uparrow}$ correspond to the upstream quatities: if $w(\texttt{k-1}) > 0$ then the upstream values are those from layer `k-1`, otherwise, if $w(\texttt{k+1}) < 0$ then the upstream values are those from layer `k+1`.

Vertical advection
The Smolarkievicz scheme solves *the continuity equation describing the advection of a nondiffusive quantity ψ in a flow field*, which in our one-dimensional vertical case means:

$$\frac{\partial \psi}{\partial t} + \frac{\partial}{\partial z}(w\psi) = 0 \tag{A.52}$$

The scheme is defined as follows:

$$\psi^*(\texttt{k}) = \psi(\texttt{k}) - [\texttt{smolar}(\psi(\texttt{k}), \psi(\texttt{k+1}), w(\texttt{k})) - \texttt{smolar}(\psi(\texttt{k-1}), \psi(\texttt{k}), w(\texttt{k-1}))] \tag{A.53}$$

$$\psi^{t+\mathrm{d}t}(\texttt{k}) = \psi^*(\texttt{k}) - [\texttt{smolar}(\psi^*(\texttt{k}), \psi^*(\texttt{k+1}), \hat{w}(\texttt{k})) - \texttt{smolar}(\psi(\texttt{k-1}), \psi(\texttt{k}), \hat{w}(\texttt{k-1}))] \tag{A.54}$$

where $\hat{w}(\texttt{k}) = \texttt{cievic}(\psi^*(\texttt{k}), \psi^*(\texttt{k+1}), w(\texttt{k}))$.
In the scheme, the first `smolar` term of each equation corresponds to the advection of ψ from layer `k` to layer `k+1`, the second `smolar` term then corresponds to the advection of ψ from layer `k-1` to layer `k`. So the second term corresponds to a *gain* for the layer `k` when the first term corresponds to a *loss*.
This advection scheme is stable as long as:

$$\max_{\texttt{k}} \left(|w(\texttt{k})| \frac{\mathrm{d}t}{\mathrm{d}z} \right) \leq 1 \tag{A.55}$$

which is always the case when considering the CCOPE cloud in DESCAM with the standard setup as $\dfrac{\mathrm{d}z}{\mathrm{d}t} = 50\,\mathrm{m.s}^{-1}$ and the vertical wind speeds remain below $20\,\mathrm{ms}^{-1}$.

A.3.2.1 Calculate external and lateral speeds: `diagnose`

A. Vertical advection

This subroutine solves the continuity equation of dry air, using the Smolarkievicz scheme which yields the temporal variation of ρw:

$$\frac{\partial \rho w}{\partial z} = - \left. \frac{\partial \rho}{\partial t} \right|_{\text{vert}} \tag{A.56}$$

B. Lateral advection
With the previous relation, we obtain the horizontal speed for each layer:

$$\tilde{u}(t) = -\frac{R_{\text{int}}}{2\rho(t)} \cdot \frac{-\Delta_t \rho}{\mathrm{d}t} \tag{A.57}$$

Then the volume fluxes (B_h and B_v) through the boundaries of the layer are computed, as well as the external vertical wind speed (w_e).

A.3.2.2 Advect vertical speed: `evw`

This subroutine advects the vertical speed $\psi = \rho w_m$. An additional term is taken into account after the advection scheme used for all variables: the impact of the buoyancy on the flow. This yields:

$$\left.\frac{\partial \rho w_m}{\partial t}\right|_{dyn} = \left.\frac{\partial \rho w_m}{\partial t}\right|_{\text{vert}} + \left.\frac{\partial \rho w_m}{\partial t}\right|_{\text{lat}} + \rho g \left[\frac{\theta_v - \theta_{v,e}}{\theta_{v,e}} - \frac{q_c + q_i}{\rho}\right] \tag{A.58}$$

with g the gravitational acceleration, θ_v and $\theta_{v,e}$ the virtual potential temperatures in the inner and outer cylinder and q_c and q_i the liquid and ice water content (in g.cm^{-3})[7].

A.3.2.3 Compute terminal velocities of hydrometeors: `vterm`

This subroutine derives directly from (Pruppacher and Klett, 1997, Section 10.3.6) and the assumption is made that the only difference between ice crystals and cloud droplets are their radius and density.
Using equations 10-139 and 10-140, we have the 'Cunningham' correction factor:

$$\texttt{cunh} = 1.257 \cdot \lambda = 1.257 \cdot 6.62.10^{-6} \cdot \left(\frac{p_0}{p}\right)\left(\frac{T}{T_0 + 20}\right) \tag{A.59}$$

Using equation 10-141, we have the viscosity of air (`eta` in DESCAM):

$$\eta = \begin{cases} 10^{-4} \cdot (1.718 + 4.9 \cdot 10^{-3} \cdot (T - T_0)) & \text{if} \quad T > T_0 \\ 10^{-4} \cdot (1.718 + 4.9 \cdot 10^{-3} \cdot (T - T_0) - 1.2 \cdot 10^{-5} \cdot (T - T_0)^2) & \text{else} \end{cases} \tag{A.60}$$

All radii in this subroutine have to be expressed in cm to agree with the data from Pruppacher and Klett (1997). Depending on the radius, there are four different cases:

1. $r \leq 10^{-3}\,\text{cm}$
This corresponds to the stokes regime and the terminal velocity is obtained from equations 10-138 and 10-139:

$$U_\infty = (r + 1.257 \cdot \lambda) \cdot \frac{2rg(\rho_h - \rho)}{9\eta} \tag{A.61}$$

---

[7] In Monier (2003) as well as in Emde and Kahlig (1989), the quantities q_c and q_i are defined in g$_w$.g$_{air}^{-1}$.

2. $10^{-3} < r \leq 5.35 \cdot 10^{-2}\,\mathrm{cm}$
This corresponds to the regime where drag and gravitational forces can be equated and the terminal velocity is obtained from equations 10-142 and 10-146:

$$U_\infty = \frac{\eta N_{\mathrm{Re}}}{2\rho r} = \frac{\eta}{2\rho r} \exp\left[\sum_{i=0}^{6} B_i \cdot X^i\right] \quad \text{with} \quad X = \ln(N_{\mathrm{Be}}) = \ln\left[\frac{32 r^3(\rho_h - \rho)\rho g}{3\eta^2}\right] \tag{A.62}$$

3. $5.35 \cdot 10^{-2} < r \leq 0.35\,\mathrm{cm}$
In this case, the drops can no longer be considered spherical. The same basic expression of U_∞ is used, but the expression of the reynolds number has evolved:

$$U_\infty = \frac{\eta N_{\mathrm{Re}}}{2\rho r} = \frac{\eta}{2\rho r} N_P^{1/6} \exp\left[\sum_{i=0}^{5} C_i \cdot X^i\right] \quad \text{with} \quad X = \ln\left[\frac{16}{3} N_{\mathrm{Bo}} N_P^{1/6}\right] \tag{A.63}$$

with X depending on the *Bond number* $N_{\mathrm{Bo}} = g(\rho_h - \rho)r^2/\sigma_{w/a}$ and the *'phydical property' number* $N_P = \dfrac{\sigma_{w/a}^3 \rho^2}{\eta^4 g(\rho_h - \rho)}$.
If the radius is larger than 0.35 cm, then the terminal velocity is that of a droplet of radius 0.35 cm (terminal velocity independant of size for droplets larger than 0.25 mm).

A.3.3 Vapor exchange subroutines

`ccof` corresponds to the condensation coefficient[8] ($\alpha_c = 0.04$); `Dv` corresponds to the vapor diffusion factor (in cm.s^{-1}) and `ck` corresponds to the heat diffusion factor[9] (erg.cm^{-1}.s^{-1}.K^{-1}) and are expressed as:

$$D_v = 0.221 \cdot \left(\frac{T}{T_0}\right)^{1.94} \frac{p_0}{p} \qquad \text{and} \qquad k = (5.69 + 0.0168 \cdot (T - T_0)) \cdot 4.18684.10^2 \tag{A.64}$$

A.3.3.1 Condensation/evaporation on droplets and aerosol particles: `condupkappa`

This subroutine solves the vapor exchanges with the liquid phase for a time step $\delta\mathrm{d}t$.

A. Calculation of the growth speed factors
The growth of the droplets is based on chapter 13, section 2 Growth of an Individual Stationary Drop from Pruppacher and Klett (1997). The main equation is equation 13-28 and is expressed as:

$$\frac{\mathrm{d}r_d}{\mathrm{d}t} \simeq \frac{1}{r_d} \frac{s_{v,w} - y}{\dfrac{\rho_w R_v T}{p_{\mathrm{sat},w} D_v^*} + \dfrac{L_e \rho_w}{kT}\left(\dfrac{L_e}{R_v T} - 1\right)} \tag{A.65}$$

which in descam is decomposed as follows:

---

[8] The value for α_c is taken from Fujikawa et al. (1982), but there are large discreptancies in the calculation of this coefficient for atmospheric purposes, *e.g.* Persad and Ward (2016)

[9] One must keep in mind that the expression in Pruppacher and Klett (1997) is expressed in calories, hence the 4.19.10^2 factor

$$\frac{\mathrm{d}r_d}{\mathrm{d}t} = \frac{g \cdot (s_{v,w} - y)}{r_d} \quad \text{with} \quad g = 10^8 \left(\frac{\tau_3}{D_v^*} + \tau_2 \right)^{-1} \quad \text{where} \quad D_v^* = D_v \cdot \left(1 + \frac{D_v \tau_1}{r_d} \right)^{-1} \tag{A.66}$$

The factor 10^8 in g corresponds to the conversion from $\mathrm{cm}^2.\mathrm{s}^{-1}$ to $\mu\mathrm{m}^2.\mathrm{s}^{-1}$. The τ terms are:

$$\tau_1 = \frac{1}{\alpha_c} \sqrt{\frac{2\pi}{R_v T}} \quad , \quad \tau_2 = \rho_w \frac{L_e}{kT} \left(\frac{L_e}{R_v T} - 1 \right) \quad \text{and} \quad \tau_3 = \frac{\rho_w R_v T}{10^3 p_{\mathrm{sat},w}(T)} \tag{A.67}$$

The saturation pressure p_{sat} is expressed in hPa which correspond to $\mathrm{J.m}^{-3}$ which in CGS units are expressed as $10^3\,\mathrm{erg.cm}^{-3}$, hence the 10^3 factor appearing to the denominator in τ_3. Those equations are based on the assumption that $k^* = k$ and in D_v^*, $\Delta_v = 0$ (eq 13-14). It is also assumed that the temperature is homogeneneous and equal to T
The curvature and solute effects y can be expressed as:

$$y = \frac{2\sigma_{s/a}}{R_v T \rho_w r_d} - \frac{\nu \Phi_s m_s M_w / M_s}{\rho_w V_d - m_s} \tag{A.68}$$

which in our case, based on the κ-Köhler theory becomes:

$$y = \frac{2\sigma_{s/a}}{R_v T \rho_w r_d} - \kappa \frac{V_a}{V_w} \tag{A.69}$$

B. Evaporation and deactivation

This section solves the simplified Köhler equation (equation 24 from chapter 1 in Leroy, 2007):

$$\ln(RH_d) = \frac{2\sigma_{s/a}}{R_v T \rho_w} \frac{1}{r_{eq}} - \kappa \frac{r_{a,\mathrm{dry}}^3}{r_{eq}^3} \quad \Rightarrow \quad r_{a,\mathrm{dry}} = \sqrt[3]{\frac{r_{eq}^2}{\kappa} \left[\frac{2\sigma_{s/a}}{R_v T \rho_w} - \ln(RH_d) r_{eq} \right]} \tag{A.70}$$

First, the equivalent dry radius of particulate matter in the droplet is calculated (r_a, `ARX`), then, using the simplified Köhler equation, by varying r_{eq} (`rap(ia)`) on the grid of the aerosol particles (yielding a minorant `ARG` and a majorant `ARD`), the appropriate deactivation radius is found. If no equilibrium radius is found in the grid, the appropriate extrema value is taken for the deactivation radius.
Finally, the transfer in the calculated aerosol bin is made.

C. Activation

This section uses the Köhler equation to calculate the activation radius (`anue`) of the aerosol particles (equation 25 from chapter 1 in Leroy, 2007):

$$r_{\mathrm{act}}(RH_d, T) = \frac{2\sigma_{s/a}}{R_v T \rho_w} \cdot \frac{2}{3(RH_d - 1)} \tag{A.71}$$

The obtained activation radius is then transposed in terms of bin number (`RKK`) to compute the sources of droplets. If the activation radius is smaller than that of the smallest droplet bin, the activated aerosol particles are transferred into the first bin of droplets.

D. Advection of droplets due to condensation/evaporation

This section corresponds to the previous `subroutine advctb` and calls the Bott scheme for advection of droplets.

Before calculation of the growth of the droplets, the growth speed `wr` is once again divided by `dnlrp` and r_d in order to get an adimensional growth speed in term of bins per second.

1. Calculation of the growth speed and time step splitting

This step consists in the calculation of the maximal growth speed in order to set the time step subdivision ($\delta \mathrm{d}t$) for the advection calculation: the maximal growth speed cannot exceed one size been per subdivided time step.

The courant number for the Bott advection scheme is set to $\frac{\mathrm{d}r}{\mathrm{d}t} \cdot \delta \mathrm{d}t$.

2. Advection calculation

This step calls the Bott advection scheme based on the number of droplets (determined with `adv4p`, A.3.6.3), then applied to each of the different size distribution (computed with `advctschm`, A.3.6.4), before taking into account the sources previously calculated, adding only a portion $\delta \mathrm{d}t/\mathrm{d}t$ of the total amount of the activated quantities.

3. Total evaporation calculation

If in the droplet, most of the volume (over 85%) is occupied by the aerosol particle, then the droplet is no longer considered as such and is therefore transferred back into the aerosol particles reservoir.

4. Flux through the lower boundary of drops grid

If the growth speed of the smallest droplet bin is negative, then there has to be a transfer into the according aerosol particles reservoir.

E. Advection of APs due to condensation/evaporation

This final section computes the advection on the aerosol particles grid, based on the simplified Köhler equation. It is based on (Leroy, 2007, Appendix B).

A.3.3.2 Deposition/sublimation on ice crystals: `advctice2`

The growth of the ice crystals is based on (Pruppacher and Klett, 1997, Chapter 13, section 3). The main equation is equation 13-76 expressed here with a capacitance for a spherical crystal ($C = r_i$):

$$\frac{\mathrm{d}m_i}{\mathrm{d}t} \simeq \frac{4\pi r_i \cdot s_{v,i}}{\dfrac{R_v T}{p_{\mathrm{sat},i} D_v^*} + \dfrac{L_s}{k^* T}\left(\dfrac{L_s}{R_v T} - 1\right)} \tag{A.72}$$

The variation of mass can be expressed in term of variation of radius with:

$$\frac{\mathrm{d}m_i}{\mathrm{d}t} = \frac{\mathrm{d}r_i}{\mathrm{d}t} \cdot \rho_i 4\pi r_i^2 \tag{A.73}$$

which yields an equation for the growth of spherical ice crystal identical to that of droplets (to the difference of all idexes w are replaced by i) with neglected curvature and solute effects ($y \simeq 0$):

$$\frac{\mathrm{d}r_i}{\mathrm{d}t} \simeq \frac{1}{r_i} \frac{s_{v,i}}{\frac{\rho_i R_v T}{p_{\mathrm{sat},i} D_v^*} + \frac{L_s \rho_i}{kT}\left(\frac{L_s}{R_v T} - 1\right)} \tag{A.74}$$

Therfore, the decomposition of `wr` for ice crystals is the same as for cloud droplets.

This subroutine is structured in the exact same way as `subroutine condupkappa` to the exception of the activation which is done through `subroutine INAS_deposition`.

A.3.4 Ice nucleation subroutines

A.3.4.1 Homogeneous nucleation: `nuclhom`

The ice nucleation scheme is based on Koop et al. (2000) as adapted by Monier (2003, Chapter 1, section 3.4.1.3).
The homogeneous nucleation probability for a cloud droplet or an aerosol particle is defined as follows:

$$P_{hom} = 1 - \exp(-J_{hom} \bar{V}_w \mathrm{d}t) \tag{A.75}$$

where $\log(J_{hom}) = -906.7 + 8502\Delta a_w - 26924\Delta a_w^2 + 29180\Delta a_w^3$ is the nucleation rate (cm^{-3}.s$-$1)with $\Delta a_w = RH_d - a_w^i(T)$ and $V_w = V_d - V_{a,\mathrm{dry}} = V_d - \frac{\mathcal{M}_d}{N_d}\frac{1}{\rho_a}$ is the volume of water in the droplet or aerosol particle

A. Freezing rate calculation
`deltaw`$=\Delta a_w$ is computed in the main program upon calling the subroutine and used as input variable.
`xJls` corresponds to J_{hom}.
`vol`$=\bar{V}_w$ is computed using the effective amount of water in the droplet or aerosol particle.
The freezing rate (homogeneous nucleation probability) for cloud droplets (`xJhod`) and aerosol particles (`xJhoa`) is then computed for each bin.

B. Transfers between the different reservoirs
For each reservoirs, the transfer is computed for each bin with a security to prevent negative values from appearing. Each quantity is transferred using the freezing rate for the considered bin. For aerosol particles, if the radius of the original aerosol particle bin is smaller than the smallest bin of crystals, new ice crystals are put in the first bin; otherwise the new bin is calculated using `kshift`.
The amount of new ice crystals is then added to the `frozcryst` counter with categories 5 and 6 corresponding to the new crystals due to homogeneous nucleation for droplets and aerosol particles respectively.

A.3.4.2 INAS freezing nucleation: `INAS_freezing`

This subroutine computes freezing nucleation based on the ice nucleating active sites (INAS) density approach (see Chapter 6). In this subroutine, the freezing nucleation is treated differently depending on the radius of the droplet:

- for freshly formed droplets, with a radius smaller than 16 µm, we assume externally mixed aerosol particles (each droplet contains only one aerosol particle) — this assumption is referred to as condensation freezing;
- for older droplets, grown by collision/coalescence, with a radius larger than 16 µm, we assume internally mixed aerosol particles (all the droplets contain the same population of aerosol particles) — this assumption is referred to as immersion freezing.

I - Condensation freezing
This section solves the following equation:

$$\mathrm{d}\mathcal{N}_i(\mathtt{j},\mathtt{kt}) = \max\left[0, (\mathcal{N}_d(\mathtt{j},\mathtt{kt}) + \mathcal{N}_i(\mathtt{j},\mathtt{kt}))\cdot(1-\alpha(\mathtt{j},\mathtt{kt})) - \mathcal{N}_i(\mathtt{j},\mathtt{kt})\right] \tag{A.76}$$

where:

$$\alpha(\mathtt{j},\mathtt{kt}) = \exp\left(-n_s(\mathtt{kt})\cdot\frac{\mathcal{S}_d(\mathtt{j},\mathtt{kt})+\mathcal{S}_i(\mathtt{j},\mathtt{kt})}{\mathcal{N}_d(\mathtt{j},\mathtt{kt})+\mathcal{N}_i(\mathtt{j},\mathtt{kt})}\right) \tag{A.77}$$

Based on the assumption that the aerosol particles are externally mixed, the number of new ice crystals `dn` is determined as the sum of `df(kt)`, the variation of $\mathcal{N}_i$.

The number of new ice crystals is stored in the first category of `frozcryst`.

II - Immersion freezing
This section solves the following equation:

$$\mathrm{d}N_i(\mathtt{j}) = \max\left[0, (N_d(\mathtt{j}) + N_i(\mathtt{j}))\cdot(1-\prod_{\mathtt{kt}}\alpha(\mathtt{j},\mathtt{kt})) - N_i(\mathtt{j})\right] \tag{A.78}$$

where:

$$\alpha(\mathtt{j},\mathtt{kt}) = \exp\left(-n_s(\mathtt{kt})\cdot\frac{\mathcal{S}_d(\mathtt{j},\mathtt{kt})+\mathcal{S}_i(\mathtt{j},\mathtt{kt})}{N_d(\mathtt{j})+N_i(\mathtt{j})}\right) \tag{A.79}$$

This time, the number of new ice crystals `dn` is directly determined.

The number of new ice crystals is stored in the fourth category of `frozcryst`

A.3.4.3 INAS deposition nucleation: `INAS_deposition`

This subroutine computes deposition nucleation based on the INAS density approach. Because of the lack of correspondence between the size of the ice crystals and the aerosol particles, the deposition nucleation calculation is done using a bulk scheme.

A. Calculation of freezing rates
This section solves the following equation:

$$\mathrm{d}\mathcal{N}_i(\mathtt{kt}) = \max\left[0, \left(\sum_{\mathtt{j>jlim}} \mathcal{N}_a(\mathtt{j},\mathtt{kt}) + \sum_{\mathtt{i}} \mathcal{N}_i(\mathtt{i},\mathtt{kt})\right) \cdot [1-\widetilde{\alpha}(\mathtt{kt})] - \sum_{\mathtt{i}} \mathcal{N}_i(\mathtt{i},\mathtt{kt})\right] \tag{A.80}$$

where $\widetilde{\alpha}$ is given by the INAS density:

$$\widetilde{\alpha}(\mathtt{kt}) = \exp\left(-n_s(\mathtt{kt}) \cdot \frac{\sum_{\mathtt{j>jlim}} \mathcal{S}_a(\mathtt{j},\mathtt{kt}) + \sum_{\mathtt{i}} \mathcal{S}_i(\mathtt{i},\mathtt{kt})}{\sum_{\mathtt{j>jlim}} \mathcal{N}_a(\mathtt{j},\mathtt{kt}) + \sum_{\mathtt{i}} \mathcal{N}_i(\mathtt{i},\mathtt{kt})}\right) \tag{A.81}$$

The computation schemes yields a total number of new ice crystals. They then have to be distributed onto the entire spectrum of aerosol particles. This is done using the INAS density and the surface per aerosol particle in each bin:

$$\mathtt{dnistar}(\mathtt{j},\mathtt{kt}) = \mathcal{N}_a(\mathtt{j},\mathtt{kt}) \cdot \left[1 - \exp\left(-n_s(\mathtt{kt}) \cdot \frac{\mathcal{S}_a(\mathtt{j},\mathtt{kt})}{\mathcal{N}_a(\mathtt{j},\mathtt{kt})}\right)\right] \tag{A.82}$$

B. Transfers between the APs and ice crystals reservoirs
The redistribution into the different bins is calculated using the following equation:

$$\mathtt{dn}(\mathtt{j},\mathtt{kt}) = \mathrm{d}\mathcal{N}_i(\mathtt{kt}) \cdot \frac{\mathtt{dnistar}(\mathtt{j},\mathtt{kt})}{\sum_{\mathtt{j>jlim}} \mathtt{dnistar}(\mathtt{j},\mathtt{kt})} \tag{A.83}$$

The number of created ice crystals is stored in the second category of `frozcryst`.

A.3.4.4 Heterogeneous nucleation using the Meyers et al. parameterization: `nuclhet`

This subroutine computes condensation freezing and deposition nucleation using the Meyers et al. (1992) parameterization. The total number of new ice crystals is given by the parameterization for all aerosol particles and hydrometeors smaller than 16 µm, which yields a nucleation global nucleation rate `xJ`.
This nucleation rate is prorated into the aerosol particles (`xJdep`) and the droplets (`xJcond`) depending on the total number concentration of each category. There is no distinction in size.

The transfers between the categories are calculated in the same fashion as for `nuclhom` and the number new created crystals is stored in the categories 1 and 2 of `frozcryst` for droplets and ice crystals respectively.

A.3.4.5 Non–aerosol specific immersion freezing: `imm_freezing`

This subroutine computes immersion freezing using the Bigg (1953) parameterization. Only droplets larger than 16 µm are considered in this subroutine. The freezing rate for each bin is calculated using the following formula:

$$\mathtt{xjvol}(\mathtt{j}) = \min\left[B \cdot \exp[a \cdot (273.15 - T)] \cdot V_d(\mathtt{j}), 1\right] \tag{A.84}$$

with V_d the volume of the droplet and a and B the Bigg coefficients.

The transfers between the categories are calculated in the same fashion as for the previous subroutines and the number of new created ice crystals is stored in the fourth category of `frozcryst`.

A.3.5 Collision–coalescence subroutines

A.3.5.1 Collision between free aerosol particles and cloud droplets and contact freezing: `APCOLLDR_cntctfreez`

This subroutine calculates the collision of free aerosol particles with droplets as well as contact freezing.

The base equations for the collection of aerosol particles for the number concentrations are:

$$\frac{\partial \mathcal{N}_a}{\partial t}(m_a) = - \int \mathcal{N}_a(m_a) \cdot K_{a,d}(m_a, m_d) \cdot N_d(m_d) \mathrm{d}m_d \tag{A.85}$$

$$\frac{\partial N_d}{\partial t}(m_d) = - \frac{\partial}{\partial m_d} \left[\int m_a \cdot \mathcal{N}_a(m_a) \cdot K_{a,d}(m_a, m_d) \cdot N_d(m_d) \mathrm{d}m_a \right] \tag{A.86}$$

with $K_{a,d}$ the collection kernel for droplet/particle collection. For the other size distributions (surface and mass in all reservoirs and number of aerosol particles in the hydrometeors — only the mass is expressed hereafter), the base equations are expressed as follows:

$$\frac{\partial \mathcal{M}_a}{\partial t}(m_a) = - \int \mathcal{M}_a(m_a) \cdot K_{a,d}(m_a, m_d) \cdot N_d(m_d) \mathrm{d}m_d \tag{A.87}$$

$$\frac{\partial \mathcal{M}_d}{\partial t}(m_d) = \int \mathcal{M}_a(m_a) \cdot K_{a,d}(m_a, m_d) \cdot N_d(m_d) \cdot \mathrm{d}m_a - \frac{\partial}{\partial m_d} \left[\int m_a \cdot \mathcal{M}_a(m_a) \cdot K_{a,d}(m_a, m_d) \cdot N_d(m_d) \mathrm{d}m_a \right] \tag{A.88}$$

The first term on the right–hand side of [the last equation] *represents the contribution due to the collection of aerosol particles and the second term represents the contribution due to the shift of the whole drop number distribution resulting from the drop growth by intake of aerosol particles* (Flossmann, 1987, Chapter II, section 7).

When taking into account contact freezing, equations A.86 and A.88 are changed to represent the freezing in the droplets. We introduce a new factor Γ_{cont} which represents the fraction of ice nuclei among the aerosol particles.
When using the Meyers et al. parameterization, the factor is defined as:

$$\Gamma_{\text{cont,Meyers}} = \frac{\exp[0.262 \cdot (273.15 - T_{drop}) - 2.80]}{\sum (\mathcal{N}_a + \mathcal{N}_d + \mathcal{N}_i)} \cdot 10^{-3} \tag{A.89}$$

When considering the INAS densities approach, Γ_{cont} becomes:

$$\Gamma_{\text{cont,INAS}} = n_s \cdot \frac{\mathcal{S}_a}{\mathcal{N}_a} \tag{A.90}$$

Equations A.86 and A.88 then become:

$$\begin{aligned}\frac{\partial N_d}{\partial t}(m_d) = &-\int \mathcal{N}_a(m_a)\cdot K_{a,d}(m_a,m_d)\cdot \Gamma_{\text{cont}}\cdot N_d(m_d)\cdot \mathrm{d}m_a \\ &- \frac{\partial}{\partial m_d}\left[\int m_a\cdot \mathcal{N}_a(m_a)\cdot K_{a,d}(m_a,m_d)\cdot(1-\Gamma_{\text{cont}})\cdot N_d(m_d)\mathrm{d}m_a\right]\end{aligned} \tag{A.91}$$

$$\begin{aligned}\frac{\partial \mathcal{M}_d}{\partial t}(m_d) = &\int \mathcal{M}_a(m_a)\cdot K_{a,d}(m_a,m_d)\cdot(1-\Gamma_{\text{cont}})N_d(m_d)\cdot \mathrm{d}m_a \\ &- \frac{\partial}{\partial m_d}\left[\int m_a\cdot \mathcal{M}_a(m_a)\cdot K_{a,d}(m_a,m_d)\cdot(1-\Gamma_{\text{cont}})\cdot N_d(m_d)\mathrm{d}m_a\right]\end{aligned} \tag{A.92}$$

and for the ice crystals:

$$\begin{aligned}\frac{\partial N_i}{\partial t}(m_i) = &\int \mathcal{N}_a(m_a)\cdot K_{a,d}(m_a,m_i)\cdot \Gamma_{\text{cont}}\cdot N_d(m_d)\cdot \mathrm{d}m_a \\ &- \frac{\partial}{\partial m_i}\left[\int m_a\cdot \mathcal{N}_a(m_a)\cdot K_{a,d}(m_a,m_i)\cdot\Gamma_{\text{cont}}\cdot N_i(m_i)\mathrm{d}m_a\right]\end{aligned} \tag{A.93}$$

$$\begin{aligned}\frac{\partial \mathcal{M}_i}{\partial t}(m_i) = &\int \mathcal{M}_a(m_a)\cdot K_{a,d}(m_a,m_i)\cdot \Gamma_{\text{cont}}\cdot N_d(m_d)\cdot \mathrm{d}m_a \\ &- \frac{\partial}{\partial m_i}\left[\int m_a\cdot \mathcal{M}_a(m_a)\cdot K_{a,d}(m_a,m_i)\cdot\Gamma_{\text{cont}}\cdot N_i(m_i)\mathrm{d}m_a\right]\end{aligned} \tag{A.94}$$

The growth speeds of the hydrometeors by collection of aerosol particles are given by:

$$\left(\frac{\mathrm{d}m_d}{\mathrm{d}t}\right)_{\text{coll,cont}} = \int m_a\cdot\mathcal{N}_a\cdot\ (1-\Gamma_{\text{cont}})\ \cdot K_{a,d}\cdot \mathrm{d}m_a \tag{A.95}$$

$$\left(\frac{\mathrm{d}m_i}{\mathrm{d}t}\right)_{\text{coll,cont}} = \int m_a\cdot\mathcal{N}_a\cdot\Gamma_{\text{cont}}\cdot K_{a,d}\cdot \mathrm{d}m_a \tag{A.96}$$

A. Calculation of the contact freezing rates

In this first section, `frac` $=\Gamma_{\text{cont}}$, the fraction of aerosol particles acting as ice nuclei, is computed.

B. Preparation for collection of aerosol particles

This section first calculates the mean volumic mass of the cloud droplets (*see* A.3.6.1), based on the equations presented in A.3.6.1. Then, depending on the relative humidity, the collection kernel is computed:

$$\begin{aligned}K_{a,d}(\mathtt{j},\mathtt{i}) = &\ \pi[r_a(\mathtt{i})+r_d(\mathtt{j})]^2 w_{\infty,d}(\mathtt{j}) \\ &\cdot \exp(C_e(\mathtt{j},\mathtt{i}) + \left([C_e(\mathtt{j},\mathtt{i})-C_e(\mathtt{j},\mathtt{i})]\cdot\frac{RH_d - RH_1(\mathtt{L_s})}{\Delta RH_1(\mathtt{L_s})}\right)\end{aligned} \tag{A.97}$$

with C_e the collection efficiency of aerosol particles as computed by Quérel et al. (2014), and $RH_1(\mathtt{L_s}) = (100, 95, 75, 50)$ and $\Delta RH_1(\mathtt{L_s}) = RH_1(\mathtt{L_s\text{+}1}) - RH_1(\mathtt{L_s})$ where $\mathtt{L_s}$ depends on the relative humidity.

This section also computes the fraction of each aerosol size distribution captured by the droplets (equations A.85 and A.86)

$$\texttt{colf(i)} = \frac{1}{2}\sum_{\texttt{j=1}}^{\texttt{nrp}} \left[N_d(\texttt{j})K_{a,d}(\texttt{j},\texttt{i}) + N_d(\texttt{j+1})K_{a,d}(\texttt{j+1},\texttt{i})\right] \tag{A.98}$$

Finally, the ratio of frozen droplets through ice nucleation is computed:

$$\begin{aligned}\texttt{dtdt(j)} = \frac{1}{2}\sum_{\texttt{i=1}}^{\texttt{nac-1}}\sum_{\texttt{kt=1}}^{\texttt{ktyp}} [&\mathcal{N}_a(\texttt{i},\texttt{kt})\cdot K_{a,d}(\texttt{j},\texttt{i})\cdot \texttt{frac}(\texttt{i},\texttt{kt}) \\ &+\mathcal{N}_a(\texttt{i+1},\texttt{kt})\cdot K_{a,d}(\texttt{j},\texttt{i+1})\cdot \texttt{frac}(\texttt{i+1},\texttt{kt})]\end{aligned} \tag{A.99}$$

C. Add the captured aerosol in each droplet category (eq. A.91 and A.92)
This section first calculates the quantity to be added in each size distribution.
Also, based on the volume of water captured by the droplets, the subroutines determines the growth using an upstream advection scheme (A.3.6.2):

$$\frac{\mathrm{d}m_{w,d}}{\mathrm{d}t}(\texttt{j}) = \frac{1}{2}\sum_{\texttt{i=1}}^{\texttt{nac-1}} \frac{B(\texttt{i}) + B(\texttt{i+1})}{m_{w,d}(\texttt{j})} \tag{A.100}$$

where

$$B(\texttt{i}) = \sum_{\texttt{kt=1}}^{\texttt{ktyp}} m_{w,a}(\texttt{i})\mathcal{N}_a(\texttt{i},\texttt{j})\cdot K_{a,d}(\texttt{j},\texttt{i})\cdot[1-\texttt{frac}(\texttt{i},\texttt{kt})] \tag{A.101}$$

The sum of B is divided by $m_{w,d}$ in order to have a growth speed of the droplets in terms of bin number only (it is therefore also divided by the grid parameter `dlnrp` later on).

D. Add the captured aerosol in each ice crystal category (eq. A.93 and A.94)
The exact same calculation is done for the ice crystals, replacing $1-\texttt{frac}$ by `frac`.

E. Update the size distributions after collection
When the advection of droplets and ice crystals has been done, the size distributions are updated by added the quantities previously computed and the frozen droplets are transferred to the crystals.
The number of frozen droplets is stored in the third category of `frozcryst`.

A.3.5.2 Collision–coalescence of droplets: `coalsbott`

This subroutine calculates the collision between cloud droplets and their subsequent growth and eventual break–up, using the Bott (1998) scheme[10].

---

[10] The original scheme in Fortran is available at Andreas Bott's personal page on the University of Bonn's website: www2.meteo.uni-bonn.de/forschung/gruppen/tgwww/people/index_german.php?memid=2&page=fortran.html (visited March 6, 2018)

The stochastic collection equation for the number concentration is expressed as:

$$\frac{\partial N_d}{\partial t}(m_f) = \int_{m=0}^{m_f} \int_{m'=m}^{m_f} N_d(m) \cdot K(m, m') \cdot N_d(m') \mathrm{d}m' \mathrm{d}m \\ - \int_0^{\infty} N_d(m_f) \cdot K(m_f, m) \cdot N_d(m) \mathrm{d}m \tag{A.102}$$

The first term on the right–hand side describes the gain of drops of mass m_f due to collision and coalescence of drops [of mass] *m and $m' = m_f - m$, while the second term gives the loss of drops of mass m_f due to collision with any drop* (Flossmann, 1987, Chapter II, section 8).

For the aerosol particle distributions ($\mathcal{N}_d$, $\mathcal{S}_d$ and $\mathcal{M}_d$), $N_d(m)$ is replaced by the appropriate variable, whereas $N_d(m')$ remains unchanged[11].

A. Initialize calculation

The coalescence scheme works with mass distribution functions instead of number concentration distribution functions (Bott, 1998), we therefore introduce a new function[12]

$$\texttt{gtanp(j)} \equiv g(\texttt{i}) = N_d(\texttt{i}) \cdot m(\texttt{i}) \tag{A.103}$$

For the rest of the subroutine, $m = m(\texttt{i})$ and $m' = m(\texttt{j})$.

Note that when large droplets collide, the model considers a transitory state in which they can have a larger radius than the radius of the largest bin of the initial grid. Therefore, the subroutine uses five additional bins.

B. Collision and coalescence calculation

The size of the smallest bin containing droplets of mass m_f is determined using `ima` and the corresponding bin is referred to as `kk`. The mass of the formed droplets is therefore such as:

$$m(\texttt{kk}) \leq m_f(\texttt{i}, \texttt{j}) \leq m(\texttt{kk+1}) \tag{A.104}$$

As is shown in equation A.104, the combined mass of drops from bins `i` and `j` does not necessarily exactly corresponds to the mass of bin `kk`. Thus the mass density increase has to be split up in bins `kk` and `kk+1`.
In the present scheme, this partitioning is done in a two–step procedure. First the mass density increase is entirely added to bin `kk`; in the second step, a certain fraction of the new mass is transported into bin `kk+1`.

---

[11] these are not the equations presented in the original model by Flossmann (1987) as the scheme now used to compute is more recent

[12] As is the case frequently in the model, the equivalent mass of the droplet here is computed to a factor `cc1`.

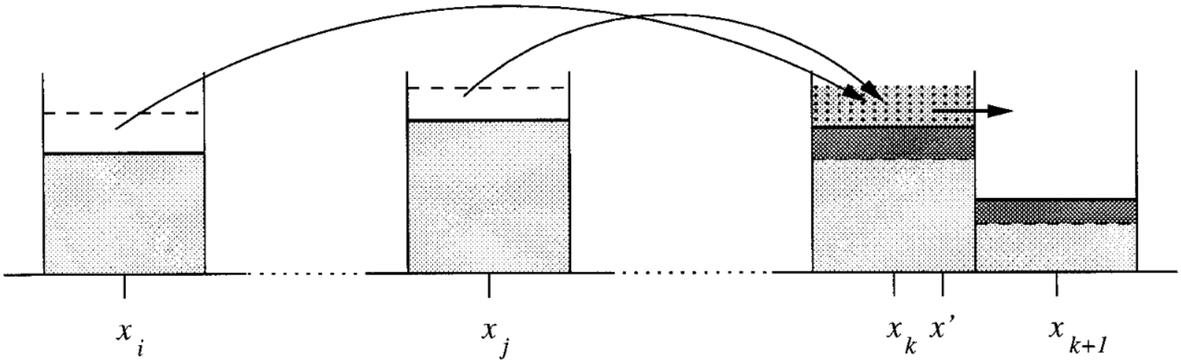

Figure A.3 – Schematic illustration of the flux method of redistribution of droplets of mass $m_f\ (x')$ into bins `kk` and `kk+1` (from Bott, 1998)

1. Droplet number size distribution

The evolution of the mass distribution functions for each bin are determined as follows:

$$g(\mathtt{i}) = g(\mathtt{i}) - g(\mathtt{i})\cdot\frac{\overline{K}(\mathtt{i},\mathtt{j})}{m(\mathtt{j})}\cdot g(\mathtt{j}) \qquad = g(\mathtt{i}) - \delta_i \tag{A.105}$$

$$g(\mathtt{j}) = g(\mathtt{j}) - g(\mathtt{i})\cdot\frac{\overline{K}(\mathtt{i},\mathtt{j})}{m(\mathtt{i})}\cdot g(\mathtt{j}) \qquad = g(\mathtt{j}) - \delta_j \tag{A.106}$$

$$g_k(\mathtt{i},\mathtt{j}) = g(\mathtt{kk}) + g(\mathtt{i})\cdot\overline{K}(\mathtt{i},\mathtt{j})\cdot g(\mathtt{j})\cdot\frac{m_f(\mathtt{i},\mathtt{j})}{m(\mathtt{i})m(\mathtt{j})} \qquad = g(\mathtt{kk}) + \delta_i + \delta_j \tag{A.107}$$

where $\overline{K}$ is an average value of the collection kernel obtained in the subroutine `hall` (A.3.5.4) and $g_k(\mathtt{i},\mathtt{j})$ corresponds to the mass density at grid point `kk` after the first step of the Bott scheme.

The flux, $f_{\mathtt{kk+1/2}}(\mathtt{i},\mathtt{j})$, from bin `kk` to bin `kk+1` is defined as:

$$f_{\mathtt{kk+1/2}}(\mathtt{i},\mathtt{j}) = w(\mathtt{i},\mathtt{j})\cdot\sum_{s=0}^{l}\frac{a_{\mathtt{ij},s}}{(s+1)2^{s+1}}\cdot\left[1-(1-2c_{\mathtt{ij}})^{s+1}\right] \tag{A.108}$$

In this version of DESCAM, the linear flux method ($l = 1$) is used, with:

$$a_{\mathtt{ij},0} = g_k(\mathtt{i},\mathtt{j}) \qquad \text{and} \qquad a_{\mathtt{i},\mathtt{j},1} = g(\mathtt{kk}+1) - g_k(\mathtt{i},\mathtt{j}) \tag{A.109}$$

and

$$w(\mathtt{i},\mathtt{j}) = \frac{\delta_i+\delta_j}{g_k(\mathtt{i},\mathtt{j})} \tag{A.110}$$

The transcription into the model was directly done from the source code of Andreas Bott called `coal1d.f`.

2. APs in the droplets size distributions

Once the evolution of the number size distribution has been computed, all size distributions concerning aerosol particles in the droplets are treated with the subroutine `bottschm` (A.3.6.5).

D. Break-up calculation

In a first step, the values for each size distribution in bins larger than `nrp` are counted and added into four separate counters.

Then, based on the redistribution of large droplets due to their break-up (function `Pcent`, determined in the subroutine `colint`), the size distributions are updated.

A.3.5.3 Collision of droplets and ice crystals and subsequent freezing: `riming`

This subroutine works in the exact same way as the collision–coalescence subroutine. All coalesced elements are transferred to the ice crystals reservoir.

The obtained ice crystals in bins larger than `nic` are lost as no break-up mechanism is considered.

A.3.5.4 Calculation of the collection kernel: `hall`

This subroutine computes the kernel (`cck`) for the collision coalescence process:

$$K(m,m') = \pi \cdot (r+r')^2 \cdot |U_\infty(r) - U_\infty(r')| \cdot E(m,m') \tag{A.111}$$

with r and r' the radii for hydrometeors of mass m and m' respectively, U_∞ their terminal velocities (A.3.2.3) and $E(m,m')$ the collection efficiency calculated based on Hall (1980).

The calculated kernel is then averaged to obtain $\overline{K}$, the kernel used in the Bott scheme (A.3.5.2):

$$\overline{K}(\mathtt{i},\mathtt{j}) = \frac{1}{8} \cdot [K(\mathtt{i\text{-}1},\mathtt{j}) + K(\mathtt{i},\mathtt{j\text{-}1}) + 4K(\mathtt{i},\mathtt{j}) + K(\mathtt{i\text{+}1},\mathtt{j}) + K(\mathtt{i},\mathtt{j\text{+}1})] \tag{A.112}$$

A.3.6 Technical subroutines

A.3.6.1 Compute LWC and IWC: `lwcap` & `lwciwc`

Those two subroutines are using the equations II-11 to II-30 from Flossmann (1987). The equations define the calculation of the liquid water content in aerosol particles and cloud droplets based on the three main following relations (eq. II-26):

$$\bar{\rho} r_d^3 = \rho_w \bar{r}_w^3 + \rho_a r_a^3 \quad \text{total mass of the droplet} \tag{A.113}$$

$$r_d^3 = \bar{r}_w^3 + r_a^3 \quad \text{total volume of the droplet} \tag{A.114}$$

$$Q_{a,d} = \frac{\rho_a r_a^3}{\bar{\rho} r_d^3} \quad \text{mixing ratio of aerosol particle mass in the drop} \tag{A.115}$$

with $\bar{\rho}$ the actual density of the droplet and $\bar{r}_w$ the equivalent radius of the water mass in the drop. This yields:

$$\bar{\rho} r_d^3 = \rho_w (r_d^3 - r_a^3) + \rho_a r_a^3 \tag{A.116}$$

$$\bar{\rho} \left(1 + \frac{r_a^3 (\rho_w - \rho_a)}{\bar{\rho} r_d^3} \right) = \rho_w \tag{A.117}$$

$$\bar{\rho} = \frac{\rho_w \rho_a}{\rho_a - \dfrac{\rho_a r_a^3}{\bar{\rho} r_d^3} (\rho_a - \rho_w)} \tag{A.118}$$

$$\bar{\rho} = \frac{\rho_w \rho_a}{\rho_a - Q_{a,d} (\rho_a - \rho_w)} \qquad \text{(eq. II-27)} \tag{A.119}$$

Furthermore, using equation (II-11: $Q_{a,d} = \dfrac{\mathcal{M}_d}{\bar{\rho} \bar{V}_w N_d}$), we obtain the expression of the mixing ratio of aerosol particle mass:

$$Q_{a,d} = \frac{\mathcal{M}_d}{\bar{V}_w N_d} \left(\frac{\rho_a}{\rho_w \rho_a} - \frac{Q_{a,d} (\rho_a - \rho_w)}{\rho_w \rho_a} \right) \tag{A.120}$$

$$Q_{a,d} \left(1 + \frac{\mathcal{M}_d}{\bar{V}_w N_d} \frac{(\rho_a - \rho_w)}{\rho_w \rho_a} \right) = \frac{\mathcal{M}_d}{\bar{V}_w N_d} \left(\frac{1}{\rho_w} \right) \tag{A.121}$$

$$Q_{a,d} = \frac{\mathcal{M}_d}{\rho_w \bar{V}_w N_d \left(1 + \dfrac{\mathcal{M}_d}{\bar{V}_w N_d} \dfrac{(\rho_a - \rho_w)}{\rho_w \rho_a} \right)} \tag{A.122}$$

$$Q_{a,d} = \frac{\rho_a \mathcal{M}_d}{\rho_w \rho_a \frac{4}{3} \pi r_d^3 N_d + \mathcal{M}_d (\rho_a - \rho_w)} \qquad \text{(eq. II-28)} \tag{A.123}$$

We have the same equations for aerosol particles (eq. II-29 and II-30 in Flossmann, 1987). If $Q_{a,d} = 0$ then the droplet consists only of water, if $Q_{a,d} = 1$ then the droplet consists only of a dry particle. The denominator of $Q_{a,d}$ (corresponding to the variable `den` in DESCAM) is strictly positive (as $\rho_a > \rho_w$), therefore, `den` $= 0$ can only correspond to cases where $N_d = 0$.
Using equations II-22 and II-23, we obtain the liquid water content:

$$LWC_d = \sum_{\mathtt{j=1}}^{\mathtt{nrp}} \bar{\rho} V_d^3 N_d(\mathtt{j}) (1 - Q_{a,d}(\mathtt{j})) \quad \text{and} \quad LWC_a = \sum_{\mathtt{j=1}}^{\mathtt{nac}} \bar{\rho} V_a^3 \mathcal{N}_a(\mathtt{j}) (1 - Q_{APa}(\mathtt{j})) \tag{A.124}$$

The same formula is used to compute the IWC, given that all classes are equivalent in terms of water mass.

A.3.6.2 Upstream advection scheme: `advctupstrm`

This subroutine calculates the upstream advection scheme for the evolution of distribution f:

$$\varphi(\mathtt{j}) = \begin{cases} w(j) \cdot f^n(\mathtt{j+1}) & \text{if} \quad w < 0 \\ w(j) \cdot f^n(\mathtt{j}) & \text{otherwise} \end{cases} \qquad \text{and} \qquad f^{n+1}(\mathtt{j}) = f^n(\mathtt{j}) - [\varphi(\mathtt{j}) - \varphi(\mathtt{j-1})] \tag{A.125}$$

In this subroutine, the growth speed w is normalized in terms of *distance* (due to the division by $6 \cdot$ `dlnrp` and by `idt`) before calling the subroutine, $\dfrac{\Delta x}{\Delta t} = 1$. Therefore, they don't appear in the scheme.

A.3.6.3 Bott (1989) advection scheme applied to the number concentration: `adv4p`

This subroutine solves the continuity equation for the transport of a non–diffusive quantity in a one–dimensional case:

$$\frac{\partial \psi}{\partial t} = -\frac{\partial u \psi}{\partial x} \tag{A.126}$$

In the considered case (growth of hydrometeors particles), the spacial variable corresponds to the radius of the hydrometeors.

This subroutine uses the Bott (1989) positive definite advection scheme defined with (adapted from eq. 13):

$$\psi^{t+\Delta t}(\mathtt{j}) = \psi^{t}(\mathtt{j}) - \left[F_{\mathtt{j+1/2}} - F_{\mathtt{j-1/2}}\right] \tag{A.127}$$

with $F_{\mathtt{j+1/2}}$ and $F_{\mathtt{j-1/2}}$ the ψ–fluxes through the right and left boundary of the grid box, respectively, defined as:

$$F_{\mathtt{j+1/2}} = \left[i^{+}_{\mathtt{j+1/2}} \cdot \frac{\psi(\mathtt{j})}{i_{\mathtt{j}}} - i^{-}_{\mathtt{j+1/2}} \cdot \frac{\psi(\mathtt{j+1})}{i_{\mathtt{j+1}}} \right] \tag{A.128}$$

where

$$i^{+}_{\mathtt{j+1/2}} = \max\left[0, I^{+}(c_{\mathtt{j+1/2}})\right] \tag{A.129}$$

$$i^{-}_{\mathtt{j+1/2}} = \max\left[0, I^{-}(c_{\mathtt{j+1/2}})\right] \tag{A.130}$$

$$i^{+}_{\mathtt{j+1/2}} = \max\left[I_{\mathtt{j}}, i^{+}_{\mathtt{j+1/2}} + i^{-}_{\mathtt{j-1/2}} + \epsilon\right] \tag{A.131}$$

where $c_{\mathtt{j}} = w_r(\mathtt{j}) \cdot \dfrac{\Delta t}{\Delta x}$ is the courant number. Finally, I^{+} and I^{-} are defined as:

$$I^{+}(c_{\mathtt{j+1/2}}) = \sum_{k=0}^{4} \frac{a_{\mathtt{j},k}}{(k+1)2^{k+1}} \left[1 - (1 - 2c^{+}_{\mathtt{j}})^{k+1}\right] \tag{A.132}$$

$$I^{-}(c_{\mathtt{j+1/2}}) = \sum_{k=0}^{4} \frac{a_{\mathtt{j+1},k}}{(k+1)2^{k+1}} (-1)^{k} \left[1 - (1 - 2c^{-}_{\mathtt{j}})^{k+1}\right] \tag{A.133}$$

The details for the coefficients $a_{\mathtt{j},k}$ are to be found in (Bott, 1989, Table 1).

In the subroutine, `y` corresponds to ψ, and `c` to the courant number (`cl` $\equiv c^-$ and `cr` $\equiv c^+$). The variables `fm` and `fp` correspond to the fluxes for negative and positive growth speed respectively:

$$\mathtt{fm(j)} = i^-_{\mathtt{j+1/2}} \cdot \mathtt{w(j+1)} = i^-_{\mathtt{j+1/2}} \cdot \frac{\psi\mathtt{(j+1)}}{i_{\mathtt{j+1}}} \tag{A.134}$$

$$\mathtt{fp(j)} = i^+_{\mathtt{j+1/2}} \cdot \mathtt{w(j)} \quad = i^+_{\mathtt{j+1/2}} \cdot \frac{\psi\mathtt{(j)}}{i_{\mathtt{j}}} \tag{A.135}$$

The size distribution used in input as `y` is updated at the end of the subroutine

$$\psi^{t+\Delta t}\mathtt{(j)} = \psi^t\mathtt{(j)} - [\mathtt{fm(j-1)} + \mathtt{fp(j)}] + [\mathtt{fm(j)} + \mathtt{fp(j-1)}] \tag{A.136}$$

`fm` and `fp` are used as output for the calculation of the advection of the aerosol particles size distributions.

A.3.6.4 Bott (1989) advection scheme applied to the aerosol particles in hydrometeors size distributions: `advctschm`

Once the advection scheme has been applied to the number concentration of hydrometeors, the computed fluxes are used to update the aerosol particles in hydrometeors size distributions ($\mathcal{N}$, $\mathcal{S}$ and $\mathcal{M}$).
For these distributions, the scheme is a modified version of equation A.136, where ψ, in the case of the mass of aerosol particles in the droplets, is expressed as:

$$\psi\mathtt{(j)} = \frac{\mathcal{M}_d\mathtt{(j)}}{N_d\mathtt{(j)}} \tag{A.137}$$

Equation A.136 then becomes:

$$\begin{aligned}\psi^{t+\Delta t}\mathtt{(j)} = \psi^t\mathtt{(j)} &- [\mathtt{fm(j-1)} + \mathtt{fp(j)}] \cdot \psi\mathtt{(j)} \\ &+ [\mathtt{fm(j)} \cdot \psi\mathtt{(j+1)} + \mathtt{fp(j-1)} \cdot \psi\mathtt{(j-1)}]\end{aligned} \tag{A.138}$$

A.3.6.5 Bott (1998) coalescence scheme

This subroutine computes the coalescence of droplets for the aerosol particles in hydrometeors size distributions. The first step of the scheme for these size distributions, here expressed for the mass of aerosol particles in the droplets, becomes:

$$\delta_i = \mathcal{M}_d\mathtt{(i)} \cdot \frac{\overline{K}\mathtt{(i,j)}}{m\mathtt{(j)}} \cdot g\mathtt{(j)} \tag{A.139}$$

$$\delta_j = g\mathtt{(i)} \cdot \frac{\overline{K}\mathtt{(i,j)}}{m\mathtt{(i)}} \cdot \mathcal{M}_d\mathtt{(j)} \tag{A.140}$$

$$\mathcal{M}_{d,k} = \mathcal{M}_d\mathtt{(kk)} + \delta_i + \delta_j \tag{A.141}$$

Finally, the flux between bins `kk` and `kk+1` is expressed as:

$$f_{\mathtt{kk+1/2}}\mathtt{(i,j)} = \mathcal{M}_{d,k} \cdot \left(1 - \frac{g\mathtt{(kk)}}{g_k\mathtt{(i,j)}}\right) \tag{A.142}$$

A.3.7 Balance sheet subroutines

To make sure the model is conservative for water and aerosol particles quantities, regular checks are set into the model using three subroutines

A.3.7.1 Exchanges due the dynamical advection: `bal_flux`

During the dynamical advection with the Smolarkievicz scheme, the amounts of particles and hydrometeors quantities exchanged through the bottom, top and side boundaries are added to corresponding variables contained in the `exchanges` module (A.2.2.7).
In the `bal_flux` subroutine, first, the transferred quantity of water (in g.cm^{-3}) are computed (`fromwat`, `towat` and `sidewat`); then this quantity is stored into the balance sheet for the layer.
Finally, the exchanges of aerosol particles in terms of number, surface area and mass are added to the corresponding variables.

A.3.7.2 Balance sheet for a given layer: `bal_layer`

This subroutine probes the amount of water and aerosol particles in a given layer at a given time in the model. The results as well as the amount in each phase of water and the balance sheet for the layer are then written in the corresponding file.

In this subroutine, as well as the next one, it is possible to use as input a string variable called `localisation` which can be employed to specify where the subroutine was called in the model. This proves to be very useful when debugging the model.

A.3.7.3 Balance sheet on the entire column of atmosphere: `bal_overall`

This subroutine integrates all the values obtained in `bal_layer` and writes the output in a file similar to that of `bal_layer`.

The reason for the existence of two different subroutines is that it might be useful to call `bal_layer` in the microphysics computation, where the layers are treated separately.

A.4 Files

A.4.1 Inputs

Four files are used as input in the 1.5–D version of DESCAM using the INAS density approach.

daten39arn.dat
This file contains the collection efficiencies for aerosol particles capture by droplets. The data in the file come from Quérel et al. (2014).

input_v8.dat
This file contains the settings for the runs: which ice nucleation mechanisms are active (their value then equals 1) as well as the value for r_{lim} and the proportion of mineral aerosol particles.

input_IN.dat
This file is similar to `input_v8.dat` but contains the information on which mineral aerosol particles are active.

output_v8.dat
This file contains the information on which files should be active for the output. The input value has to be logical (*i.e.* `T` or `F`) to be read.

A.4.2 Outputs

All output files have a similar structure: a radical name depicting which file it is, the number of the version and an extension indicating in which conditions it was generated.

Structure of `extension`
In the final version corresponding to Chapter 6 of this thesis, the extension is a string of 17 characters structured as follows: `_**-**-***-******`

The first two stars correspond to the mechanism code:

$$\texttt{code} = \mathrm{Imm} + 2 \cdot \mathrm{Dep} + 4 \cdot \mathrm{Cont} + 8 \cdot \mathrm{Hom} \tag{A.143}$$

The next two stars correspond to the mineral aerosols code:

$$\texttt{codeIN} = \mathrm{KFS} + 2 \cdot \mathrm{Ill} + 4 \cdot \mathrm{Kao} + 8 \cdot \mathrm{Qrz} \tag{A.144}$$

The three stars correspond to the value of r_{lim} in µm: `0.1` or `0.5`.
The last six stars correspond to the amount of mineral aerosol particles included in the model: for the standard case, `1.E-01`.

A.4.2.1 des180.dat

The original output file. It contains most of the outputs that may be useful for analyzing the results.

A.4.2.2 des360.dat

`des360.dat` contains the most relevant information for the cloud properties from `des180.dat` restricted to bulk values to ensure a relatively lighter file (4 to 5 times lighter).
The files contains the evolution in time and altitude, captured every tenth time step for:

- the thermodynamical variables: vertical wind (col. 3), temperature (4), air density (5), relative humidity over water (10) and ice (11);

- the integrated water values: water vapor content (col. 6), liquid water content (7), ice water content (8) and total condensed water content (9);
- the radar reflectivity (col. 12);
- the distinctions in LWC and IWC: cloud water content (col. 13), rain water content (14), cloud ice water content (15) and snow water content (16).

A.4.2.3 cumuls.dat

This files contains the time evolution of the cumulative rain to the ground (col. 2), the rainfall rate (3), the cumulative mass of all aerosol particles (4), their accumulation rate (5) and the same information for each of the particle types (number of column depending on the number of types).

A.4.2.4 nucl.dat and mapnucl.dat

These files contain information on how ice nucleation took place during the simulation. The mechanisms are distributed as follows: condensation (col. 1), deposition (2), contact (3), immersion (4), homogeneous nucleation on droplets (5) and on aerosol particles (6).

nucl.dat contains the time evolution of the integrated value of the number of new ice crystals by each of the mechanisms.

mapnucl.dat contains the rate of ice nucleation (in $\text{min}^{-1}.\text{m}^{-3}$) for all and each of the ice nucleation mechanism as a function of altitude and time. As was the case for `des360.dat`, the data is recorded every tenth time step with an averaged value of the number of frozen crystals.

A.4.2.5 meanwf.dat

This file contains information on the rain hydrometeors: their critical fall diameter (col. 2 and 4), the mean speed of the falling hydrometeors (3, 5 and 6) and the vertical wind (7).

A.4.2.6 grid***.dat

Three files are generated containing the radii of each bin for the different categories.

A.4.2.7 profini.dat

This file contains the profiles at $t = 0$ for the temperature (col. 2), pressure (3), mass of water vapor (4), air density (5), potential temperature (6), relative humidity over water (7).

A.4.2.8 capini.dat

The initial aerosol particles size distributions are stored in this file (col. 3 to $3 + \texttt{ktyp}$).

A.4.2.9 checkwater.dat

In this file is stored the integrated water balance:

- the flux of water through the lower (col. 2), upper (3) and lateral (4) boundaries of the air columns and the total flux through the closed surface (5);
- the integrated mass of water vapor (col. 6), liquid water (7), ice (8) and the total mass of water molecules (9);
- the balance of water in the column (col. 10);
- the place in the model at which the subroutine was called (col. 11).

A.4.2.10 checkAP.dat

Several files are generated: `checkAPnumb` (`im`=1), `checkAPsurf` (`im`=2) and `checkAPmass` (`im`=3), each structured in the same way. In order to find all files easily, the `checkAP` files are stored in a `checkAP` folder that needs to exist before the simulation starts. At the end of each file name, the number of the aerosol particle type `kt` is precised.

These files are structured as follows (with the example of aerosol particle number):

- the flux of aerosol through the lower (col. 2), upper (3) and lateral (4) boundaries of the air columns and the total flux through the closed surface (5);
- the integrated number of dry aerosol particles (col. 6), of aerosol particles in the cloud droplets (7), and in the ice crystals (8) and the number of aerosol particles (9);
- the balance of aerosol particles number in the column (col. 10);
- the place in the model at which the subroutine was called (col. 11).

A.4.2.11 layer***.dat

These files have a similar structure to `checkwater` and `checkAP`. When `balance` is set to true, up to 1500 files can be created. So many files generally lead to a `core dump`. Therefore, the amount of file created (*i.e.* the type and layers involved) have to be chosen carefully.
Given the large amount of files created, they are store in a folder containing the information of the run (version and extension) inside a folder called `layerwat`. Both folders should be created before the simulation starts. (Generally, as the first print in the files is done at `t=2`, it is quite easy to let the simulation start and to copy the name of the extension folder.)

These files are structured as follows:

- the flux of water through the lower (col. 2), upper (3) and lateral (4) boundaries of the layer and the total flux through the closed surface (5);
- the mass of water in the aerosol particles (col. 6), in the droplets (7), the relative humidity (8), the ratio of water in the droplets (9), the mass of water vapor (10), of liquid water (11), the mass of ice (12) and the total mass of water molecules (13);
- the balance of water in the layer (col. 14);
- the place in the model at which the subroutine was called (col. 15).

for `layerwat` and for `layerAP*`, we have:

- the total flux of aerosol particles through the closed surface (col. 2);
- the number of dry aerosol particles (col. 3), of aerosol particles in the cloud droplets (4), and in the ice crystals (5) and the number of aerosol particles (6);
- the balance of aerosol particles number in the layer (col. 7);
- the place in the model at which the subroutine was called (col. 8).

A.4.2.12 spectra.dat

These files contain the spectra for all the size distributions at a given altitude for a given type of aerosol particles. By default, they are written every fifth time step and every fifth layer.
As was the case for the previous files, the output is stored in a folder containing the information of the run inside a folader called `spectra`.

The spectra files are structured as follows:

- radius of the aerosol particles bin (col.2), their number (3), total surface area (5) and mass (4);
- radius of the droplet bin (col. 6), their number (7), the total number of aerosol particles in the droplets (10), their mass (8) and surface area (9);
- radius of the ice crystals bin (col. 11), their number (12), the total number of aerosol particles in the ice crystals (15), their mass (13) and surface area (14).

A.4.2.13 readme.dat

This file contains in written form the information contained in the file extension.